

AFRL-AFOSR-UK-TR-2015-0018



GRAPHENE-BASED POLYMER NANOCOMPOSITES

Professor Robert J. Young

**University of Manchester
School of Materials
Oxford Road
Manchester M13 9PL, United Kingdom**

EOARD GRANT #FA8655-12-1-2058

Report Date: March 2015

Final Report from 1 April 2012 to 31 March 2015

Distribution Statement A: Approved for public release distribution is unlimited.

**Air Force Research Laboratory
Air Force Office of Scientific Research
European Office of Aerospace Research and Development
Unit 4515, APO AE 09421-4515**

REPORT DOCUMENTATION PAGE				Form Approved OMB No. 0704-0188	
<p>Public reporting burden for this collection of information is estimated to average 1 hour per response, including the time for reviewing instructions, searching existing data sources, gathering and maintaining the data needed, and completing and reviewing the collection of information. Send comments regarding this burden estimate or any other aspect of this collection of information, including suggestions for reducing the burden, to Department of Defense, Washington Headquarters Services, Directorate for Information Operations and Reports (0704-0188), 1215 Jefferson Davis Highway, Suite 1204, Arlington, VA 22202-4302. Respondents should be aware that notwithstanding any other provision of law, no person shall be subject to any penalty for failing to comply with a collection of information if it does not display a currently valid OMB control number.</p> <p>PLEASE DO NOT RETURN YOUR FORM TO THE ABOVE ADDRESS.</p>					
1. REPORT DATE (DD-MM-YYYY) 31 March 2015		2. REPORT TYPE Final Report		3. DATES COVERED (From – To) 1 April 2012 – 31 March 2015	
4. TITLE AND SUBTITLE GRAPHENE-BASED POLYMER NANOCOMPOSITES				5a. CONTRACT NUMBER EOARD 12-2058	
				5b. GRANT NUMBER FA8655-12-1-2058	
				5c. PROGRAM ELEMENT NUMBER 61102F	
				5d. PROJECT NUMBER	
6. AUTHOR(S) Prof. Robert J. Young				5d. TASK NUMBER	
				5e. WORK UNIT NUMBER	
7. PERFORMING ORGANIZATION NAME(S) AND ADDRESS(ES) University of Manchester School of Materials Oxford Road Manchester M13 9PL, United Kingdom				8. PERFORMING ORGANIZATION REPORT NUMBER N/A	
9. SPONSORING/MONITORING AGENCY NAME(S) AND ADDRESS(ES) EOARD Unit 4515 APO AE 09421-4515				10. SPONSOR/MONITOR'S ACRONYM(S) AFRL/AFOSR/IOE (EOARD)	
				11. SPONSOR/MONITOR'S REPORT NUMBER(S) AFRL-AFOSR-UK-TR-2015-0018	
12. DISTRIBUTION/AVAILABILITY STATEMENT Distribution A: Approved for public release; distribution is unlimited.					
13. SUPPLEMENTARY NOTES					
14. ABSTRACT <p>The reinforcement mechanisms in graphene-based nanocomposites have been studied in this project, which primarily consists of three parts: the size and orientation effects of the graphene-based nano-fillers and their interfacial adhesion with the matrix. Overall Raman spectroscopy has been demonstrated to be a powerful technique to study the graphene-based nanocomposites. The deformation of small size graphene has been followed and a new model has been established. Additionally, the deformation of monolayer graphene oxide (GO) has been followed for the first time. It appears that continuum mechanics is still valid, and the approximately constant strain distribution along the GO flake suggests a better stress transfer efficiency of GO than that of graphene. The spatial orientation of graphene has been studied based on the Raman scattering obtained from transverse sections of graphene, where the Raman bands intensities show a strong polarization dependence. Based on this, a new model has been established to quantify the spatial orientation of graphene in terms of an orientation distribution function, and the spatial orientation of monolayer graphene has been further confirmed by its surface roughness. It is also shown how the spatial orientation of graphene-based fillers affects the mechanical properties of the nanocomposites, through the first determination of the Krenchel orientation factor for nanoplatelets. The findings on both the size and orientation effects have been employed to study the deformation mechanics of bulk GO reinforced nanocomposite films. It has been demonstrated for the first time that the effective modulus of GO can be estimated using the Raman D band shift rate, and this is in agreement with the value measured using conventional mechanical testing. The effective modulus of GO is found to be lower than its Young's modulus, probably due to the mis-orientation, waviness, wrinkling and agglomeration of the GO fillers.</p>					
15. SUBJECT TERMS EOARD, Materials, nanocomposites, graphene					
16. SECURITY CLASSIFICATION OF:			17. LIMITATION OF ABSTRACT SAR	18. NUMBER OF PAGES 182	19a. NAME OF RESPONSIBLE PERSON Matthew Snyder
a. REPORT UNCLAS	b. ABSTRACT UNCLAS	c. THIS PAGE UNCLAS			19b. TELEPHONE NUMBER (Include area code) +44 (0)1895 616420

FINAL TECHNICAL REPORT

Grant Number: FA8655-12-1-2058

Research Title: GRAPHENE-BASED
POLYMER NANOCOMPOSITES

PI Name: Professor Robert J Young

School of Materials, University of
Manchester, Oxford Road, Manchester M13
9PL, UK

Period of Performance: 1 April 2012 - 31

March 2015

Contents

Abstract	6
List of Symbols.....	7
List of Abbreviations	11
Acknowledgements	12
Objectives and Structure of the Thesis	13
Chapter 1 Graphene-based Nanocomposites	16
1.1 Graphene.....	16
1.1.1 Preparation	16
1.1.2 Mechanical Properties.....	18
1.2 Graphene Oxide	20
1.2.1 Preparation	20
1.2.2 Mechanical Properties.....	21
1.3 Graphene-based Polymer Nanocomposites	22
1.3.1 Preparation	22
1.3.1.1 Solvent Blending	22
1.3.1.2 <i>In-situ</i> Polymerization.....	22
1.3.1.3 Melt Blending.....	23
1.4 Mechanics and Characterization	24
1.4.1 Interface	25
1.4.2 Aspect Ratio	29
1.4.3 Orientation	31
1.5 Conclusions.....	36
References	36
Chapter 2 Raman Spectroscopy of Graphene	45
2.1 Introduction.....	45
2.2 Principle of Raman Scattering	45
2.2.1 Classical Theory	45
2.2.2 Quantum Theory.....	47

2.3 Instrumentation	49
2.3.1 Raman Spectrometer.....	49
2.3.2 <i>In-situ</i> Deformation Raman Spectroscopy	50
2.3.3 Raman Spectroscopy Data Analysis	51
2.4 Raman Spectroscopy of Graphene and Graphene Oxide.....	51
2.4.1 Raman G band.....	52
2.4.2 Raman D, D' and 2D bands	53
2.4.3 Strain in Graphene	56
2.4.4 Orientation of Graphene	62
2.4.4.1 Graphene In-Plane Rotation	63
2.4.4.2 Graphene Out-of-Plane Rotation	65
2.5 Conclusions	67
References	67
Chapter 3 The Deformation of Wrinkled Graphene	75
3.1 Introduction.....	75
3.2 Experimental	75
3.2.1 Materials	75
3.2.2 Characterization.....	76
3.3 Results and Discussion	76
3.3.1 Size of Graphene Islands.....	76
3.3.2 Raman Spectroscopy	77
3.3.3 Measurement of Laser Spot Size	80
3.3.4 Modelling	81
3.4 Conclusions	89
References	90
Chapter 4 Deformation of Monolayer Graphene Oxide.....	93
4.1 Introduction.....	93
4.2 Experimental	94
4.2.1 Materials	94
4.2.2 Preparation	94
4.2.3 Characterization.....	95
4.3 Results and Discussion	95
4.3.1 Microstructure of the GO Flakes	95
4.3.2 Deformation of Monolayer GO	97
4.3.3 Deformation Mechanics of Monolayer GO	102

4.4 Conclusions.....	105
References	105
 Chapter 5 Quantitative Determination of the Spatial Orientation of Graphene by Polarized Raman Spectroscopy 109	
5.1 Introduction.....	109
5.2 Experimental	110
5.2.1 Preparation	110
5.2.2 Characterization.....	111
5.3 Results and Discussion	112
5.3.1 Graphene-Cu	112
5.3.2 Graphene-PET	116
5.3.3 Spatial Orientation of Graphene.....	120
5.3.4 HOPG and Graphene Paper	124
5.3.5 Orientation Distribution Function	126
5.4 Conclusions.....	130
References	131
 Chapter 6 Determination of the Degree of Orientation of Graphene-based Nanoplatelets in Nanocomposites..... 134	
6.1 Introduction.....	134
6.2 Experimental	135
6.2.1 Materials	135
6.2.2 Preparation	135
6.2.3 Characterization.....	136
6.3 Result and Discussion.....	137
6.3.1 Model of Spatial Orientation.....	137
6.3.2 GO/PVA Nanocomposites	139
6.3.3 GO/epoxy and GO/PMMA	142
6.3.4 Orientation distribution function (ODF).....	144
6.3.5 Krenchel orientation factor η_o	145
6.3.6 Comparison with the Hermans' model	147
6.4 Conclusions.....	149
References	149
 Chapter 7 Interfacial Stress Transfer in Graphene Oxide Nanocomposites ... 151	
7.1 Introduction.....	151

7.2 Experimental	152
7.2.1 Materials	152
7.2.2 Preparation	152
7.2.3 Characterization.....	153
7.3 Results and Discussion	154
7.3.1 Microstructure of GO and GO/PVA Films	154
7.3.2 Mechanical Properties of GO/PVA Films.....	158
7.3.3 Deformation of Nanocomposites.....	161
7.3.4 Mechanics of Deformation.....	164
7.4 Conclusions.....	169
References	170
Chapter 8 Conclusions and Suggestions for Future Work.....	174
8.1 Conclusions.....	174
8.1.1 Model Monolayer Graphene and Graphene Oxide Nanocomposites	174
8.1.2 Spatial Orientation of Graphene and GO	175
8.1.3 Deformations Mechanics of GO in Nanocomposites	176
8.2 Suggestions for Future Work	177
8.2.1 Deformation Mechanics of Mono- and Few- Layer GO Flake	177
8.2.2 Nanocomposites Reinforced Using Liquid Exfoliated Graphene.....	177
8.2.3 Wrinkling of Graphene and GO	178
8.2.4 Other Two-Dimensional (2D) Materials.....	178
References	179

Abstract

The reinforcement mechanisms in graphene-based nanocomposites have been studied in this project, which primarily consists of three parts: the size and orientation effects of the graphene-based nano-fillers and their interfacial adhesion with the matrix. Overall Raman spectroscopy has been demonstrated to be a powerful technique to study the graphene-based nanocomposites.

The deformation of small size graphene has been followed and a new model has been established to consider both the non-uniformity of strain along the graphene and laser intensity within the laser spot, which interprets the observed unusual Raman band shift well. Additionally, the deformation of monolayer graphene oxide (GO) has been followed for the first time. It appears that continuum mechanics is still valid, and the approximately constant strain distribution along the GO flake suggests a better stress transfer efficiency of GO than that of graphene.

The spatial orientation of graphene has been studied based on the Raman scattering obtained from transverse sections of graphene, where the Raman bands intensities show a strong polarization dependence. Based on this, a new model has been established to quantify the spatial orientation of graphene in terms of an orientation distribution function, and the spatial orientation of monolayer graphene has been further confirmed by its surface roughness. This model has been extended to a variety of graphene-based materials and nanocomposites. It is also shown how the spatial orientation of graphene-based fillers affects the mechanical properties of the nanocomposites, through the first determination of the Krenchel orientation factor for nanoplatelets.

The findings on both the size and orientation effects have been employed to study the deformation mechanics of bulk GO reinforced nanocomposite films. It has been demonstrated for the first time that the effective modulus of GO can be estimated using the Raman D band shift rate, and this is in agreement with the value measured using conventional mechanical testing. The effective modulus of GO is found to be lower than its Young's modulus, probably due to the mis-orientation, waviness, wrinkling and agglomeration of the GO fillers.

List of Symbols

A	Amplitude
a_n	Proportion of fibres at an angle to the stress direction
C_1/C_2	Parameter in quantitative orientation analysis
c	Speed of light
d	Thickness for flake filler or diameter for fibre filler
E	Oscillating electric field
E_0	Amplitude of vibration
E_1/E_2	Molecular energy before/after scattering
E_i/E_s	Incident/scattered photon energy
E_{comp}	Young's modulus of the composites
$E_{\text{eff}}(\text{GO})$	effective modulus of the graphene oxide
E_{filler}	Young's modulus of the filler
E_{GO}	Young's modulus of the graphene oxide
E_{gra}	Young's modulus of the graphene
E_{m}	Young's modulus of the matrix
\vec{e}_i / \vec{e}_s	Unit vectors of the incident/scattered laser radiation
$FWHM$	full width at half maximum of the Raman band
$FWHM_{2D}$	full width at half maximum of the Raman 2D band
$dFWHM_{2D}/d\varepsilon$	The broadening rate of Raman 2D band
$(dFWHM_{2D}/d\varepsilon)_{\text{ref}}$	The reference broadening rate of Raman 2D band
f	Hermans' orientation factor
$f_N(\theta)$	Orientation distribution function
G_{m}	Shear modulus of matrix
h	Planck's constant
I	Intensity of the Raman band
$I_{2D}/I_D/I_G$	Intensity of the Raman 2D/D/G band
I_{gra}	Raman band intensity of single graphene sheet

$I_{\text{laser}}(L,T)$	Raman band intensity of unit (L,T)
I_o	Amplitude in the intensity fitting
I_p	Raman band intensity at the peak position.
$I_{\text{sample}}^{\text{VV}}(\Phi)/I_{\text{sample}}^{\text{VH}}(\Phi)$	Raman band intensity of the sample relative to Φ in VV/HV laser polarization
$I_{\text{Total}}(\omega)$	Intensity of the simulated Raman band
$I(\delta)$	X-ray scattering intensity in the azimuthal scan
$I(r)$	Raman band intensity within laser spot
$I(\omega,L,T)$	Raman band intensity of the unit (L,T)
L_c	Critical length
l	Length of filler or graphene
$P_i(\cos \theta)$	Legendre polynomial of the i th degree
$\langle P_i(\cos \theta) \rangle$	Average value of $P_i(\cos \theta)$
q	Nuclear displacement
q_o	Amplitude of molecule nuclear vibration
r	Distance to the centre of the laser spot
r_0	Radius of the laser beam
s	Aspect ratio of filler
t	Thickness of filler
t_0	Time
t_{GO}	Thickness of graphene oxide
t_{gra}	Thickness of graphene
t_m	Thickness of elementary matrix
V_{filler}	Volume fraction of the filler
V_{GO}	Volume fraction of the graphene oxide
V_m	Volume fraction of the matrix
w_{GO}	Mass fraction of the graphene oxide
x	Distance along the filler from one end
x_0	Position of the graphene edge
x_l	Position of the laser spot

Φ	Angle of laser polarization
$\Phi_X/\Phi_Y/\Phi_Z$	Angle of laser polarization in the X/Y/Z direction
α	Polarizability tensor
α_0	Polarizability tensor at equilibrium
α_i	Polarizability tensor for any band
$\alpha_{A_{1g}}/\alpha_{E_{2g}}$	Polarizability tensor for A_{1g}/E_{2g} band
$(\partial\alpha/\partial q)_0$	Change rate of α against the molecule nuclear displacement
β	Shear potential
$\gamma_{2D}/\gamma_D/\gamma_G$	Grüneisen parameter of the Raman 2D/D/G band
δ	Angle in the azimuthal
ε	Strain
$\varepsilon_l/\varepsilon_t$	Strain in the longitudinal/transverse directions
ε_m	Strain of the matrix
ε_r	Real strain of the filler
ζ	Angle between the element and the stress direction
η	Reinforcement efficiency factor
η_l	Size factor
η_o	Krenchel orientation factor
Θ	Angle between the incident and the scattering X-ray
θ	Angle between the surface normal of graphene and sample
λ	Wavelength of laser or X-ray
λ_2/λ_4	Parameter in orientation distribution function
μ	Molecular dipole moment
ν	Poisson's ratio
ν_0	Frequency of the light beam
$\Delta\nu_0$	Frequency change of the incident and scattered photon
ν_q	Frequency of molecule nuclear vibration
ξ	Rotation angle of graphene
ρ_{GO}	Density of GO
ρ_{PVA}	Density of PVA

σ_{filler}	Axial stress in the filler
$\overline{\sigma}_{\text{filler}}$	Averaged axial stress in the filler
τ	Shear stress
φ	Angle between the incident laser polarization and reference direction (graphene edge, axis of carbon fibre, nanotube and graphite whisker. etc)
φ_w	Angle between the graphite layers and the whisker axis
ω	Raman wavenumber
ω_0	Raman band position
ω_D / ω_{2D}	Position of Raman D/2D band
$\omega_D^0 / \omega_G^0 / \omega_{2D}^0$	Position of Raman D/G/2D band at zero strain
$\omega_{L,T}$	Position of the simulated Raman band of the unit (L, T)
$\Delta\omega_G^\pm$	Variation of Raman G+(G-) band position
$\Delta\omega_{2D}$	Variation of Raman 2D band position
$d\omega_D/d\varepsilon$	Raman D band position shift rate
$(d\omega_D/d\varepsilon)_{\text{ref}}$	Reference Raman D band position shift rate
$d\omega_{2D}/d\varepsilon$	Raman 2D band position shift rate
$(d\omega_{2D}/d\varepsilon)_{\text{ref}}$	Reference Raman 2D band position shift rate
ϕ	Orientational angle of graphene

List of Abbreviations

AFM	Atomic force microscope
BZ	Brillouin zone
C	Carbon
°C	Celsius degree
CNT	Carbon nanotube
Cu	Copper
CVD	Chemical vapour deposition
DR	Double resonance
DMF	Dimethylformamide
DMTA	Dynamic mechanical thermal analysis
eV	Electronvolt
fGO	Functionalized graphene oxide
GO	Graphene oxide
GPa	GigaPascal
HI	Hydrogen iodide
HOPG	Highly ordered pyrolytic graphite
min	Minute
MMT	Montmorillonite
MPa	MegaPascal
mW	Microwatt
nm	Nanometer
NMP	N-methyl-2-pyrrolidone
ODF	Orientation distribution function
PA6	Polyamide 6
PANI	Polyaniline
PC	Polycarbonate
PE	Polyethylene

PET	Poly(ethylene terephthalate)
PMMA	Poly(methyl methacrylate)
PP	Polypropylene
PS	Polystyrene
PVA	Poly(vinyl alcohol)
rGO	Reduced graphene oxide
SAXS	Small-angle X-ray scattering
SEM	Scanning electron microscope
SiO ₂	Silicon dioxide
TEM	Transmission electron microscope
TPa	TeraPascal
UV	Ultraviolet
vol%	Volume fraction
WAXS	Wide-angle X-ray scattering
wt%	Mass fraction
XRD	X-ray diffraction
μm	Micrometer

Objectives and Structure of the Report

Since its isolation in 2004, graphene has attracted tremendous attention in both academia and industry. Among all of the potential applications of graphene, its application in nanocomposites is clearly one of the most promising and achievable. Its large surface area, exceptional mechanical properties and also the multifunctionality make it stand out as the reinforcement filler for the next generation composites, as do its derivatives, such as graphene oxide (GO), reduced GO (rGO) and functionalized GO (fGO). Each of them has its own advantages but also disadvantages. From the mechanical point of view, pristine graphene has a high modulus of about 1 TPa, but suffers from poor interfacial adhesion due to its inert surface. GO, fGO and rGO are able to interact with matrix but have intrinsic stiffness of only one fourth of that of graphene. Hence the choice of the filler indeed relies on its target applications.

A number of types of graphene and various methods can be employed to prepare the nanocomposites. To avoid trial-and-error, it would be significantly instructive to focus on the key issues from the mechanics point of view, so that the reinforcement efficiency can be generally evaluated. So far, a systematic method for this purpose is still needed.

To solve these problems, this thesis aims at establishing models to quantitatively analyse the major factors that control the reinforcement of the nanocomposites, that is, lateral dimension and orientation of the graphene-based fillers, and the interfacial adhesion between them and matrix.

Chapter 1 briefly reviews the development of graphene-based nanocomposites, including the nature of graphene/GO and the preparation methods. Focus is paid on three major aspects of the mechanics of nanocomposites: the interface, aspect ratio and orientation, where some of the characterization methods and the models for evaluation are discussed. Chapter 2 reviews some of the literature on the characterization of graphene using Raman spectroscopy, which is the primary characterization method in this thesis. It briefly introduces the principles of Raman

scattering and the origins of the different Raman bands of graphene. Attention is focused on the stress/strain induced Raman band position shift, and the polarization dependence of the Raman band intensity upon the orientation of graphene.

Chapters 3&4 study the size effect of the filler on the reinforcement of nanocomposites. Chapter 3 presents a study on monitoring the deformation of small size graphene, which is different from the large size exfoliated graphene studied before. A model to consider the non-uniformity of the strain distribution in the graphene, and the laser intensity within the spot size is established, which explains the observed abnormal Raman band shift well. Chapter 4 presents a study on the deformation mechanics of GO. It is found that, similar to that of graphene, the Raman D band downshifts as the GO is deformed, and the shift rate can be used to monitor the variation of strain along the GO flake, particularly from the edge. The almost constant strain distribution along the GO flake demonstrates that it also follows continuum mechanics, and also implies a better stress transfer efficiency of GO than that of graphene when used as fillers in nanocomposites.

Chapters 5&6 study the orientation effect of the filler on the reinforcement of nanocomposites. Chapter 5 reports the observation of Raman scattering signal from the transverse section of monolayer graphene, and the Raman bands intensities show a strong polarization dependence. Based on this, a model is established based on the polarizability tensors to not only quantify the spatial orientation of graphene but also reconstruct the orientation distribution function. This model is further extended to other graphene-based bulk material such as HOPG and specimen with a lower orientation degree such as graphene paper. Chapter 6 further develops the model to quantify the spatial orientation of GO in three types of nanocomposites. Through the determination of the classical Krenchel orientation factor for three-dimensionally aligned platelets, the effect of spatial orientation of filler on the mechanical properties of the composites is revealed.

Chapter 7 presents a study on the mechanics of GO reinforced poly(vinyl alcohol) bulk nanocomposites, taking into account both the size and orientation effect of the GO flakes discussed before. According to the knowledge of Grüneisen parameter, the Raman D band shift rate with strain is further developed to estimate the effective

modulus of GO in the nanocomposites, and it is further confirmed by the good agreement of the modulus calculated in this way and the values obtained using conventional mechanical testing. It is found that the effective modulus of GO in nanocomposites is significantly lower than its Young's modulus, the possible reasons could be mis-orientation, waviness, wrinkling and agglomeration of the GO fillers.

Chapter 8 presents the conclusions for this work. Additionally, it features some of the future work that can be studied based upon this thesis, including the mechanics of few-layer GO flakes, mechanics of liquid-phase exfoliated graphene, wrinkling of graphene/GO and relevant studies on other 2D crystals.

Chapter 1 Graphene-based Nanocomposites

1.1 Graphene

Graphene is a two-dimensional atomically thick carbon sheet with all the carbon atoms arranged in a hexagonal lattice, and is the basic building block of all the graphitic carbon materials [1]. It has attracted tremendous attentions since its first isolation and identification by mechanical cleavage in 2004 [2].

1.1.1 Preparation

Graphene was prepared firstly by mechanical cleavage using ‘Scotch tape’ method [2]. Apart from that, many other methods have been developed, with each of which possessing its own advantages and disadvantages. The methods can be generally grouped into two categories, one is termed the ‘top-down’ method, where the starting materials are bulk materials such as graphite; while the other one is known as the ‘bottom-up’ method, which starts with small molecules [3].

1) Top-Down

‘Top-down’ stands for the separation of graphene layers from bulk materials. The well-known ‘Scotch-tape’ method belongs to this category, where people used commercial Scotch tape to separate graphene repeatedly from highly-ordered pyrolytic graphite (HOPG) [2], followed by transferring it to different substrates such as a silicon wafers or poly(methyl methacrylate) (PMMA) beam. Graphene prepared by this method is suitable for fundamental studies because of the high quality and large lateral dimension [4, 5], but not for production scale-up (Fig. 1.1(a)).

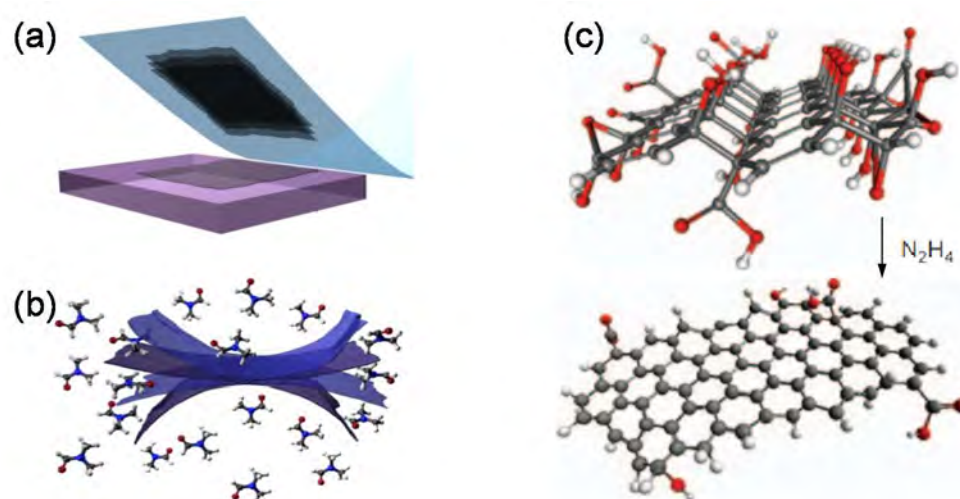


Figure 1.1 Schematic illustration of the ‘top-down’ method (a) mechanical cleavage [2, 6], (b) liquid exfoliation [6, 7] and (c) reduction of GO [8].

Liquid-phase exfoliation can also be employed to isolate graphene. It was reported that with the assistance of centrifuge and sonication, graphene layers as large as 1 μm can be exfoliated in organic solvents such as N-methyl-2-pyrrolidone (NMP) [7, 9] and dimethylformamide (DMF) [10] for which the surface energy is comparable to the energy needed to peel graphene apart [7]. This method is better for scale-up production however it suffers from the production of small size graphene flakes (Fig. 1.1(b)). Similarly, graphene can also be prepared by electrochemical exfoliation [11].

Another alternative route is the reduction of graphene oxide (GO), a derivative of graphene with a large amount of functional groups. After reduction the graphitic structure is partially restored [12]. This method facilitates remarkably the dispersion of graphene in matrix for a composite application but attention should be paid to the increased defect density (Fig. 1.1(c)) [12].

2) Bottom-Up

In the ‘bottom-up’ method, graphene is synthesised from the carbon atoms of other small molecules. Chemical vapour deposition (CVD) is a typical process in this category [13], where carbon atoms from the decomposed gas molecules deposit onto the catalyst substrate at high temperature to form graphene (Fig. 1.2(a)). The graphene size and stacking order [13-15] can be optimized by changing the gas source [16], temperature [17], pressure [18] as well as the substrate underneath [19].

This method provides high quality graphene at low cost so it is regarded as one of the most promising production methods once the transfer and recycling process is optimized [6, 20].

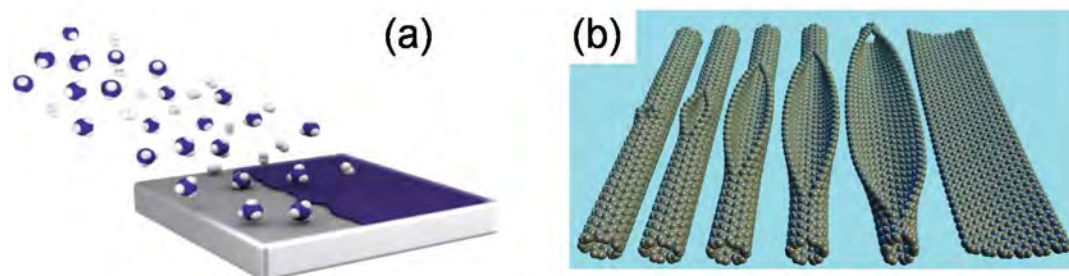


Figure 1.2 Schematic illustration of ‘bottom-up’ graphene preparation (a) CVD [6, 13] and (b) Unzipping of CNTs [21].

The epitaxial growth process is a substrate-based method [22], where the thermal treatment sublimates the silicon atoms of a SiC substrate, and the remaining carbon atoms subsequently re-organize into high-quality graphene layers [23]. However the cost of the SiC substrate is high [6].

Besides these two methods, other methods have also been reported including polymerization of monomer precursors [24], and the unzipping of carbon nanotube (CNT) (Fig. 1.2(b)) [21, 25].

1.1.2 Mechanical Properties

By indenting graphene suspended over a hole using an atomic force microscope (AFM) tip (Fig. 1.3(a)), Lee et al. [26] directly measured the strength and Young’s modulus of monolayer graphene to be around 130 GPa and 1 TPa, respectively. These values are widely accepted nowadays. The lower value of 0.5 TPa measured earlier Frank et al. [27] using a similar method but with few-layer graphene is probably due to the low shear modulus between graphene layers [28, 29].

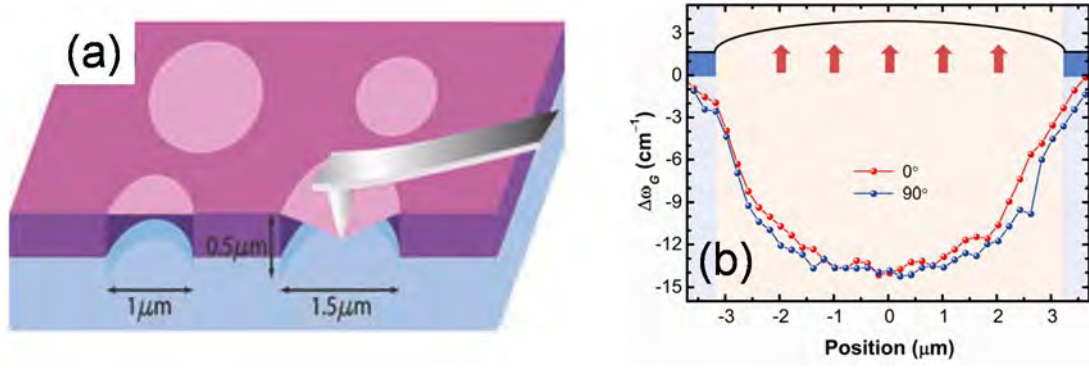


Figure 1.3 (a) Schematic illustration of the nanoindentation test on graphene suspended on holes [26]. (b) Raman G band position in a line scanning across a suspended graphene flake [30].

Other than direct measurement, Raman spectroscopy [30] is another candidate method based on the stress/strain induced Raman band shift [31]. By mapping the Raman spectra at different positions of a pressured graphene (Fig. 1.3(b)), the Young's modulus of mono- and bi-layer graphene was estimated to be 2.4 and 2.0 TPa, respectively. The value higher than expected was interpreted as due to the non-linear behaviour of graphene that being stiffer at low strain, yet it is in contrast to the reported stiffening at higher strain due to wrinkle flattening [32, 33].

Beyond the in-plane properties, the interlayer shear modulus has been estimated by Tan et al. [28] to be around 4.3 GPa using a Raman active vibrational mode resulting from the relative motion of adjacent graphene layers. This low interlayer shear modulus might be responsible for the low modulus of multilayer graphene in nanocomposites [34] and the reversible loss of Bernal stacking of few-layer graphene under deformation [29].

In reality, however, different types of defects [35] affect the mechanical properties of graphene unavoidably [36], especially for materials prepared using the CVD method with massive detrimental grain boundaries and ripples [32, 37].

1.2 Graphene Oxide

1.2.1 Preparation

Generally graphite oxide is prepared by treating graphite using strong oxidizing agents [38], followed by removing the residual chemicals. It was originally prepared by Brodie et al. [39] and Staudenmaier et al. [40], yet most of the methods [41] used nowadays are based on the less time-consuming and hazardous Hummers' method [42]. After dispersing to few-layers, it is generally called 'graphene oxide'.

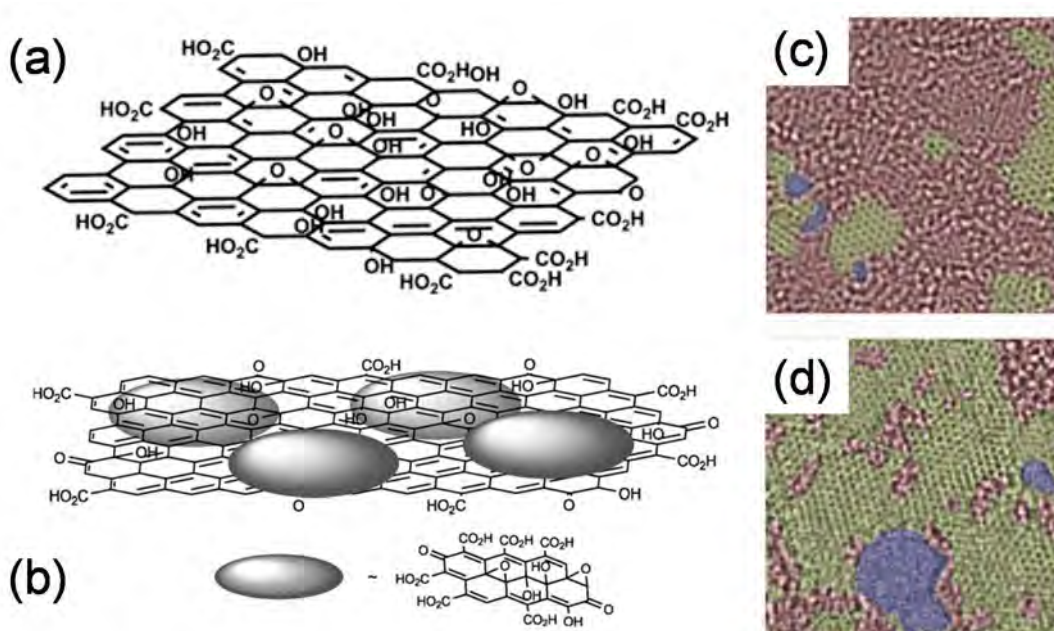


Figure 1.4 Schematic structure of (a) GO [43] and (b) GO and oxidative debris [44]. Transmission electron microscope (TEM) images of the suspended monolayer (c) GO and (d) rGO [12]. The green, red and blue area in (c) and (d) indicate graphitic, disordered and hole areas.

There are a large number of oxygen functional groups in GO, primarily hydroxyl and epoxy groups on the basal plane and carboxyl and carbonyl groups at the edges, which make GO chemically active and hydrophilic [45]. Although the oxidation degree can be defined simply by the C:O ratio [46], the atomic structure of GO (Fig. 1.4(a)) is still under debate as both ring [47] and hexagonal [48] diffraction patterns have been observed, corresponding to amorphous and crystal structures, respectively. One breakthrough was the successful separation of the graphitic basal planes from

the oxidative debris in basic media (Fig. 1.4(b)), thus known as the ‘based wash’ method [44, 49]. The oxidative debris, acts as a surfactant to stabilize GO in suspension. Either chemical [50, 51] or thermal [52] treatment is able to remove the oxygen functional groups and partially restores the graphitic structure [53], albeit with an increased hole density in reduced GO (rGO) (Figs. 1.4(c) and (d)) [12].

1.2.2 Mechanical Properties

The massive defects and functional groups reduce the stiffness and strength of GO [54]. Using a similar indentation method to that for monolayer graphene, Gómez-Navarro et al. [55] measured the stiffness of rGO to be ~ 0.25 TPa, and similar value of ~ 208 GPa was also obtained using a similar method (Fig. 1.5(a)) [56]. Moreover, in contrast to what was found previously on graphene [26, 27], Suk et al. [56] found an almost constant Young’s modulus of GO membranes with different number of GO layers (Fig. 1.5(a)), possibly implying a higher interlayer shear modulus than graphene.

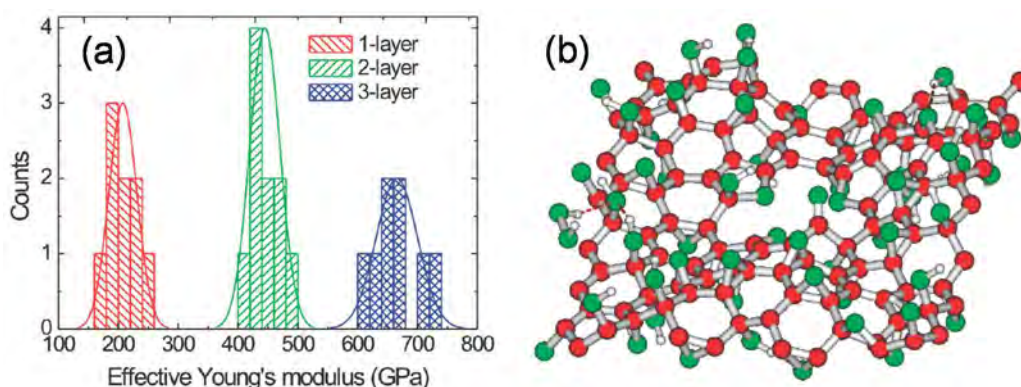


Figure 1.5 (a) Histogram of the Young’s modulus of GO with different number of layers assuming the thick to be one layer for all the membranes [56]. (b) Schematic illustration of GO structure containing hole defects. The red and green balls represent carbon and oxygen atoms, respectively [57].

Using computer simulation, Paci et al. [57] showed a decrease of modulus by a factor of ~ 2 when the monolayer graphene is oxidized and defects are introduced (Fig. 1.5(b)), with the actual values being different for the ordered and amorphous region [58]. At the same time, the almost doubled thickness of GO compared to that of graphene halves the modulus further.

1.3 Graphene-based Polymer Nanocomposites

The exceptional mechanical properties and the large surface areas enable graphene and GO to be promising fillers to reinforce polymer composites, and their various properties also endow extra advantages to be applied in multifunctional nanocomposites [10].

1.3.1 Preparation

The reinforcement of composites materials with graphite [59] and graphite oxide [60] was reported number of years ago, however monolayer-level dispersion is not easy to obtain due to van der Waals forces. The first breakthrough was reported by Stankovich et al. [10] by functionalizing GO to improve its dispersion in polystyrene (PS) matrix. The composites showed optimized electrical conductivity and a low percolation threshold.

In general there are generally three methods to prepare graphene-based nanocomposites: solvent blending, *in-situ* polymerization and melt blending.

1.3.1.1 Solvent Blending

The solvent blending method facilitates the dispersion of graphene and GO in a matrix by involving an intermediary solvent to dissolve the filler and matrix individually. The two components are then mixed [61, 62], followed by removing the solvent. Graphene can be dispersed in this way in a matrix like poly(vinyl alcohol) (PVA) [63] but GO is more commonly used, for its active surface, to reinforce matrixes such as PVA [61, 64, 65], epoxy resins [62, 66, 67] and polyethylene (PE) [68]. Vacuum filtration is sometimes employed to align the graphene flakes [69, 70].

1.3.1.2 *In-situ* Polymerization

In-situ polymerization is a process in which the monomers polymerize *in-situ* around the fillers or even graft to them [71], thus it overcomes the problem of dramatically increased viscosity of the polymer when filler is incorporated [72].

A high concentration of graphene can be obtained without any agglomeration being observed in the PMMA matrix [73]. Additionally, *in-situ* polymerization is also applicable for a variety of polymers [71]. It is particularly useful for some insoluble and thermally-unstable polymers such as polyaniline (PANI) [74, 75].

1.3.1.3 Melt Blending

Melt blending is where the fillers are mixed with the polymer in the melt state, followed by extrusion or injection moulding to exfoliate the graphene or GO with a strong shear force [76]. It is simple for scale-up production, and can be applied to a number of polymers, such as PE [77], PP [78, 79], polycarbonate (PC) [80] and PMMA [81]. The nanocomposite properties can be tuned by controlling the shear rate, temperature as well as mixing time [75]. An enhanced mechanical property was shown by simply exfoliating graphite into a PP matrix using solid-state shear pulverization in a twin-screw extruder [79]. However compared to the other two methods, it suffers from the relative poor filler dispersion, increased polymer viscosity during processing and filler damage due to thermal degradation or strong shear forces [3, 82].

At this stage GO seems more suitable as a nano-filler because of its active surface [83]. During or even after nanocomposites preparation, GO can be reduced to restore the graphitic structure using hydrazine [65, 84] or hydrogen iodide (HI) [85], although it sometimes sacrifices dispersion and results in re-aggregation [68, 73]. Kim et al. compared the three methods thoroughly using rGO or functionalized GO (fGO) filled thermoplastic polyurethane (PU), and it was concluded that the reinforcement of filler for nanocomposites is generally less effective when prepared by melting blending [3, 86]. Actually in order to optimize nanocomposite properties, the methods can be employed synergistically, such as by solvent assisted melt blending [87] or polymerization [83]. Some of the advantages and disadvantages of these methods are summarized in Table 1.1.

Table 1.1 Advantages and disadvantages of the three nanocomposites preparation methods [23].

	Advantages	Disadvantages
Solvent Blending	<ul style="list-style-type: none"> • Good filler dispersion 	<ul style="list-style-type: none"> • Environment problems • Specific polymers
<i>In-situ</i> Polymerization	<ul style="list-style-type: none"> • High filler concentration • Strong interfaces 	<ul style="list-style-type: none"> • Only in solvent
Melt Blending	<ul style="list-style-type: none"> • Economic and convenient • Environment-friendly 	<ul style="list-style-type: none"> • Poor filler dispersion • Filler damage

1.4 Mechanics and Characterization

The mechanics of the reinforcement of matrix have already been studied in detail [88, 89]. The ‘rule of mixtures’ is a classical approximation to estimate the stiffness of composites [88], where its uniform strain/stress cases are widely accepted as the upper/lower bounds [90]. In the uniform strain situation, the Young’s modulus of composites E_{comp} is given as:

$$E_{\text{comp}} = E_{\text{filler}} V_{\text{filler}} + E_{\text{m}} V_{\text{m}} = E_{\text{filler}} V_{\text{filler}} + E_{\text{m}} (1 - V_{\text{filler}}) \quad (1.1)$$

where E_{filler} , E_{m} denote the Young’s modulus of the filler and matrix, respectively. V_{filler} and V_{m} correspond to the volume fraction of the filler and matrix. As a simple approximation, there are some assumptions in the model. Generally three of them are critical to determine E_{comp} [91]:

1. Good interfacial adhesion between filler and matrix without any interface failure.
2. The filler size is infinite so stress is uniform along the filler.
3. All the fillers are aligned unidirectionally along the uniaxial load.

However, in nanocomposites, the assumptions are not always satisfied. Given an intact interface, the size factor η_l and Krenchel orientation factor η_o can be included to correct derivations from the model [89]:

$$E_{\text{comp}} = \eta_l \eta_o E_{\text{filler}} V_{\text{filler}} + E_m (1 - V_{\text{filler}}) \quad (1.2)$$

To reinforce a matrix, it is still trade-off between graphene, GO or other forms of fGO. Graphene has a high modulus of about 1 TPa, but suffers from poor interfacial adhesion due to its inert surface. GO or fGO can interact with matrix but have intrinsic strengths of only one fourth of that of graphene. The reduction of GO partially restores the graphite structure thus enhances its stiffness but sacrifices some of the interface bonding [53].

In this case, an accurate estimation of their contribution to the mechanical properties of nanocomposites is of great practical importance. If $\eta = \eta_l \eta_o$ is defined as the ‘reinforcement efficiency factor’ [92], then Eq. 1.2 is simplified as:

$$E_{\text{comp}} = \eta E_{\text{filler}} V_{\text{filler}} + E_m (1 - V_{\text{filler}}) \quad (1.3)$$

and the term ηE_{filler} , can be defined as ‘effective modulus’, as a measure of the filler modulus that takes into account the effect of both size and orientation of fillers in the nanocomposites.

1.4.1 Interface

The filler-matrix interface plays a significant role in deciding the properties of composites as a strong interface is the premise for the filler to bear load [82, 93]. It is particularly important for nanocomposites, as one of the advantages of nano-fillers is their large surface area.

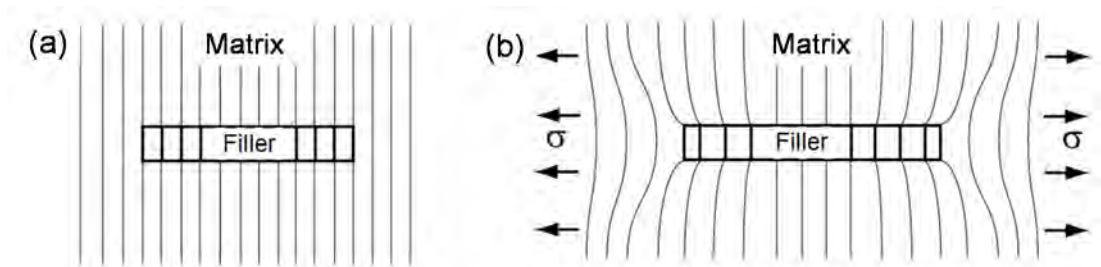


Figure 1.6 Deformation pattern of a nanocomposite with filler incorporated [94].

Given the filler is aligned along the stress direction, the different stiffness of filler and matrix lead to their different axial displacement (Fig. 1.6) [95]. Hence it is assumed that the stress is transferred from matrix to the filler primarily through interfacial shear stress, and the axial stress in the filler σ_{filler} is given as [96]:

$$\sigma_{\text{filler}} = \frac{4}{d} \int_0^x \tau dx \quad (1.4)$$

where τ is the interfacial shear stress, d is the thickness for flake filler or diameter for fibre filler, and x is the distance along the filler from one end. If the interface is stronger than the matrix, the matrix yields first, otherwise the interface debonds [45]. Therefore, in order to reveal the deformation mechanisms, τ must be estimated along the filler. Basically there are two models: the Kelly-Tyson model [95] and Cox model [97]. In both models, the filler is considered to be linearly elastic [98], however different assumptions are made regarding the matrix [96].

1) Kelly-Tyson model

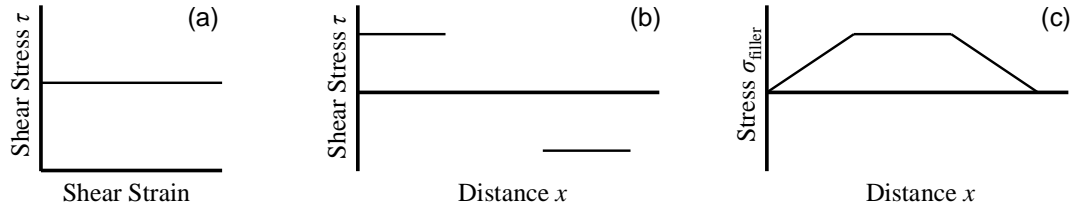


Figure 1.7 The Kelly-Tyson model: (a) Stress-strain curve of the plastic matrix material. (b) Shear stress and (c) axial stress distribution along the filler [96].

In the Kelly-Tyson model [95], the matrix is assumed to be plastic (Fig. 1.7(a)) [96], leading to a constant τ (Fig. 1.7(b)), and thus there is a linear increase of σ_{filler} at both ends of filler along the stress direction (Fig. 1.7(c)) [98]:

$$\sigma_{\text{filler}} = \frac{4}{d} \tau x \quad (1.5)$$

2) Cox model

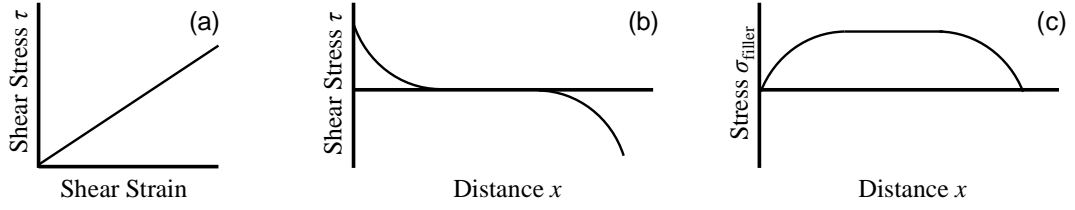


Figure 1.8 The Cox model: (a) Stress-strain curve of the elastic matrix material. (b) Shear stress and (c) axial stress distribution along the filler [96].

The Cox model [95, 97] is also known as ‘shear-lag’ model, where the matrix is assumed to be linearly elastic (Fig. 1.8(a)). In this case, τ along the filler varies as (Fig. 1.8(b)):

$$\tau = nE_{\text{filler}}\epsilon_m \frac{\sinh\left(ns \cdot \left(\frac{x}{l} - \frac{1}{2}\right)\right)}{\cosh\left(\frac{ns}{2}\right)} \quad (1.6)$$

This leads to a non-linear increase of σ_{filler} at both ends of filler (Fig. 1.8(c)):

$$\sigma_{\text{filler}} = E_{\text{filler}}\epsilon_m \left[1 - \frac{\cosh\left(\frac{ns}{l} \cdot \left(x - \frac{l}{2}\right)\right)}{\cosh\left(\frac{ns}{2}\right)} \right] \quad (1.7)$$

$$n = \sqrt{\frac{2G_m}{E_{\text{filler}}} \left(\frac{t}{t_m - t} \right)} \approx \sqrt{\frac{2G_m}{E_{\text{filler}}} \left(\frac{t}{t_m} \right)} \quad (1.8)$$

where ϵ_m is the matrix strain, G_m is the shear modulus of the matrix, t and t_m are the thickness of filler and elementary matrix, respectively. l is the length of filler and $s(=l/t)$ is its aspect ratio. The term ns is regarded as a measure of the stress transfer efficiency, depending on the filler morphology and interfacial adhesion [94]. As $t \ll t_m$, n can be approximated as shown in Eq. 1.8.

In both models, σ_{filler} increases from the filler ends to its maximum after a certain distance, where the filler strain is equivalent to the matrix strain [96]. Twice this

distance is defined as the ‘critical length’ L_c (Fig. 1.9). If the filler size is considerably larger than L_c , the σ_{filler} plateau will be large enough, and the polymer matrix can be better reinforced. However, if the filler size is comparable to or even less than L_c , the σ_{filler} variation along the filler should be considered. Three different σ_{filler} distributions with regard to the filler size are shown in Fig. 1.9 [96]:

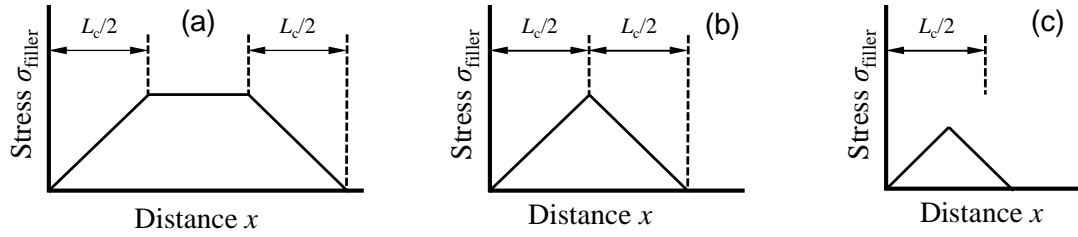


Figure 1.9 Stress distribution calculated by the ‘Kelly-Tyson model’ along the fillers with different sizes: (a) longer than L_c , (b) equal to L_c and (c) shorter than L_c [96].

It should be noted that these models are not rigorous and only provide a simple approximation [94]. For example, τ is usually larger than that calculated near the filler ends due to stress concentrations [95, 96].

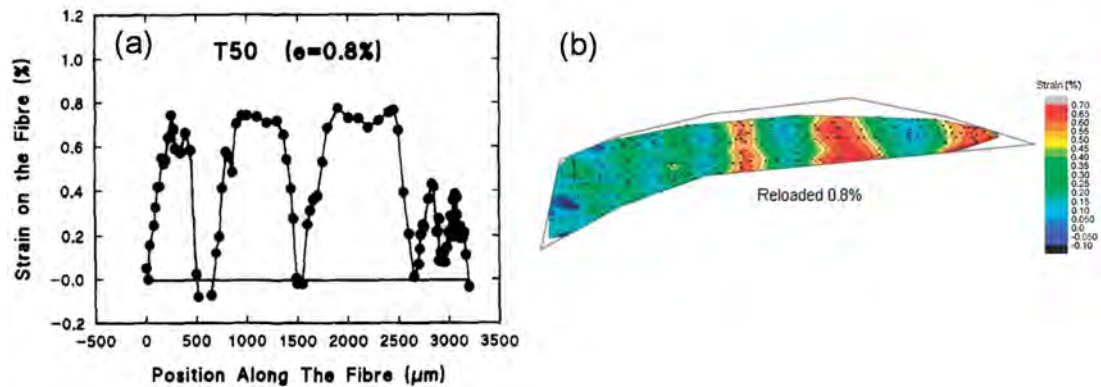


Figure 1.10 (a) Strain distribution of T50 carbon fibre in epoxy resin matrix at a matrix strain of 0.8 % [99]. (b) Strain distribution of a monolayer graphene in a polymer matrix at a strain of 0.8 % [100].

The interfacial properties of conventional composites can be measured by numbers of methods such as pull-out test, micro-droplet test, microcompression and fragmentation [101]. In nanocomposites the interfacial strength has been estimated by detaching a filler from the matrix [102, 103]. Also the stress/strain sensing of the

Raman band positions has been used to follow the non-uniform stress distribution in both fibres [99, 104] and graphene (Fig. 1.10) [94, 100]. For graphene, the coincidence with the theoretical models demonstrates that it still follows continuous mechanics at this scale. The interfacial shear stress was calculated to be order of 2 MPa [94, 105], consistent with the calculations for carbon nanotube/polymer interfaces [106], indicating the van der Waals force is dominant for graphene/polymer interfaces without any interfacial bonding.

In order to strengthen the interface, non-covalent [45, 107] and covalent [66, 108] functionalization of pristine graphene can be utilized [86]. The chemically-inert basal plane can be non-covalently functionalized *via* the π - π interaction [107], while the active defects and edges enable graphene to be covalent functionalized and grafted by other molecules. Particularly, interfacial strength is further enhanced if polymer-grafted graphene is used to reinforce a chemically similar polymer matrix [109].

1.4.2 Aspect Ratio

The filler aspect ratio s is defined here as $s=l/t$, that is, the ratio of lateral size and thickness for flake or the ratio of length and diameter for fibre [63]. The filler size is usually determined using AFM [64, 110], scanning electron microscope (SEM) (Figs. 1.11(a) and (b)) [64, 110] or TEM [9] images, and the filler thickness can be measured by means of AFM height profile scans (Fig. 1.11(c)) [10]. Young et al. [90] presented a thorough discussion on the effect of aspect ratio on the mechanical properties of nanocomposites.

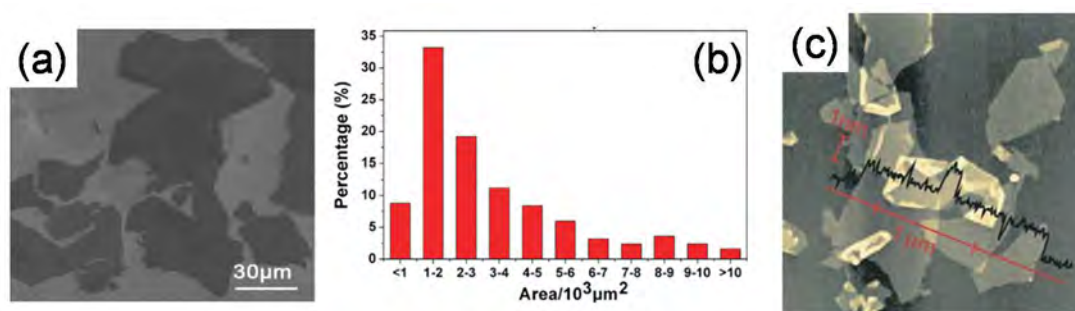


Figure 1.11 (a) SEM image and (b) area distribution of GO sheet [110]. (c) AFM image of the fGO showing the thickness to be ~1 nm [10].

It was discussed in Section 1.4.1 that better reinforcement efficiency is achieved when the filler has a large lateral size [111]. An instructive minimum s value for graphene has been calculated to be 300 or 1000 for rigid polymer or elastomer [45]. Considering the non-uniformity of both the σ_{filler} distribution along the filler and the aspect ratio of all fillers, the average axial stress $\bar{\sigma}_{\text{filler}}$ that fillers take can be given by modifying Eq. 1.7 as [89]:

$$\bar{\sigma}_{\text{filler}} = \frac{1}{l} \int_0^l \sigma_{\text{filler}} dx = E_{\text{filler}} \epsilon_m \left(1 - \frac{\tanh\left(\frac{ns}{2}\right)}{\frac{ns}{2}} \right) \quad (1.9)$$

For bulk nanocomposites, the graphene thickness t and matrix thickness t_m can be converted to the filler volume fraction V_{filler} and matrix volume fraction $(1-V_{\text{filler}})$. Combined with Eq. 1.8, the size factor η_l of the fillers in the nanocomposites can be obtained as [63, 89, 91]:

$$\eta_l = 1 - \frac{\tanh\left(\frac{ns}{2}\right)}{\frac{ns}{2}} \quad (1.10)$$

where

$$n = \sqrt{\frac{2G_m}{E_{\text{filler}}} \left(\frac{V_{\text{filler}}}{1-V_{\text{filler}}} \right)} \quad (1.11)$$

η_l quantifies the effect of the filler aspect ratio s on the composites mechanical properties, and the variation as the function of s was shown elsewhere [63].

In order to enlarge the aspect ratio of fillers for better reinforcement, one can increase the filler size [110, 112], or on the other hand, disperse the filler homogeneously into matrix to obtain thinner layers [61]. It should be noted that for large size fillers, distortion and wrinkles [113] need to be avoided, as they not only deteriorate the reinforcement but also tend to break the filler into small segments. The structural discontinuity caused in this circumstance reduces the stress transfer [99, 100], giving the filler a small η_l . One issue here for graphene is that its interlayer

shear modulus is as low as 5 GPa [28], which means, if graphene cannot be exfoliated homogeneously, interlayer sliding will cause a further decrease in reinforcement [34].

1.4.3 Orientation

The filler orientation also affects the mechanical properties of composites remarkably [114, 115], especially for nanocomposites, where controlling and characterizing the nano-filler orientation is complicated. Many experimental methods have been developed to characterize filler orientation, such as microscopy [61, 85, 116], X-ray scattering [80, 117-119], Raman spectroscopy [70, 120], Fourier transform infrared (FTIR) [121] and UV-Vis spectroscopy [122].

Microscopy is the most straight forward in that the filler orientation distribution and the average orientation can be given by simply counting the number of fillers at different angles in SEM (Fig. 1.12(a)) [85] or TEM (Fig. 1.12(b)) [116] images, however it is time consuming. A quantitative orientation factor can be further derived by processing the images using fast Fourier transformation [123, 124].

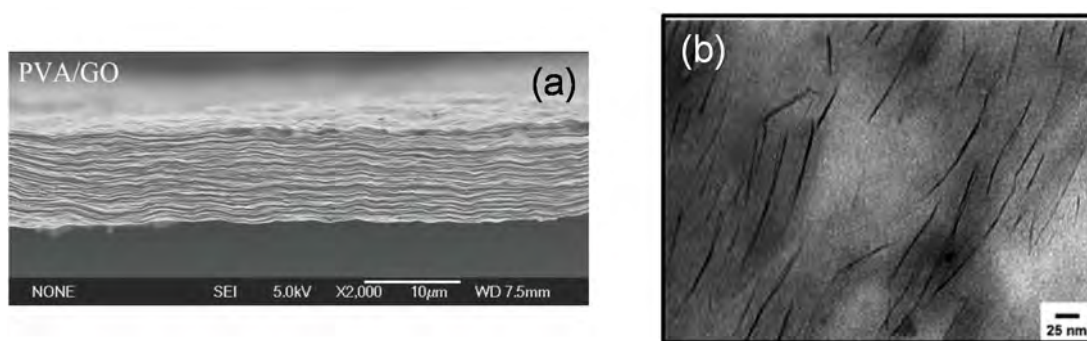


Figure 1.12 (a) SEM image of the fracture surface of GO/PVA nanocomposite film [85]. (b) TEM image of a clay reinforced Nylon-6 nanocomposite [116].

X-ray scattering is another extensively applied technique, based on the variant scattering intensity with respect to the incident X-ray beam direction. In the azimuthal scan (Fig. 1.13(a)), the sample was rotated in order to obtain the intensity over the full angle range [80]. The sample can be fixed and the scattering intensity at full angle range can be resolved from the ring pattern if a film detector is employed. In this case, there are two kinds of broadly-similar techniques [125], namely small-

angle X-ray scattering (SAXS) (Fig. 1.13(b)) and wide-angle X-ray scattering (WAXS), with the distance between sample and detector being longer in SAXS. Consequently, it detects the X-ray scattering at smaller 2θ angle thus provides information at a larger scale [125]. Some of the early works were carried out on cellulose [117], graphite [118] and clay [119] and the anisotropy of the materials is clearly reflected by the scattering intensity at different angles, which typically follows a Gaussian [126, 127] or Lorentzian [80] distribution function.

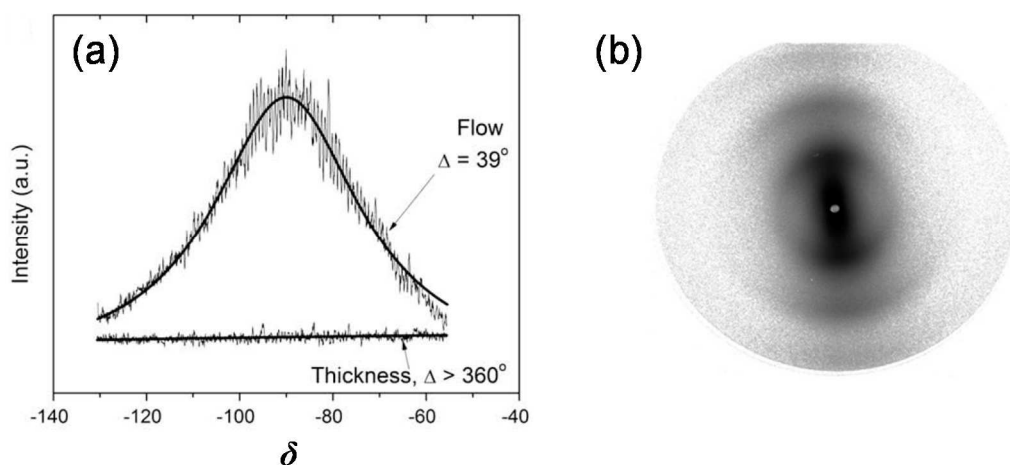


Figure 1.13 (a) Azimuthal X-ray scattering intensity of $2\theta=26.4^\circ\pm0.4$ for a graphene reinforced PC nanocomposite. The scattered and the smooth curve are the experimental data and the curve fitting with Lorentzian function, respectively [80]. (b) SAXS patterns obtained edge-on for a hot-pressed clay-based nanocomposite [128].

Polarized Raman spectroscopy is another powerful technique based on the anisotropic Raman scattering intensity of the sample with respect to the laser polarization, particularly useful for carbon materials [1]. So far studies have been reported on the orientation of isolated CNTs [120, 129] and also in nanocomposites [130], where the Raman scattering intensity was the maximum/minimum when the laser polarization was parallel/perpendicular to the axis of the single-wall CNTs (Fig. 1.14). Despite the simple and convenient depolarization ratio [130], a more rigorous model using the Legendre polynomials to quantify the CNT orientation has been employed [131, 132]. There are also studies on the orientation of graphite flakes, which will be discussed in detail in Chapter 2.

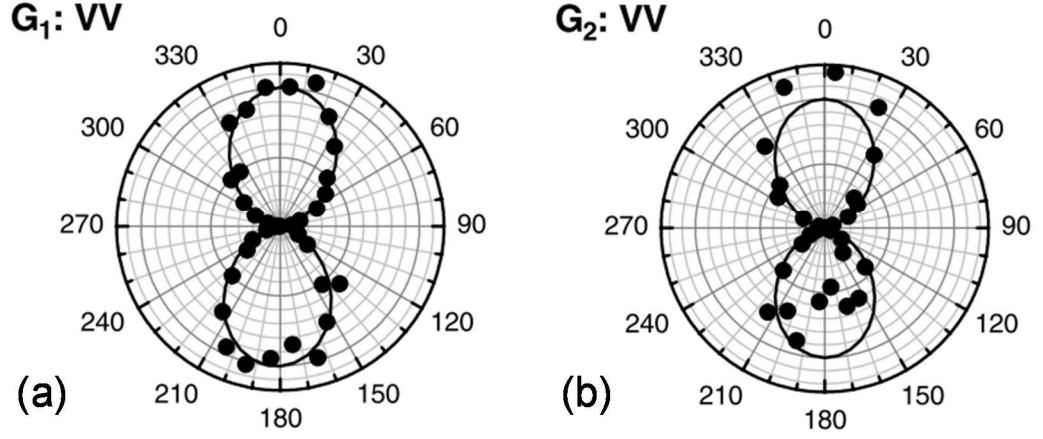


Figure 1.14 Single wall CNT Raman (a) G1 and (b) G2 band intensity as a function of the angle between CNT axis and the laser 'VV' polarization direction [120].

In order to better quantify the filler orientation, theoretical models have been proposed, among which, the Hermans' model [117] and Krenchel model [133] have been extensively used.

1) Hermans' model

The Hermans' model was first established on cellulose fibre using X-ray [117], calculated as the average of the crystal face orientation [134]:

$$\langle \cos^2 \theta \rangle = \frac{\int_0^{\pi/2} I(\delta) \cos^2 \delta \sin \delta d\delta}{\int_0^{\pi/2} I(\delta) \sin \delta d\delta} \quad (1.12)$$

where $I(\delta)$ is the X-ray scattering intensity at the azimuthal angle δ , and θ is the orientational angle of the filler. Herein the Hermans' orientation factor f is expressed as [117, 134]:

$$f = \frac{3\langle \cos^2 \theta \rangle - 1}{2} \quad (1.13)$$

Hermans' orientation factor enables a quantitative analysis on the orientation of both 1D and 2D fillers [128, 134], and its values for typical situations are summarized in Table 1.2.

Table 1.2 Values of Hermans' orientation factor f for typical situations [134].

Parallel to reference	1
Randomly oriented	0
Perpendicular to reference direction	-1/2

2) Krenchel model

The Krenchel model is another model based on mechanics analysis, and it initially dealt with the effect of fibre orientation on the reinforcement of composites [133]. By dividing the fibres into groups (Fig. 1.15(a)), the orientation of all fibres can be considered as the summation of the mechanical contributions of each group:

$$\eta_o = \sum a_n \cdot \cos^4 \zeta \quad (1.14)$$

where η_o is the Krenchel orientation factor, ζ is the angle between the fibre group and the stress direction, and a_n is the proportion of this group to the entirety. More generally, the summation can be replaced by integration [133].

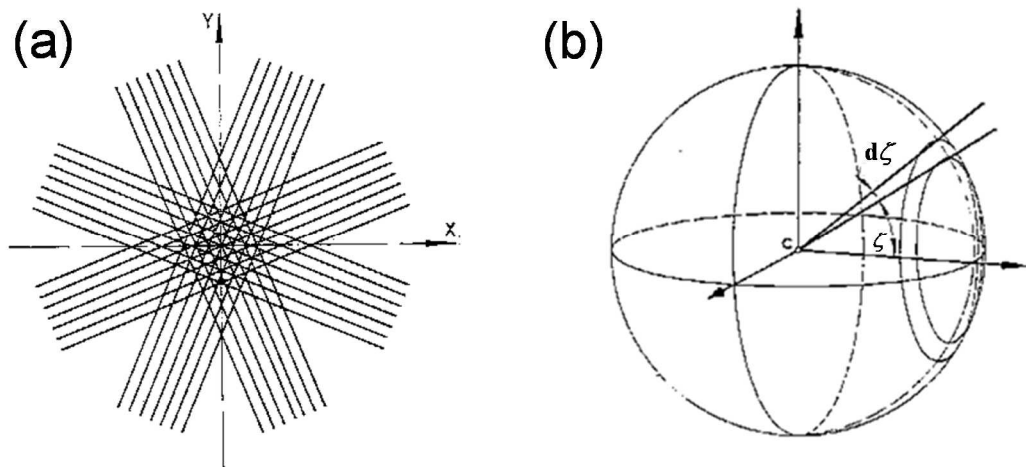


Figure 1.15 Fibres aligned (a) in-plane and (b) three-dimensionally in the Krenchel model analysis [133].

There are some typical fibre arrangements that have been considered. For example, if all the fibres are unidirectionally aligned, the Krenchel orientation factor η_o is unity '1'; if the fibres are randomly oriented in a 2D plane (Fig.1.15(a)), the corresponding η_o is calculated as [133]:

$$\eta_o = \frac{1}{\pi} \int_{-\pi/2}^{\pi/2} \cos^4 \zeta d\zeta = \frac{3}{8} \quad (1.15)$$

If the fibres are oriented randomly in bulk, Eq. 1.14 is modified using a 3D sphere element model to give the corresponding η_o as (Fig. 1.15(b)) [133]:

$$\eta_o = \int_0^{\pi/2} \cos^4 \zeta \sin \zeta d\zeta = \frac{1}{5} \quad (1.16)$$

The values of η_o of 1D fibre fillers for these typical situations are summarized in Table 1.3. For a 2D flake filler, a value of 1 is obtained for the Krenchel orientation factor for both the unidirectional and in-plane orientation, as those flake fillers can be regarded as a 1D fibre analogy viewed edge-on. However, for flake filler 3D randomly orientated in bulk materials, a systematic analysis has not yet been performed.

Table 1.3 Values of Krenchel orientation factor η_o for typical situations [133, 135].

	1D filler	2D filler
Unidirectional oriented	1	1
In plane oriented	3/8	1
Randomly oriented	1/5	N/A

Since the Krenchel model is based on a mechanics analysis, it is favourable to be used to directly correlate the filler orientation to composites mechanical properties. Beyond Hermans' and Krenchel models, others like the Halpin-Tsai model [64, 65, 136], and the Mori-Tanaka model [116, 135] also provide valuable information about the orientation of both 1D rod- [137] and 2D flake-like fillers [64, 65, 92].

The spatial orientation of fillers is affected by filler concentration [128] and processing method [80], and it can be greatly improved by methods such as vacuum filtration [69, 70].

1.5 Conclusions

The recent progress on the graphene-based nanocomposites has been reviewed. The preparation for the nanocomposites can be primarily divided into three groups: solvent blending, *in-situ* polymerization and melt blending. To analyze the reinforcement of the polymer matrix using graphene-based fillers, three main major aspects from the mechanics point of view have been discussed: interface, aspect ratio and orientation. It is concluded that better reinforcement of the nanocomposites along the stress direction can be achieved when the fillers have strong interface with the polymer matrix, have large lateral dimension, and are unidirectionally aligned along the stress direction.

References

1. Saito, R.; Hofmann, M.; Dresselhaus, G.; Jorio, A.; Dresselhaus, M. S., Raman Spectroscopy of Graphene and Carbon Nanotubes. *Advances in Physics* **2011**, 60, 413-550.
2. Novoselov, K. S.; Geim, A. K.; Morozov, S. V.; Jiang, D.; Zhang, Y.; Dubonos, S. V.; Grigorieva, I. V.; Firsov, A. A., Electric Field Effect in Atomically Thin Carbon Films. *Science* **2004**, 306, 666-669.
3. Kim, H.; Abdala, A. A.; Macosko, C. W., Graphene/Polymer Nanocomposites. *Macromolecules* **2010**, 43, 6515-6530.
4. Ponomarenko, L. A.; Gorbachev, R. V.; Yu, G. L.; Elias, D. C.; Jalil, R.; Patel, A. A.; Mishchenko, A.; Mayorov, A. S.; Woods, C. R.; Wallbank, J. R.; Mucha-Kruczynski, M.; Piot, B. A.; Potemski, M.; Grigorieva, I. V.; Novoselov, K. S.; Guinea, F.; Fal'ko, V. I.; Geim, A. K., Cloning of Dirac Fermions in Graphene Superlattices. *Nature* **2013**, 497, 594-597.
5. Meyer, J. C.; Geim, A. K.; Katsnelson, M. I.; Novoselov, K. S.; Booth, T. J.; Roth, S., The Structure of Suspended Graphene Sheets. *Nature* **2007**, 446, 60-63.
6. Novoselov, K. S.; Falko, V. I.; Colombo, L.; Gellert, P. R.; Schwab, M. G.; Kim, K., A Roadmap for Graphene. *Nature* **2012**, 490, 192-200.
7. Hernandez, Y.; Nicolosi, V.; Lotya, M.; Blighe, F. M.; Sun, Z.; De, S.; McGovern, I. T.; Holland, B.; Byrne, M.; Gun'ko, Y. K.; Boland, J. J.; Niraj, P.; Duesberg, G.; Krishnamurthy, S.; Goodhue, R.; Hutchison, J.; Scardaci, V.; Ferrari, A. C.; Coleman, J. N., High-Yield Production of Graphene by Liquid-Phase Exfoliation of Graphite. *Nature Nanotechnology* **2008**, 3, 563-568.

8. Tung, V. C.; Allen, M. J.; Yang, Y.; Kaner, R. B., High-Throughput Solution Processing of Large-Scale Graphene. *Nature Nanotechnology* **2009**, 4, 25-29.
9. Khan, U.; O'Neill, A.; Lotya, M.; De, S.; Coleman, J. N., High-Concentration Solvent Exfoliation of Graphene. *Small* **2010**, 6, 864-871.
10. Stankovich, S.; Dikin, D. A.; Dommett, G. H. B.; Kohlhaas, K. M.; Zimney, E. J.; Stach, E. A.; Piner, R. D.; Nguyen, S. T.; Ruoff, R. S., Graphene-Based Composite Materials. *Nature* **2006**, 442, 282-286.
11. Abdelkader, A. M.; Kinloch, I. A.; Dryfe, R. A. W., Continuous Electrochemical Exfoliation of Micrometer-Sized Graphene Using Synergistic Ion Intercalations and Organic Solvents. *ACS Applied Materials & Interfaces* **2014**, 6, 1632-1639.
12. Erickson, K.; Erni, R.; Lee, Z.; Alem, N.; Gannett, W.; Zettl, A., Determination of the Local Chemical Structure of Graphene Oxide and Reduced Graphene Oxide. *Advanced Materials* **2010**, 22, 4467-4472.
13. Li, X.; Cai, W.; An, J.; Kim, S.; Nah, J.; Yang, D.; Piner, R.; Velamakanni, A.; Jung, I.; Tutuc, E.; Banerjee, S. K.; Colombo, L.; Ruoff, R. S., Large-Area Synthesis of High-Quality and Uniform Graphene Films on Copper Foils. *Science* **2009**, 324, 1312-1314.
14. Zhang, Y.; Gao, T.; Gao, Y.; Xie, S.; Ji, Q.; Yan, K.; Peng, H.; Liu, Z., Defect-Like Structures of Graphene on Copper Foils for Strain Relief Investigated by High-Resolution Scanning Tunneling Microscopy. *ACS Nano* **2011**, 5, 4014-4022.
15. Yan, Z.; Peng, Z.; Tour, J. M., Chemical Vapor Deposition of Graphene Single Crystals. *Accounts of Chemical Research* **2014**, 47, 1327-1337.
16. Lewis, A. M.; Derby, B.; Kinloch, I. A., Influence of Gas Phase Equilibria on the Chemical Vapor Deposition of Graphene. *ACS Nano* **2013**, 7, 3104-3117.
17. Li, X.; Magnuson, C. W.; Venugopal, A.; An, J.; Suk, J. W.; Han, B.; Borysiak, M.; Cai, W.; Velamakanni, A.; Zhu, Y.; Fu, L.; Vogel, E. M.; Voelkl, E.; Colombo, L.; Ruoff, R. S., Graphene Films with Large Domain Size by a Two-Step Chemical Vapor Deposition Process. *Nano Letters* **2010**, 10, 4328-4334.
18. Li, X.; Magnuson, C. W.; Venugopal, A.; Tromp, R. M.; Hannon, J. B.; Vogel, E. M.; Colombo, L.; Ruoff, R. S., Large-Area Graphene Single Crystals Grown by Low-Pressure Chemical Vapor Deposition of Methane on Copper. *Journal of the American Chemical Society* **2011**, 133, 2816-2819.
19. Li, X.; Cai, W.; Colombo, L.; Ruoff, R. S., Evolution of Graphene Growth on Ni and Cu by Carbon Isotope Labeling. *Nano Letters* **2009**, 9, 4268-4272.
20. Gao, L.; Ren, W.; Xu, H.; Jin, L.; Wang, Z.; Ma, T.; Ma, L.-P.; Zhang, Z.; Fu, Q.; Peng, L.-M.; Bao, X.; Cheng, H.-M., Repeated Growth and Bubbling Transfer of Graphene with Millimetre-Size Single-Crystal Grains Using Platinum. *Nature Communications* **2012**, 3, 699.
21. Kosynkin, D. V.; Higginbotham, A. L.; Sinitskii, A.; Lomeda, J. R.; Dimiev, A.; Price, B. K.; Tour, J. M., Longitudinal Unzipping of Carbon Nanotubes to Form Graphene Nanoribbons. *Nature* **2009**, 458, 872-876.
22. Sutter, P. W.; Flege, J.-I.; Sutter, E. A., Epitaxial Graphene on Ruthenium. *Nature Materials* **2008**, 7, 406-411.
23. Zheng, Q.; Li, Z.; Yang, J.; Kim, J.-K., Graphene Oxide-Based Transparent Conductive Films. *Progress in Materials Science* **2014**, 64, 200-247.
24. Cai, J.; Ruffieux, P.; Jaafar, R.; Bieri, M.; Braun, T.; Blankenburg, S.; Muoth, M.; Seitsonen, A. P.; Saleh, M.; Feng, X.; Mullen, K.; Fasel, R.,

- Atomically Precise Bottom-up Fabrication of Graphene Nanoribbons. *Nature* **2010**, 466, 470-473.
25. Jiao, L.; Zhang, L.; Wang, X.; Diankov, G.; Dai, H., Narrow Graphene Nanoribbons from Carbon Nanotubes. *Nature* **2009**, 458, 877-880.
 26. Lee, C.; Wei, X.; Kysar, J. W.; Hone, J., Measurement of the Elastic Properties and Intrinsic Strength of Monolayer Graphene. *Science* **2008**, 321, 385-388.
 27. Frank, I. W.; Tanenbaum, D. M.; van der Zande, A. M.; McEuen, P. L., Mechanical Properties of Suspended Graphene Sheets. *Journal of Vacuum Science & Technology B* **2007**, 25, 2558-2561.
 28. Tan, P. H.; Han, W. P.; Zhao, W. J.; Wu, Z. H.; Chang, K.; Wang, H.; Wang, Y. F.; Bonini, N.; Marzari, N.; Pugno, N.; Savini, G.; Lombardo, A.; Ferrari, A. C., The Shear Mode of Multilayer Graphene. *Nature Materials* **2012**, 11, 294-300.
 29. Gong, L.; Young, R. J.; Kinloch, I. A.; Haigh, S. J.; Warner, J. H.; Hinks, J. A.; Xu, Z.; Li, L.; Ding, F.; Riaz, I.; Jalil, R.; Novoselov, K. S., Reversible Loss of Bernal Stacking During the Deformation of Few-Layer Graphene in Nanocomposites. *ACS Nano* **2013**, 7, 7287-7294.
 30. Lee, J.-U.; Yoon, D.; Cheong, H., Estimation of Young's Modulus of Graphene by Raman Spectroscopy. *Nano Letters* **2012**, 12, 4444-4448.
 31. Ni, Z. H.; Yu, T.; Lu, Y. H.; Wang, Y. Y.; Feng, Y. P.; Shen, Z. X., Uniaxial Strain on Graphene: Raman Spectroscopy Study and Band-Gap Opening. *ACS Nano* **2008**, 2, 2301-2305.
 32. Ruiz-Vargas, C. S.; Zhuang, H. L.; Huang, P. Y.; van der Zande, A. M.; Garg, S.; McEuen, P. L.; Muller, D. A.; Hennig, R. G.; Park, J., Softened Elastic Response and Unzipping in Chemical Vapor Deposition Graphene Membranes. *Nano Letters* **2011**, 11, 2259-2263.
 33. Lin, Q.-Y.; Jing, G.; Zhou, Y.-B.; Wang, Y.-F.; Meng, J.; Bie, Y.-Q.; Yu, D.-P.; Liao, Z.-M., Stretch-Induced Stiffness Enhancement of Graphene Grown by Chemical Vapor Deposition. *ACS Nano* **2013**, 7, 1171-1177.
 34. Gong, L.; Young, R. J.; Kinloch, I. A.; Riaz, I.; Jalil, R.; Novoselov, K. S., Optimizing the Reinforcement of Polymer-Based Nanocomposites by Graphene. *ACS Nano* **2012**, 6, 2086-2095.
 35. Banhart, F.; Kotakoski, J.; Krashenninnikov, A. V., Structural Defects in Graphene. *ACS Nano* **2010**, 5, 26-41.
 36. Grantab, R.; Shenoy, V. B.; Ruoff, R. S., Anomalous Strength Characteristics of Tilt Grain Boundaries in Graphene. *Science* **2010**, 330, 946-948.
 37. Zhang, J.; Zhao, J.; Lu, J., Intrinsic Strength and Failure Behaviors of Graphene Grain Boundaries. *ACS Nano* **2012**, 6, 2704-2711.
 38. He, H.; Klinowski, J.; Forster, M.; Lerf, A., A New Structural Model for Graphite Oxide. *Chemical Physics Letters* **1998**, 287, 53-56.
 39. Brodie, B. C., On the Atomic Weight of Graphite. *Philosophical Transactions of the Royal Society of London* **1859**, 149, 249-259.
 40. Staudenmaier, L., Verfahren Zur Darstellung Der Graphitsäure. *Berichte der deutschen chemischen Gesellschaft* **1898**, 31, 1481-1487.
 41. Xu, Y.; Sheng, K.; Li, C.; Shi, G., Self-Assembled Graphene Hydrogel via a One-Step Hydrothermal Process. *ACS Nano* **2010**, 4, 4324-4330.
 42. Hummers, W. S.; Offeman, R. E., Preparation of Graphitic Oxide. *Journal of the American Chemical Society* **1958**, 80, 1339-1339.

43. Potts, J. R.; Dreyer, D. R.; Bielawski, C. W.; Ruoff, R. S., Graphene-Based Polymer Nanocomposites. *Polymer* **2011**, 52, 5-25.
44. Rourke, J. P.; Pandey, P. A.; Moore, J. J.; Bates, M.; Kinloch, I. A.; Young, R. J.; Wilson, N. R., The Real Graphene Oxide Revealed: Stripping the Oxidative Debris from the Graphene-Like Sheets. *Angewandte Chemie International Edition* **2011**, 50, 3173-3177.
45. Terrones, M.; Martín, O.; González, M.; Pozuelo, J.; Serrano, B.; Cabanelas, J. C.; Vega-Díaz, S. M.; Baselga, J., Interphases in Graphene Polymer-Based Nanocomposites: Achievements and Challenges. *Advanced Materials* **2011**, 23, 5302-5310.
46. Dreyer, D. R.; Park, S.; Bielawski, C. W.; Ruoff, R. S., The Chemistry of Graphene Oxide. *Chemical Society Reviews* **2010**, 39, 228-240.
47. Mkhoyan, K. A.; Contryman, A. W.; Silcox, J.; Stewart, D. A.; Eda, G.; Mattevi, C.; Miller, S.; Chhowalla, M., Atomic and Electronic Structure of Graphene-Oxide. *Nano Letters* **2009**, 9, 1058-1063.
48. Wilson, N. R.; Pandey, P. A.; Beanland, R.; Young, R. J.; Kinloch, I. A.; Gong, L.; Liu, Z.; Suenaga, K.; Rourke, J. P.; York, S. J.; Sloan, J., Graphene Oxide: Structural Analysis and Application as a Highly Transparent Support for Electron Microscopy. *ACS Nano* **2009**, 3, 2547-2556.
49. Fan, X.; Peng, W.; Li, Y.; Li, X.; Wang, S.; Zhang, G.; Zhang, F., Deoxygenation of Exfoliated Graphite Oxide under Alkaline Conditions: A Green Route to Graphene Preparation. *Advanced Materials* **2008**, 20, 4490-4493.
50. Stankovich, S.; Dikin, D. A.; Piner, R. D.; Kohlhaas, K. A.; Kleinhammes, A.; Jia, Y.; Wu, Y.; Nguyen, S. T.; Ruoff, R. S., Synthesis of Graphene-Based Nanosheets via Chemical Reduction of Exfoliated Graphite Oxide. *Carbon* **2007**, 45, 1558-1565.
51. Gao, W.; Alemany, L. B.; Ci, L.; Ajayan, P. M., New Insights into the Structure and Reduction of Graphite Oxide. *Nature Chemistry* **2009**, 1, 403-408.
52. Zhu, Y.; Stoller, M. D.; Cai, W.; Velamakanni, A.; Piner, R. D.; Chen, D.; Ruoff, R. S., Exfoliation of Graphite Oxide in Propylene Carbonate and Thermal Reduction of the Resulting Graphene Oxide Platelets. *ACS Nano* **2010**, 4, 1227-1233.
53. Gómez-Navarro, C.; Meyer, J. C.; Sundaram, R. S.; Chuvilin, A.; Kurasch, S.; Burghard, M.; Kern, K.; Kaiser, U., Atomic Structure of Reduced Graphene Oxide. *Nano Letters* **2010**, 10, 1144-1148.
54. Schniepp, H. C.; Kudin, K. N.; Li, J.-L.; Prud'homme, R. K.; Car, R.; Saville, D. A.; Aksay, I. A., Bending Properties of Single Functionalized Graphene Sheets Probed by Atomic Force Microscopy. *ACS Nano* **2008**, 2, 2577-2584.
55. Gómez-Navarro, C.; Burghard, M.; Kern, K., Elastic Properties of Chemically Derived Single Graphene Sheets. *Nano Letters* **2008**, 8, 2045-2049.
56. Suk, J. W.; Piner, R. D.; An, J.; Ruoff, R. S., Mechanical Properties of Monolayer Graphene Oxide. *ACS Nano* **2010**, 4, 6557-6564.
57. Paci, J. T.; Belytschko, T.; Schatz, G. C., Computational Studies of the Structure, Behavior Upon Heating, and Mechanical Properties of Graphite Oxide. *The Journal of Physical Chemistry C* **2007**, 111, 18099-18111.

58. Liu, L.; Zhang, J.; Zhao, J.; Liu, F., Mechanical Properties of Graphene Oxides. *Nanoscale* **2012**, 4, 5910-5916.
59. Chen, G.; Wu, D.; Weng, W.; Wu, C., Exfoliation of Graphite Flake and Its Nanocomposites. *Carbon* **2003**, 41, 619-621.
60. Kotov, N. A.; Dékány, I.; Fendler, J. H., Ultrathin Graphite Oxide–Polyelectrolyte Composites Prepared by Self-Assembly: Transition between Conductive and Non-Conductive States. *Advanced Materials* **1996**, 8, 637-641.
61. Xu, Y.; Hong, W.; Bai, H.; Li, C.; Shi, G., Strong and Ductile Poly(Vinyl Alcohol)/Graphene Oxide Composite Films with a Layered Structure. *Carbon* **2009**, 47, 3538-3543.
62. Li, Z.; Young, R. J.; Wang, R.; Yang, F.; Hao, L.; Jiao, W.; Liu, W., The Role of Functional Groups on Graphene Oxide in Epoxy Nanocomposites. *Polymer* **2013**, 54, 5821-5829.
63. May, P.; Khan, U.; O'Neill, A.; Coleman, J. N., Approaching the Theoretical Limit for Reinforcing Polymers with Graphene. *Journal of Materials Chemistry* **2012**, 22, 1278-1282.
64. Liang, J.; Huang, Y.; Zhang, L.; Wang, Y.; Ma, Y.; Guo, T.; Chen, Y., Molecular-Level Dispersion of Graphene into Poly(Vinyl Alcohol) and Effective Reinforcement of Their Nanocomposites. *Advanced Functional Materials* **2009**, 19, 2297-2302.
65. Zhao, X.; Zhang, Q.; Chen, D.; Lu, P., Enhanced Mechanical Properties of Graphene-Based Poly(Vinyl Alcohol) Composites. *Macromolecules* **2010**, 43, 2357-2363.
66. Li, Z.; Wang, R.; Young, R. J.; Deng, L.; Yang, F.; Hao, L.; Jiao, W.; Liu, W., Control of the Functionality of Graphene Oxide for Its Application in Epoxy Nanocomposites. *Polymer* **2013**, 54, 6437-6446.
67. Rafiee, M. A.; Rafiee, J.; Wang, Z.; Song, H.; Yu, Z.-Z.; Koratkar, N., Enhanced Mechanical Properties of Nanocomposites at Low Graphene Content. *ACS Nano* **2009**, 3, 3884-3890.
68. Cheng, S.; Chen, X.; Hsuan, Y. G.; Li, C. Y., Reduced Graphene Oxide-Induced Polyethylene Crystallization in Solution and Nanocomposites. *Macromolecules* **2011**, 45, 993-1000.
69. Putz, K. W.; Compton, O. C.; Palmeri, M. J.; Nguyen, S. T.; Brinson, L. C., High-Nanofiller-Content Graphene Oxide–Polymer Nanocomposites via Vacuum-Assisted Self-Assembly. *Advanced Functional Materials* **2010**, 20, 3322-3329.
70. Liang, Q.; Yao, X.; Wang, W.; Liu, Y.; Wong, C. P., A Three-Dimensional Vertically Aligned Functionalized Multilayer Graphene Architecture: An Approach for Graphene-Based Thermal Interfacial Materials. *ACS Nano* **2011**, 5, 2392-2401.
71. Kuilla, T.; Bhadra, S.; Yao, D.; Kim, N. H.; Bose, S.; Lee, J. H., Recent Advances in Graphene Based Polymer Composites. *Progress in Polymer Science* **2010**, 35, 1350-1375.
72. Vallés, C.; Young, R.; Lomax, D.; Kinloch, I., The Rheological Behaviour of Concentrated Dispersions of Graphene Oxide. *Journal of Materials Science* **2014**, 49, 6311-6320.
73. Potts, J. R.; Lee, S. H.; Alam, T. M.; An, J.; Stoller, M. D.; Piner, R. D.; Ruoff, R. S., Thermomechanical Properties of Chemically Modified

- Graphene/Poly(Methyl Methacrylate) Composites Made by in Situ Polymerization. *Carbon* **2011**, 49, 2615-2623.
74. Wang, D.-W.; Li, F.; Zhao, J.; Ren, W.; Chen, Z.-G.; Tan, J.; Wu, Z.-S.; Gentle, I.; Lu, G. Q.; Cheng, H.-M., Fabrication of Graphene/Polyaniline Composite Paper via in Situ Anodic Electropolymerization for High-Performance Flexible Electrode. *ACS Nano* **2009**, 3, 1745-1752.
 75. Sun, X.; Sun, H.; Li, H.; Peng, H., Developing Polymer Composite Materials: Carbon Nanotubes or Graphene? *Advanced Materials* **2013**, 25, 5153-5176.
 76. Kim, H.; Macosko, C. W., Morphology and Properties of Polyester/Exfoliated Graphite Nanocomposites. *Macromolecules* **2008**, 41, 3317-3327.
 77. Kim, S.; Do, I.; Drzal, L. T., Thermal Stability and Dynamic Mechanical Behavior of Exfoliated Graphite Nanoplatelets-LDPE Nanocomposites. *Polymer Composites* **2010**, 31, 755-761.
 78. Kalaitzidou, K.; Fukushima, H.; Drzal, L. T., A New Compounding Method for Exfoliated Graphite-Polypropylene Nanocomposites with Enhanced Flexural Properties and Lower Percolation Threshold. *Composites Science and Technology* **2007**, 67, 2045-2051.
 79. Wakabayashi, K.; Pierre, C.; Dikin, D. A.; Ruoff, R. S.; Ramanathan, T.; Brinson, L. C.; Torkelson, J. M., Polymer-Graphite Nanocomposites: Effective Dispersion and Major Property Enhancement via Solid-State Shear Pulverization. *Macromolecules* **2008**, 41, 1905-1908.
 80. Kim, H.; Macosko, C. W., Processing-Property Relationships of Polycarbonate/Graphene Composites. *Polymer* **2009**, 50, 3797-3809.
 81. Vallés, C.; Kinloch, I. A.; Young, R. J.; Wilson, N. R.; Rourke, J. P., Graphene Oxide and Base-Washed Graphene Oxide as Reinforcements in PMMA Nanocomposites. *Composites Science and Technology* **2013**, 88, 158-164.
 82. Hull, D., *An Introduction to Composite Materials*. 1st ed.; Cambridge University Press: Cambridge, 1981.
 83. Wang, J.; Shi, Z.; Ge, Y.; Wang, Y.; Fan, J.; Yin, J., Solvent Exfoliated Graphene for Reinforcement of PMMA Composites Prepared by in Situ Polymerization. *Materials Chemistry and Physics* **2012**, 136, 43-50.
 84. Yang, X.; Li, L.; Shang, S.; Tao, X.-m., Synthesis and Characterization of Layer-Aligned Poly(Vinyl Alcohol)/Graphene Nanocomposites. *Polymer* **2010**, 51, 3431-3435.
 85. Li, Y.-Q.; Yu, T.; Yang, T.-Y.; Zheng, L.-X.; Liao, K., Bio-Inspired Nacre-Like Composite Films Based on Graphene with Superior Mechanical, Electrical, and Biocompatible Properties. *Advanced Materials* **2012**, 24, 3426-3431.
 86. Kim, H.; Miura, Y.; Macosko, C. W., Graphene/Polyurethane Nanocomposites for Improved Gas Barrier and Electrical Conductivity. *Chemistry of Materials* **2010**, 22, 3441-3450.
 87. Ramanathan T; Abdala, A. A.; Stankovich S; Dikin, D. A.; Herrera Alonso, M.; Piner, R. D.; Adamson, D. H.; Schniepp, H. C.; Chen X; Ruoff, R. S.; Nguyen, S. T.; Aksay, I. A.; Prud'Homme, R. K.; Brinson, L. C., Functionalized Graphene Sheets for Polymer Nanocomposites. *Nature Nanotechnology* **2008**, 3, 327-331.

88. Young, R. J.; Lovell, P. A., *Introduction to Polymers*. 3rd ed.; CRC Press: Boca Raton, 2011.
89. Chou, T.-W., *Microstructural Design of Fiber Composites*. Cambridge University Press: Cambridge, 1992.
90. Young, R. J.; Kinloch, I. A.; Gong, L.; Novoselov, K. S., The Mechanics of Graphene Nanocomposites: A Review. *Composites Science and Technology* **2012**, 72, 1459-1476.
91. Padawer, G. E.; Beecher, N., On the Strength and Stiffness of Planar Reinforced Plastic Resins. *Polymer Engineering & Science* **1970**, 10, 185-192.
92. Yousefi, N.; Gudarzi, M. M.; Zheng, Q.; Lin, X.; Shen, X.; Jia, J.; Sharif, F.; Kim, J.-K., Highly Aligned, Ultralarge-Size Reduced Graphene Oxide/Polyurethane Nanocomposites: Mechanical Properties and Moisture Permeability. *Composites Part A: Applied Science and Manufacturing* **2013**, 49, 42-50.
93. Paul, D. R.; Robeson, L. M., Polymer Nanotechnology: Nanocomposites. *Polymer* **2008**, 49, 3187-3204.
94. Gong, L.; Kinloch, I. A.; Young, R. J.; Riaz, I.; Jalil, R.; Novoselov, K. S., Interfacial Stress Transfer in a Graphene Monolayer Nanocomposite. *Advanced Materials* **2010**, 22, 2694-2697.
95. Kelly, A.; Macmillan, N. H., *Strong Solids*. 3rd ed.; Clarendon Press: Oxford, 1986.
96. Gibson, R. F., *Principles of Composite Material Mechanics*. McGraw-Hill: New York, 1994.
97. Cox, H. L., The Elasticity and Strength of Paper and Other Fibrous Materials. *British Journal of Applied Physics* **1952**, 3, 72.
98. Zhandarov, S. F.; Pisanova, E. V., Two Interfacial Shear Strength Calculations Based on the Single Fiber Composite Test. *Mechanics of Composite Materials* **1996**, 31, 325-336.
99. Huang, Y.; Young, R. J., Analysis of the Fragmentation Test for Carbon-Fibre/Epoxy Model Composites by Means of Raman Spectroscopy. *Composites Science and Technology* **1994**, 52, 505-517.
100. Young, R. J.; Gong, L.; Kinloch, I. A.; Riaz, I.; Jalil, R.; Novoselov, K. S., Strain Mapping in a Graphene Monolayer Nanocomposite. *ACS Nano* **2011**, 5, 3079-3084.
101. Carlsson, L. A.; Adams, D. F.; Pipes, R. B., *Experimental Characterization of Advanced Composite Materials*. 4th Edition ed.; CRC Press: Boca Raton, 2014.
102. Cooper, C. A.; Cohen, S. R.; Barber, A. H.; Wagner, H. D., Detachment of Nanotubes from a Polymer Matrix. *Applied Physics Letters* **2002**, 81, 3873-3875.
103. Kranbuehl, D. E.; Cai, M.; Glover, A. J.; Schniepp, H. C., Measurement of the Interfacial Attraction between Graphene Oxide Sheets and the Polymer in a Nanocomposite. *Journal of Applied Polymer Science* **2011**, 122, 3739-3743.
104. Andrews, M. C.; Day, R. J.; Hu, X.; Young, R. J., Deformation Micromechanics in High-Modulus Fibres and Composites. *Composites Science and Technology* **1993**, 48, 255-261.
105. Jiang, T.; Huang, R.; Zhu, Y., Interfacial Sliding and Buckling of Monolayer Graphene on a Stretchable Substrate. *Advanced Functional Materials* **2014**, 24, 396-402.

106. Frankland, S. J. V.; Caglar, A.; Brenner, D. W.; Griebel, M., Molecular Simulation of the Influence of Chemical Cross-Links on the Shear Strength of Carbon Nanotube–Polymer Interfaces. *The Journal of Physical Chemistry B* **2002**, 106, 3046-3048.
107. Xu, Y.; Bai, H.; Lu, G.; Li, C.; Shi, G., Flexible Graphene Films via the Filtration of Water-Soluble Noncovalent Functionalized Graphene Sheets. *Journal of the American Chemical Society* **2008**, 130, 5856-5857.
108. Fang, M.; Wang, K.; Lu, H.; Yang, Y.; Nutt, S., Covalent Polymer Functionalization of Graphene Nanosheets and Mechanical Properties of Composites. *Journal of Materials Chemistry* **2009**, 19, 7098-7105.
109. Bansal, A.; Yang, H.; Li, C.; Benicewicz, B. C.; Kumar, S. K.; Schadler, L. S., Controlling the Thermomechanical Properties of Polymer Nanocomposites by Tailoring the Polymer–Particle Interface. *Journal of Polymer Science Part B: Polymer Physics* **2006**, 44, 2944-2950.
110. Zhao, J.; Pei, S.; Ren, W.; Gao, L.; Cheng, H.-M., Efficient Preparation of Large-Area Graphene Oxide Sheets for Transparent Conductive Films. *ACS Nano* **2010**, 4, 5245-5252.
111. Fu, S.-Y.; Feng, X.-Q.; Lauke, B.; Mai, Y.-W., Effects of Particle Size, Particle/Matrix Interface Adhesion and Particle Loading on Mechanical Properties of Particulate–Polymer Composites. *Composites Part B: Engineering* **2008**, 39, 933-961.
112. Chatterjee, S.; Nafezarefi, F.; Tai, N. H.; Schlagenhauf, L.; Nüesch, F. A.; Chu, B. T. T., Size and Synergy Effects of Nanofiller Hybrids Including Graphene Nanoplatelets and Carbon Nanotubes in Mechanical Properties of Epoxy Composites. *Carbon* **2012**, 50, 5380-5386.
113. Shen, X.; Lin, X.; Yousefi, N.; Jia, J.; Kim, J.-K., Wrinkling in Graphene Sheets and Graphene Oxide Papers. *Carbon* **2014**, 66, 84-92.
114. Weon, J. I.; Sue, H. J., Effects of Clay Orientation and Aspect Ratio on Mechanical Behavior of Nylon-6 Nanocomposite. *Polymer* **2005**, 46, 6325-6334.
115. Galgali, G.; Agarwal, S.; Lele, A., Effect of Clay Orientation on the Tensile Modulus of Polypropylene–Nanoclay Composites. *Polymer* **2004**, 45, 6059-6069.
116. Fornes, T. D.; Paul, D. R., Modeling Properties of Nylon 6/Clay Nanocomposites Using Composite Theories. *Polymer* **2003**, 44, 4993-5013.
117. Hermans, J. J.; Hermans, P. H.; Vermaas, D.; Weidinger, A., Quantitative Evaluation of Orientation in Cellulose Fibres from the X-Ray Fibre Diagram. *Recueil des Travaux Chimiques des Pays-Bas* **1946**, 65, 427-447.
118. Bacon, G. E., A Method for Determining the Degree of Orientation of Graphite. *Journal of Applied Chemistry* **1956**, 6, 477-481.
119. Taylor, R. M.; Norrish, K., The Measurement of Orientation Distribution and Its Application to Quantitative X-Ray Diffraction Analysis. *Clay Minerals* **1966**, 6, 127-142.
120. Duesberg, G. S.; Loa, I.; Burghard, M.; Syassen, K.; Roth, S., Polarized Raman Spectroscopy on Isolated Single-Wall Carbon Nanotubes. *Physical Review Letters* **2000**, 85, 5436-5439.
121. Fan, Y.; Lu, Y. C.; Lou, J.; Tang, C. C.; Shinozaki, D. M., Structure Orientation and Micromechanical Characterization of Platelet-Reinforced Polyethylene Nanocomposites. *Journal of Applied Polymer Science* **2013**, 127, 1387-1393.

122. Sonobe, K.; Kikuta, K.; Takagi, K., Dispersion and Alignment of Organic–Clay Composites within Polysilicate Thin Films by the Sol–Gel Method. *Chemistry of Materials* **1999**, 11, 1089-1093.
123. Lin, X.; Shen, X.; Zheng, Q.; Yousefi, N.; Ye, L.; Mai, Y.-W.; Kim, J.-K., Fabrication of Highly-Aligned, Conductive, and Strong Graphene Papers Using Ultralarge Graphene Oxide Sheets. *ACS Nano* **2012**, 6, 10708-10719.
124. Sun, T.; Chen, F.; Dong, X.; Zhou, Y.; Wang, D.; Han, C. C., Shear-Induced Orientation in the Crystallization of an Isotactic Polypropylene Nanocomposite. *Polymer* **2009**, 50, 2465-2471.
125. Pujari, S.; Dougherty, L.; Mobuchon, C.; Carreau, P.; Heuzey, M.-C.; Burghardt, W., X-Ray Scattering Measurements of Particle Orientation in a Sheared Polymer/Clay Dispersion. *Rheologica Acta* **2011**, 50, 3-16.
126. Loo, L. S.; Gleason, K. K., Investigation of Polymer and Nanoclay Orientation Distribution in Nylon 6/Montmorillonite Nanocomposite. *Polymer* **2004**, 45, 5933-5939.
127. Zevin, L.; Viaene, W., Impact of Clay Particle Orientation on Quantitative Clay Diffractometry. *Clay Minerals* **1990**, 25, 401-418.
128. Nawani, P.; Burger, C.; Rong, L.; Chu, B.; Hsiao, B. S.; Tsou, A. H.; Weng, W., Characterization of Nanoclay Orientation in Polymer Nanocomposite Film by Small-Angle X-Ray Scattering. *Polymer* **2010**, 51, 5255-5266.
129. Rao, A. M.; Jorio, A.; Pimenta, M. A.; Dantas, M. S. S.; Saito, R.; Dresselhaus, G.; Dresselhaus, M. S., Polarized Raman Study of Aligned Multiwalled Carbon Nanotubes. *Physical Review Letters* **2000**, 84, 1820-1823.
130. Gommans, H. H.; Alldredge, J. W.; Tashiro, H.; Park, J.; Magnuson, J.; Rinzler, A. G., Fibers of Aligned Single-Walled Carbon Nanotubes: Polarized Raman Spectroscopy. *Journal of Applied Physics* **2000**, 88, 2509-2514.
131. Liu, T.; Kumar, S., Quantitative Characterization of SWNT Orientation by Polarized Raman Spectroscopy. *Chemical Physics Letters* **2003**, 378, 257-262.
132. Perez, R.; Banda, S.; Ounaies, Z., Determination of the Orientation Distribution Function in Aligned Single Wall Nanotube Polymer Nanocomposites by Polarized Raman Spectroscopy. *Journal of Applied Physics* **2008**, 103, 074302-9.
133. Krenchel, H., *Fibre Reinforcement*. Akademisk Forlag: Copenhagen, 1964.
134. Bitinis, N.; Sanz, A.; Nogales, A.; Verdejo, R.; Lopez-Manchado, M. A.; Ezquerro, T. A., Deformation Mechanisms in Polylactic Acid/Natural Rubber/Organoclay Bionanocomposites as Revealed by Synchrotron X-Ray Scattering. *Soft Matter* **2012**, 8, 8990-8997.
135. Liu, H.; Brinson, L. C., Reinforcing Efficiency of Nanoparticles: A Simple Comparison for Polymer Nanocomposites. *Composites Science and Technology* **2008**, 68, 1502-1512.
136. Halpin, J. C.; Kardos, J. L., The Halpin-Tsai Equations: A Review. *Polymer Engineering & Science* **1976**, 16, 344-352.
137. Zhang, X.; Liu, T.; Sreekumar, T. V.; Kumar, S.; Moore, V. C.; Hauge, R. H.; Smalley, R. E., Poly(Vinyl Alcohol)/SWNT Composite Film. *Nano Letters* **2003**, 3, 1285-1288.

Chapter 2 Raman Spectroscopy of Graphene

2.1 Introduction

Infrared absorption and Raman scattering are the main spectroscopic technologies that are used widely and complementarily nowadays to detect vibrations in molecules. Infrared absorption is due to a change of the molecular dipole moment while Raman scattering results from the change of the polarizability [1].

The early 1920s was a time of interest in the scattering of radiation [2]. The inelastic scattering of light by molecule was first predicted by Smekal [3] and then observed by Indian physicist Sir Chandrasekhara V. Raman [4] using crude instrumentation, where sunlight was the light source and his eyes the detector [5]. Raman scattering is inherently so weak that approximately one of $10^6 \sim 10^8$ photons [1] in the light can be scattered that it is hard to be detected. This is the reason why Raman spectroscopy was not widely employed until 1960s, when significant improvement took place on the components of Raman spectrometer, such as the high power laser excitation sources and better detection systems [5].

After decades of development, Raman spectroscopy is now a powerful technique to characterize molecular vibrations, especially for carbon materials [6-8]. It is non-destructive under low laser power and the sample preparation is simple, and even the signals from aqueous samples can be detected due to weak Raman vibrations of water molecule [9]. However, it still suffers from some problems, for example, the fluorescence background and the degradation of samples under high laser power [2].

2.2 Principle of Raman Scattering

2.2.1 Classical Theory

An incident light beam can be considered as an oscillating electric field E at a given time t_0 [5]:

$$E = E_0 \cos 2\pi \nu_0 t_0 \quad (2.1)$$

where E_0 is the vibrational amplitude and ν_0 is the frequency of the light beam.

If a molecule is placed in this oscillating electric field, the field interacts with the molecule and distort its charge distribution [10]. It alternates the molecular dipole moment μ and gives rise to the scattering [9]:

$$\mu = \alpha E \quad (2.2)$$

where α is the molecular polarizability, which measures the ability of a molecule to be polarized, namely, to response dynamically to the electric field [9]. It is crucial in the theory of the Raman effect, and the change of size, shape and orientation of the polarizability ellipsoid can be used to identify if a vibration is Raman-active [5]. For a small amplitude of vibration, α can be written as [2, 5]:

$$\alpha = \alpha_0 + \left(\frac{\partial \alpha}{\partial q} \right)_0 q + \dots \quad (2.3)$$

where α_0 is the polarizability at equilibrium position, and $(\partial \alpha / \partial q)_0$ is the change rate of α against the molecule nuclear displacement q , which is given as [5]:

$$q = q_0 \cos 2\pi \nu_q t_0 \quad (2.4)$$

where q_0 and ν_q are the vibrational amplitude and frequency of the nuclear, respectively. Accordingly, substituting Eqs. 2.1, 2.3 and 2.4 into Eq. 2.2:

$$\mu = \alpha_0 E_0 \cos 2\pi \nu_0 t_0 + \frac{1}{2} q_0 E_0 \left(\frac{\partial \alpha}{\partial q} \right)_0 \left\{ \cos[2\pi(\nu_0 - \nu_q)t_0] + \cos[2\pi(\nu_0 + \nu_q)t_0] \right\} \quad (2.5)$$

The two terms in Eq. 2.5 represent three major scatterings considered here. The first term denotes the elastic ‘Rayleigh scattering’, which has the same frequency ν_0 as E ; the second term accounts for the ‘Raman scattering’, including the Stokes mode and anti-Stokes mode, with different vibrational frequency $(\nu_0 - \nu_q)$ and $(\nu_0 + \nu_q)$ [2, 5]. For

the Raman scattering to occur, $(\partial\alpha/\partial q)_0 \neq 0$ [5], that is, the change of α is required for a vibration to be Raman-active [11].

2.2.2 Quantum Theory

The Raman scattering can also be understood in terms of quantum theory, where the incident light E is regarded as a beam of photons [10], and its energy is expressed as:

$$E = h\nu_0 \quad (2.6)$$

where ν_0 is the vibrational frequency and h is the Planck's constant.

The photons in the light beam interact with the electrons in the molecule. If the photon energy matches the energy gap between the ground and the excited state of the molecule, the energy is absorbed to promote the molecule to the excited state [1]. Otherwise it can also excite the molecule to a 'virtual state'. The virtual state is not stable and will immediately re-radiate to a lower excited or ground state [5]. Fig. 2.1 shows a brief diagram of the electronic transition of a molecule in terms of the Rayleigh scattering and Raman scattering.

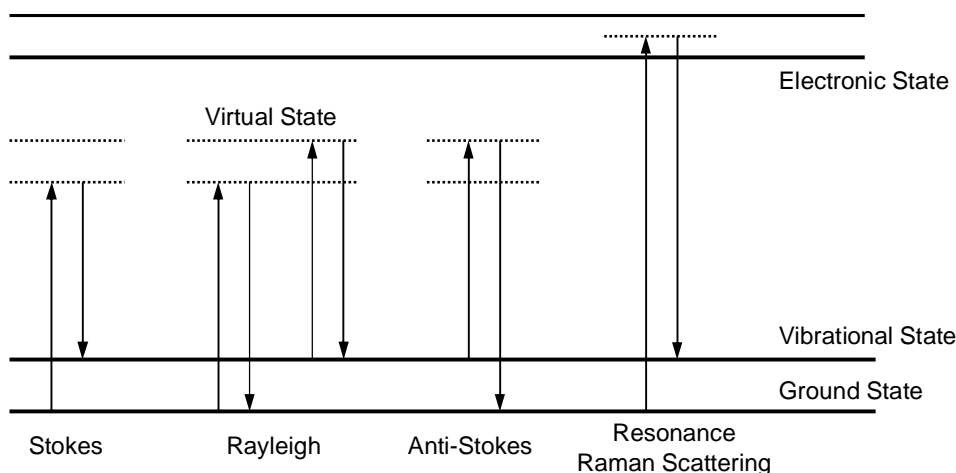


Figure 2.1 Diagram of the Rayleigh scattering, Raman Stokes mode, Raman anti-Stokes mode and resonance Raman scattering [1, 5].

According to the 'conservation of energy' principle [10]:

$$E_i + E_i = E_2 + E_s \quad (2.7)$$

where E_1 , E_2 , E_i and E_s denote the molecular energy before and after scattering, the incident and scattered photon energy, respectively. Substituting Eq. 2.6, it can be obtained that:

$$\omega = \frac{E_i - E_s}{hc} = \frac{\Delta\nu_0}{c} \quad (2.8)$$

where c represents the speed of light, and $\Delta\nu_0$ denotes the frequency change of the incident photon and scattered photon. ω is the corresponding wavenumber shift, referred to as ‘Raman shift’ (Raman wavenumber), with a unit of Δcm^{-1} but usually used as cm^{-1} for simplicity. ω can be divided into three groups:

1) $\omega=0$, elastic scattering.

This elastic scattering process is called ‘Rayleigh scattering’, where the molecule absorbs the energy of the photons, excited to the ‘virtual state’ and immediately re-radiates and backs to the original state. It ends up with both the molecule and the photon being at the same energy level as before scattering, and no energy transfer occurs between the two.

2) $\omega \neq 0$, inelastic scattering [1].

$\omega > 0$ means the photon energy decreases after scattering, known as the ‘Stokes mode’. In this process, after re-radiating, the molecule goes back to excited state rather than its original ground state (Fig. 2.1). As a result, the molecule absorbs the energy from the photons.

$\omega < 0$, the photon energy increases after scattering, known as the ‘anti-Stokes mode’. In this mode, the molecule is originally at the excited state but ends up in the ground state after energy is transferred from the molecule to the photons.

Generally, the value of ω for the Stokes mode and anti-Stokes mode are the same. However, the intensity of Stokes mode is much higher than that of the anti-Stokes mode, because of the considerably lower population of molecules in the excited state than that in the ground state at room temperature [1]. As the temperature increases,

the population of molecules in the excited state increases, leading to a rise of the anti-Stokes scattering intensity compared to that of the Stokes scattering [1].

The Raman scattering can also occur in resonance process, where the excitation overlaps with, or closes to, the electronic transition of a molecule (Fig. 2.1) [5]. Hence the molecule is excited to around a real electronic state rather than a ‘virtual state’, and causes a significant enhancement of the scattering intensity by a factor of 10^3 to 10^6 [12].

2.3 Instrumentation

2.3.1 Raman Spectrometer

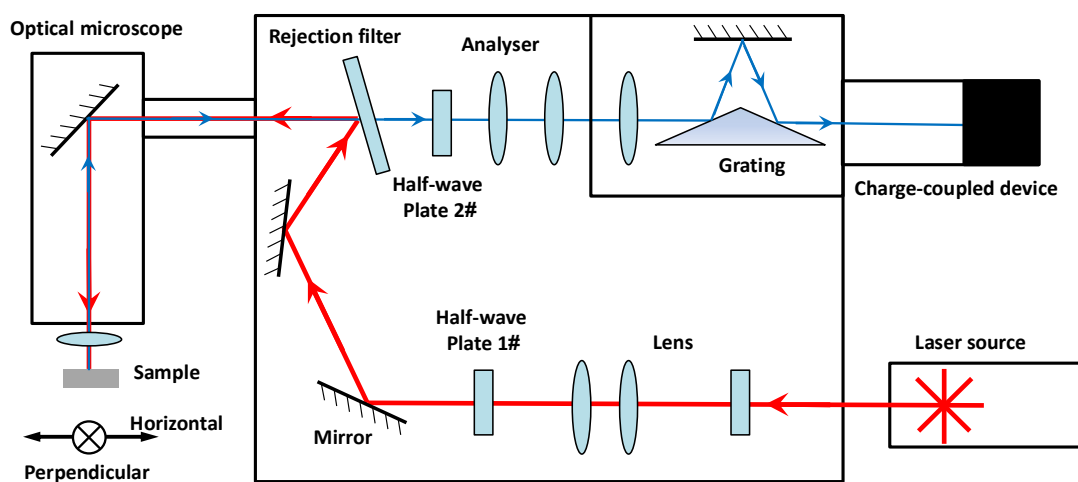


Figure 2.2 Schematic diagram of the Raman spectrometer. The red and the blue line represent the incident and scattered radiation, respectively. The arrows represent the laser propagation directions [10].

Raman spectra were collected using Renishaw 1000/2000 spectrometers equipped with Olympus BH-2 microscope or Horiba LabRAM HR Evolution Raman spectrometer. The lasers used were HeNe laser ($\lambda = 633$ nm, $E_{\text{laser}} = 1.96$ eV) and Ar⁺ laser ($\lambda = 514$ nm, $E_{\text{laser}} = 2.41$ eV). A schematic diagram of the instrument is shown in Fig. 2.2. The laser beam was focused on the sample surface using a 50x or 100x objective lens and the diameter of the laser spot on the sample was estimated to be around 1~2 μm . The laser power was less than 1 mW to avoid the local laser heating [10, 12]. For scanning, generally the exposure time was up to 60s depending on

different samples and the scanning was accumulated to increase the signal-noise ratio.

Different polarization configurations are shown in Table 2.1 [10]. The laser polarization was changed through two half-wave plates and one analyser. The horizontal direction is defined as ‘V’ and represented by ‘//’; the perpendicular direction is termed ‘H’ and represented by ‘ \perp ’, and ‘N’ means the laser is polarized in all the directions, represented by ‘ \ast ’. In the polarization configuration abbreviations such as ‘VH’, the first and second letter represents the direction of the incident and scattered radiation, respectively. ‘In’ or ‘out’ mean the corresponding optical component is placed into, or taken away from the laser pathway. Commonly a ‘VN’ configuration was used as stated in each chapter but an analyzer was used for ‘VV’ configuration for the orientation study. In the tests, the Raman laser polarization was always fixed and the samples were rotated on a rotation stage.

Table 2. 1 Different polarization configurations and their corresponding instrumental settings [10, 12].

	VN	VV	VH	HN	HH	HV
Incident Radiation	//	//	//	\perp	\perp	\perp
Scattered Radiation	\ast	//	\perp	\ast	\perp	//
Half-wave Plate 1#	In	In	In	Out	Out	Out
Half-wave Plate 2#	Out	Out	In	Out	In	Out
Analyser	Out	In	In	Out	In	In

2.3.2 In-situ Deformation Raman Spectroscopy

The deformation of specimens was carried out by placing a PMMA beam with specimens on its top into a four-point bending rig (Fig. 2.3). This was placed onto the optical microscope stage in the Raman spectrometer so the Raman spectra could be collected *in-situ* the deformation of specimen. A resistance strain gauge was bonded to the specimen surface to measure the surface strain, which can be read through the resistance by a connected multimeter. The beam was deformed stepwise

and Raman spectra were collected from the central area of specimen at each strain level [10]. For the deformation tests, the polarization of the incident laser was kept parallel to the tensile direction [13].

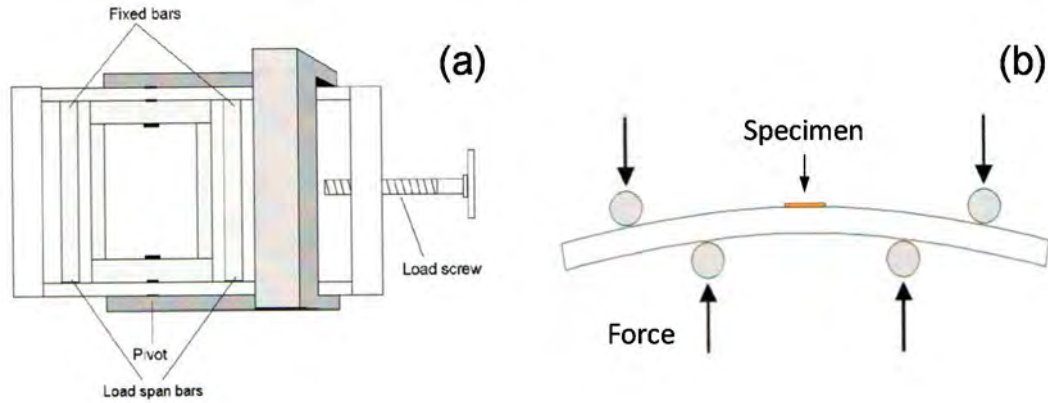


Figure 2.3 Schematic diagram of (a) the four-point bending rig and (b) the tensile deformation test [11].

2.3.3 Raman Spectroscopy Data Analysis

Generally the band position and intensity was obtained by fitting the Raman spectroscopy data using a Lorentzian function [12]:

$$I = \frac{I_p \cdot FWHM}{(\omega - \omega_0)^2 + (FWHM)^2} \quad (2.9)$$

I is the intensity of Raman band at any Raman wavenumber ω , and I_p is the intensity of the Raman band at its peak position ω_0 . $FWHM$ is the full width at half maximum of the Raman band.

2.4 Raman Spectroscopy of Graphene and Graphene Oxide

Raman spectroscopy has been proved to be one of most powerful techniques for charactering carbon materials [6, 10, 14, 15]. The isolation of graphene [16] enables this one atomic thick building block of graphitic materials to be studied in-depth in this way on its strain level [17-21], stacking order [22-25], functionalization [26, 27], doping level [28-30] and crystalline structure [10, 18, 21]. There are three prominent

bands in the Raman spectrum of graphene, the D band, G band and 2D band (also termed G' band) (Fig. 2.4(a)) [14, 15].

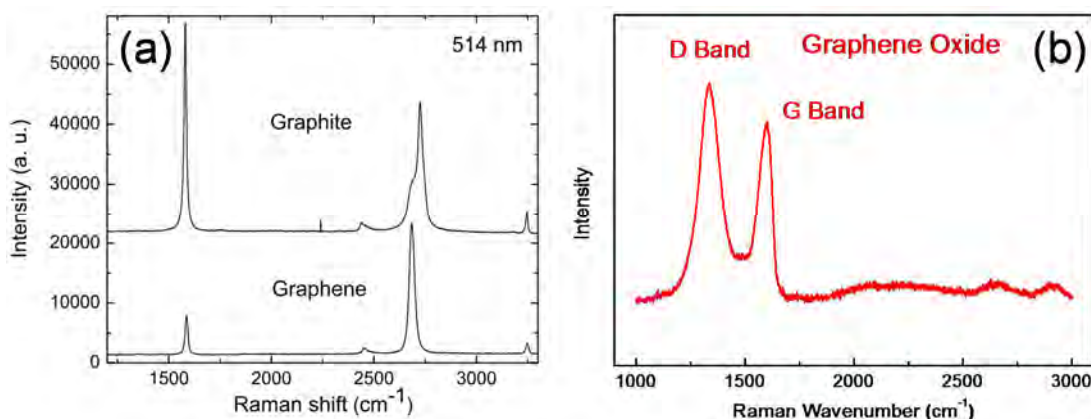


Figure 2.4 Raman spectra of (a) graphite, graphene [14] and (b) GO.

The Raman spectrum of graphene oxide (GO) is generally similar to that of graphene (Fig. 2.4(b)) [26]. However, the strong oxidation breaks the sp^2 carbon network and grafts a large number of functional groups [31]. This destroys the lattice symmetry and leads to the absence of the 2D band [32], and a broadened D band and G band with a higher intensity ratio of the D band and G band (I_D/I_G) [33-36], making its Raman spectrum resemble that of amorphous carbon [37]. By restoring its graphitic structure through reduction of GO, some recovery of the Raman 2D band can be sometimes observed [32, 38].

2.4.1 Raman G band

The G band, centred around 1580 cm^{-1} , is from the first order scattering process (Fig. 2.5(a)). It is associated with the doubly-degenerate (iTO and LO) phonon mode (E_{2g} symmetry) at the Brillouin zone (BZ) centre (Γ point) [6, 7].

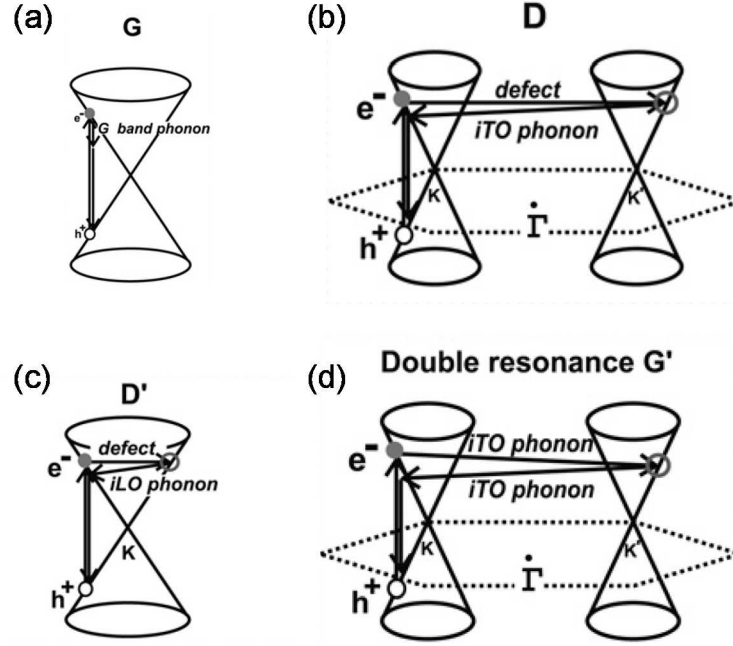


Figure 2.5 (a) First order process G band. Second order process (b) D band, (c) D' band and (d) 2D (G') band [6].

2.4.2 Raman D, D' and 2D bands

The D band ($1300\sim 1400\text{ cm}^{-1}$), D' band ($\sim 1620\text{ cm}^{-1}$) and 2D band ($2600\sim 2700\text{ cm}^{-1}$) are the second order scattering, originating from a double resonance (DR) process [10] (Figs. 2.5(b), (c) and (d)).

The D band involves one iTO phonon of A_{1g} symmetry and one defect near the BZ \mathbf{K} point [31]. The 2D band is the overtone of D band, resulting from two iTO phonons with opposite momentum in the highest optical branch near the \mathbf{K} point [14]. Unlike the 'intervalley' process of D band connecting \mathbf{K} and a nearby \mathbf{K}' points, the DR process for the D' band [6, 39] is an 'intravalley' process, where the scattering takes place in the circle around the same \mathbf{K} point [6]. For the D and 2D band, generally the DR process [14, 40] involves four steps: (a) an electron with a wave vector \mathbf{k} is excited by the incident photon. (b) the electron is inelastically scattered by a phonon with a momentum \mathbf{q} to the nearby \mathbf{K}' point; (c) the electron is scattered by a phonon in 2D band (a defect in D band) with a momentum $-\mathbf{q}$ back to the original \mathbf{K} point; (d) the electron-hole pair recombines [14]. The 2D band consists of

two inelastic scattering process by phonons, while the D band originates one inelastic phonon scattering process and one elastic defect scattering process [41, 42].

The D band can be employed to determine the geometry of graphene edges using the knowledge of crystalline structure that the adjacent edges ideally should have an angle of a multiple of 30° between them (Fig. 2.6(a)) [43-45]. Although ideally the D band is selectively active at the armchair edges, where only the armchair edge vector $-\mathbf{q}$ is able to scatter electron back to the original \mathbf{K} point under certain excitation (Fig. 2.6(b)) [43], in reality the nanoscale roughness [45] gives rise to the presence of D band at almost all edge geometries. The dominant edge geometry can still be identified, however, using the edge direction dependent D band intensity (Section 2.4.4) [43, 45, 46].

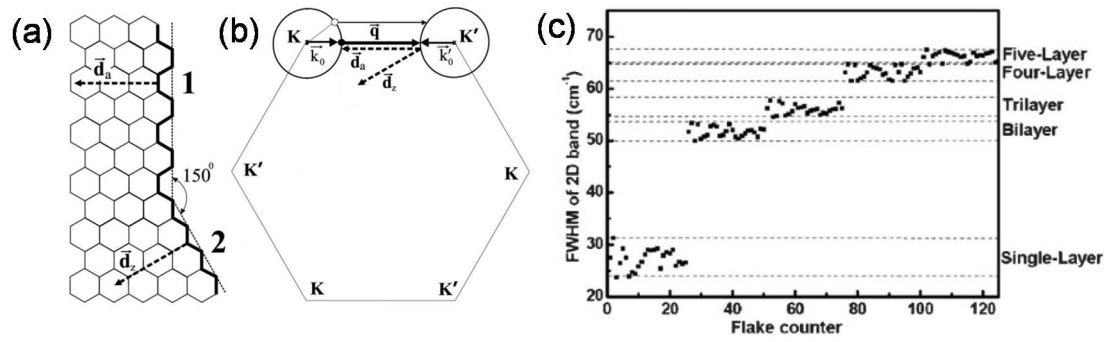


Figure 2.6 (a) (1) Armchair and (2) zigzag edge geometry. (b) First Brillouin zone of graphene, showing the DR process for both edges [43]. (c) $FWHM_{2D}$ against the number of layers of graphene [23].

As no defect is required in the scattering process, the 2D band is allowed in defect-free graphene samples and its geometry sheds light on the number of graphene layers. For monolayer graphene the 2D band is very sharp and can be fitted with single Lorentzian peak with a full width at half maximum ($FWHM_{2D}$) less than 30 cm^{-1} (Fig. 2.6(c)) [6, 23], though slightly larger for less crystallized materials such as graphene prepared *via* CVD [47, 48]. For bi-layer graphene, it consists of four components with the width of each component being around $\sim 24 \text{ cm}^{-1}$ (Fig. 2.7(a)) [6]. The 2D band of tri-layer graphene contains fifteen components, however usually six peaks are used to fit as some of them are overlapped [6]. The shape of the 2D band changes towards that of graphite for graphene more than 5 layers (Fig. 2.7(a)) [6, 14].

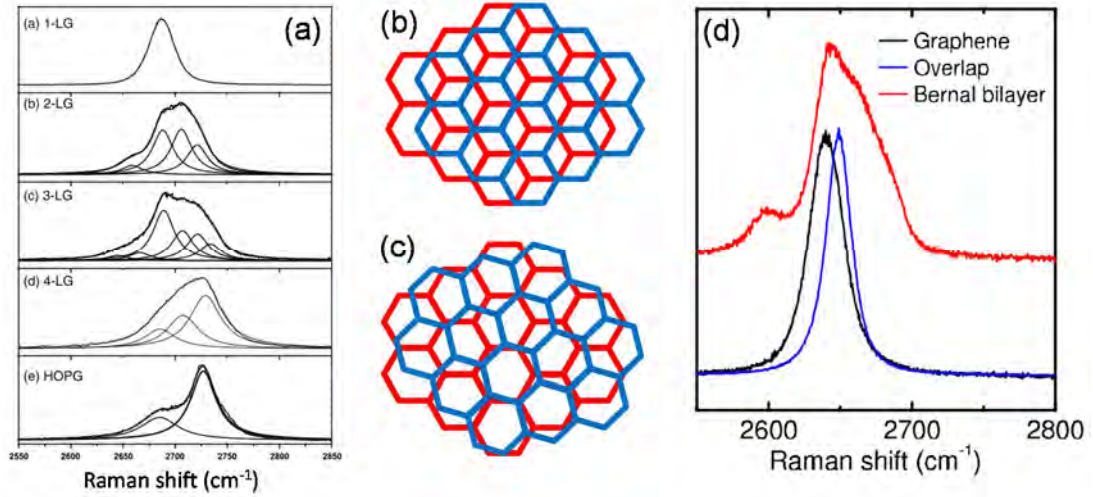


Figure 2.7 (a) The measured 2D band for 1-layer graphene (1-LG), 2-LG, 3-LG, 4-LG and HOPG, with the Lorentzian peaks for fitting [6]. (b) Bernal stacking bi-layer graphene. (c) Twisted bi-layer graphene. (d) The Raman 2D band for monolayer, Bernal-stacked and twisted bi-layer graphene [24].

It should be noted that the bi-layer graphene described above follows the Bernal stacking (AB stacking) order, where the centre of the hexagon at one layer corresponds to one carbon atom in adjacent layers (Fig. 2.7(b)) [6]. Under twisting (Fig. 2.7(c)), the interaction between the two layers weakens hence the Raman 2D band resembles that of the monolayer graphene (Fig. 2.7(d)) [24, 49].

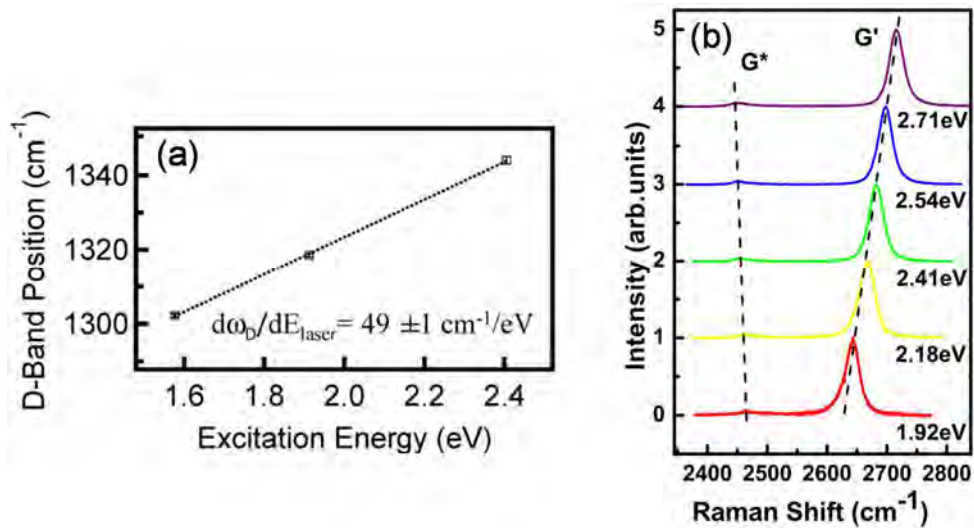


Figure 2.8 Dispersion of the Raman (a) D band [45] and (b) 2D band [50].

The D and 2D bands also show dispersive behaviour. As the excitation energy increases, the wave vector \mathbf{k} in the resonance moves away from the \mathbf{K} point that increases the phonon wave vector \mathbf{q} [6]. Due to the extra phonon involved, the dispersion of the 2D band of $\sim 100 \text{ cm}^{-1}/\text{eV}$ [50] is approximately double that of the D band $\sim 50 \text{ cm}^{-1}/\text{eV}$ (Fig. 2.8) [40, 45, 51].

A high intensity ratio of 2D band and G band (I_{2D}/I_G) ~ 4 (Fig. 2.4(a)) is commonly regarded as one of the figureprints for monolayer graphene [14]. As defects (edge, grain boundaries etc.) are required to activate the D band, the I_D/I_G ratio is usually employed to quantify the disorder and also the flake size, of graphene [7, 52-54].

2.4.3 Strain in Graphene

Basically when a carbon material is strained, the C-C bonds are distorted, which is accompanied by a change of bonding energy. The tension/compression softens/hardens the phonon, shown as the down-/up-shift of the Raman wavenumber [17-21]. The D, G and 2D band exhibit the similar trend, however, with different shift rates with strain [55]. This phenomenon has long been observed and used to monitor the micromechanical deformation of composites [56]. An empirical calibration has been established to correlate Raman 2D band shift rate to the Young's modulus of carbon fibres, with a value of $-50 \sim -60 \text{ cm}^{-1}/\%$ strain/TPa [57].

The isolation of graphene enabled the mechanism to be revealed [16]. There are many ways to strain graphene such as bending [17-21, 49, 58-65], stretching [66], depression or bubble pressuring [67-70], hydro compression [71, 72] and so on [73]. At an early stage, Yu et al. [58] and Ni et al. [17] bent a PET substrate with graphene on top, and found a downshift of the Raman 2D band of graphene under tension with shift rate being $-7.8 \text{ cm}^{-1}/\%$, and $-27.8 \text{ cm}^{-1}/\%$. It is similar to the value of around $-21 \text{ cm}^{-1}/\%$ observed by Huang et al. [18] by stretching the graphene on PDMS substrate, yet a value around $-60 \text{ cm}^{-1}/\%$ was also found by Tsoukleri et al. [19] by stretching graphene by bending the PMMA substrate. The later value was confirmed by Mohiuddin et al. [21] using the knowledge of Gruneisen parameter [74], which is a measure of the sensitivity of the phonon frequency (Raman band position) to the

change of the crystal unit cell volume (Eq. 2.10 for E_{2g} mode G band and Eq. 2.11 for A_{1g} mode 2D band):

$$\Delta\omega_G^\pm = -\omega_G^0 \gamma_G (\varepsilon_l + \varepsilon_t) \pm \frac{1}{2} \beta \omega_G^0 (\varepsilon_l - \varepsilon_t) \quad (2.10)$$

$$\Delta\omega_{2D} = -\omega_{2D}^0 \gamma_{2D} (\varepsilon_l + \varepsilon_t) \quad (2.11)$$

where γ_G and γ_{2D} are the Gruneisen parameter for E_{2g} mode G band and A_{1g} mode 2D band, respectively. β denotes the shear potential. $\Delta\omega_G^\pm$ ($\Delta\omega_{2D}$) and ω_G^0 (ω_{2D}^0) are the Raman band position shift and intinial wavenumber of G (2D) band, respectively. ε_l and ε_t are the strain in the longitugal and transverse directions, respectively.

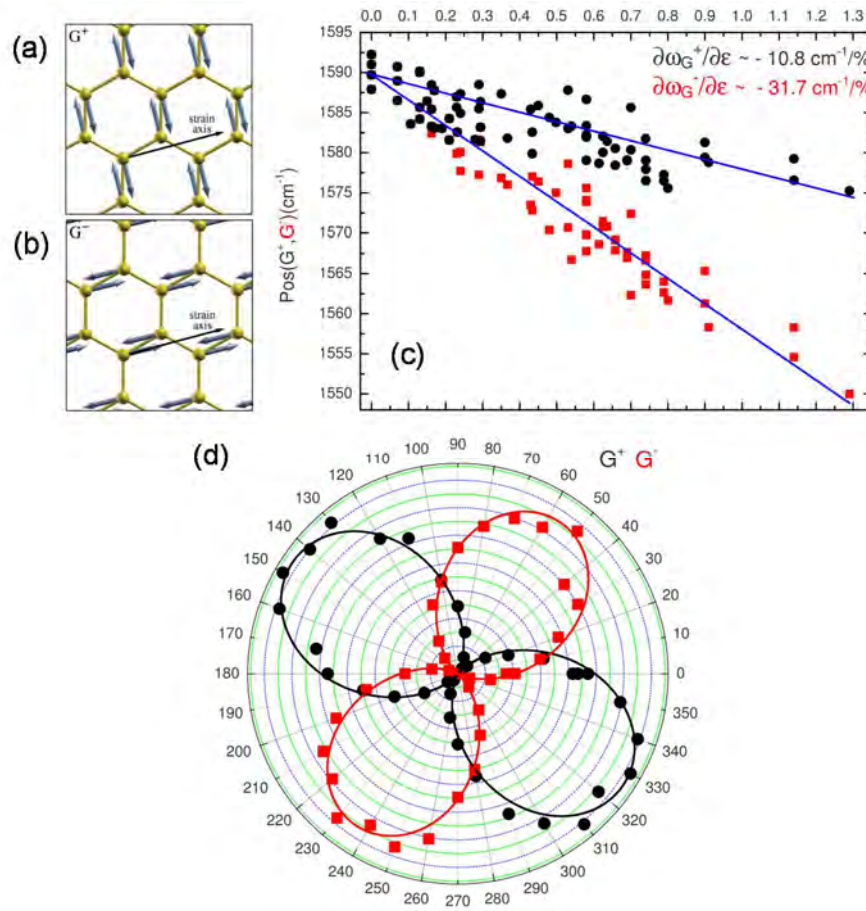


Figure 2.9 (a) Graphene lattice vibration for G+ and G- mode, respectively. (b) The Raman G+ and G- band position as function of uniaxial strain. (d) Polar plot of the intensity of G- (red) and G+ (black) band relative to the incident laser polarization [21].

Uniaxial strain forces the phonons of graphene to be parallel and perpendicular to the strain axis (Figs. 2.9(a) and (b)), splitting the Raman G band to G- and G+ bands with different shift rate under strain (Fig. 2.9(c)) [21, 59]. This finding was further utilized to determine the crystallographic orientation of graphene [10, 18, 21]. When the scattered laser polarization was kept parallel to the strain, variations of the intensity of G- and G+ bands as the function of the angle between the incident laser polarization and strain direction clearly showed the crystallographic orientation of graphene relative to the strain direction (Fig. 2.9(d)) [21].

Splitting of the Raman 2D band under strain has also been observed [60-63], because it was initially only observed along the high symmetric (zig-zag or armchair) directions (Fig. 2.10), it was attributed to the inside-loop scattering mechanism [62, 63] instead of the outside loop mechanism [14]. In contrast, it was also suggested that both the inner and outer process contribute to the splitting [60, 75], and it seems become more significant under excitation with lower laser energy [60].

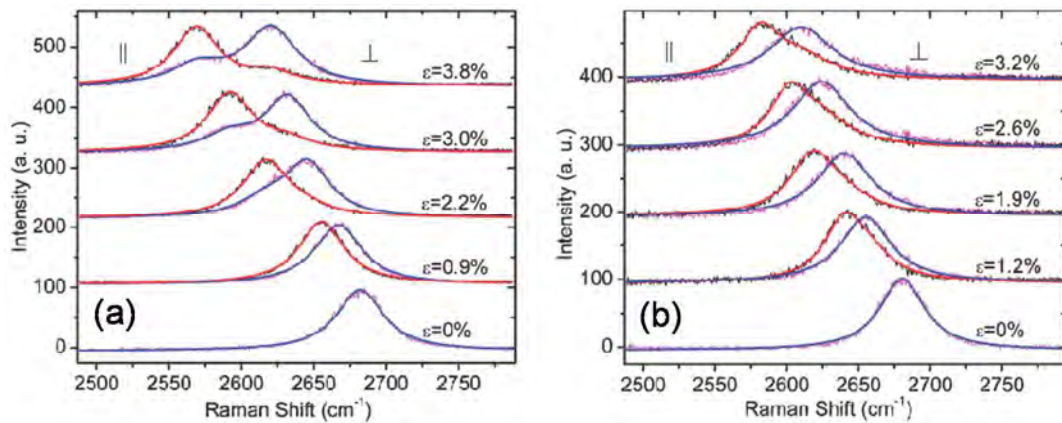


Figure 2.10 Splitting of the Raman 2D band for graphene under uniaxial strain along (a) zigzag (b) armchair directions, where the incident laser polarization was parallel (red) or perpendicular (blue) to the strain direction [62].

The scattered Raman band position shift rate can be technically assigned to the different Poisson's ratio of the substrates [10], or the accuracy of calibration of the correct strain in graphene. The use of Gruneisen parameter [55] enables the reference shift rate of different bands under uniaxial [17, 18, 21, 63, 76, 77] and biaxial strain [67-70, 73], to be estimated. However, Cheng et al. proposed that the value of

Gruneisen parameter could be a variable that depends on strain level and orientation of graphene [76].

The stress/strain induced Raman band position shift was further employed to monitor the micromechanics of graphene-based nanocomposites [78]. Gong et al. [20] identified the strain distribution of a monolayer graphene, where the strain builds up from the end of graphene and becomes a plateau in the middle region of graphene along the strain direction (Fig. 2.11(a)). The good match of the experimental finding with the well-established shear lag theory [79, 80] validated the continuous mechanics at this scale. As strain increases, the strain distribution of graphene becomes non-uniform with some small segments seen [20, 65], indicating a collapse of the matrix or the interface (Figs. 2.11(b) and (c)). In addition to a complete failure, a reversible interfacial sliding has been observed on a stretchable PET substrate [66].

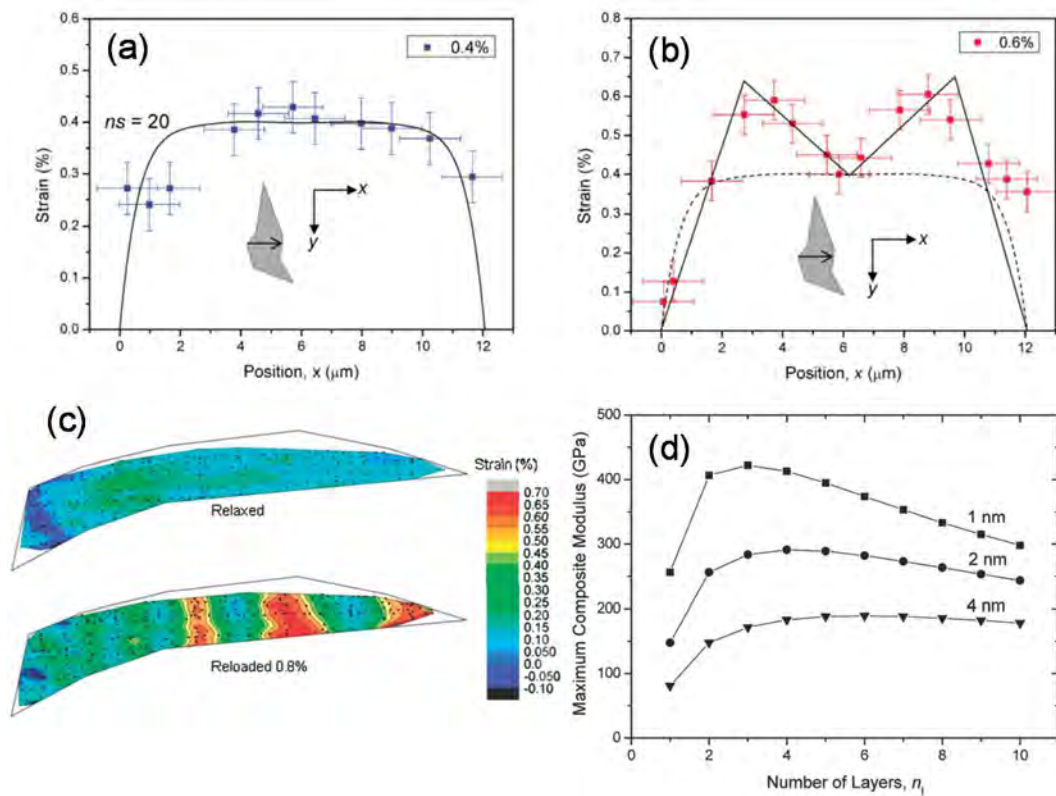


Figure 2.11 (a) Strain distribution of monolayer graphene under 0.4 % strain. (b) Strain distribution of monolayer graphene under 0.6 % strain [20]. (c) Strain distribution of monolayer graphene when reloading to 0.8 % strain [65]. (d) Predicted Young's modulus of the nanocomposites as the function of the number of graphene layers for different polymer thickness between graphene flakes [64].

It has been found [61, 64] that the shift rate of the 2D band becomes less significant as layer number increase, until reaching an almost-zero value for graphite, due to the low shear modulus of ~ 5 GPa between graphene layers [81] that can further lead to a loss of Bernal stacking of graphene under strain [49]. This is probably the reason why many of the studies on strained graphite were carried out under compression rather than tension [72, 82-84]. The finding can also be understood as the poor interlayer stress transfer and based on the 'rule of mixtures', Gong et al. [64] proposed that the Young's modulus of the nanocomposites is optimized when reinforced with bi- or tri-layer graphene (Fig. 2.11(d)). The flexural rigidity under compression can be significantly enhanced when graphene is embedded, that a shorter linear correlation of the 2D band position shift with strain was observed, indicating reduced stability and progressive buckling of the graphene (Fig. 2.12) [59].

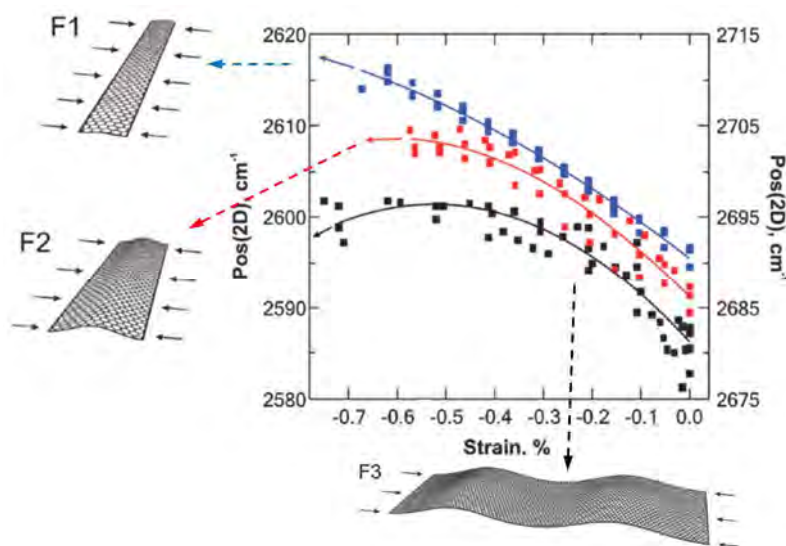


Figure 2.12 Raman 2D band position shift under compression for different graphene flakes, and their corresponding schematic rectangular shell geometries [59].

The previous finding on carbon fibres [56] has also been re-interpreted (Fig. 2.13(a)) based on the Raman studies on graphene and a universal correlation of the G band position shift with stress was plotted as approximately $-5 \omega_G^0 \text{ cm}^{-1} \text{ MPa}^{-1}$ [85]. The G band was also found to consist of G-, G+ and D' bands in GO papers, and their shift rate were used to monitor the deformation mechanics (Figs. 2.13(b), (c) and (d)) [86].

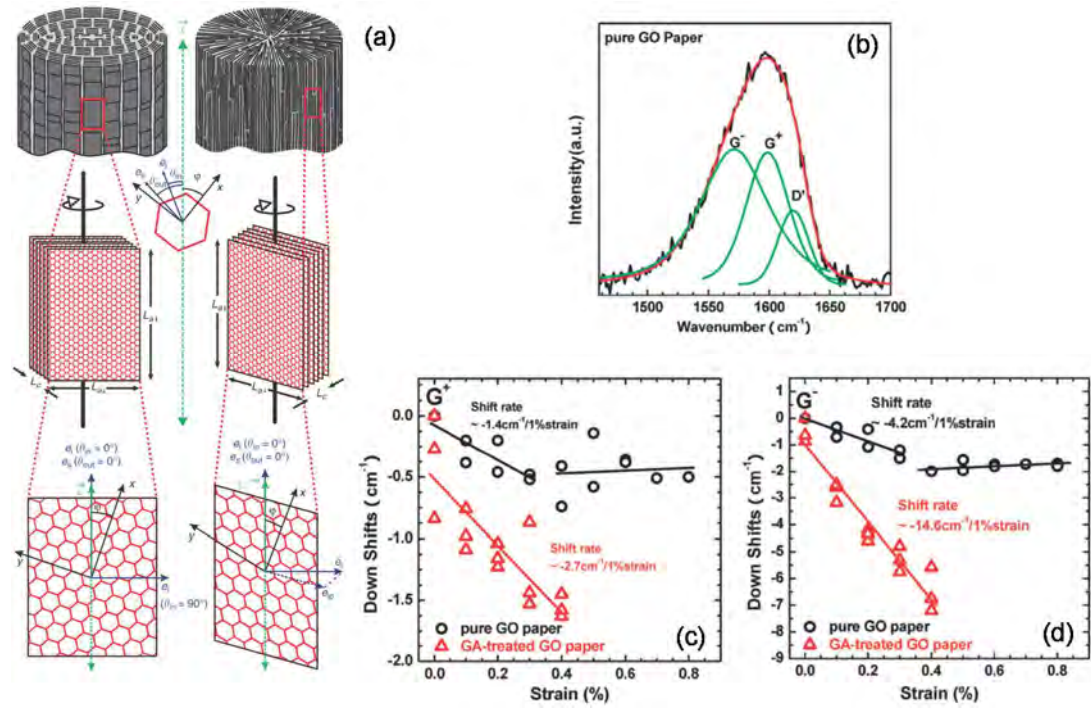


Figure 2.13 (a) Schematic diagram of the experimental geometries for onion skin and radial carbon fibre [85]. (b) The Raman G band for GO, fitted with G+, G- and D' band. (b) G+ and (c) G- band position as function of strain for as-received and glutaraldehyde-treated GO papers [86].

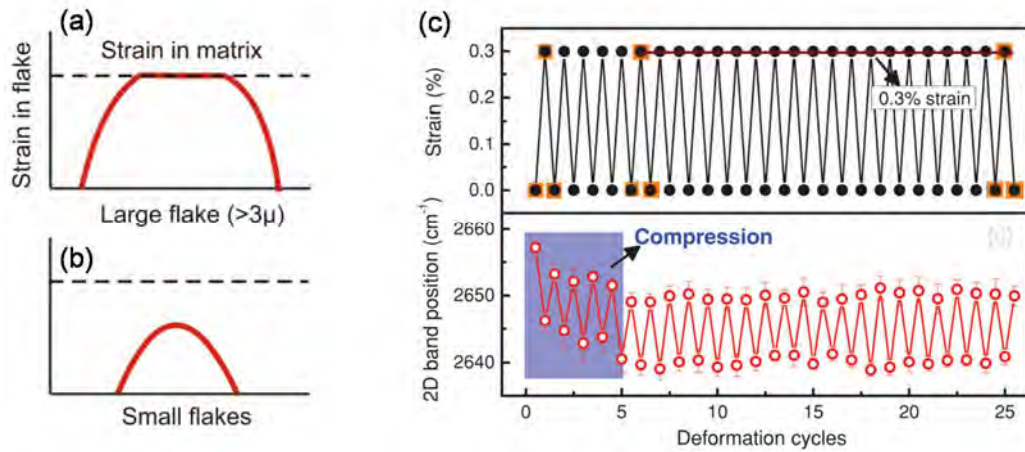


Figure 2.14 Strain distribution of graphene under (a) perfect and (b) imperfect stress transfer. (c) The strain applied to the CVD graphene at the deformation cycles and the corresponding Raman 2D band position obtained [87].

Many of the theoretical and experimental Raman deformation studies were undertaken upon single crystal graphene [20, 21, 55, 73]. However for the graphene grown *via* the CVD routine, the finite grain or flake size can decrease the stress

transfer from the matrix to graphene hence lower the band shift rate (Figs. 2.14(a) and (b)) [87]. Despite of this, the reversible Raman band shifts of CVD graphene still shows its potential to be used as a strain sensor (Fig. 2.14(c)) [87].

2.4.4 Orientation of Graphene

Apart from the Raman band position of graphene, its intensity also contains considerable information. According to group theory, the Raman scattering intensity is given by [88, 89]:

$$I \propto \sum_i |\vec{e}_s \cdot \alpha_i \cdot \vec{e}_i|^2 \quad (2.12)$$

where \vec{e}_i and \vec{e}_s are the unit vectors of incident and scattered radiations, respectively. α_i is the polarizability tensor, and is given for the A_{1g} symmetry D band and 2D band and the E_{2g} symmetry G band as [90]:

$$\alpha_{A_{1g}} = \begin{pmatrix} 1 & 0 & 0 \\ 0 & 1 & 0 \\ 0 & 0 & 0 \end{pmatrix} \quad (2.13)$$

$$\alpha_{E_{2g}(1)} = \begin{pmatrix} 1 & 0 & 0 \\ 0 & -1 & 0 \\ 0 & 0 & 0 \end{pmatrix} \quad \text{and} \quad \alpha_{E_{2g}(2)} = \begin{pmatrix} 0 & 1 & 0 \\ 1 & 0 & 0 \\ 0 & 0 & 0 \end{pmatrix} \quad (2.14)$$

Accordingly the Raman band intensity is highly dependent on the laser polarization and graphene crystal orientation, which has been observed for many years on graphite [7, 91] and carbon nanotubes [92-95]. Models were developed to describe the orientation of carbon nanotubes [96] and were further adapted [97] to study how the orientation of carbon nanotubes in composite fibres or films, can be correlated to their effective Young's modulus using the Raman spectroscopy [12, 98, 99].

So far the polarization studies on graphite and graphene can be primarily divided into two groups (Fig. 2.15):

1. Graphene planes were rotated along the Z axis (surface normal) perpendicular to its plane. The Raman laser was also propagated along the Z axis (Fig. 2.15(a)).
2. Graphene planes were rotated along the X axis that is perpendicular to its transverse section. The Raman laser was also propagated along the X axis (Fig. 2.15(b)).

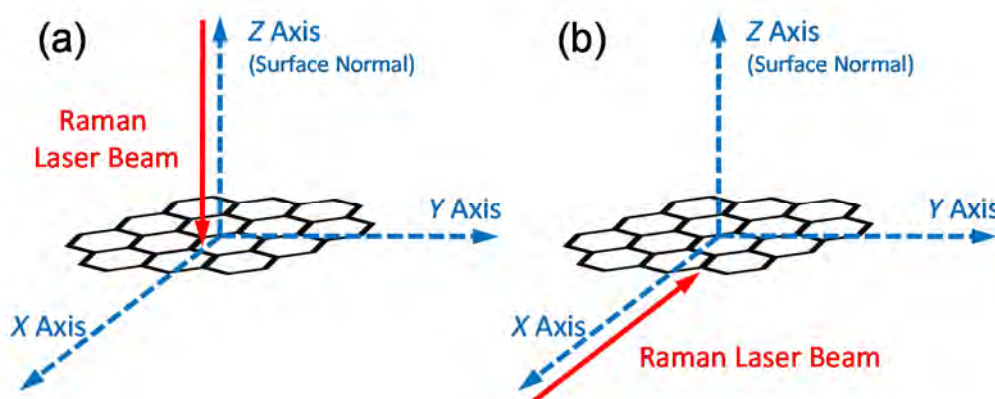


Figure 2.15 Schematic diagram of the polarization studies on graphene. Graphene is rotating along (a) the Z axis and (b) the X axis.

2.4.4.1 Graphene In-Plane Rotation

Many of the studies have been undertaken in this way with the Raman laser beam perpendicular to the graphene planes (Fig. 2.15(a)). Tuinstra et al. [7] firstly reported on single crystal graphite that the G band intensity (I_G) is not affected by either the direction or the polarization of the laser beam. The behaviour has been verified on monolayer [88, 100] and bilayer [100, 101] strain-free graphene that in the basal plane, a constant G band intensity is present (Fig. 2.16(a)) [45, 46, 102]. This constant intensity can be easily understood using the definition of Raman band intensity [88]. However the lattice symmetry breaks down at the graphene edge, so an angular dependence of I_G (Figs. 2.16(c) and (d)) was observed to be dependent upon both edge direction [103] and edge geometries [102]. I_G is maximum when the laser polarization is parallel (perpendicular) to armchair (zigzag) edges, as a result of the unequal contribution of the LO and iTO phonons at different graphene edges [104].

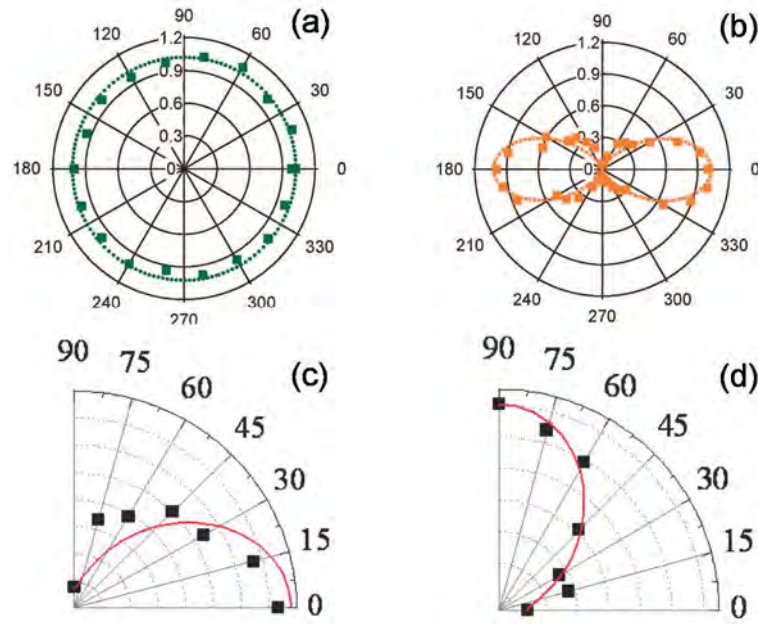


Figure 2.16 Polar plot of (a) I_G measured at the basal plane and (b) I_D measured at the edge of graphene as the function of the polarization angle [45]. Polar plot of I_G at the graphene (c) armchair and (d) zigzag edge [102].

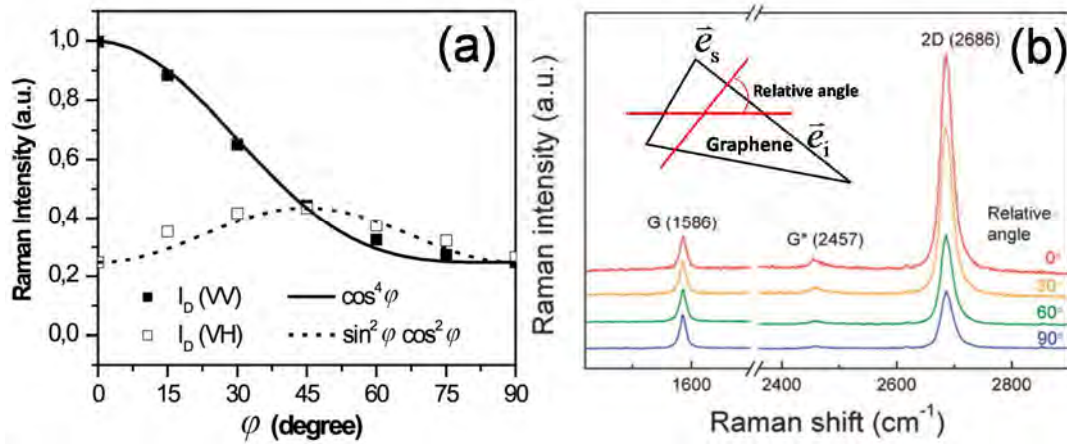


Figure 2.17 (a) Dependence of I_D as the function of polarization angle under the ‘VV’ and ‘VH’ configurations measured at an armchair edge [43]. (b) Polarized Raman spectra obtained when the relative angle between incident and scattered radiation changes [88].

Unlike the G band, the D band is ideally absent at the zig-zag edge but present at an armchair edge [43]. The D band selection rule fails with a rough edge [46] but becomes clearer as edges smoothen [45]. Generally the angular dependence of I_D at graphene edge follows a form of $I_D = \cos^4 \phi$ under ‘VV’ polarization (Figs. 2.16(b)),

and $I_D = \cos^2 \varphi \sin^2 \varphi$ using ‘VH’ polarization, where φ is the angle between the graphene edge and the incident polarization (Fig. 2.17(a)) [45]. The correlation in ‘VV’ polarization was further modified to $I_D = C_2 + C_1 \cos^4 \varphi$ and the value of C_2/C_1 is suggested to be an indication of the non-uniformity of the edge. This method was developed to identify the edge purity of the graphene [44, 105] as well as to follow the dynamic rearrangement of the graphene edges at high temperature [106].

The Raman 2D band intensity is independent of sample orientation when the incident and scattered radiation parallel to each other [107], but changes with the angle between the incident and scattered radiation direction (Fig. 2.17(b)) [88, 100, 101].

2.4.4.2 Graphene Out-of-Plane Rotation

In this circumstance, the Raman laser beam is propagated parallel to the graphene plane. The first Raman measurements in this case were undertaken by Tuinstra et al. [7] and Vidano et al. [91] on different kinds of pyrolytic graphite. They found both I_D and I_G were strongest when the incident laser polarization was parallel to the graphite plane, consistent with their corresponding in-plane A_{1g} and E_{2g} modes. Similar behaviour of the Raman D’ and 2D band implied all of the four bands originate from the in-plane vibration modes [91].

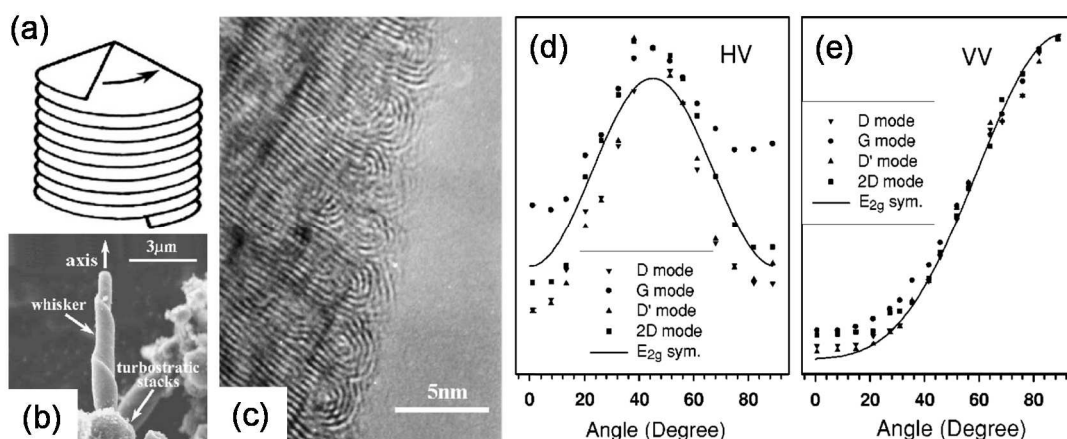


Figure 2.18 (a) Schematic diagram, (b) SEM image and (c) TEM image of the structure of a graphite whisker. Dependence of the Raman D band, G band, D’ band and 2D band intensity as the function of polarization angle under (d) the ‘HV’ and (e) the ‘VV’ polarization configurations [89].

More fundamentally, Tan et al. [89] used the Raman polarizability tensors to calculate the intensity of E_{2g} symmetry mode of the synthesized graphite whisker (Fig. 2.18) for the ‘VV’ and ‘HV’ polarization configurations, respectively:

$$I_{VV} = I_o \cdot [\cos^2 \varphi_w \cos^2 \varphi + \sin^2 \varphi]^2 \quad (2.15)$$

$$I_{HV} = I_o \cdot [\cos^4 \varphi_w \cos^2 \varphi \sin^2 \varphi + \cos^2 \varphi_w (\cos^4 \varphi + \sin^4 \varphi) + \cos^2 \varphi \sin^2 \varphi] \quad (2.16)$$

where φ is the angle between the ‘V’ polarization direction and whisker axis, and φ_w is the angle between graphite layers and the whisker axis (Fig. 2.18), I_o is the amplitude. As the laser polarization varied with respect to the graphite whisker axis, the Raman D band, G band and 2D band intensity changed (Figs. 2.18(d) and (e)) as predicted (Eqs. 2.15 and 2.16) [7, 89].

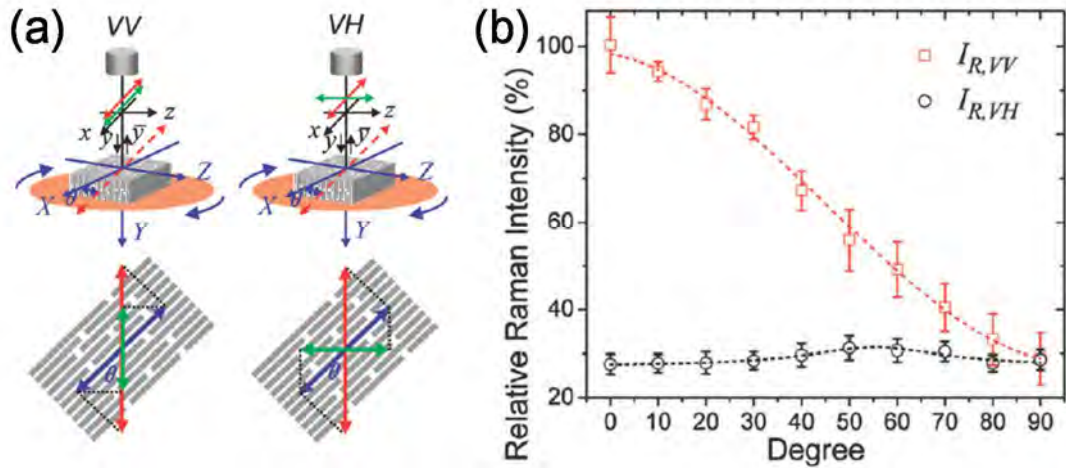


Figure 2.19 (a) Schematic diagram of polarized Raman spectroscopy for ‘VV’ and ‘VH’ configurations. (b) Dependence of I_G on the polarization angle φ in the ‘VV’ and ‘VH’ configurations [108].

Similar methods were employed on different types of graphitic materials. López-Honorato et al. [109] verified this technology by showing a good consistency between the result of polarized Raman spectroscopy and TEM. Barros et al. [110] resolved the stacked and turbostratic graphite structure in the wall of graphite foam based on the different origins of the two sub-bands in the Raman 2D band [111]. Recently the alignment of graphene in graphene paper has been determined (Fig.

2.19) [108, 112] as indicated by the low depolarization ratio deduced from carbon nanotubes [96].

2.5 Conclusions

Raman spectroscopy has been demonstrated to be a powerful technique to characterize graphene. It can be used to study the number of layers and disorder of graphene. Particularly, the Raman bands positions shift when the graphene is strained, and this phenomenon has been used to monitor the deformation of both suspended and embedded graphene. Furthermore, the Raman bands intensities show strong polarization dependence, which has been employed to reveal the crystallographic orientation and spatial orientation of graphene flakes.

References

1. Smith, E.; Dent, G., Front Matter. In *Modern Raman Spectroscopy – a Practical Approach*, John Wiley & Sons, Ltd: 2005; pp i-xi.
2. Grasselli, J. G.; Bulkin, B. J., *Analytical Raman Spectroscopy*. New York ; Chichester : Wiley 1991.
3. Smekal, A., Zur Quantentheorie Der Dispersion. *Naturwissenschaften* **1923**, 11, 873-875.
4. Raman, C. V., A Change of Wave-Length in Light Scattering. *Nature* **1923**, 121, 619-619.
5. Ferraro, J. R.; Nakamoto, K., *Introductory Raman Spectroscopy*. Academic Press, Inc.: San Diego, 1994.
6. Malard, L. M.; Pimenta, M. A.; Dresselhaus, G.; Dresselhaus, M. S., Raman Spectroscopy in Graphene. *Physics Reports* **2009**, 473, 51-87.
7. Tuinstra, F.; Koenig, J. L., Raman Spectrum of Graphite. *The Journal of Chemical Physics* **1970**, 53, 1126-1130.
8. Dresselhaus, M. S.; Dresselhaus, G.; Saito, R.; Jorio, A., Raman Spectroscopy of Carbon Nanotubes. *Physics Reports* **2005**, 409, 47-99.
9. Tobin, M. C., *Laser Raman Spectroscopy*. New York ; Chichester : Wiley-Interscience 1971.
10. Gong, L., *Deformation Micromechanics of Graphene Nanocomposites*, PhD Thesis, The University of Manchester, 2013.
11. Cooper, C. A., *Structure/Property Relationships in Particulate Composites*, PhD, The University of Manchester, 2000.
12. Deng, L., *Raman Spectroscopic Studies of Carbon Nanotube Composite Fibres*, PhD Thesis, The University of Manchester, 2010.
13. Deng, L.; Eichhorn, S. J.; Kao, C.-C.; Young, R. J., The Effective Young's Modulus of Carbon Nanotubes in Composites. *ACS Applied Materials & Interfaces* **2011**, 3, 433-440.

14. Ferrari, A. C.; Meyer, J. C.; Scardaci, V.; Casiraghi, C.; Lazzeri, M.; Mauri, F.; Piscanec, S.; Jiang, D.; Novoselov, K. S.; Roth, S.; Geim, A. K., Raman Spectrum of Graphene and Graphene Layers. *Physical Review Letters* **2006**, 97, 187401.
15. Ferrari, A. C.; Basko, D. M., Raman Spectroscopy as a Versatile Tool for Studying the Properties of Graphene. *Nature Nanotechnology* **2013**, 8, 235-246.
16. Novoselov, K. S.; Geim, A. K.; Morozov, S. V.; Jiang, D.; Zhang, Y.; Dubonos, S. V.; Grigorieva, I. V.; Firsov, A. A., Electric Field Effect in Atomically Thin Carbon Films. *Science* **2004**, 306, 666-669.
17. Ni, Z. H.; Yu, T.; Lu, Y. H.; Wang, Y. Y.; Feng, Y. P.; Shen, Z. X., Uniaxial Strain on Graphene: Raman Spectroscopy Study and Band-Gap Opening. *ACS Nano* **2008**, 2, 2301-2305.
18. Huang, M.; Yan, H.; Chen, C.; Song, D.; Heinz, T. F.; Hone, J., Phonon Softening and Crystallographic Orientation of Strained Graphene Studied by Raman Spectroscopy. *Proceedings of the National Academy of Sciences* **2009**, 106, 7304-7308.
19. Tsoukleri, G.; Parthenios, J.; Papagelis, K.; Jalil, R.; Ferrari, A. C.; Geim, A. K.; Novoselov, K. S.; Galiotis, C., Subjecting a Graphene Monolayer to Tension and Compression. *Small* **2009**, 5, 2397-2402.
20. Gong, L.; Kinloch, I. A.; Young, R. J.; Riaz, I.; Jalil, R.; Novoselov, K. S., Interfacial Stress Transfer in a Graphene Monolayer Nanocomposite. *Advanced Materials* **2010**, 22, 2694-2697.
21. Mohiuddin, T. M. G.; Lombardo, A.; Nair, R. R.; Bonetti, A.; Savini, G.; Jalil, R.; Bonini, N.; Basko, D. M.; Galiotis, C.; Marzari, N.; Novoselov, K. S.; Geim, A. K.; Ferrari, A. C., Uniaxial Strain in Graphene by Raman Spectroscopy: G Peak Splitting, Grüneisen Parameters, and Sample Orientation. *Physical Review B* **2009**, 79, 205433.
22. Cançado, L. G.; Takai, K.; Enoki, T.; Endo, M.; Kim, Y. A.; Mizusaki, H.; Speziali, N. L.; Jorio, A.; Pimenta, M. A., Measuring the Degree of Stacking Order in Graphite by Raman Spectroscopy. *Carbon* **2008**, 46, 272-275.
23. Hao, Y.; Wang, Y.; Wang, L.; Ni, Z.; Wang, Z.; Wang, R.; Koo, C. K.; Shen, Z.; Thong, J. T. L., Probing Layer Number and Stacking Order of Few-Layer Graphene by Raman Spectroscopy. *Small* **2010**, 6, 195-200.
24. Poncharal, P.; Ayari, A.; Michel, T.; Sauvajol, J. L., Raman Spectra of Misoriented Bilayer Graphene. *Physical Review B* **2008**, 78, 113407.
25. Rao, R.; Podila, R.; Tsuchikawa, R.; Katoch, J.; Tishler, D.; Rao, A. M.; Ishigami, M., Effects of Layer Stacking on the Combination Raman Modes in Graphene. *ACS Nano* **2011**, 5, 1594-1599.
26. Kudin, K. N.; Ozbas, B.; Schniepp, H. C.; Prud'homme, R. K.; Aksay, I. A.; Car, R., Raman Spectra of Graphite Oxide and Functionalized Graphene Sheets. *Nano Letters* **2007**, 8, 36-41.
27. Yang, D.; Velamakanni, A.; Bozoklu, G.; Park, S.; Stoller, M.; Piner, R. D.; Stankovich, S.; Jung, I.; Field, D. A.; Ventrice Jr, C. A.; Ruoff, R. S., Chemical Analysis of Graphene Oxide Films after Heat and Chemical Treatments by X-Ray Photoelectron and Micro-Raman Spectroscopy. *Carbon* **2009**, 47, 145-152.
28. Ferrari, A. C., Raman Spectroscopy of Graphene and Graphite: Disorder, Electron-Phonon Coupling, Doping and Nonadiabatic Effects. *Solid State Communications* **2007**, 143, 47-57.

29. Bruna, M.; Ott, A. K.; Ijäs, M.; Yoon, D.; Sassi, U.; Ferrari, A. C., Doping Dependence of the Raman Spectrum of Defected Graphene. *ACS Nano* **2014**, 8, 7432-7441.
30. Kalbac, M.; Reina-Cecco, A.; Farhat, H.; Kong, J.; Kavan, L.; Dresselhaus, M. S., The Influence of Strong Electron and Hole Doping on the Raman Intensity of Chemical Vapor-Deposition Graphene. *ACS Nano* **2010**, 4, 6055-6063.
31. Ferrari, A. C.; Robertson, J., Interpretation of Raman Spectra of Disordered and Amorphous Carbon. *Physical Review B* **2000**, 61, 14095-14107.
32. Moon, I. K.; Lee, J.; Ruoff, R. S.; Lee, H., Reduced Graphene Oxide by Chemical Graphitization. *Nature Communications* **2010**, 1, 73.
33. Chieu, T. C.; Dresselhaus, M. S.; Endo, M., Raman Studies of Benzene-Derived Graphite Fibers. *Physical Review B* **1982**, 26, 5867-5877.
34. Martins Ferreira, E. H.; Moutinho, M. V. O.; Stavale, F.; Lucchese, M. M.; Capaz, R. B.; Achete, C. A.; Jorio, A., Evolution of the Raman Spectra from Single-, Few-, and Many-Layer Graphene with Increasing Disorder. *Physical Review B* **2010**, 82, 125429.
35. Stankovich, S.; Dikin, D. A.; Piner, R. D.; Kohlhaas, K. A.; Kleinhammes, A.; Jia, Y.; Wu, Y.; Nguyen, S. T.; Ruoff, R. S., Synthesis of Graphene-Based Nanosheets via Chemical Reduction of Exfoliated Graphite Oxide. *Carbon* **2007**, 45, 1558-1565.
36. Wang, H.; Robinson, J. T.; Li, X.; Dai, H., Solvothermal Reduction of Chemically Exfoliated Graphene Sheets. *Journal of the American Chemical Society* **2009**, 131, 9910-9911.
37. Robertson, J., Amorphous Carbon. *Advances in Physics* **1986**, 35, 317-374.
38. Lim, J.; Choi, K.; Rani, J. R.; Kim, J.-S.; Lee, C.; Hoon Kim, J.; Chan Jun, S., Terahertz, Optical, and Raman Signatures of Monolayer Graphene Behavior in Thermally Reduced Graphene Oxide Films. *Journal of Applied Physics* **2013**, 113, 183502-5.
39. Saito, R.; Jorio, A.; Souza Filho, A. G.; Dresselhaus, G.; Dresselhaus, M. S.; Pimenta, M. A., Probing Phonon Dispersion Relations of Graphite by Double Resonance Raman Scattering. *Physical Review Letters* **2001**, 88, 027401.
40. Thomsen, C.; Reich, S., Double Resonant Raman Scattering in Graphite. *Physical Review Letters* **2000**, 85, 5214-5217.
41. Cançado, L. G.; Pimenta, M. A.; Saito, R.; Jorio, A.; Ladeira, L. O.; Grueneis, A.; Souza-Filho, A. G.; Dresselhaus, G.; Dresselhaus, M. S., Stokes and Anti-Stokes Double Resonance Raman Scattering in Two-Dimensional Graphite. *Physical Review B* **2002**, 66, 035415.
42. Luo, Z.; Cong, C.; Zhang, J.; Xiong, Q.; Yu, T., The Origin of Sub-Bands in the Raman D-Band of Graphene. *Carbon* **2012**, 50, 4252-4258.
43. Cançado, L. G.; Pimenta, M. A.; Neves, B. R. A.; Dantas, M. S. S.; Jorio, A., Influence of the Atomic Structure on the Raman Spectra of Graphite Edges. *Physical Review Letters* **2004**, 93, 247401.
44. You, Y.; Ni, Z.; Yu, T.; Shen, Z., Edge Chirality Determination of Graphene by Raman Spectroscopy. *Applied Physics Letters* **2008**, 93, 163112-3.
45. Gupta, A. K.; Russin, T. J.; Gutiérrez, H. R.; Eklund, P. C., Probing Graphene Edges via Raman Scattering. *ACS Nano* **2008**, 3, 45-52.
46. Casiraghi, C.; Hartschuh, A.; Qian, H.; Piscanec, S.; Georgi, C.; Fasoli, A.; Novoselov, K. S.; Basko, D. M.; Ferrari, A. C., Raman Spectroscopy of Graphene Edges. *Nano Letters* **2009**, 9, 1433-1441.

47. Chen, S.; Cai, W.; Piner, R. D.; Suk, J. W.; Wu, Y.; Ren, Y.; Kang, J.; Ruoff, R. S., Synthesis and Characterization of Large-Area Graphene and Graphite Films on Commercial Cu–Ni Alloy Foils. *Nano Letters* **2011**, 11, 3519-3525.
48. Ismach, A.; Druzgalski, C.; Penwell, S.; Schwartzberg, A.; Zheng, M.; Javey, A.; Bokor, J.; Zhang, Y., Direct Chemical Vapor Deposition of Graphene on Dielectric Surfaces. *Nano Letters* **2010**, 10, 1542-1548.
49. Gong, L.; Young, R. J.; Kinloch, I. A.; Haigh, S. J.; Warner, J. H.; Hinks, J. A.; Xu, Z.; Li, L.; Ding, F.; Riaz, I.; Jalil, R.; Novoselov, K. S., Reversible Loss of Bernal Stacking During the Deformation of Few-Layer Graphene in Nanocomposites. *ACS Nano* **2013**, 7, 7287-7294.
50. Mafra, D. L.; Samsonidze, G.; Malard, L. M.; Elias, D. C.; Brant, J. C.; Plentz, F.; Alves, E. S.; Pimenta, M. A., Determination of LA and TO Phonon Dispersion Relations of Graphene near the Dirac Point by Double Resonance Raman Scattering. *Physical Review B* **2007**, 76, 233407.
51. Matthews, M. J.; Pimenta, M. A.; Dresselhaus, G.; Dresselhaus, M. S.; Endo, M., Origin of Dispersive Effects of the Raman D Band in Carbon Materials. *Physical Review B* **1999**, 59, R6585-R6588.
52. Cançado, L. G.; Jorio, A.; Ferreira, E. H. M.; Stavale, F.; Achete, C. A.; Capaz, R. B.; Moutinho, M. V. O.; Lombardo, A.; Kulmala, T. S.; Ferrari, A. C., Quantifying Defects in Graphene via Raman Spectroscopy at Different Excitation Energies. *Nano Letters* **2011**, 11, 3190-3196.
53. Khan, U.; O'Neill, A.; Lotya, M.; De, S.; Coleman, J. N., High-Concentration Solvent Exfoliation of Graphene. *Small* **2010**, 6, 864-871.
54. Lucchese, M. M.; Stavale, F.; Ferreira, E. H. M.; Vilani, C.; Moutinho, M. V. O.; Capaz, R. B.; Achete, C. A.; Jorio, A., Quantifying Ion-Induced Defects and Raman Relaxation Length in Graphene. *Carbon* **2010**, 48, 1592-1597.
55. Ferralis, N., Probing Mechanical Properties of Graphene with Raman Spectroscopy. *Journal of Materials Science* **2010**, 45, 5135-5149.
56. Robinson, I. M.; Zakikhani, M.; Day, R. J.; Young, R. J.; Galiotis, C., Strain Dependence of the Raman Frequencies for Different Types of Carbon Fibres. *Journal of Materials Science Letters* **1987**, 6, 1212-1214.
57. Cooper, C. A.; Young, R. J.; Halsall, M., Investigation into the Deformation of Carbon Nanotubes and Their Composites through the Use of Raman Spectroscopy. *Composites Part A: Applied Science and Manufacturing* **2001**, 32, 401-411.
58. Yu, T.; Ni, Z.; Du, C.; You, Y.; Wang, Y.; Shen, Z., Raman Mapping Investigation of Graphene on Transparent Flexible Substrate: The Strain Effect. *The Journal of Physical Chemistry C* **2008**, 112, 12602-12605.
59. Frank, O.; Tsoukleri, G.; Parthenios, J.; Papagelis, K.; Riaz, I.; Jalil, R.; Novoselov, K. S.; Galiotis, C., Compression Behavior of Single-Layer Graphenes. *ACS Nano* **2010**, 4, 3131-3138.
60. Frank, O.; Mohr, M.; Maultzsch, J.; Thomsen, C.; Riaz, I.; Jalil, R.; Novoselov, K. S.; Tsoukleri, G.; Parthenios, J.; Papagelis, K.; Kavan, L.; Galiotis, C., Raman 2d-Band Splitting in Graphene: Theory and Experiment. *ACS Nano* **2011**, 5, 2231-2239.
61. Frank, O.; Bouša, M.; Riaz, I.; Jalil, R.; Novoselov, K. S.; Tsoukleri, G.; Parthenios, J.; Kavan, L.; Papagelis, K.; Galiotis, C., Phonon and Structural Changes in Deformed Bernal Stacked Bilayer Graphene. *Nano Letters* **2011**, 12, 687-693.

62. Huang, M.; Yan, H.; Heinz, T. F.; Hone, J., Probing Strain-Induced Electronic Structure Change in Graphene by Raman Spectroscopy. *Nano Letters* **2010**, 10, 4074-4079.
63. Yoon, D.; Son, Y.-W.; Cheong, H., Strain-Dependent Splitting of the Double-Resonance Raman Scattering Band in Graphene. *Physical Review Letters* **2011**, 106, 155502.
64. Gong, L.; Young, R. J.; Kinloch, I. A.; Riaz, I.; Jalil, R.; Novoselov, K. S., Optimizing the Reinforcement of Polymer-Based Nanocomposites by Graphene. *ACS Nano* **2012**, 6, 2086-2095.
65. Young, R. J.; Gong, L.; Kinloch, I. A.; Riaz, I.; Jalil, R.; Novoselov, K. S., Strain Mapping in a Graphene Monolayer Nanocomposite. *ACS Nano* **2011**, 5, 3079-3084.
66. Jiang, T.; Huang, R.; Zhu, Y., Interfacial Sliding and Buckling of Monolayer Graphene on a Stretchable Substrate. *Advanced Functional Materials* **2014**, 24, 396-402.
67. Metzger, C.; Rémi, S.; Liu, M.; Kusminskiy, S. V.; Castro Neto, A. H.; Swan, A. K.; Goldberg, B. B., Biaxial Strain in Graphene Adhered to Shallow Depressions. *Nano Letters* **2009**, 10, 6-10.
68. Zabel, J.; Nair, R. R.; Ott, A.; Georgiou, T.; Geim, A. K.; Novoselov, K. S.; Casiraghi, C., Raman Spectroscopy of Graphene and Bilayer under Biaxial Strain: Bubbles and Balloons. *Nano Letters* **2011**, 12, 617-621.
69. Lee, J.-U.; Yoon, D.; Cheong, H., Estimation of Young's Modulus of Graphene by Raman Spectroscopy. *Nano Letters* **2012**, 12, 4444-4448.
70. Kitt, A. L.; Qi, Z.; Rémi, S.; Park, H. S.; Swan, A. K.; Goldberg, B. B., How Graphene Slides: Measurement and Theory of Strain-Dependent Frictional Forces between Graphene and SiO₂. *Nano Letters* **2013**, 13, 2605-2610.
71. del Corro, E.; Taravillo, M.; Baonza, V. G., Nonlinear Strain Effects in Double-Resonance Raman Bands of Graphite, Graphene, and Related Materials. *Physical Review B* **2012**, 85, 033407.
72. Proctor, J. E.; Gregoryanz, E.; Novoselov, K. S.; Lotya, M.; Coleman, J. N.; Halsall, M. P., High-Pressure Raman Spectroscopy of Graphene. *Physical Review B* **2009**, 80, 073408.
73. Ding, F.; Ji, H.; Chen, Y.; Herklotz, A.; Dörr, K.; Mei, Y.; Rastelli, A.; Schmidt, O. G., Stretchable Graphene: A Close Look at Fundamental Parameters through Biaxial Straining. *Nano Letters* **2010**, 10, 3453-3458.
74. Grimvall, G., Phonons in Real Crystals: Anharmonic Effects. In *Thermophysical Properties of Materials*, Elsevier Science B.V.: Amsterdam, 1999; pp 136-152.
75. Mohr, M.; Maultzsch, J.; Thomsen, C., Splitting of the Raman 2D Band of Graphene Subjected to Strain. *Physical Review B* **2010**, 82, 201409.
76. Cheng, Y. C.; Zhu, Z. Y.; Huang, G. S.; Schwingenschlögl, U., Grüneisen Parameter of the G Mode of Strained Monolayer Graphene. *Physical Review B* **2011**, 83, 115449.
77. Huang, C.-W.; Shiue, R.-J.; Chui, H.-C.; Wang, W.-H.; Wang, J.-K.; Tzeng, Y.; Liu, C.-Y., Revealing Anisotropic Strain in Exfoliated Graphene by Polarized Raman Spectroscopy. *Nanoscale* **2013**, 5, 9626-9632.
78. Young, R. J.; Kinloch, I. A.; Gong, L.; Novoselov, K. S., The Mechanics of Graphene Nanocomposites: A Review. *Composites Science and Technology* **2012**, 72, 1459-1476.

79. Cox, H. L., The Elasticity and Strength of Paper and Other Fibrous Materials. *British Journal of Applied Physics* **1952**, 3, 72.
80. Kelly, A.; Macmillan, N. H., *Strong Solids*. 3rd ed.; Clarendon Press: Oxford, 1986.
81. Tan, P. H.; Han, W. P.; Zhao, W. J.; Wu, Z. H.; Chang, K.; Wang, H.; Wang, Y. F.; Bonini, N.; Marzari, N.; Pugno, N.; Savini, G.; Lombardo, A.; Ferrari, A. C., The Shear Mode of Multilayer Graphene. *Nature Materials* **2012**, 11, 294-300.
82. Liu, Z.; Wang, L.; Zhao, Y.; Cui, Q.; Zou, G., High-Pressure Raman Studies of Graphite and Ferric Chloride-Graphite. *Journal of Physics: Condensed Matter* **1990**, 2, 8083.
83. del Corro, E.; de la Roza, A. O.; Taravillo, M.; Baonza, V. G., Raman Modes and Grüneisen Parameters of Graphite under Compressive Biaxial Stress. *Carbon* **2012**, 50, 4600-4606.
84. Hanfland, M.; Beister, H.; Syassen, K., Graphite under Pressure: Equation of State and First-Order Raman Modes. *Physical Review B* **1989**, 39, 12598-12603.
85. Frank, O.; Tsoukleri, G.; Riaz, I.; Papagelis, K.; Parthenios, J.; Ferrari, A. C.; Geim, A. K.; Novoselov, K. S.; Galiotis, C., Development of a Universal Stress Sensor for Graphene and Carbon Fibres. *Nature Communications* **2011**, 2, 255.
86. Gao, Y.; Liu, L.-Q.; Zu, S.-Z.; Peng, K.; Zhou, D.; Han, B.-H.; Zhang, Z., The Effect of Interlayer Adhesion on the Mechanical Behaviors of Macroscopic Graphene Oxide Papers. *ACS Nano* **2011**, 5, 2134-2141.
87. Raju, A. P. A.; Lewis, A.; Derby, B.; Young, R. J.; Kinloch, I. A.; Zan, R.; Novoselov, K. S., Wide-Area Strain Sensors Based Upon Graphene-Polymer Composite Coatings Probed by Raman Spectroscopy. *Advanced Functional Materials* **2014**, 24, 2865-2874.
88. Yoon, D.; Moon, H.; Son, Y.-W.; Samsonidze, G.; Park, B. H.; Kim, J. B.; Lee, Y.; Cheong, H., Strong Polarization Dependence of Double-Resonant Raman Intensities in Graphene. *Nano Letters* **2008**, 8, 4270-4274.
89. Tan, P.; Hu, C.; Dong, J.; Shen, W.; Zhang, B., Polarization Properties, High-Order Raman Spectra, and Frequency Asymmetry between Stokes and Anti-Stokes Scattering of Raman Modes in a Graphite Whisker. *Physical Review B* **2001**, 64, 214301.
90. Loudon, R., The Raman Effect in Crystals. *Advances in Physics* **1964**, 13, 423-482.
91. Vidano, R.; Fischbach, D. B., New Lines in the Raman Spectra of Carbons and Graphite. *Journal of the American Ceramic Society* **1978**, 61, 13-17.
92. Duesberg, G. S.; Loa, I.; Burghard, M.; Syassen, K.; Roth, S., Polarized Raman Spectroscopy on Isolated Single-Wall Carbon Nanotubes. *Physical Review Letters* **2000**, 85, 5436-5439.
93. Hwang, J.; Gommans, H. H.; Ugawa, A.; Tashiro, H.; Haggemueller, R.; Winey, K. I.; Fischer, J. E.; Tanner, D. B.; Rinzler, A. G., Polarized Spectroscopy of Aligned Single-Wall Carbon Nanotubes. *Physical Review B* **2000**, 62, R13310-R13313.
94. Saito, R.; Takeya, T.; Kimura, T.; Dresselhaus, G.; Dresselhaus, M. S., Raman Intensity of Single-Wall Carbon Nanotubes. *Physical Review B* **1998**, 57, 4145-4153.

95. Kannan, P.; Eichhorn, S. J.; Young, R. J., Deformation of Isolated Single-Wall Carbon Nanotubes in Electrospun Polymer Nanofibres. *Nanotechnology* **2007**, 18, 235707.
96. Gommans, H. H.; Alldredge, J. W.; Tashiro, H.; Park, J.; Magnuson, J.; Rinzler, A. G., Fibers of Aligned Single-Walled Carbon Nanotubes: Polarized Raman Spectroscopy. *Journal of Applied Physics* **2000**, 88, 2509-2514.
97. Liu, T.; Kumar, S., Quantitative Characterization of SWNT Orientation by Polarized Raman Spectroscopy. *Chemical Physics Letters* **2003**, 378, 257-262.
98. Young, K.; Blighe, F. M.; Vilatela, J. J.; Windle, A. H.; Kinloch, I. A.; Deng, L.; Young, R. J.; Coleman, J. N., Strong Dependence of Mechanical Properties on Fiber Diameter for Polymer–Nanotube Composite Fibers: Differentiating Defect from Orientation Effects. *ACS Nano* **2010**, 4, 6989-6997.
99. Blighe, F. M.; Young, K.; Vilatela, J. J.; Windle, A. H.; Kinloch, I. A.; Deng, L.; Young, R. J.; Coleman, J. N., The Effect of Nanotube Content and Orientation on the Mechanical Properties of Polymer–Nanotube Composite Fibers: Separating Intrinsic Reinforcement from Orientational Effects. *Advanced Functional Materials* **2011**, 21, 364-371.
100. Sahoo, S.; Palai, R.; Katiyar, R. S., Polarized Raman Scattering in Monolayer, Bilayer, and Suspended Bilayer Graphene. *Journal of Applied Physics* **2011**, 110, 044320-5.
101. Lee, J.-U.; Seck, N. M.; Yoon, D.; Choi, S.-M.; Son, Y.-W.; Cheong, H., Polarization Dependence of Double Resonant Raman Scattering Band in Bilayer Graphene. *Carbon* **2014**, 72, 257-263.
102. Cong, C.; Yu, T.; Wang, H., Raman Study on the G Mode of Graphene for Determination of Edge Orientation. *ACS Nano* **2010**, 4, 3175-3180.
103. Cançado, L. G.; Pimenta, M. A.; Neves, B. R. A.; Medeiros-Ribeiro, G.; Enoki, T.; Kobayashi, Y.; Takai, K.; Fukui, K.-i.; Dresselhaus, M. S.; Saito, R.; Jorio, A., Anisotropy of the Raman Spectra of Nanographite Ribbons. *Physical Review Letters* **2004**, 93, 047403.
104. Sasaki, K.-i.; Saito, R.; Wakabayashi, K.; Enoki, T., Identifying the Orientation of Edge of Graphene Using G Band Raman Spectra. *Journal of the Physical Society of Japan* **2010**, 79, 044603.
105. Begliarbekov, M.; Sul, O.; Kalliakos, S.; Yang, E.-H.; Strauf, S., Determination of Edge Purity in Bilayer Graphene Using μ -Raman Spectroscopy. *Applied Physics Letters* **2010**, 97, 031908-3.
106. Xu, Y. N.; Zhan, D.; Liu, L.; Suo, H.; Ni, Z. H.; Nguyen, T. T.; Zhao, C.; Shen, Z. X., Thermal Dynamics of Graphene Edges Investigated by Polarized Raman Spectroscopy. *ACS Nano* **2010**, 5, 147-152.
107. Livneh, T.; Haslett, T. L.; Moskovits, M., Distinguishing Disorder-Induced Bands from Allowed Raman Bands in Graphite. *Physical Review B* **2002**, 66, 195110.
108. Liang, Q.; Yao, X.; Wang, W.; Liu, Y.; Wong, C. P., A Three-Dimensional Vertically Aligned Functionalized Multilayer Graphene Architecture: An Approach for Graphene-Based Thermal Interfacial Materials. *ACS Nano* **2011**, 5, 2392-2401.

109. López-Honorato, E.; Meadows, P. J.; Shatwell, R. A.; Xiao, P., Characterization of the Anisotropy of Pyrolytic Carbon by Raman Spectroscopy. *Carbon* **2010**, 48, 881-890.
110. Barros, E. B.; Demir, N. S.; Souza Filho, A. G.; Mendes Filho, J.; Jorio, A.; Dresselhaus, G.; Dresselhaus, M. S., Raman Spectroscopy of Graphitic Foams. *Physical Review B* **2005**, 71, 165422.
111. Cançado, L. G.; Reina, A.; Kong, J.; Dresselhaus, M. S., Geometrical Approach for the Study of G' Band in the Raman Spectrum of Monolayer Graphene, Bilayer Graphene, and Bulk Graphite. *Physical Review B* **2008**, 77, 245408.
112. Yousefi, N.; Gudarzi, M. M.; Zheng, Q.; Aboutalebi, S. H.; Sharif, F.; Kim, J.-K., Self-Alignment and High Electrical Conductivity of Ultralarge Graphene Oxide-Polyurethane Nanocomposites. *Journal of Materials Chemistry* **2012**, 22, 12709-12717.

Chapter 3 The Deformation of Wrinkled Graphene*

3.1 Introduction

The chemical vapour deposition method (CVD) opens a route to grow large size, continuous and defect-free graphene at low cost [1]. However, the grain boundaries formed during its formation [2] and wrinkles induced during the transfer process [3, 4] are thought to alter the mechanical stretchability [5] of the CVD graphene. It is also thought that the presence of wrinkles can affect the deformation of graphene in shear [6] and the deformation of graphene oxide paper [7]. However, there has been no systematic experimental study of its effect upon the mechanical response of graphene.

In this chapter, Raman spectroscopy is employed to monitor the deformation mechanics of monolayer CVD graphene on a poly(ethylene terephthalate) substrate (CVD graphene/PET) where the PET film is flat but the microstructure of the CVD graphene consists of a hexagonal array of islands of flat monolayer graphene separated by wrinkled material. The observed unusual Raman band behaviours are attributed to the small size of the graphene caused by the wrinkles. Its deformation behaviour is modelled by considering the distribution of strain in the graphene islands and the laser intensity variation within the laser spot. It will demonstrate how the size of graphene flakes can affect their reinforcement of nanocomposites.

3.2 Experimental

3.2.1 Materials

The mechanically exfoliated graphene was kindly supplied by Prof. K.S. Novoselov, The University of Manchester. It was made by mechanical cleavage and then transferred to a PMMA substrate [8].

* This chapter is based on a paper, 'The Deformation of Wrinkled Graphene', *ACS Nano* (2015); DOI: 10.1021/nn507202c.

The graphene-PET specimen was kindly supplied by Bluestone Global Tech, USA. It was grown on copper using a conventional methane feedstock and was then transferred onto PET film.

3.2.2 Characterization

Scanning electron microscope (SEM) images were obtained using a Philips XL30 FEGSEM. The sample surface was coated with gold before analysis. Atomic force microscope (AFM) images were obtained from the surfaces of the CVD graphene using a Dimension 3100 AFM (Bruker) in the tapping mode in conjunction with the 'TESPA' probe (Bruker).

Raman spectra were obtained using Renishaw 1000 spectrometers equipped with an Argon laser ($\lambda = 514$ nm). For the bending test, the CVD graphene/PET film was attached to PMMA beam by PMMA solution adhesive. The sample on the PMMA was deformed in a four-point bending rig, with the strain monitored using a resistance strain gauge attached to the PMMA beam adjacent to the CVD graphene/PET. In all cases, the incident laser polarization was kept parallel to the strain. The simulation of Raman spectra was carried out using Wolfram Mathematica 9.

3.3 Results and Discussion

3.3.1 Size of Graphene Islands

The SEM images in Fig. 3.1(a) of the surface of the CVD graphene/PET show the network of CVD graphene islands separated by wrinkles with a height of around 20 nm, as revealed by AFM (Figs. 3.1(b) and (d)).

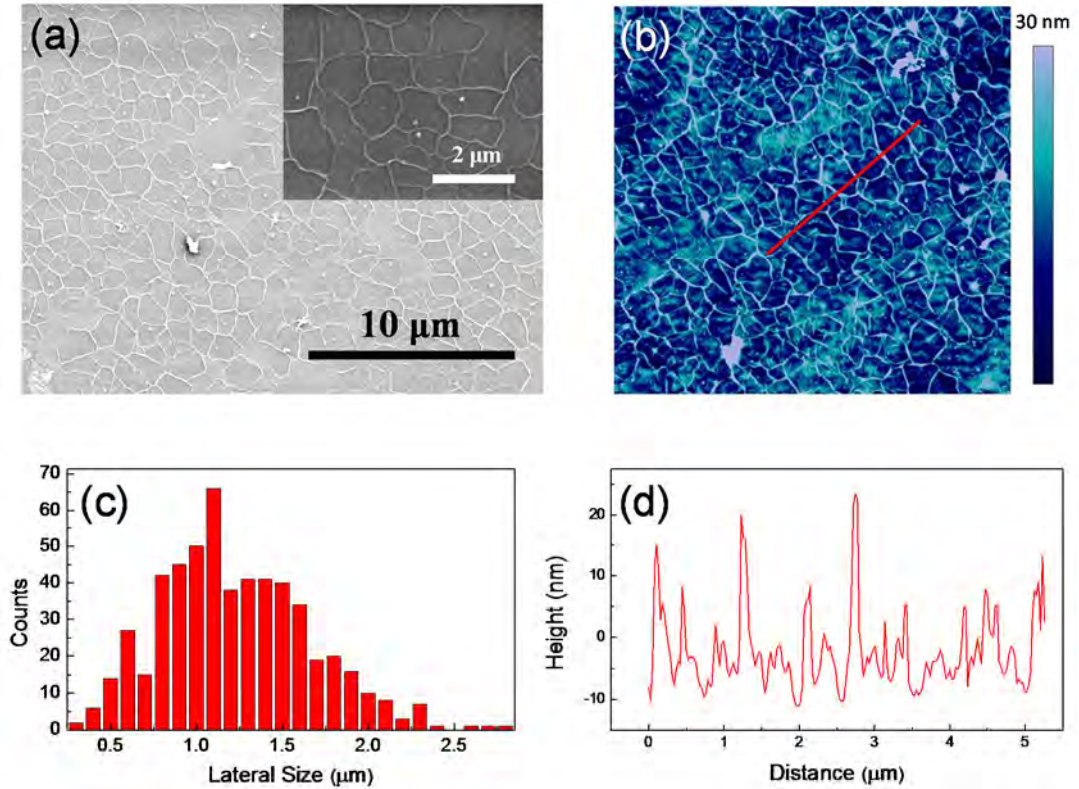


Figure 3.1 (a) SEM and (b) AFM images of the CVD graphene. (c) The distribution of the lateral dimensions of the graphene islands. (d) The AFM height profile of the inset red line in (b) showing the height of the wrinkles.

The wrinkled graphene microstructure resembles those found previously [9, 10], and is probably forming during the transfer process due to the difference in thermal coefficients between the graphene and PET substrate [11], which results in the development of a biaxial compressive field. It bears a strong similarity to the wrinkled microstructure found for thin films of copper on layered-crystal surfaces, formed through a mismatch in thermal expansion coefficients [12]. The wrinkles separate the graphene surface into small isolated islands with their size distribution, based upon more than 500 measurements, shown in Fig. 3.1(c). It can be seen that there is a broad distribution of the lateral dimensions of the islands, with a mean value around 1.2 μm , but also with some large islands of up to 3 μm in diameter.

3.3.2 Raman Spectroscopy

Raman spectroscopy has been employed to monitor interfacial stress transfer from the PET substrate to the CVD graphene and the whole CVD graphene/PET film has

been modelled as a nanocomposite structure [8, 13]. The Raman spectra of the PET substrate and the CVD graphene/PET are shown in Fig. 3.2. The 2D band at around 2700 cm^{-1} (also known as the G' band) results from two phonons with opposite momentum in the highest optical branch near the **K** point [14]. The graphene G band overlaps partially with the PET band (Fig. 3.2) and so only the 2D band has been used here for the analysis of stress transfer. The lack of a visible D band suggests the absence of defects (grain boundaries, etc) even at the wrinkles [2]. An estimate of the intensity ratio of the 2D band to the G band (after deconvolution from the strong adjacent PET band), along with a sharp 2D band with a full width at half maximum around 30 cm^{-1} , demonstrates that the CVD graphene is essentially a monolayer [14, 15].

The initial position of the 2D band of the CVD graphene on the PET film of $2696.0 \pm 2.2\text{ cm}^{-1}$ compared with the stress-free value of $\sim 2677\text{ cm}^{-1}$ from mechanically exfoliated monolayer graphene with 514 nm laser excitation [16] clearly indicates that graphene on the substrate is in compression. It appears that the graphene islands are able to support the compressive loads and it is only at the island boundaries that the compressive load is relieved by wrinkling.

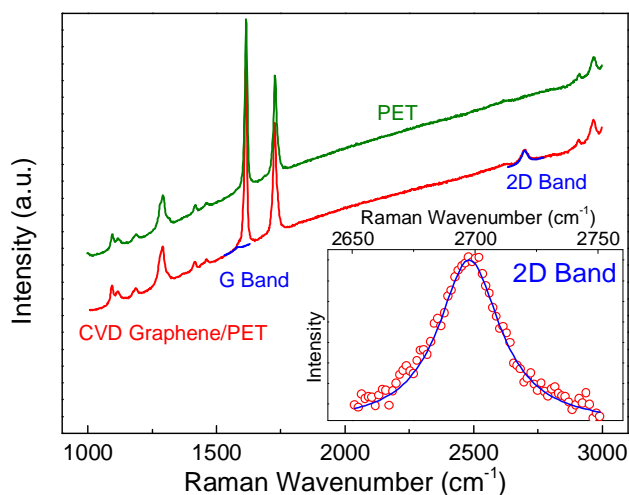


Figure 3.2 Raman spectra of the CVD graphene/PET and neat PET substrate. Inset shows the experimental data (red circles) and the Lorentzian fitting (blue line) for the 2D band.

The CVD graphene/PET was subjected to tensile deformation and the shift of the graphene Raman 2D band, fitted with a Lorentzian function, was monitored to

elucidate the deformation mechanics [17-19]. When the specimen was strained uniaxially in tension the 2D band position (ω_{2D}) downshifted with strain ε at a rate $d\omega_{2D}/d\varepsilon = -12.8 \text{ cm}^{-1}/\%$ (Fig. 3.3(a)). At the same time the 2D band broadened with strain and its full width at half maximum ($FWHM_{2D}$) increased approximately linearly with ε at a rate of $dFWHM_{2D}/d\varepsilon = 9.3 \text{ cm}^{-1}/\%$ (Fig. 3.3(b)). The absence of discontinuities in the data in Fig. 3.3 implies that the interface between the CVD graphene and the PET film remains intact up to a strain of at least 0.4% [20].

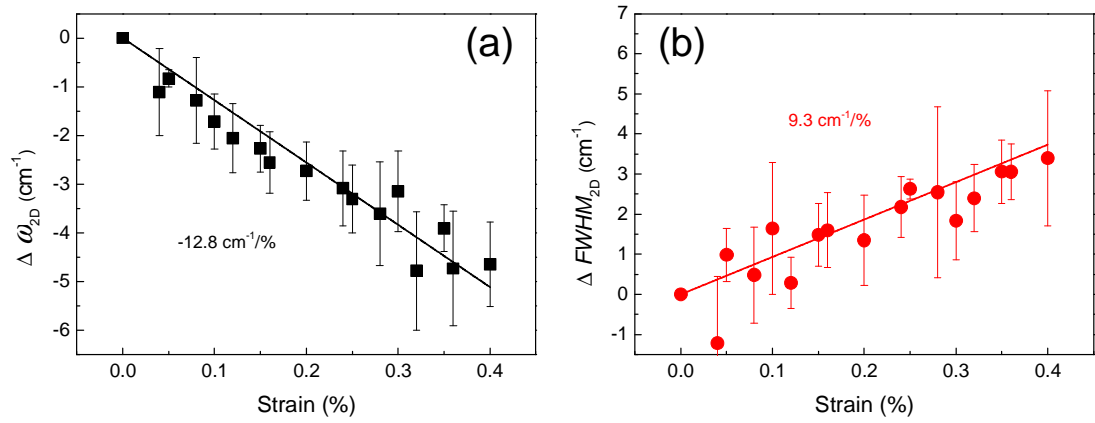


Figure 3.3 The variation of (a) ω_{2D} and (b) $FWHM_{2D}$ under uniaxial strain. The straight lines are linear fits for both sets of data (mean values of 8 sets of measurements).

Generally tensile strain induces phonon softening in graphene [18], which can be estimated using the knowledge of the Grüneisen parameter (Chapter 2) [21-23]. For an ideal flat monolayer of graphene under uniaxial strain [22], the reference 2D band shift rate $(d\omega_{2D}/d\varepsilon)_{\text{ref}}$ is given as:

$$\left(\frac{d\omega_{2D}}{d\varepsilon} \right)_{\text{ref}} = -\omega_{2D}^0 \gamma_{2D} (1 - \nu) \quad (3.1)$$

where ω_{2D}^0 is the ω_{2D} at zero strain, γ_{2D} is the Grüneisen parameter for 2D band, and ν is the Poisson's ratio of the substrate. As reported recently [24], the value of $(d\omega_{2D}/d\varepsilon)_{\text{ref}}$ is dependent on the Poisson's ratio of the matrix. In this study, if $\gamma_{2D} = 3.55$ and $\nu = 0.35$ is taken for PET [22], the value of $(d\omega_{2D}/d\varepsilon)_{\text{ref}}$ is estimated to be around $-60 \text{ cm}^{-1}/\%$ for flat monolayer on PET substrate, similar to the experimental value [22]. Additionally, the reference 2D band broadening rate with ε

$((dFWHM_{2D}/d\varepsilon)_{\text{ref}})$ is found experimentally to be $\sim 12 \text{ cm}^{-1}/\%$ using the 514 nm laser excitation [18]. That is to say, when the monolayer graphene on PET substrate is fully stretched to a strain of 1%, ω_{2D} downshifts by 60 cm^{-1} while at the same time $FWHM_{2D}$ increases by 12 cm^{-1} . Hence, in present study (Fig. 3.3), the measured value of 2D band shift $d\omega_{2D}/d\varepsilon$ is less than 25% of $(d\omega_{2D}/d\varepsilon)_{\text{ref}}$, while the broadening rate $dFWHM_{2D}/d\varepsilon$ is nearly 75% of that of $(dFWHM_{2D}/d\varepsilon)_{\text{ref}}$ [18, 22, 25, 26]. It will now be demonstrated that the low band shift rate $d\omega_{2D}/d\varepsilon$ and higher-than-expected rate of broadening $dFWHM_{2D}/d\varepsilon$ during deformation are both the result of the graphene monolayer being wrinkled.

3.3.3 Measurement of Laser Spot Size

Because of the comparable size of the graphene island to the Raman laser spot, it is also necessary to consider the effect of laser spot size [27]. It can be assumed that the laser intensity $I(r)$ within the spot of a Gaussian laser beam follows the Gaussian distribution [28]:

$$I(r) = \exp\left(-2 \cdot \frac{r^2}{r_0^2}\right) \quad (3.2)$$

where r is the distance to the laser spot centre, and r_0 is the radius of the laser beam, defined as the radius of the plane where $I(r)$ decreases to $1/e^2$ of its maximum value.

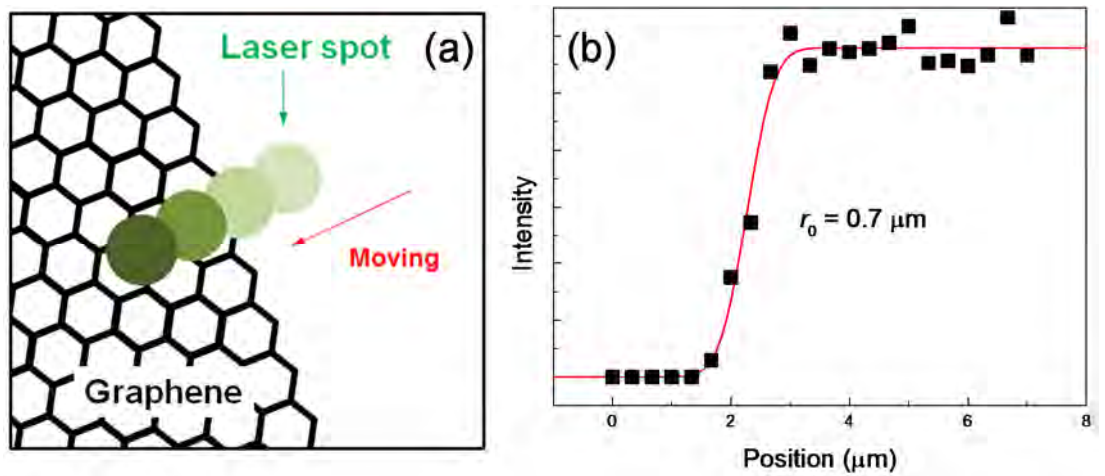


Figure 3.4 (a) Schematic diagram of the method used to measure the laser spot size. (b) Variation of I_{2D} when the laser beam is moving across a well-defined graphene edge.

The spot size of the Gaussian beam laser [28] was estimated by moving the laser spot inwards from outside a mechanical exfoliated monolayer graphene towards its centre (Fig. 3.4(a)), and the 2D band intensity I_{2D} can be fitted as the function of laser position x_l (Fig. 3.4(b)) [27]:

$$I_{2D} = \sqrt{\frac{\pi}{8}} A r_0 \left(1 + \operatorname{erf} \left(\frac{\sqrt{2}(x_l - x_0)}{r_0} \right) \right) \quad (3.3)$$

where x_0 is the graphene edge location and A is the amplitude. For spectra for which the 2D band was not resolvable, I_{2D} was set as zero. By fitting I_{2D} with Eq. 3.3, the radius of the laser beam r_0 is obtained as $\sim 0.7 \mu\text{m}$. Thus the effective diameter of the laser spot size is estimated to be $1.4 \mu\text{m}$ [29], similar to the size of the graphene islands.

3.3.4 Modelling

In order to model this deformation behaviour, it has been assumed that the microstructure of the graphene consists of a series of graphene islands bonded to the PET substrate, averaging $1.2 \mu\text{m}$ in diameter, separated by wrinkles that do not allow the transfer of stress between the isolated islands as shown in Fig. 3.5(a). Hence, in each individual island the axial strain will build up from zero at the wrinkles to become a maximum in the middle of the island. The exact form of the strain distribution will depend upon the size of the island and the efficiency of stress transfer from the underlying PET substrate.

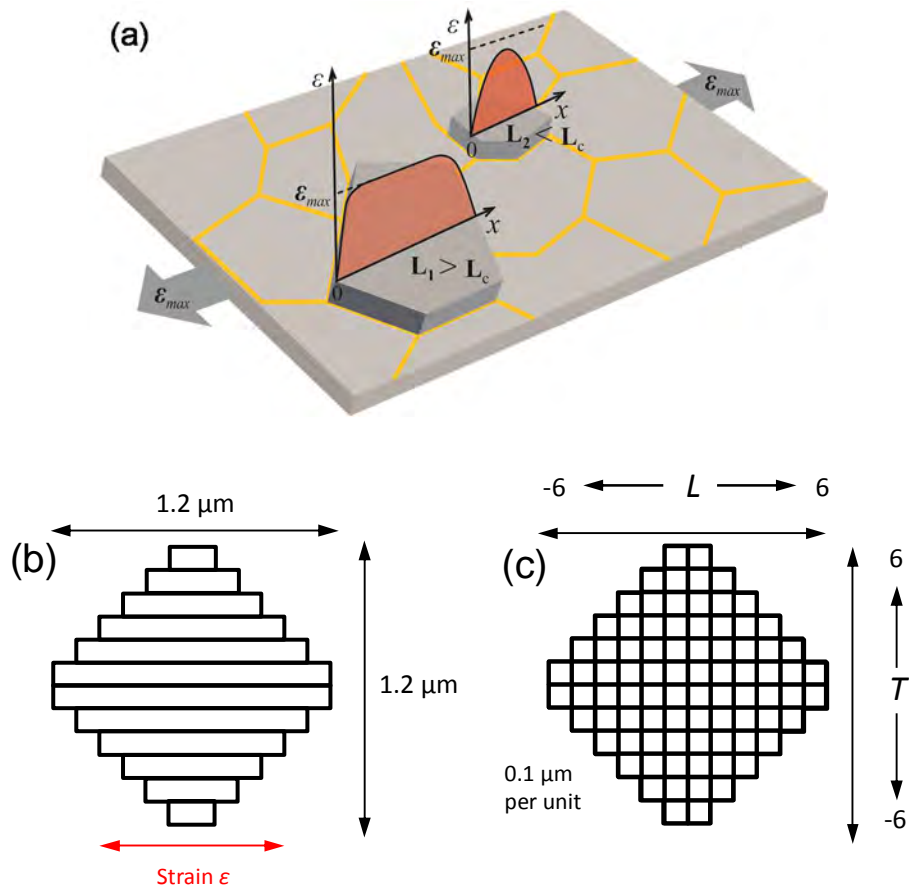


Figure 3.5 Schematic diagram of (a) the proposed stress transfer mechanism (L_i is the length of the i -crystallite and L_c the critical transfer length) (Courtesy of Prof. C. Galiotis, FORTH/ ICE-HT), (b) the strips in the graphene islands and (c) the corresponding elementary units.

It is then assumed that the $\sim 1.2 \mu\text{m}$ diameter graphene islands can be modelled as 12 strips of $\sim 0.1 \mu\text{m}$ wide mechanically-independent graphene nanoribbons lying parallel to the direction of tensile stress (Fig. 3.5(b)). Furthermore, it is assumed that the strain distributions in each nanoribbon can be estimated using ‘shear-lag theory’ as has been done earlier for exfoliated graphene flakes subjected to deformation on a polymer substrate [8, 30]. Considering the size of the wrinkles, it is reasonable to assume that most of the laser spot intensity ($\sim 90\%$) is within the graphene island. Also it is assumed there is no mechanical contribution from the wrinkle networks as it detaches from the substrate. Hence in order to calculate the spatial distribution of local strain and laser beam intensity, each strip is further divided into $\sim 0.1 \mu\text{m}$ square elementary units with their coordinates given by the longitudinal (L) and transverse (T) position parameters, where $(-6 \leq L \leq 6)$ and $(-6 \leq T \leq 6)$ (Fig. 3.5(c)).

We now consider how stress transfer takes place from the PET substrate to graphene nanoribbon. It was shown using shear-lag theory [30, 31] that for an exfoliated monolayer graphene flake deformed on a polymer substrate, the strain in the graphene should be zero near the edges and increase towards the centre of the flake such that [8]:

$$\varepsilon_r = \varepsilon_m \left[1 - \frac{\cosh\left(ns \frac{x}{l}\right)}{\cosh\left(\frac{ns}{2}\right)} \right] \quad (3.4)$$

$$\text{where } n = \sqrt{\frac{2G_m}{E_{\text{gra}}} \left(\frac{t_{\text{gra}}}{t_m} \right)} \quad (3.5)$$

where ε_m is the matrix strain and ε_r is the real strain of graphene as a function of longitudinal position x along the stress direction. In this case, l is the length of the graphene nanoribbon along the stress direction. G_m and E_{gra} are the shear modulus of the matrix and the Young's modulus of graphene, respectively. t_{gra} and t_m are the thickness of graphene and the elementary matrix, respectively. Also s ($= l/t_{\text{gra}}$) is defined as the nanoribbon aspect ratio. The parameter ns is generally accepted to be a measure of stress transfer efficiency, being higher for better stress transfer efficiency, and also increasing proportionally with the size of the monolayer graphene flake or nanoribbon [8]. This theory implies a non-uniform strain in the graphene nanoribbons (and therefore the graphene islands) along the direction of axial stress, particularly when the nanoribbon is smaller than the 'critical length' L_c (twice of the distance it needs for strain to increase to the plateau value) [8]. This model of graphene islands isolated mechanically by wrinkles is analogous to the case of short fibre reinforcement in composites where there is no stress transfer across the fibre ends [32].

The value of ns is proportional to the length of the graphene nanoribbon l (since $s \propto l$) thus both ns and l should be the function of the transverse position parameter T (Fig. 3.5(c)), i.e. $(ns)_T$ and l_T . Typically, the value of ns is taken to be of the order of 2 for a graphene nanoribbon $1.2 \mu\text{m}$ ($T = \pm 1$) along the stress direction [8]. It may also

vary with the efficiency of stress transfer between the substrate and graphene as will be discussed later. Due to the symmetry of the strain and laser spot intensity distributions, only the units with positions ($1 \leq L \leq 6$, $1 \leq T \leq 6$) have been considered here, and the distance between each unit (Fig. 3.5(c)) is calculated through the unit centre (i.e. the distance of unit (5,0) to the island centre is calculated as $0.1 \times 5 - 0.05 = 0.45 \mu\text{m}$). Based on this, Eq. 3.4 can be modified to determine the strain in each individual unit $\varepsilon_r(L,T)$ in Fig. 3.5(c) as:

$$\varepsilon_r(L,T) = \varepsilon_m \left[1 - \frac{\cosh\left(\frac{(ns)_T}{l_T} (0.1L - 0.05)\right)}{\cosh\left(\frac{(ns)_T}{2}\right)} \right] \quad (3.6)$$

Similarly, the local laser intensity at unit (L,T) , $I_{\text{laser}}(L,T)$ is given by modification of Eq. 3.2 as:

$$I_{\text{laser}}(L,T) = \exp\left[-2 \cdot \frac{(0.1L - 0.05)^2 + (0.1T - 0.05)^2}{r_0^2}\right] \quad (3.7)$$

In order to simulate the effect of deformation of the CVD graphene/PET upon the shift of the graphene 2D Raman band, however, both the non-uniform strain in the islands and any local variation in laser spot intensity have been taken into account. Fig. 3.6(a) shows the predicted strain distribution within a $\sim 1.2 \mu\text{m}$ diameter graphene island for a PET substrate strain of 0.4%. It can be seen that the strain is zero at the edges of the island and increases to a maximum of only 0.14% in the centre of the island. This demonstrates clearly that the presence of the wrinkles reduces the efficiency of stress transfer to the graphene monolayer. Fig. 3.6(b) shows the intensity distribution within the laser spot calculated using Eq. 3.7.

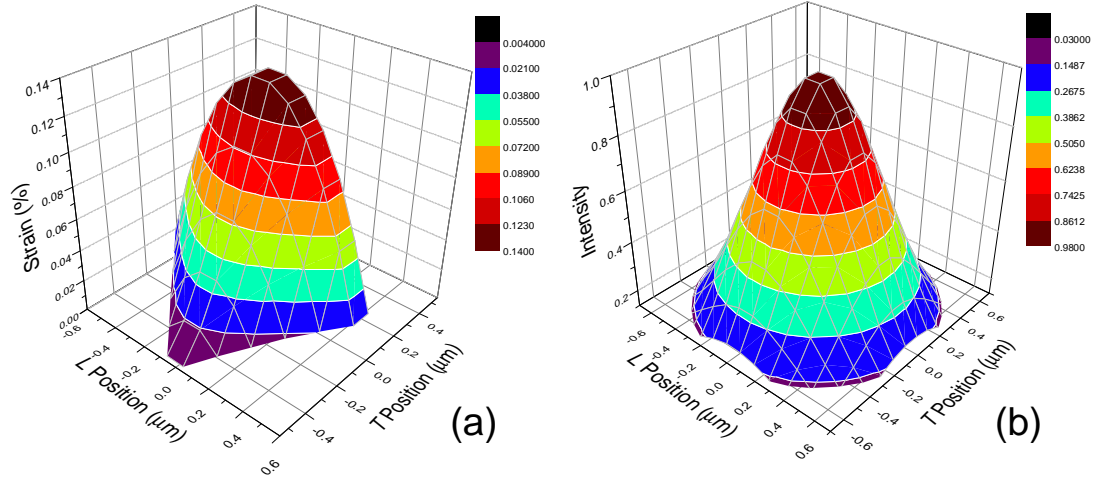


Figure 3.6 (a) Strain distribution in one island and (b) intensity distribution in the laser spot.

The 2D Raman band intensity collected from a unit (L, T) (Fig. 3.5(c)) may be represented in the form of a Lorentzian function $I(\omega, L, T)$ [33]:

$$I(\omega, L, T) \propto \frac{FWHM / 2}{(\omega - \omega_{L,T})^2 + (FWHM / 2)^2} \quad (3.8)$$

where $\omega_{L,T}$ is the position of the simulated band and $FWHM$ is its full width at half maximum. As constant band intensity persists even though the band position shifts so the maximum band intensity at $\omega_{L,T}$ is normalized to be unity by a factor of $FWHM/2$, without affecting its other band parameters. Combining Eqs. 3.6, 3.7 and 3.8, the normalized intensity distribution for the 2D Raman band under strain for each unit (L, T) in the graphene island may be given as:

$$I(\omega, L, T) = \frac{\left[\left(FWHM_{2D} + \varepsilon_i(L, T) \left(\frac{dFWHM_{2D}}{d\varepsilon} \right)_{\text{ref}} \right) / 2 \right]^2}{\underbrace{\left(\omega - \omega_{L,T} - \varepsilon_i(L, T) \left(\frac{d\omega_{2D}}{d\varepsilon} \right)_{\text{ref}} \right)^2 + \left[\left(FWHM_{2D} + \varepsilon_i(L, T) \left(\frac{dFWHM_{2D}}{d\varepsilon} \right)_{\text{ref}} \right) / 2 \right]^2}_{\text{Strain}}} \cdot \underbrace{\exp \left[-2 \frac{(0.1L - 0.05)^2 + (0.1T - 0.05)^2}{r_0^2} \right]}_{\text{Intensity}} \quad (3.9)$$

This equation takes into account both the local strain in the unit and the local intensity of the laser spot. The 2D Raman band collected in the whole island $I_{\text{Total}}(\omega)$ can then be determined as the summation of the contribution of all the elementary units (L, T) in the island:

$$I_{\text{Total}}(\omega) = \sum_{T=1}^6 \sum_{L=1}^6 I(\omega, L, T) \quad (3.10)$$

For strain-free graphene, all the $\omega_{L,T}$ are taken as zero for simplicity, and $FWHM_{2D}$ is taken as the average value for a graphene monolayer flake of 27 cm^{-1} [34, 35]. The ideal values from exfoliated flat graphene flakes of $(d\omega_{2D}/d\varepsilon)_{\text{ref}} = -60 \text{ cm}^{-1}/\%$ (Eq. 3.1) and $(dFWHM_{2D}/d\varepsilon)_{\text{ref}} = 12 \text{ cm}^{-1}/\%$ can be used for 514 nm laser excitation, assuming a perfect interfacial adhesion within the graphene island [18]. As mentioned earlier, a typical value of $n_s=2$ is used for a monolayer graphene of length $1.2 \text{ }\mu\text{m}$ along the stress direction. The Raman 2D band for whole graphene island calculated using Eqs. 3.9 and 3.10 is shown in Fig. 3.7.

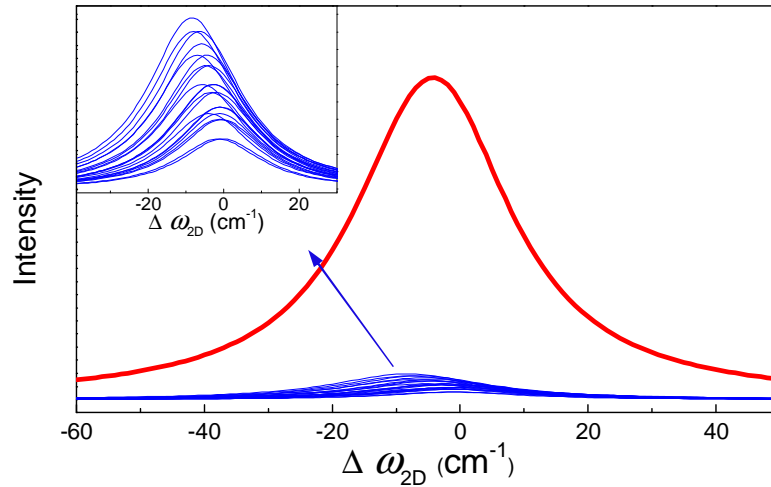


Figure 3.7 Simulated shift of Raman 2D band for each unit ($1 \leq L \leq 6$, $1 \leq T \leq 6$, blue curves) and the integrated 2D band for the whole graphene island (red curve).

Consequently, the unusual band shift and broadening behaviour of the wrinkled graphene can be determined from the summation of the Raman scattering from the different elementary units under strain. The lower rate of band shift per unit strain is the result of the small size of the graphene islands limiting the maximum strain and the non-uniform strain distribution causing more band broadening than would

otherwise be expected. These effects are not found in larger flat graphene flakes since the strain in them is reasonably uniform, except at the edges [8, 17, 18].

In reality, the value of ns will vary depending upon the quality of interfacial stress transfer. With poor interfacial stress transfer, the ns value will be lower, leading to a less strained graphene island and a lower maximum strain at the island centre. This less-strained graphene also results in different values of measured $d\omega_{2D}/d\varepsilon$ and $dFWHM_{2D}/d\varepsilon$. In this case, the variation of ω_{2D} and $FWHM_{2D}$ are predicted based on Eqs. 3.9 and 3.10 using sets of ns values corresponding to different levels of interfacial adhesion (Fig. 3.8). It can be seen that both sets of experimental data fall close to the line for $ns=2$ and 3, demonstrating that the stress transfer between the PET and the CVD graphene within the graphene island is fairly good, and comparable to the interface between exfoliated graphene and SU8/poly(methyl methacrylate) [8].

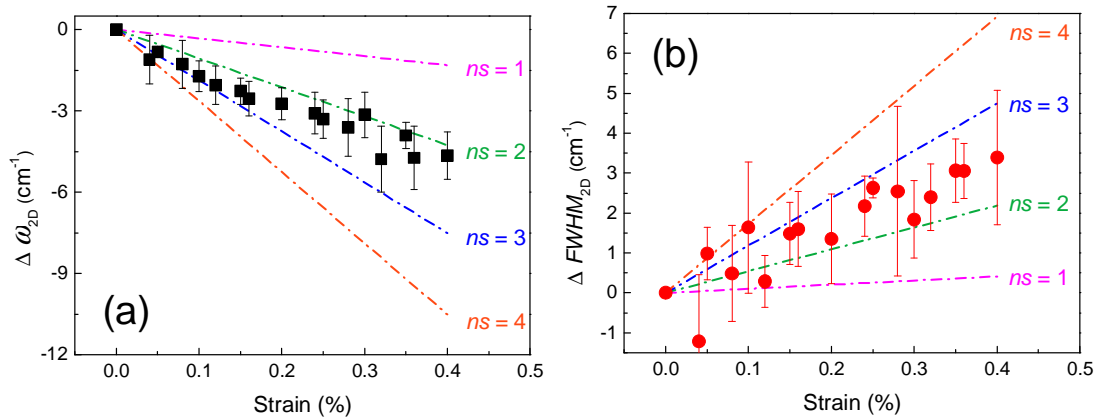


Figure 3.8 Predicted variation of (a) ω_{2D} (b) $FWHM_{2D}$ as the function of strain for different ns values (used in Eq. 3.9 (coloured lines)). The data points are the experimental results from Fig. 3.3.

The data in Fig. 3.8 have been modelled assuming that the graphene islands and laser spots are approximately concentric. In reality, the Raman laser spot could be centred at any position relative to the graphene islands, either at their centre, on their edges (Fig. 3.9) or at any intermediate position. This behaviour has also been modelled where the laser spot is approximated to a square and Fig. 3.9 shows the situation where the laser spot is centred at the wrinkles. The overlapped region of graphene islands and laser spot contributes to the calculated Raman spectra, and only the

region marked by dashed red lines was taken into calculation due to its symmetrical geometry.

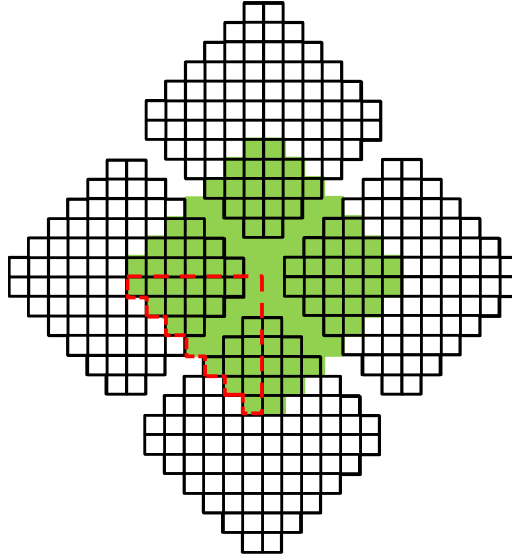


Figure 3.9 Schematic diagram of the laser spot being centred at the wrinkles (the gap) between the graphene islands (black squares). The overlapped region of graphene islands and laser spot (green square) contributes to the calculated Raman spectra.

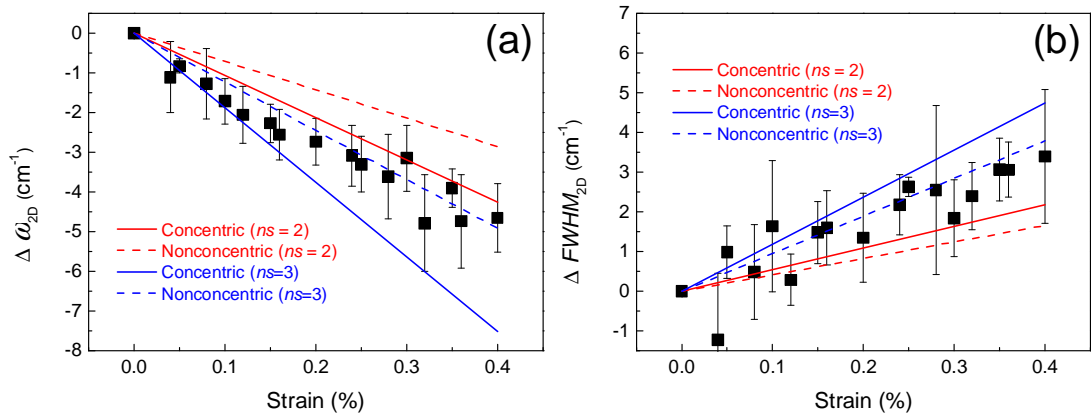


Figure 3.10 Predicted variation of (a) ω_{2D} (b) $FWHM_{2D}$ as the function of strain when graphene island and laser spot are concentric (solid lines) and nonconcentric (dashed lines), with an ns value of 2 (red lines) and 3 (blue lines). Black squares are the experimental results.

The variation of ω_{2D} and $FWHM_{2D}$ with strain for either the laser beam centred in the middle of the graphene island or at the edges have been calculated (Fig. 3.10), again

using ns values of 2 and 3. It can be seen that the predicted variations of ω_{2D} and $FWHM_{2D}$ with strain vary significantly with the position of the laser spot. Nevertheless, it is possible to fit the simulated lines to the experimental data by choosing appropriate ns values for any laser spot position. The fact that both the band shift and band broadening data can be fitted using the same value of ns gives confidence in the validity of the model.

Finally, it is worth considering the effect of wrinkles upon the ability of graphene to reinforce nanocomposites. To a first approximation, the effective Young's modulus of the graphene scales with the Raman band shift rate per unit strain (Chapter 7) [36]. Hence the band shift rate of the wrinkled graphene, being less than 25% of that of flat exfoliated material, implies that it will have an effective Young's modulus of only around 250 GPa, as opposed to ~1TPa for flat graphene [37]. This can also be understood using the knowledge of size factor η_l discussed in Chapter 1:

$$\eta_l = 1 - \frac{\tanh\left(\frac{ns}{2}\right)}{\frac{ns}{2}} \quad (3.11)$$

The value of ns in the study is between 2 and 3, substituting these values into Eq. 3.11 gives the value of η_l to be around 0.24~0.4, implying a low mechanical reinforcement efficiency.

In this present study, however, the graphene has only one interface with the polymer substrate whereas there would be two for wrinkled graphene fully embedded in a polymer matrix. This should give better stress transfer and a higher effective Young's modulus. The results on the simply supported graphene show clearly that it is of extreme importance to take wrinkles into account in future studies of the mechanics of reinforcement of nanocomposites by graphene [38].

3.4 Conclusions

The deformation of wrinkled CVD graphene on PET substrate has been monitored through the use of Raman spectroscopy. It has been demonstrated that the unusual

Raman band shift behaviour observed is a result of the graphene microstructure, with mechanically-isolated graphene island of a comparable size to the Raman laser spot. By deconvoluting the Raman spectra obtained from the graphene networks, a model has been proposed to take account both the non-uniformity of local strain in the graphene microstructure and the intensity distribution in the laser spot. The good fit between the experimental data and the prediction confirms the appropriateness of this model, validating the use of this technique in estimating the effect of defects such as wrinkles on the performance of graphene-based devices. It also implies that when the characteristic dimensions of the microstructural units are of similar size to the spatial resolution of the Raman spectrometer laser spot, the conventional analysis has to be corrected to take into account both the structural non-uniformity and the resolution of the laser beam.

References

1. Novoselov, K. S.; Falko, V. I.; Colombo, L.; Gellert, P. R.; Schwab, M. G.; Kim, K., A Roadmap for Graphene. *Nature* **2012**, 490, 192-200.
2. Yu, Q.; Jauregui, L. A.; Wu, W.; Colby, R.; Tian, J.; Su, Z.; Cao, H.; Liu, Z.; Pandey, D.; Wei, D.; Chung, T. F.; Peng, P.; Guisinger, N. P.; Stach, E. A.; Bao, J.; Pei, S.-S.; Chen, Y. P., Control and Characterization of Individual Grains and Grain Boundaries in Graphene Grown by Chemical Vapour Deposition. *Nature Materials* **2011**, 10, 443-449.
3. Zhu, W.; Low, T.; Perebeinos, V.; Bol, A. A.; Zhu, Y.; Yan, H.; Tersoff, J.; Avouris, P., Structure and Electronic Transport in Graphene Wrinkles. *Nano Letters* **2012**, 12, 3431-3436.
4. Kim, K. S.; Zhao, Y.; Jang, H.; Lee, S. Y.; Kim, J. M.; Kim, K. S.; Ahn, J.-H.; Kim, P.; Choi, J.-Y.; Hong, B. H., Large-Scale Pattern Growth of Graphene Films for Stretchable Transparent Electrodes. *Nature* **2009**, 457, 706-710.
5. Bao, W.; Miao, F.; Chen, Z.; Zhang, H.; Jang, W.; Dames, C.; Lau, C. N., Controlled Ripple Texturing of Suspended Graphene and Ultrathin Graphite Membranes. *Nature Nanotechnology* **2009**, 4, 562-566.
6. Min, K.; Aluru, N. R., Mechanical Properties of Graphene under Shear Deformation. *Applied Physics Letters* **2011**, 98, 013113.
7. Shen, X.; Lin, X.; Yousefi, N.; Jia, J.; Kim, J.-K., Wrinkling in Graphene Sheets and Graphene Oxide Papers. *Carbon* **2014**, 66, 84-92.
8. Gong, L.; Kinloch, I. A.; Young, R. J.; Riaz, I.; Jalil, R.; Novoselov, K. S., Interfacial Stress Transfer in a Graphene Monolayer Nanocomposite. *Advanced Materials* **2010**, 22, 2694-2697.
9. Pirkle, A.; Chan, J.; Venugopal, A.; Hinojos, D.; Magnuson, C. W.; McDonnell, S.; Colombo, L.; Vogel, E. M.; Ruoff, R. S.; Wallace, R. M., The Effect of Chemical Residues on the Physical and Electrical Properties of

- Chemical Vapor Deposited Graphene Transferred to SiO₂. *Applied Physics Letters* **2011**, 99, 122108-3.
10. Gao, L.; Ni, G.-X.; Liu, Y.; Liu, B.; Castro Neto, A. H.; Loh, K. P., Face-to-Face Transfer of Wafer-Scale Graphene Films. *Nature* **2014**, 505, 190-194.
 11. Liu, N.; Pan, Z.; Fu, L.; Zhang, C.; Dai, B.; Liu, Z., The Origin of Wrinkles on Transferred Graphene. *Nano Research* **2011**, 4, 996-1004.
 12. Adelung, R.; Ernst, F.; Scott, A.; Tabib-Azar, M.; Kipp, L.; Skibowski, M.; Hollensteiner, S.; Spiecker, E.; Jäger, W.; Gunst, S.; Klein, A.; Jägermann, W.; Zaporozhchenko, V.; Faupel, F., Self-Assembled Nanowire Networks by Deposition of Copper onto Layered-Crystal Surfaces. *Advanced Materials* **2002**, 14, 1056-1061.
 13. Cooper, C. A.; Young, R. J.; Halsall, M., Investigation into the Deformation of Carbon Nanotubes and Their Composites through the Use of Raman Spectroscopy. *Composites Part A: Applied Science and Manufacturing* **2001**, 32, 401-411.
 14. Ferrari, A. C.; Meyer, J. C.; Scardaci, V.; Casiraghi, C.; Lazzeri, M.; Mauri, F.; Piscanec, S.; Jiang, D.; Novoselov, K. S.; Roth, S.; Geim, A. K., Raman Spectrum of Graphene and Graphene Layers. *Physical Review Letters* **2006**, 97, 187401.
 15. Li, X.; Cai, W.; An, J.; Kim, S.; Nah, J.; Yang, D.; Piner, R.; Velamakanni, A.; Jung, I.; Tutuc, E.; Banerjee, S. K.; Colombo, L.; Ruoff, R. S., Large-Area Synthesis of High-Quality and Uniform Graphene Films on Copper Foils. *Science* **2009**, 324, 1312-1314.
 16. Lee, J. E.; Ahn, G.; Shim, J.; Lee, Y. S.; Ryu, S., Optical Separation of Mechanical Strain from Charge Doping in Graphene. *Nature Communications* **2012**, 3, 1024.
 17. Huang, M.; Yan, H.; Chen, C.; Song, D.; Heinz, T. F.; Hone, J., Phonon Softening and Crystallographic Orientation of Strained Graphene Studied by Raman Spectroscopy. *Proceedings of the National Academy of Sciences* **2009**, 106, 7304-7308.
 18. Frank, O.; Mohr, M.; Maultzsch, J.; Thomsen, C.; Riaz, I.; Jalil, R.; Novoselov, K. S.; Tsoukleri, G.; Parthenios, J.; Papagelis, K.; Kavan, L.; Galiotis, C., Raman 2D-Band Splitting in Graphene: Theory and Experiment. *ACS Nano* **2011**, 5, 2231-2239.
 19. Bissett, M. A.; Izumida, W.; Saito, R.; Ago, H., Effect of Domain Boundaries on the Raman Spectra of Mechanically Strained Graphene. *ACS Nano* **2012**, 6, 10229-10238.
 20. Ni, Z. H.; Yu, T.; Lu, Y. H.; Wang, Y. Y.; Feng, Y. P.; Shen, Z. X., Uniaxial Strain on Graphene: Raman Spectroscopy Study and Band-Gap Opening. *ACS Nano* **2008**, 2, 2301-2305.
 21. Grimvall, G., Phonons in Real Crystals: Anharmonic Effects. In *Thermophysical Properties of Materials*, Elsevier Science B.V.: Amsterdam, 1999; pp 136-152.
 22. Mohiuddin, T. M. G.; Lombardo, A.; Nair, R. R.; Bonetti, A.; Savini, G.; Jalil, R.; Bonini, N.; Basko, D. M.; Galiotis, C.; Marzari, N.; Novoselov, K. S.; Geim, A. K.; Ferrari, A. C., Uniaxial Strain in Graphene by Raman Spectroscopy: G Peak Splitting, Grüneisen Parameters, and Sample Orientation. *Physical Review B* **2009**, 79, 205433.

23. Zabel, J.; Nair, R. R.; Ott, A.; Georgiou, T.; Geim, A. K.; Novoselov, K. S.; Casiraghi, C., Raman Spectroscopy of Graphene and Bilayer under Biaxial Strain: Bubbles and Balloons. *Nano Letters* **2011**, 12, 617-621.
24. Androulidakis, C.; Tsoukleri, G.; Koutroumanis, N.; Gkikas, G.; Pappas, P.; Parthenios, J.; Papagelis, K.; Galiotis, C., Experimentally Derived Axial Stress–Strain Relations for Two-Dimensional Materials Such as Monolayer Graphene. *Carbon* **2015**, 81, 322-328.
25. Young, R. J.; Gong, L.; Kinloch, I. A.; Riaz, I.; Jalil, R.; Novoselov, K. S., Strain Mapping in a Graphene Monolayer Nanocomposite. *ACS Nano* **2011**, 5, 3079-3084.
26. Ferralis, N., Probing Mechanical Properties of Graphene with Raman Spectroscopy. *Journal of Materials Science* **2010**, 45, 5135-5149.
27. Gupta, A. K.; Russin, T. J.; Gutiérrez, H. R.; Eklund, P. C., Probing Graphene Edges via Raman Scattering. *ACS Nano* **2008**, 3, 45-52.
28. Siegman, A. E., *Lasers*. University Science Books: Sausalito: California, 1986.
29. Cai, W.; Moore, A. L.; Zhu, Y.; Li, X.; Chen, S.; Shi, L.; Ruoff, R. S., Thermal Transport in Suspended and Supported Monolayer Graphene Grown by Chemical Vapor Deposition. *Nano Letters* **2010**, 10, 1645-1651.
30. Cox, H. L., The Elasticity and Strength of Paper and Other Fibrous Materials. *British Journal of Applied Physics* **1952**, 3, 72.
31. Kelly, A.; Tyson, W. R., Tensile Properties of Fibre-Reinforced Metals: Copper/Tungsten and Copper/Molybdenum. *Journal of the Mechanics and Physics of Solids* **1965**, 13, 329-350.
32. Huang, Y.; Young, R. J., Interfacial Micromechanics in Thermoplastic and Thermosetting Matrix Carbon Fibre Composites. *Composites Part A: Applied Science and Manufacturing* **1996**, 27, 973-980.
33. Skinner, J. L.; Auer, B. M.; Lin, Y.-S., Vibrational Line Shapes, Spectral Diffusion, and Hydrogen Bonding in Liquid Water. In *Advances in Chemical Physics*, John Wiley & Sons, Inc.: 2009; pp 59-103.
34. Yan, K.; Peng, H.; Zhou, Y.; Li, H.; Liu, Z., Formation of Bilayer Bernal Graphene: Layer-by-Layer Epitaxy via Chemical Vapor Deposition. *Nano Letters* **2011**, 11, 1106-1110.
35. Hao, Y.; Wang, Y.; Wang, L.; Ni, Z.; Wang, Z.; Wang, R.; Koo, C. K.; Shen, Z.; Thong, J. T. L., Probing Layer Number and Stacking Order of Few-Layer Graphene by Raman Spectroscopy. *Small* **2010**, 6, 195-200.
36. Frank, O.; Tsoukleri, G.; Riaz, I.; Papagelis, K.; Parthenios, J.; Ferrari, A. C.; Geim, A. K.; Novoselov, K. S.; Galiotis, C., Development of a Universal Stress Sensor for Graphene and Carbon Fibres. *Nature Communications* **2011**, 2, 255.
37. Lee, C.; Wei, X.; Kysar, J. W.; Hone, J., Measurement of the Elastic Properties and Intrinsic Strength of Monolayer Graphene. *Science* **2008**, 321, 385-388.
38. Young, R. J.; Kinloch, I. A.; Gong, L.; Novoselov, K. S., The Mechanics of Graphene Nanocomposites: A Review. *Composites Science and Technology* **2012**, 72, 1459-1476.

Chapter 4 Deformation of Monolayer Graphene Oxide

4.1 Introduction

Due to its high surface area, high strength as well as the multifunctionality, graphene is clearly a strong candidate as the nano-filler in polymer nanocomposites [1]. It is hard to disperse homogeneously in a polymer matrix because it tends to re-agglomerate and its chemically inert surface may be incompatible with the matrix. In contrast, its derivative, graphene oxide (GO), facilitates dispersion remarkably because of the function groups on its basal plane [2], but, sacrifices its intrinsic stiffness by a factor of ~ 4 [3]. Hence, it is a compromise to balance the loss of the interfacial adhesion for graphene with the loss of intrinsic stiffness, like GO and reduced GO (rGO).

The mechanics of graphene has been extensively studied, both freestanding [4] and in nanocomposites [1, 5, 6]. It was shown by using the strain sensitive Raman band position [7-9] that in microscale the deformation of graphene still follows continuum mechanics, and the interfacial shear stress with the polymer matrix to be the order of 2 MPa [6, 10]. For multilayer graphene, its reinforcement efficiency deteriorates as a result of the poor interlayer stress transfer [11, 12], which further causes a loss of the Bernal stacking of the graphene [13].

The deformation behaviour of GO has been studied which revealed a Young's modulus of ~ 250 GPa for monolayer GO [3]. The observed constant Young's modulus of the GO membranes with different number of GO layers perhaps suggests the interlayer sliding or delamination of GO multilayers is less likely to occur than that of graphene [3, 13]. The deformation mechanisms of GO-based nanocomposites and paper have also been studied [2, 14-17]. Based on continuum mechanics, a computer simulation estimated a maximum interfacial shear stress up to more than 130 MPa at rGO edges with a flake size of ~ 30 μm [18], suggesting a higher interfacial interaction of GO to a matrix than that of graphene [6, 10]. This can be further optimized by modifying the structural and chemical composition [19],

increasing flake size [20] and even the incorporation of water molecules [21]. However, the deformation of monolayer GO still has not been experimentally observed.

In this chapter, the Raman D band position (ω_D) is found to shift as the function of strain ε . The D band shift rate with strain ($d\omega_D/d\varepsilon$) is used to follow the strain distribution of the deformed monolayer GO flake, which shows an almost constant strain across the flake but with a sharp drop near the edge. This phenomenon implies a better stress transfer efficiency of GO than that of graphene. This work presents a fundamental and general method to estimate and investigate the deformation mechanics of monolayer GO.

4.2 Experimental

4.2.1 Materials

The graphite (Grade 2369) was supplied by Graphexel Ltd. All other reagents were of analytical grade and used without further purification.

4.2.2 Preparation

The GO was prepared using the modified Hummers method [22, 23]. Briefly, 3 g of graphite was added to 70 ml of concentrated sulfuric acid while stirring at room temperature. The mixture system was then cooled to 0 °C when 1.5 g sodium nitrate was added. While stirring, 9 g of potassium permanganate was added slowly, to avoid a rapid temperature rise. The mixture was then placed into a 40 °C water bath for 0.5 h, followed by the addition of 140 ml of water and it was stirred for another 15 min. An additional 500 ml water and 20 ml of 6 % w/v H_2O_2 were added subsequently after which the colour of the mixture turned from brown to yellow. The mixture was then washed repeatedly with 250 ml of 1:10 HCl aqueous solution and centrifuged 3 times. Following this, the mixture was repeatedly washed with water and centrifuged until the pH was approximately 7. Finally, the GO was dispersed in water and diluted to $< 10^{-3}$ mg/ml and deposited onto poly(methyl methacrylate) (PMMA) beam and SiO_2 substrate followed by drying under ambient condition, for

Raman spectroscopy and scanning electron microscope (SEM), respectively. Prior to GO deposition, the PMMA beam and SiO₂ substrate were treated by UV-Ozone for 20 mins to make it more hydrophilic, facilitating the spreading of the solution drop.

4.2.3 Characterization

X-ray diffraction (XRD) was carried out on dried GO powder using an X'Pert DY609 X-Ray diffractometer (Philips) with a Cu K α radiation source ($\lambda = 1.542\text{\AA}$). Optical images of the GO flakes were obtained using an Olympus BH Microscope. Atomic force microscope (AFM) images were obtained using a Dimension 3100 AFM (Bruker) in the tapping mode in conjunction with the 'TESPA' probe (Bruker). SEM images were obtained using a Philips XL30 FEGSEM.

Raman spectra were obtained using Renishaw 1000/2000 spectrometers and Horiba LabRAM HR Evolution equipped with a HeNe laser ($\lambda = 633\text{ nm}$) with a laser spot size around 1~2 μm . The incident laser polarization was parallel to the strain while the scattered radiation was randomly polarized. The specimens were bended by a four-point bending rig, and the strain was measured by strain gauge. The Raman band was fitted using a Lorentzian function [24].

4.3 Results and Discussion

4.3.1 Microstructure of the GO Flakes

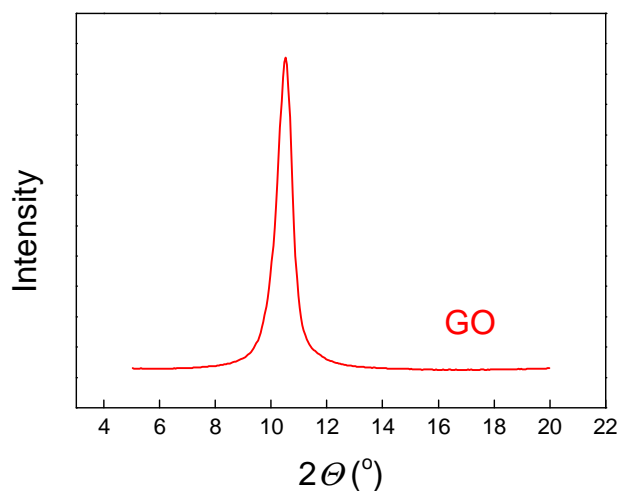


Figure 4.1 XRD pattern of the GO powder.

In the XRD patterns (Fig. 4.1), the characteristic peak of the GO at $2\theta = 10.5^\circ$ corresponds to an interlayer spacing of 0.84 nm, in good agreement with the reported value [14].

Fig. 4.2(a) shows the SEM images of the GO flakes on SiO₂ substrate. It can be seen that the GO flakes have irregular geometries. Their size is broadly distributed but with an average value of $\sim 14.85 \mu\text{m}$, as indicated in (Fig. 4.2(b)) by measuring each flake in two different directions.

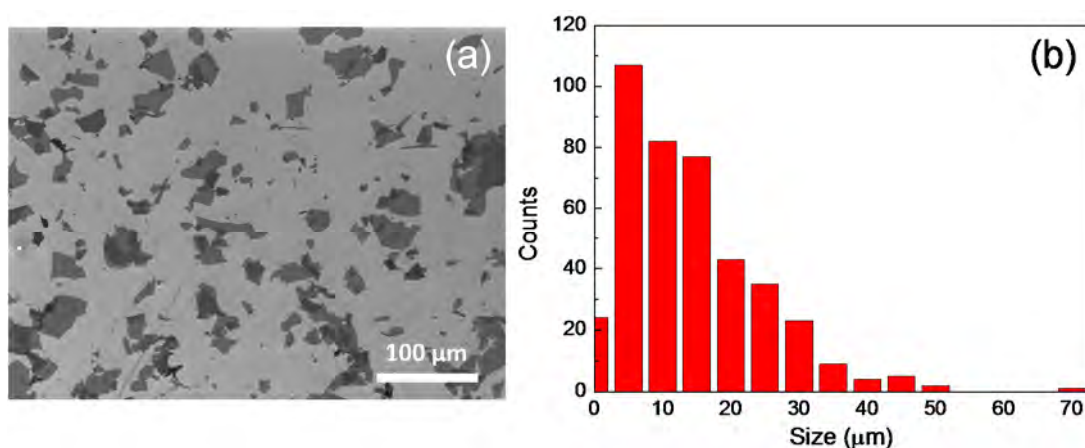


Figure 4.2 (a) SEM image and (b) lateral dimension distribution of the GO flakes.

An optical microscope and an AFM were used to identify monolayer GO, for example, GO flake #1 (Fig. 4.3). The optical image is in fact poorly resolved but a change of contrast at the GO edge is still visible, as highlighted in Fig. 4.3(a). Its geometry is much more clearly revealed by the AFM image (Fig. 4.3(e)), and it can be seen that the GO flake has a large lateral size, and is generally flat but with some wrinkles at its edge. The damage of the AFM tip to the GO flake was also studied by scanning repeatedly over a small area followed by a global scan on the whole flake (Fig. 4.3(b), (c), (d) and (e)). The almost identical height profiles (Fig. 4.3(f)) over the dashed white lines in Fig. 4.3(b), (c), (d) and (e) obtained in each cycling scan imply that the tapping mode AFM scan induces no damage and the structure of the GO flake remains intact. Additionally, those height profiles clearly demonstrate the monolayer feature of the GO flake with the thickness of the order of 1 nm (Fig. 4.3(f)) [25].

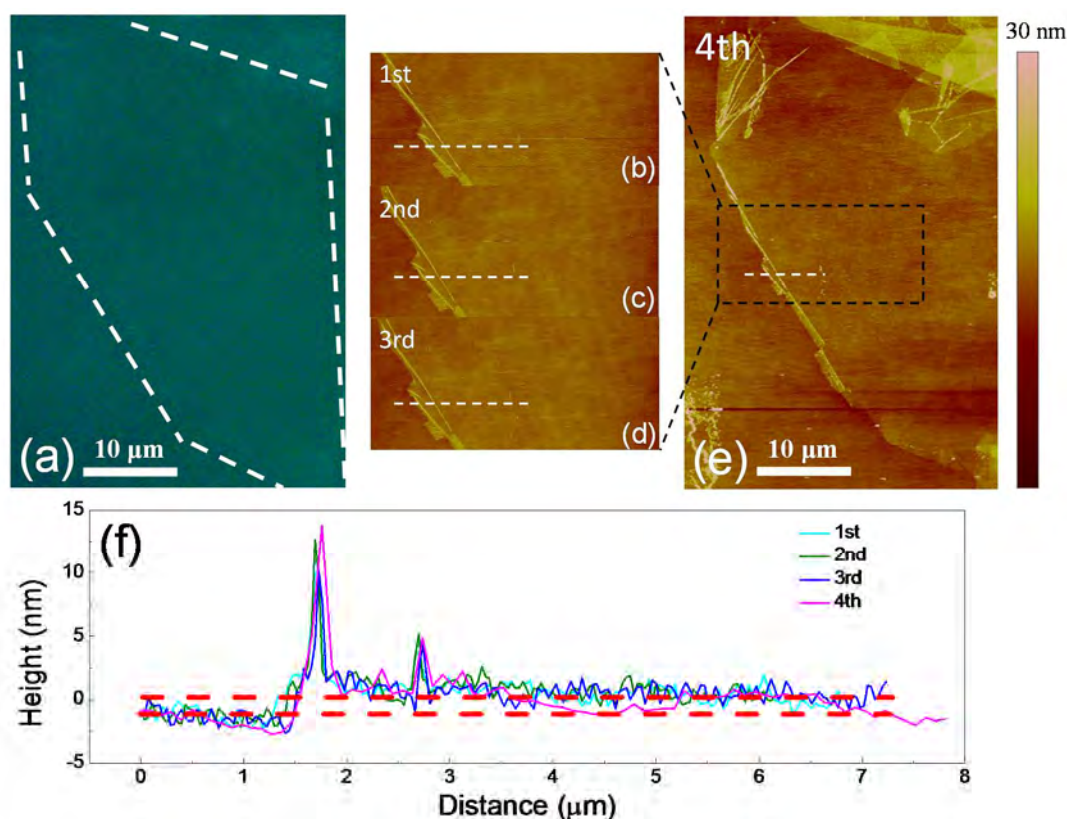


Figure 4.3 (a) Optical image of the monolayer GO #1. AFM images of the (b) 1st, (c) 2nd, (d) 3rd cycle of the local area of the GO flake and (e) the overall scan (4th time) over the whole GO flake. (f) Height profiles along the dashed lines in (b), (c), (d) and (e), respectively. The surface of GO flake and the PMMA substrate underneath are highlighted with the dashed red lines.

4.3.2 Deformation of Monolayer GO

The Raman spectroscopy deformation analysis was undertaken on monolayer GO flake #2, as indicated in Fig. 4.4. It had a lateral dimension size of over 50 μm , which ensures the complete interfacial stress transfer from the substrate to the flake as has been found for graphene [6, 10].

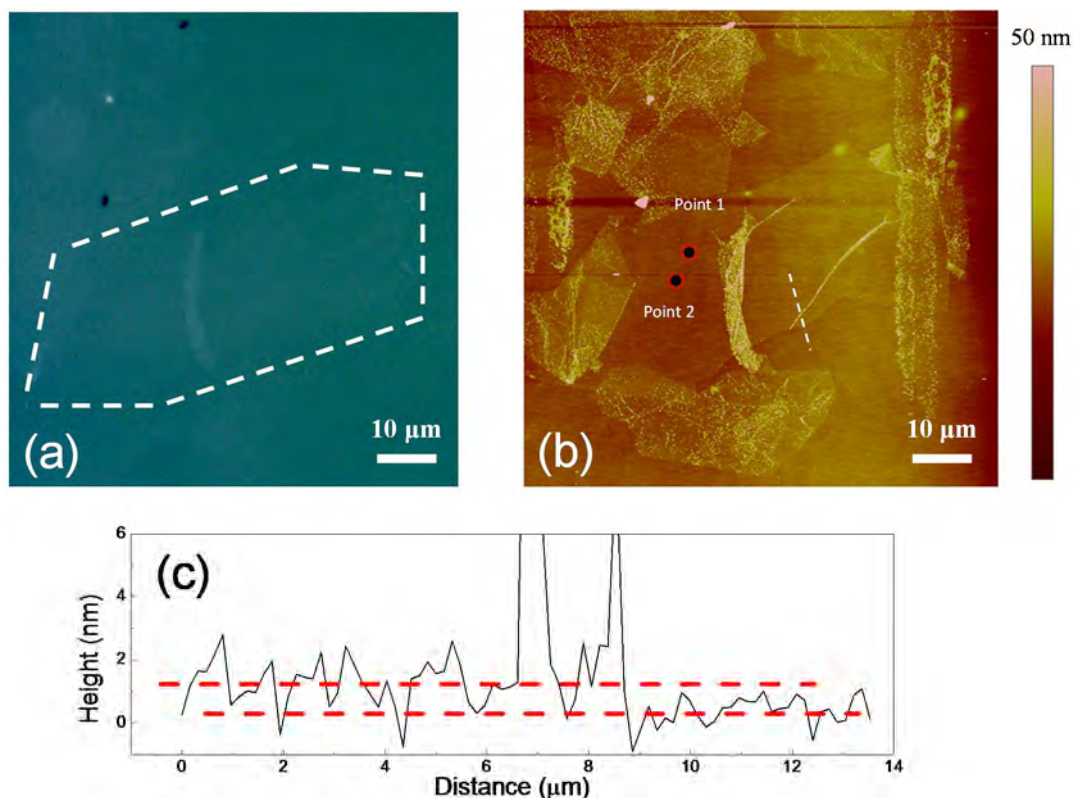


Figure 4.4 (a) Optical and (b) AFM images of the monolayer GO flake #2, where points 1&2 are indicated. (c) Height scan along the dashed lines in (b). The surface of GO flake and the PMMA substrate underneath are highlighted with the dashed red lines.

To avoid the Raman laser induced heat reduction [26-28] or photoreduction [29] of the GO flake, a laser with a long wavelength ($\lambda=633$ nm) was chosen, because GO has the absorption peak near ~ 250 nm [27]. A low laser power was chosen around ~ 10 μ W, which is sufficiently weak to avoid the local laser heating, as indicated by the constant value of the intensity ratio of D band and G band (I_D/I_G) (discussed later) [30, 31]. It has been suggested by finite element analysis that the monolayer GO is not easy to be burnt off since its insufficient absorption keeps the local temperature at low level [27].

The Raman spectrum of the monolayer GO flake #2 is shown in Fig. 4.5(a), where the most prominent bands are the G band and D band. The G band located at ~ 1600 cm^{-1} , is due to the doubly degenerated zone centre E_{2g} mode [32]. The D band, centred ~ 1330 cm^{-1} , results from the \mathbf{K} point phonons of A_{1g} symmetry [33]. The broadened D band and G band compared to that of graphene [34], is possibly due to

the loss of lattice symmetry as a result of the breaking down of the sp^2 carbon networks in pristine graphene by the strong oxidation [33, 35]. Hence it implies a higher degree of disorder [30, 36], making the Raman spectrum of GO resembles that of the amorphous carbon [37]. Empirically the value of I_D/I_G can be used as a measure of the degree of disorder of GO [30, 31]. The small band around 1450 cm^{-1} is from the PMMA substrate. However, unlike the Raman spectrum of graphene shown in Fig. 3.2, the scattered data points in Fig. 4.5(a) are a result of the damaged graphene hexagonal lattice that leads to a loss of the resonance Raman scattering.

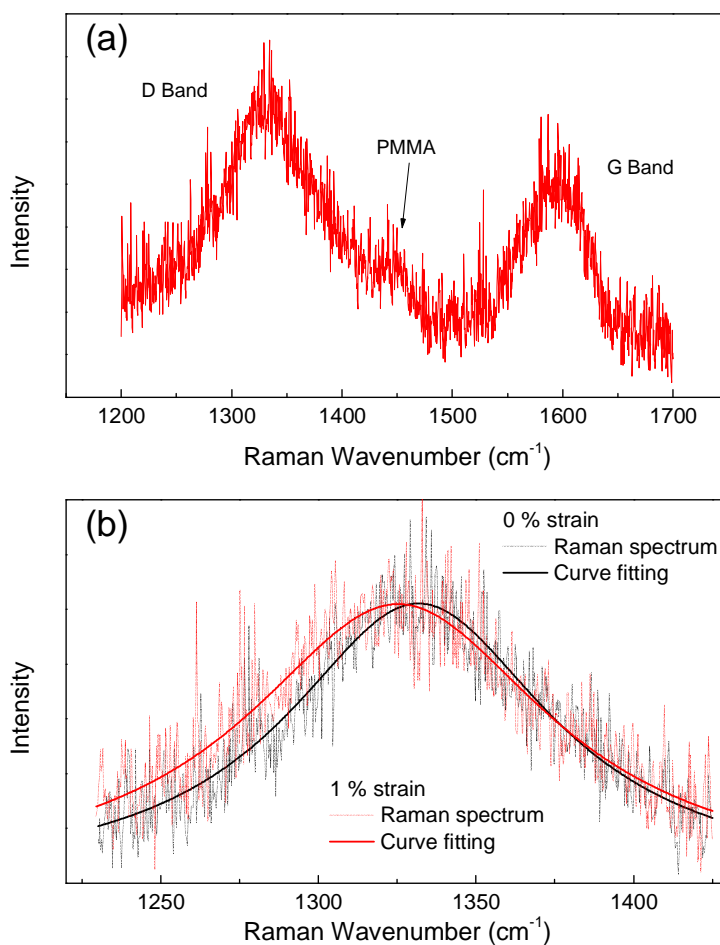


Figure 4.5 (a) Raman spectrum of the GO flake #2 on PMMA. (b) Normalized Raman D band of point 2 of the GO flake #2 before and after deformed to 1.0 % strain. The baselines have been subtracted.

As reported previously, the Raman bands downshift as graphene is stretched [9] as a result of the elongation of the C-C bonds [38]. Analyses based on 2D band and G band have been extensively performed on graphene, and their corresponding

reference shift rates were estimated to be $\sim -60 \text{ cm}^{-1}/\%$ and $-30 \text{ cm}^{-1}/\%$ using the knowledge of Grüneisen parameter [9, 39]. However, due to the broadened 2D band (Chapter 2) and the asymmetric G band in GO involving three bands [17], the Raman D band was employed here, and typical Raman D band of point 2 in (Fig. 4.4(b)) before and after deformed to 1.0 % strain are shown in Fig. 4.5(b), and a downshift of the D band can be seen. In detail, the ω_D of two individual points in Fig. 4.4(b) as the function of strain was monitored to follow the deformation of the GO flake *in-situ* (Fig. 4.6). Both of the points were in the central region of the GO flake to ensure a good stress transfer [6].

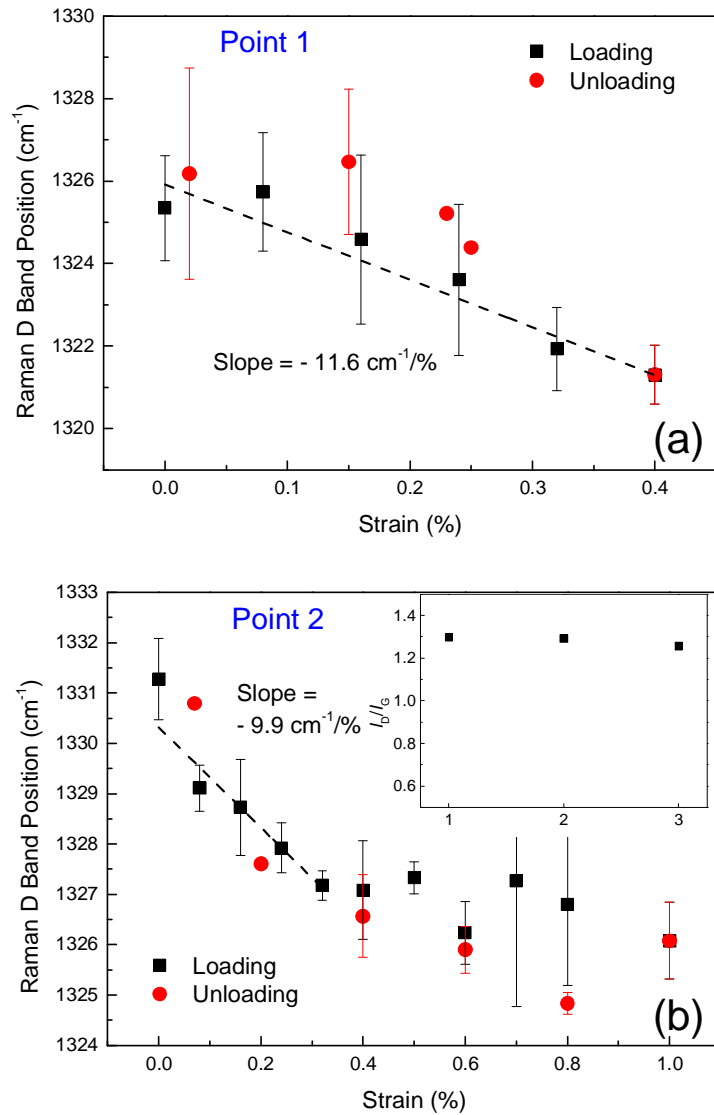


Figure 4.6 ω_D as the function of strain for (a) point 1 and (b) point 2 for GO flake #2 in Fig. 4.4(b). The inset in (b) is the I_D/I_G ratio for the first three scans of point 2 at 0 % strain.

For point 1 (Fig. 4.6(a)), the ω_D clearly showed a linear downshift as the GO was deformed to 0.4% strain with a $d\omega_D/d\varepsilon$ of $-11.6 \text{ cm}^{-1}/\%$, indicating the stretching of the C-C bonds [38] as a result of the stress transfer from the substrate to GO. When the sample was unloaded, ω_D went back to its original position, implying good interfacial adhesion hence an intact interface between the GO and substrate [6]. This reversible behaviour as well demonstrates the variation of ω_D is due to the deformation of GO rather than laser induced heating.

For point 2 (Fig. 4.6(b)), it was scanned three times when it was strain-free, and the constant value of I_D/I_G implies the absence of reduction induced by the laser heating [30, 31]. Similar to the behaviour for point 1, ω_D downshifted with a $d\omega_D/d\varepsilon$ of $-9.9 \text{ cm}^{-1}/\%$ as the specimen was deformed to a strain of 0.3~ 0.4%, but the $d\omega_D/d\varepsilon$ decreased as the strain further increased. This commonly corresponds to an interface failure [5, 6], however when the sample was unloaded, the ω_D upshifted back to the original position, and this reversible behaviour is in contrast of what has been reported for a failed interface. The possible reasons are discussed later.

For both points, the $d\omega_D/d\varepsilon$ in the elastic region is comparable to each other, with an average value of $-10.8 \pm 1.2 \text{ cm}^{-1}/\%$. According to the knowledge of Grüneisen parameter [9, 38, 40], it has been demonstrated that for an ideal graphene crystal, $d\omega_D/d\varepsilon$ under uniaxial tensile strain should be given as [9, 39]:

$$\frac{d\omega_D}{d\varepsilon} = -\omega_D^0 \gamma_D (1 - \nu) \quad (4.1)$$

where ω_D^0 is the ω_D at zero strain. γ_D is the Grüneisen parameter for the D band and ν is the Poisson's ratio of either the substrate or the graphene itself. Based on Eq. 4.1, if $\gamma_D = 3.55$ is used here [9], and ν is taken as 0.35 for the PMMA substrate [41], the $d\omega_D/d\varepsilon$ for supported graphene is given to be around $-30 \text{ cm}^{-1}/\%$ [9]. Meanwhile if ν is taken as 0.15 for monolayer graphene [42], the $d\omega_D/d\varepsilon$ for freestanding graphene is derived as $\sim -40 \text{ cm}^{-1}/\%$. According to this, the measured $d\omega_D/d\varepsilon$ ($-10.8 \text{ cm}^{-1}/\%$) can be converted to be about $-14.1 \text{ cm}^{-1}/\%$ for freestanding GO. Nevertheless this value is just 1/3~1/2 of the value for freestanding graphene ($-40 \text{ cm}^{-1}/\%$) [9, 39]. It is

noticed that the ω_D^0 obtained for the two points vary, and this can be due to the local waviness or residue strain of the GO flake [43].

There are two major reasons for the 2/3 decrease of $d\omega_D/d\varepsilon$. Firstly, the GO flake was just deposited onto the surface of the PMMA beam without any further chemical treatment. As a result, after the water evaporated, there is no direct chemical bonding between the GO flake and the PMMA beam. Secondly, as the structural distortion decreases the modulus of GO by a factor of 2 [44], it is proposed that the structural distortion also causes a decrease of $d\omega_D/d\varepsilon$, similar to its effect on the modulus. This is understandable in that the introduction of functional groups as well as defects causes sp^3 hybridization of carbon atoms and wrinkles [19, 45], hence GO is actually not perfectly flat but wrinkled and puckered showing a zig-zag geometry [46]. This results in a distorted basal plane with lower stiffness [45], and also less elongated C-C bonds under tensile deformation and thus a lower $d\omega_D/d\varepsilon$. Based on this, the reason for the reversible softening behaviour in Fig. 4.6(b) can be interpreted to be, instead of the interface failure, the flattening of puckered GO region that partially comprises the deformation of the C-C bonds, similar to the observed change of lattice parameter during deformation [46].

4.3.3 Deformation Mechanics of Monolayer GO

The deformation test has been again carried out on the GO flake #3, which also possesses a large dimensional size (Fig. 4.7(a)). The height profile (Fig. 4.7(b)) of the dashed white line in Fig. 4.7(a) indicates the monolayer GO is of the order of ~ 1 nm thick [25], and the point in Fig. 4.7(a) indicates where the Raman spectroscopy was conducted to monitor the deformation. As shown in Fig. 4.7(c), the ω_D again downshifted as the GO flake was deformed, with a similar $d\omega_D/d\varepsilon$ value of around $-9.2 \text{ cm}^{-1}/\%$.

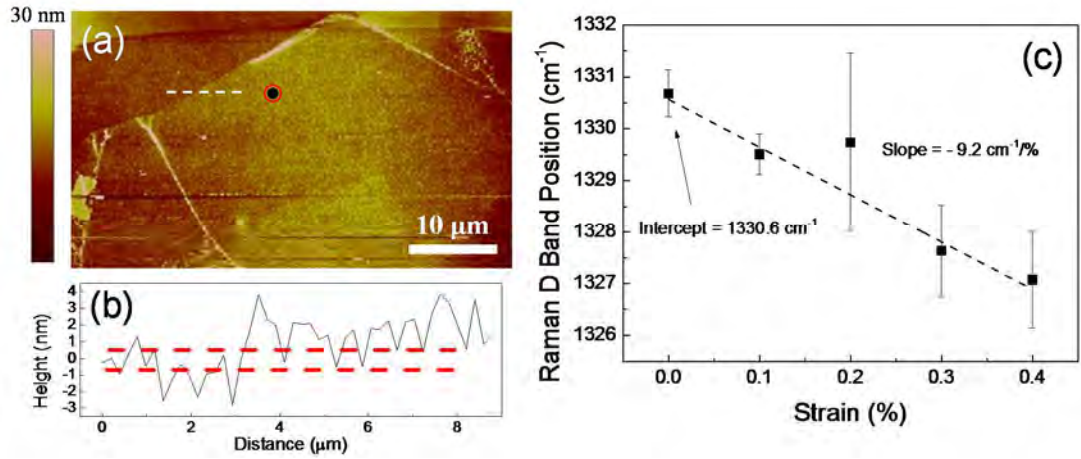


Figure 4.7 (a) AFM image of the GO flake #3. (b) Height profile along the dashed white line in (a). (c) ω_D as the function of strain of 2~3 measurements obtained on the point highlighted in (a).

As ω_D downshifted linearly with the strain, it has been used to monitor the deformation of this GO flake near its edge along the dashed white line in Fig. 4.7(a). Five points near the edge were followed at the strain of 0 % and 0.4 %, with the step between each point being 1 μm (Fig. 4.8), and the values of ω_D obtained have been converted to strain based on the linear fit in Fig. 4.7(c). It can be seen that without deformation, the strain from the GO edge to the central flake stayed around zero. When the GO flake was deformed to 0.4 %, the strain in the central region of the flake increased, however the strain at the edge still remained almost zero.

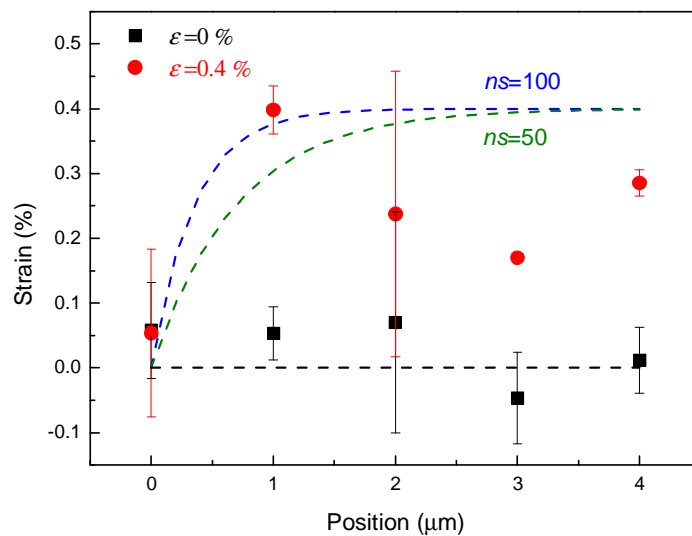


Figure 4.8 The strain distribution from the edge of the GO flake. Each point was averaged by two measurements.

This phenomenon indicates that the GO flake may also obey continuum mechanics, and it can be interpreted as the non-uniform strain distribution across the GO flake using the ‘shear-lag’ analysis [47], which has already been observed on graphene [5, 6]. As discussed in Chapter 1, the real strain ε_r from the flake edge can be given as:

$$\varepsilon_r = \varepsilon_m \left[1 - \frac{\cosh\left(\frac{ns}{l} \cdot \left(x - \frac{l}{2}\right)\right)}{\cosh\left(\frac{ns}{2}\right)} \right] \quad (4.2)$$

$$\text{where} \quad n \approx \sqrt{\frac{2G_m}{E_{GO}} \left(\frac{t_{GO}}{t_m} \right)} \quad (4.3)$$

ε_m is the matrix strain (=0.4 %). t_{GO} and t_m are the thickness of GO and elementary matrix, respectively. l is the size of the flake ($\sim 35 \mu\text{m}$ in Fig. 4.7(a)) and $s(=l/t_{GO})$ is its aspect ratio. E_{GO} is the Young’s modulus of GO and G_m is the shear modulus of the matrix. x is the position along the dashed white line in Fig. 4.7(a) starting from the GO edge, The value of the term ns can be taken as a measure of the stress transfer efficiency [6], thus by choosing different values of ns , ε_r can be estimated as the function of the lateral position x . Here two different values of ns (50 and 100) are used to fit the obtained strain distribution across the GO edge (Fig. 4.8). It can be seen that the ns value in this range fits in the obtained strain, though the data points are scattered. This ns value is higher than that obtained on monolayer graphene [6], demonstrating a stronger interface for GO [48]. The strain drops sharply at the GO edge, from which the ‘critical length’ (Chapter 1) can be estimated as $\sim 2 \mu\text{m}$, lower than that of pristine graphene, again implies better stress transfer efficiency in this situation [6, 10]. It should be pointed out, however, that the real value of ‘critical length’ may be even smaller, but due to the resolution of the Raman laser spot (around $1\sim 2 \mu\text{m}$, as discussed in Chapter 3), and the poorly resolved GO edge. Further effort is still in need for a clearer observation of the strain distribution from the edge of a deformed GO flake.

4.4 Conclusions

This work presents a method to monitor the deformation mechanics of monolayer GO using Raman spectroscopy. It has been demonstrated that the stress/strain sensitive Raman D band undergoes downshift with tensile strain, similar to what was found previously on graphene, however the value of $d\omega_D/d\varepsilon$ is just 1/2~1/3 of the value of the monolayer graphene, possibly due to the structural distortion of the GO basal plane during oxidation. The measured $d\omega_D/d\varepsilon$ has been used to follow the deformation of monolayer GO flake so that the strain distribution of the GO flake can be mapped, indicating a better stress transfer efficiency of GO compared to that of graphene. Additionally, the measured $d\omega_D/d\varepsilon$ may also be used to estimate the effective modulus of GO in nanocomposites, as will be shown in Chapter 7.

References

1. Young, R. J.; Kinloch, I. A.; Gong, L.; Novoselov, K. S., The Mechanics of Graphene Nanocomposites: A Review. *Composites Science and Technology* **2012**, 72, 1459-1476.
2. Dikin, D. A.; Stankovich, S.; Zimney, E. J.; Piner, R. D.; Dommett, G. H. B.; Evmenenko, G.; Nguyen, S. T.; Ruoff, R. S., Preparation and Characterization of Graphene Oxide Paper. *Nature* **2007**, 448, 457-460.
3. Suk, J. W.; Piner, R. D.; An, J.; Ruoff, R. S., Mechanical Properties of Monolayer Graphene Oxide. *ACS Nano* **2010**, 4, 6557-6564.
4. Lee, C.; Wei, X.; Kysar, J. W.; Hone, J., Measurement of the Elastic Properties and Intrinsic Strength of Monolayer Graphene. *Science* **2008**, 321, 385-388.
5. Young, R. J.; Gong, L.; Kinloch, I. A.; Riaz, I.; Jalil, R.; Novoselov, K. S., Strain Mapping in a Graphene Monolayer Nanocomposite. *ACS Nano* **2011**, 5, 3079-3084.
6. Gong, L.; Kinloch, I. A.; Young, R. J.; Riaz, I.; Jalil, R.; Novoselov, K. S., Interfacial Stress Transfer in a Graphene Monolayer Nanocomposite. *Advanced Materials* **2010**, 22, 2694-2697.
7. Yu, T.; Ni, Z.; Du, C.; You, Y.; Wang, Y.; Shen, Z., Raman Mapping Investigation of Graphene on Transparent Flexible Substrate: The Strain Effect. *The Journal of Physical Chemistry C* **2008**, 112, 12602-12605.
8. Huang, M.; Yan, H.; Chen, C.; Song, D.; Heinz, T. F.; Hone, J., Phonon Softening and Crystallographic Orientation of Strained Graphene Studied by Raman Spectroscopy. *Proceedings of the National Academy of Sciences* **2009**, 106, 7304-7308.
9. Mohiuddin, T. M. G.; Lombardo, A.; Nair, R. R.; Bonetti, A.; Savini, G.; Jalil, R.; Bonini, N.; Basko, D. M.; Galiotis, C.; Marzari, N.; Novoselov, K. S.; Geim, A. K.; Ferrari, A. C., Uniaxial Strain in Graphene by Raman

- Spectroscopy: G Peak Splitting, Grüneisen Parameters, and Sample Orientation. *Physical Review B* **2009**, 79, 205433.
10. Jiang, T.; Huang, R.; Zhu, Y., Interfacial Sliding and Buckling of Monolayer Graphene on a Stretchable Substrate. *Advanced Functional Materials* **2014**, 24, 396-402.
 11. Tan, P. H.; Han, W. P.; Zhao, W. J.; Wu, Z. H.; Chang, K.; Wang, H.; Wang, Y. F.; Bonini, N.; Marzari, N.; Pugno, N.; Savini, G.; Lombardo, A.; Ferrari, A. C., The Shear Mode of Multilayer Graphene. *Nature Materials* **2012**, 11, 294-300.
 12. Gong, L.; Young, R. J.; Kinloch, I. A.; Riaz, I.; Jalil, R.; Novoselov, K. S., Optimizing the Reinforcement of Polymer-Based Nanocomposites by Graphene. *ACS Nano* **2012**, 6, 2086-2095.
 13. Gong, L.; Young, R. J.; Kinloch, I. A.; Haigh, S. J.; Warner, J. H.; Hinks, J. A.; Xu, Z.; Li, L.; Ding, F.; Riaz, I.; Jalil, R.; Novoselov, K. S., Reversible Loss of Bernal Stacking During the Deformation of Few-Layer Graphene in Nanocomposites. *ACS Nano* **2013**, 7, 7287-7294.
 14. Xu, Y.; Hong, W.; Bai, H.; Li, C.; Shi, G., Strong and Ductile Poly(Vinyl Alcohol)/Graphene Oxide Composite Films with a Layered Structure. *Carbon* **2009**, 47, 3538-3543.
 15. Liang, J.; Huang, Y.; Zhang, L.; Wang, Y.; Ma, Y.; Guo, T.; Chen, Y., Molecular-Level Dispersion of Graphene into Poly(Vinyl Alcohol) and Effective Reinforcement of Their Nanocomposites. *Advanced Functional Materials* **2009**, 19, 2297-2302.
 16. Kuilla, T.; Bhadra, S.; Yao, D.; Kim, N. H.; Bose, S.; Lee, J. H., Recent Advances in Graphene Based Polymer Composites. *Progress in Polymer Science* **2010**, 35, 1350-1375.
 17. Gao, Y.; Liu, L.-Q.; Zu, S.-Z.; Peng, K.; Zhou, D.; Han, B.-H.; Zhang, Z., The Effect of Interlayer Adhesion on the Mechanical Behaviors of Macroscopic Graphene Oxide Papers. *ACS Nano* **2011**, 5, 2134-2141.
 18. Jang, H.-K.; Kim, H.-I.; Dodge, T.; Sun, P.; Zhu, H.; Nam, J.-D.; Suhr, J., Interfacial Shear Strength of Reduced Graphene Oxide Polymer Composites. *Carbon* **2014**, 77, 390-397.
 19. Wang, L.-F.; Ma, T.-B.; Hu, Y.-Z.; Wang, H., Atomic-Scale Friction in Graphene Oxide: An Interfacial Interaction Perspective from First-Principles Calculations. *Physical Review B* **2012**, 86, 125436.
 20. Wang, M. C.; Lai, Z. B.; Galpaya, D.; Yan, C.; Hu, N.; Zhou, L. M., Atomistic Simulation of Surface Functionalization on the Interfacial Properties of Graphene-Polymer Nanocomposites. *Journal of Applied Physics* **2014**, 115, 123520-6.
 21. Wang, C.; Frogley, M. D.; Cinque, G.; Liu, L.-Q.; Barber, A. H., Deformation and Failure Mechanisms in Graphene Oxide Paper Using in Situ Nanomechanical Tensile Testing. *Carbon* **2013**, 63, 471-477.
 22. Hummers, W. S.; Offeman, R. E., Preparation of Graphitic Oxide. *Journal of the American Chemical Society* **1958**, 80, 1339-1339.
 23. Xu, Y.; Sheng, K.; Li, C.; Shi, G., Self-Assembled Graphene Hydrogel via a One-Step Hydrothermal Process. *ACS Nano* **2010**, 4, 4324-4330.
 24. Deng, L.; Eichhorn, S. J.; Kao, C.-C.; Young, R. J., The Effective Young's Modulus of Carbon Nanotubes in Composites. *ACS Applied Materials & Interfaces* **2011**, 3, 433-440.

25. Stankovich, S.; Dikin, D. A.; Dommett, G. H. B.; Kohlhaas, K. M.; Zimney, E. J.; Stach, E. A.; Piner, R. D.; Nguyen, S. T.; Ruoff, R. S., Graphene-Based Composite Materials. *Nature* **2006**, 442, 282-286.
26. Everall, N. J.; Lumsdon, J.; Christopher, D. J., The Effect of Laser-Induced Heating Upon the Vibrational Raman Spectra of Graphites and Carbon Fibres. *Carbon* **1991**, 29, 133-137.
27. Zhou, Y.; Bao, Q.; Varghese, B.; Tang, L. A. L.; Tan, C. K.; Sow, C.-H.; Loh, K. P., Microstructuring of Graphene Oxide Nanosheets Using Direct Laser Writing. *Advanced Materials* **2010**, 22, 67-71.
28. Wei, Z.; Wang, D.; Kim, S.; Kim, S.-Y.; Hu, Y.; Yakes, M. K.; Laracuate, A. R.; Dai, Z.; Marder, S. R.; Berger, C.; King, W. P.; de Heer, W. A.; Sheehan, P. E.; Riedo, E., Nanoscale Tunable Reduction of Graphene Oxide for Graphene Electronics. *Science* **2010**, 328, 1373-1376.
29. Gengler, R. Y. N.; Badali, D. S.; Zhang, D.; Dimos, K.; Spyrou, K.; Gournis, D.; Miller, R. J. D., Revealing the Ultrafast Process Behind the Photoreduction of Graphene Oxide. *Nature Communications* **2013**, 4.
30. Stankovich, S.; Dikin, D. A.; Piner, R. D.; Kohlhaas, K. A.; Kleinhammes, A.; Jia, Y.; Wu, Y.; Nguyen, S. T.; Ruoff, R. S., Synthesis of Graphene-Based Nanosheets via Chemical Reduction of Exfoliated Graphite Oxide. *Carbon* **2007**, 45, 1558-1565.
31. Yang, D.; Velamakanni, A.; Bozoklu, G.; Park, S.; Stoller, M.; Piner, R. D.; Stankovich, S.; Jung, I.; Field, D. A.; Ventrice Jr, C. A.; Ruoff, R. S., Chemical Analysis of Graphene Oxide Films after Heat and Chemical Treatments by X-Ray Photoelectron and Micro-Raman Spectroscopy. *Carbon* **2009**, 47, 145-152.
32. Tuinstra, F.; Koenig, J. L., Raman Spectrum of Graphite. *The Journal of Chemical Physics* **1970**, 53, 1126-1130.
33. Ferrari, A. C.; Robertson, J., Interpretation of Raman Spectra of Disordered and Amorphous Carbon. *Physical Review B* **2000**, 61, 14095-14107.
34. Ferrari, A. C.; Meyer, J. C.; Scardaci, V.; Casiraghi, C.; Lazzeri, M.; Mauri, F.; Piscanec, S.; Jiang, D.; Novoselov, K. S.; Roth, S.; Geim, A. K., Raman Spectrum of Graphene and Graphene Layers. *Physical Review Letters* **2006**, 97, 187401.
35. Moon, I. K.; Lee, J.; Ruoff, R. S.; Lee, H., Reduced Graphene Oxide by Chemical Graphitization. *Nature Communications* **2010**, 1, 73.
36. Wang, H.; Robinson, J. T.; Li, X.; Dai, H., Solvothermal Reduction of Chemically Exfoliated Graphene Sheets. *Journal of the American Chemical Society* **2009**, 131, 9910-9911.
37. Robertson, J., Amorphous Carbon. *Advances in Physics* **1986**, 35, 317-374.
38. Cronin, S. B.; Swan, A. K.; Ünlü, M. S.; Goldberg, B. B.; Dresselhaus, M. S.; Tinkham, M., Measuring the Uniaxial Strain of Individual Single-Wall Carbon Nanotubes: Resonance Raman Spectra of Atomic-Force-Microscope Modified Single-Wall Nanotubes. *Physical Review Letters* **2004**, 93, 167401.
39. Ferralis, N., Probing Mechanical Properties of Graphene with Raman Spectroscopy. *Journal of Materials Science* **2010**, 45, 5135-5149.
40. Grimvall, G., Phonons in Real Crystals: Anharmonic Effects. In *Thermophysical Properties of Materials*, Elsevier Science B.V.: Amsterdam, 1999; pp 136-152.

41. Lu, H.; Zhang, X.; Knauss, W. G., Uniaxial, Shear, and Poisson Relaxation and Their Conversion to Bulk Relaxation: Studies on Poly(Methyl Methacrylate). *Polymer Engineering & Science* **1997**, 37, 1053-1064.
42. Kudin, K. N.; Scuseria, G. E.; Yakobson, B. I., C₂F, BN, and C Nanoshell Elasticity from *Ab Initio* Computations. *Physical Review B* **2001**, 64, 235406.
43. Frank, O.; Mohr, M.; Maultzsch, J.; Thomsen, C.; Riaz, I.; Jalil, R.; Novoselov, K. S.; Tsoukleri, G.; Parthenios, J.; Papagelis, K.; Kavan, L.; Galiotis, C., Raman 2D-Band Splitting in Graphene: Theory and Experiment. *ACS Nano* **2011**, 5, 2231-2239.
44. Paci, J. T.; Belytschko, T.; Schatz, G. C., Computational Studies of the Structure, Behavior Upon Heating, and Mechanical Properties of Graphite Oxide. *The Journal of Physical Chemistry C* **2007**, 111, 18099-18111.
45. Liu, L.; Zhang, J.; Zhao, J.; Liu, F., Mechanical Properties of Graphene Oxides. *Nanoscale* **2012**, 4, 5910-5916.
46. Pandey, K. K.; Poswal, H. K.; Deo, M. N.; Sharma, S. M.; Vasu, K. S.; Sood, A. K., A Structural and Spectroscopic Investigation of Reduced Graphene Oxide under High Pressure. *Carbon* **2014**, 70, 199-206.
47. Cox, H. L., The Elasticity and Strength of Paper and Other Fibrous Materials. *British Journal of Applied Physics* **1952**, 3, 72.
48. Terrones, M.; Martín, O.; González, M.; Pozuelo, J.; Serrano, B.; Cabanelas, J. C.; Vega-Díaz, S. M.; Baselga, J., Interphases in Graphene Polymer-Based Nanocomposites: Achievements and Challenges. *Advanced Materials* **2011**, 23, 5302-5310.

Chapter 5 Quantitative Determination of the Spatial Orientation of Graphene by Polarized Raman Spectroscopy*

5.1 Introduction

The spatial orientation of graphene is of great importance because of its two-dimensional geometry, and properties such as high strength [1]. The technique of Raman spectroscopy has been used extensively to study the orientation of graphene. However, the studies so far have only dealt with the in-plane orientation (crystallographic orientation) with the Raman laser beam aligned perpendicular to the surface of graphene [2-5]. Although Raman spectra have been obtained from transverse section of multilayer graphene or graphite crystals for the orientational analysis [6-8], there has been no systematic study to determine the spatial orientation of monolayer graphene, and also taking into account its surface roughness.

In this present study, two particular types of specimen are investigated, a graphene monolayer grown by chemical vapour deposition (CVD) on the surface of copper foil (graphene-Cu) and secondly CVD graphene grown on copper and then transferred onto a polyester film (graphene-PET). Similar to that of graphite, the intensity of Raman 2D band (I_{2D}) is found to vary as approximately the 4th power of the cosine of the angle between the axis of laser polarization and the plane of graphene when the direction of laser propagation is parallel to the graphene sheet. The approach of Liu and Kumar [9] based on carbon nanotubes has been modified for the quantitative analysis of the spatial orientation of graphene monolayers without any prior knowledge of the orientation distribution function (ODF). The ODF obtained is in agreement with level of surface roughness revealed by atomic force microscope (AFM), showing how the Raman technique may be used to

* This chapter is based on a paper, 'Quantitative Determination of the Spatial Orientation of Graphene by Polarized Raman Spectroscopy', *Carbon* (2015); DOI: 10.1016/j.carbon.2015.02.072

quantify the spatial orientation of graphene. It is also shown how the technique can be employed to quantify the orientation of graphene in highly-ordered pyrolytic graphite (HOPG) and graphene paper.

5.2 Experimental

5.2.1 Preparation

The graphene-Cu was kindly supplied by Dr. Neil Wilson, University of Warwick [10]. It was grown via low-pressure chemical vapour deposition on copper foils (99.999% purity, 0.025 mm thick, Alfa Aesar product number 10950) [11, 12], which were cleaned in acetone and isopropanol prior to use. The foils were heated from room temperature to 1000 °C in a tube furnace with a 1 inch quartz worktube under a hydrogen flow of 2 standard cubic centimetres per minute (sccm), with a resultant pressure of 10^{-2} mbar. The hydrogen flow was maintained constant throughout the growth process. After annealing for 20 minutes at 1000 °C, 35 sccm of methane was introduced for a further 10 minutes [10]. The methane flow rate was reduced to 5 sccm while the sample was cooled to 600 °C, after which, the gas flow was stopped.

The graphene-PET specimen was supplied by Bluestone Global Tech, USA. Since it is a commercial material full details of its manufacture are confidential but some information has been kindly supplied by Bluestone. The graphene was grown on copper using a conventional methane feedstock and it was then transferred onto PET film.

HOPG (43834, 10×10×1mm) was supplied by Alfa Aesar. The graphene paper was kindly provided by A.P.A. Raju, which was prepared by the direct exfoliation of graphite (Grade 2369, Branwell Graphite Ltd., UK) in N-methyl-2-pyrrolidone (NMP) (M79603, Sigma-Aldrich) in a low power ultrasonic bath (32 W, Elmasonic P70H) for 24 hours [13, 14]. The resulting suspension was centrifuged (Thermo Scientific Sorvall LEGEND XTR) for 20 min at ~4000 g following vacuum filtration of the supernatant on 47 mm anodisc membranes (pore size 0.1 µm) to form graphene paper. It was then dried overnight at 80 °C in a vacuum oven.

For the polarization tests in X-direction (transverse to the graphene planes), all samples were embedded transversely using commercial polyester-based mounting plastic. The graphene-Cu and graphene-PET specimens were prepared by either cutting and polishing or microtome sectioning to expose the graphene edges. The HOPG and graphene paper specimens were cut and polished to again expose the graphene edges.

5.2.2 Characterization

Optical images of the transverse sections of the specimens were obtained using an Olympus BH Microscope. Scanning electron microscope (SEM) images were obtained for the graphene-Cu using a Zeiss SUPRA 55-VP FEGSEM and a Philips XL 30 FEG microscope for the HOPG and graphene paper. Transmission electron microscope (TEM) images of the graphene removed from the graphene-Cu were obtained at 200 kV using a JEOL 2000FX with a Gatan Orius camera. AFM images were obtained from the surfaces of the graphene on both the graphene-Cu and graphene-PET using a Dimension 3100 AFM (Bruker) in the tapping mode in conjunction with a ‘TESPA’ probe (Bruker). The waviness of the graphene on the substrates was determined in terms of the distributions of slopes determined from the AFM height scans using Gwyddion AFM analysis software (gwyddion.net).

Polarized Raman spectra were obtained using Renishaw 1000/2000 spectrometers with a HeNe laser ($\lambda = 633$ nm) for the graphene-Cu, HOPG and graphene paper and an Argon ion laser ($\lambda = 514$ nm) for graphene-PET, both with a laser spot around 1~2 μm in diameter, using the so-called ‘VV’ polarization configuration, where the polarization of incident and scattered radiation are parallel to each other. Fig. 5.1 defines the Cartesian coordinate system with X, Y and Z axes used to describe the experimental arrangement in which the CVD graphene specimens were examined. The spectra were obtained, first of all, from the graphene with the laser beam parallel to the Z-axis which is perpendicular to the graphene surface. Spectra were then obtained from sections of the specimens with the direction of laser propagation along the X-axis parallel to the plane of the graphene. With the polarization configurations fixed, Raman spectra were then obtained with the specimens rotated to different angles, Φ_X and Φ_Z in steps of 10° , for the laser beam parallel to X and Z directions.

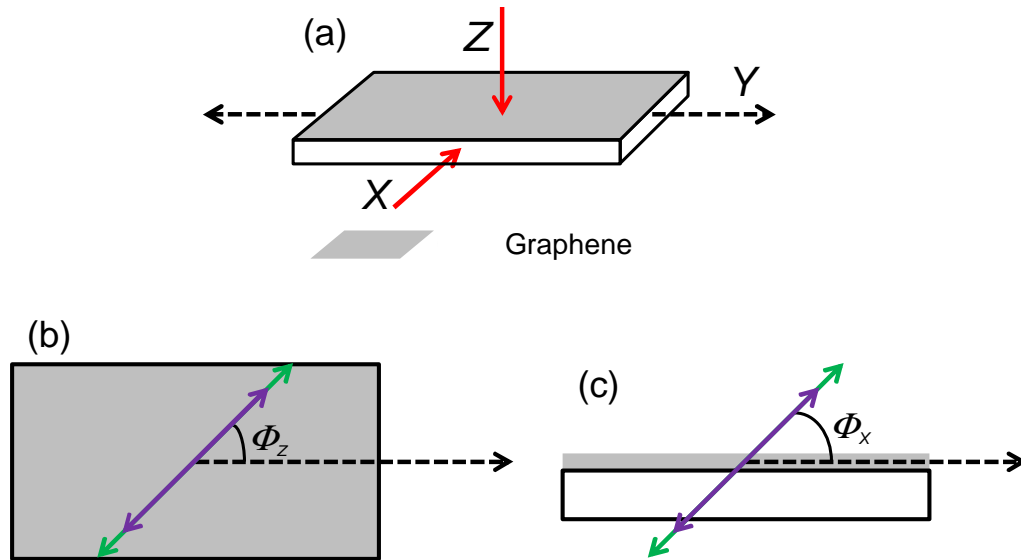


Figure 5.1 Schematic illustration of the relationships between the specimen geometries and polarization arrangements used in the Raman spectroscopic analysis. (a) The specimen in the defined Cartesian coordinate system, and the VV polarization arrangement with the laser beam parallel to the (b) Z or (c) X axis. The red arrows represent the direction of laser propagation and the purple and green arrows represent the directions of polarization of the incident radiation and scattered radiation, respectively. (The arrows with the broken line represent the Y direction)

5.3 Results and Discussion

5.3.1 Graphene-Cu

The graphene on the graphene-Cu was shown by a combination of SEM and TEM to consist predominantly of single layer material containing a few wrinkles, with evidence of small amounts of bilayer material (Fig. 5.2). Fig. 5.2(a) is a typical SEM image of the CVD graphene grown on copper foils. The surface is mostly uniform suggesting predominantly single layer graphene with bright patches indicating some remaining contamination. Some small darker regions indicate the presence of small regions of bilayer graphene and wrinkles in the graphene film. The graphene layer was transferred from the copper foil to a TEM support grid as described previously [10]. Fig. 5.2(b) shows a typical TEM bright field image. The darker lacy support can be seen along with an almost uniform coverage of graphene, with some contrast changes from wrinkles and contamination from the transfer process. Fig. 5.2(c)

shows a typical diffraction pattern from a region inside the lacy support. The pattern shows a hexagonal array of spots with spacing consistent with graphene. A line profile to compare the first order spots with the second order spots (Fig. 5.2(d)) shows comparable intensity, indicating the presence of a monolayer.

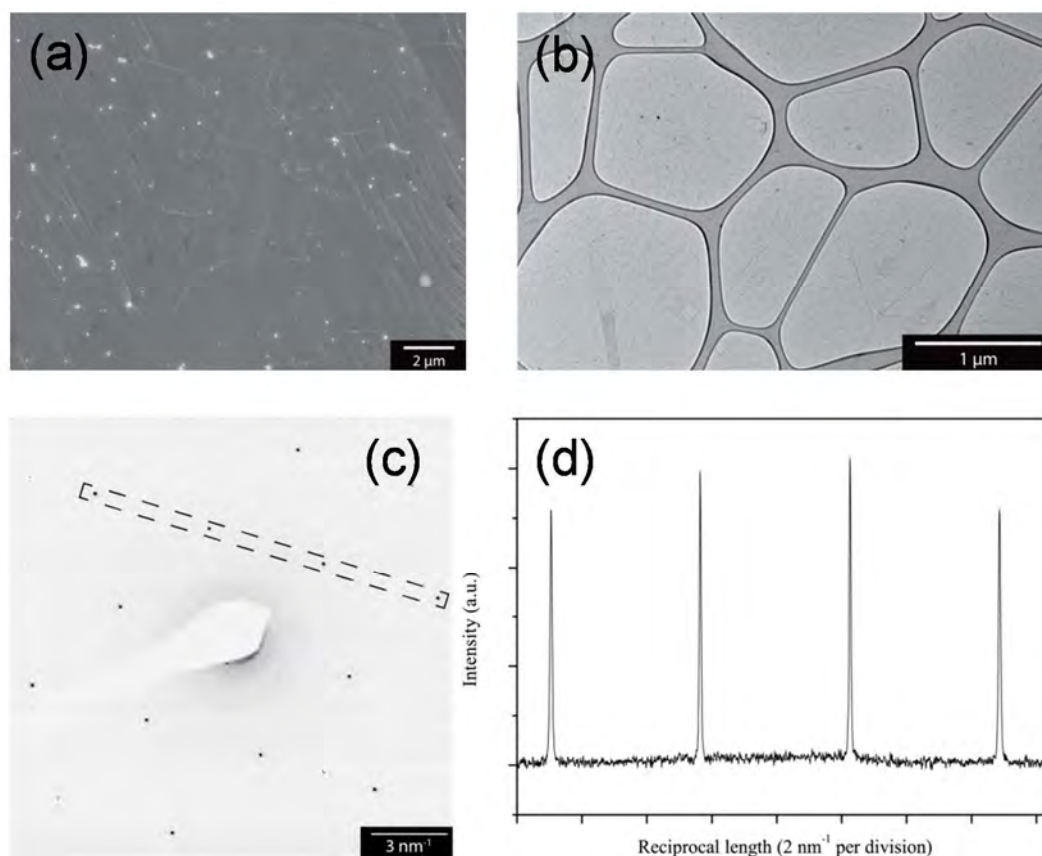


Figure 5.2 (a) SEM image of the CVD graphene on copper. Bright points on the surface are contaminants remaining after growth. (b) Bright field TEM of graphene after transfer to lacy carbon grid. (c) TEM diffraction pattern and (d) line profile of the diffraction intensity from the marked area in (c). The inner spots are of comparable intensity to the outer spots indicating single-layer graphene. (Courtesy of A. Marsden, University of Warwick)

Fig. 5.3 shows the results for the polarized Raman analysis of the graphene-Cu. An optical micrograph of a microtome sectioned transverse section of the copper foil is shown in Fig. 5.3(a) along with a schematic diagram of the mounted specimen in Fig. 5.3(b). The Raman spectrum from the graphene-Cu with the direction of propagation of the laser beam parallel to the Z-axis (perpendicular to the surface of the foil) is shown in Fig. 5.3(c) and is a typical spectrum of CVD-grown monolayer graphene

[11]. The G band in the spectrum, located at around 1580 cm^{-1} , corresponds to the E_{2g} phonon at the Brillouin zone centre (Γ point) [15]. The strong 2D band at around 2650 cm^{-1} (also known as the G' band) results from the two phonons with opposite momentum in the highest optical branch near the K point [16]. The D band centred at around 1300 cm^{-1} and the D' band at around 1620 cm^{-1} originate from inter- and intra-valley scattering at the Brillouin zone boundary [17], indicating the presence of defects in the graphene. The high ratio of the intensity of Raman 2D band (I_{2D}) to the intensity of Raman G band (I_G) [18], as well as the sharp 2D band with a full width at half maximum of $\sim 35\text{ cm}^{-1}$ are both characteristic of monolayer graphene [19, 20].

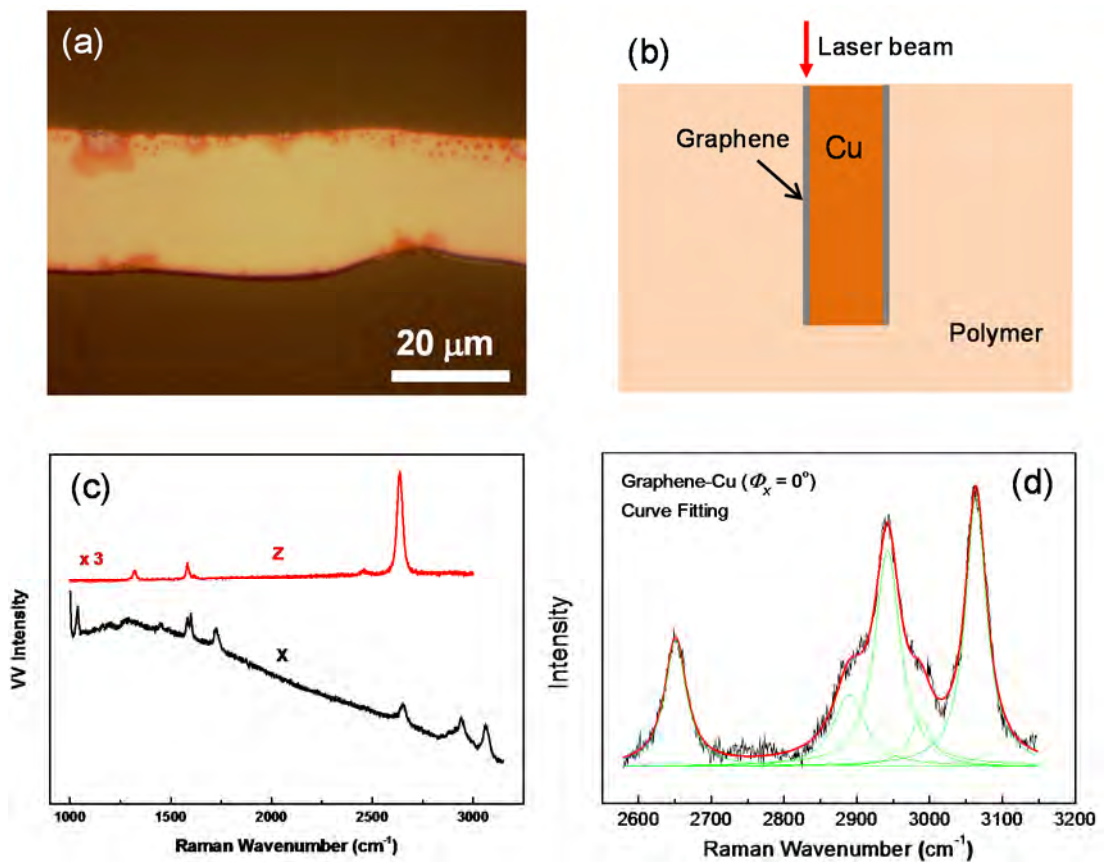


Figure 5.3 (a) Optical micrograph of a microtomed transverse section of the copper foil. (b) Schematic diagram of the transverse section of the copper foil mounted in a polymer resin. (c) Raman spectrum of the graphene-Cu obtained with the laser beam parallel to the Z-axis ($\Phi_Z = 0^\circ$) and the X-axis ($\Phi_X = 0^\circ$), respectively. (d) Fitting procedure employed to determine the band intensity. The experimental spectrum, fitting for the spectrum and fitting for individual band are shown with black, red and green lines, respectively.

Fig. 5.3(c) also shows the Raman spectrum obtained with the direction of laser propagation parallel to X and with $\Phi_X = 0^\circ$. In this case the 2D band is much weaker than with the direction of laser propagation parallel to Z but is still observable, similar to the result reported recently from a transverse section of graphene [21]. The G and D bands from the graphene overlap with the Raman bands from the polyester-based mounting polymer. The laser beam is around $2\ \mu\text{m}$ in diameter so most of the light scattered will be from the mounting resin rather than the $0.34\ \text{nm}$ thick section of the graphene monolayer, leading to a high fluorescence background. However, the very strong resonant Raman scattering from graphene monolayer enables its Raman spectrum still to be resolvable [16]. Fig. 5.3(d) shows the procedure employed to measure the I_{2D} . In this case the 2D band is well separated from the Raman bands from the polymer-based mounting material which are found in the range $2800\ \text{cm}^{-1}$ to $3100\ \text{cm}^{-1}$.

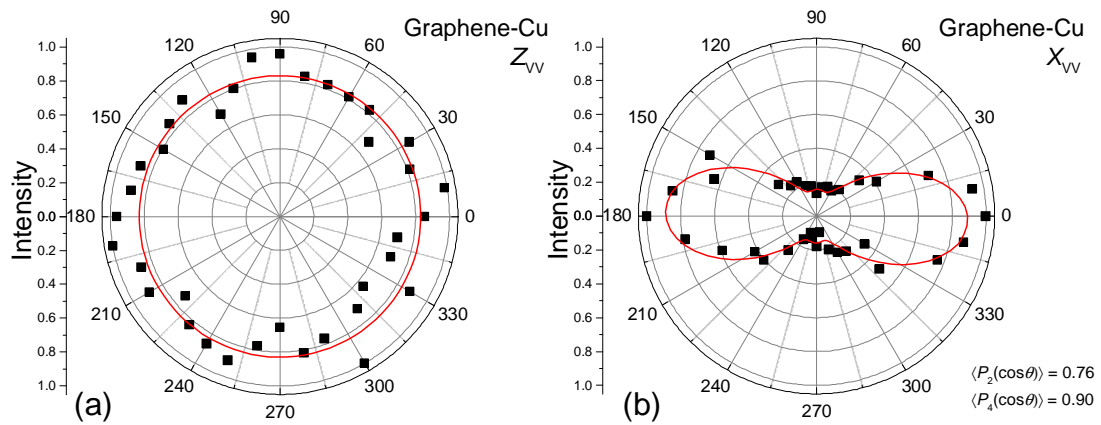


Figure 5.4 (a) I_{2D} variation with the laser beam parallel to the Z -axis as a function of the angle Φ_Z measured on one point. (b) I_{2D} variation with the laser beam parallel to the X -axis as a function of the angle Φ_X measured on one point. The red lines are the average value in (a) and curve fitting using Eq. 5.10 in (b), for the data points.

Finally, the dependence of I_{2D} upon the polarization angle in both axes was determined. Fig. 5.4(a) shows that in the case of the direction of laser propagation parallel to the Z axis (i.e. perpendicular to the surface of the graphene) I_{2D} is independent of Φ_Z as expected [2, 18]. In contrast in the transverse section, with the direction of laser propagation parallel to the X axis, there is strong dependence of I_{2D}

upon the angle Φ_X . It is the most intense when $\Phi_X = 0^\circ$ and 180° , and is minimum when $\Phi_X = 90^\circ$ and 270° (Fig. 5.4(b)).

While I_{2D} varies for the graphene-Cu upon rotating in X direction, the intensity of the Raman band from the mounting polymer ($\sim 3060 \text{ cm}^{-1}$ in Fig. 5.3(d)) does not change (Fig. 5.5). The same behaviour was found when the mounting polymer alone was tested in a similar way.

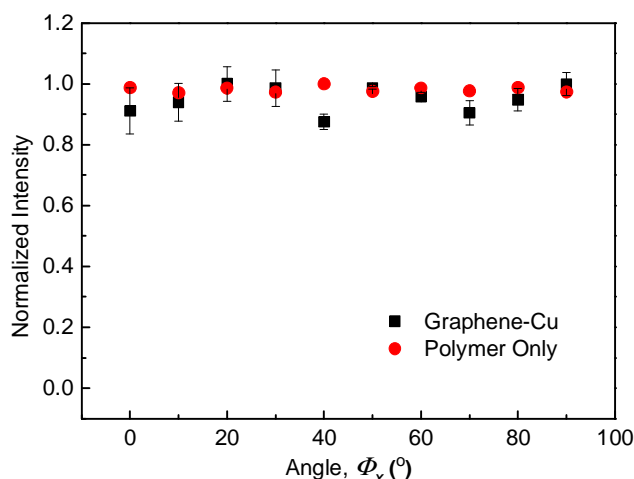


Figure 5.5 The intensity of the polymer band at $\sim 3060 \text{ cm}^{-1}$ as the function of Φ_X obtained along with graphene-Cu and from another individual polarized Raman spectroscopy test on the mounting polymer only.

5.3.2 Graphene-PET

A similar analysis was undertaken upon the monolayer graphene-PET as shown in Fig. 5.6. In this case the graphene 2D band was found to partially overlap with a PET band around 2615 cm^{-1} when excited with the 633 nm laser, so a laser with $\lambda = 514 \text{ nm}$ was used to move the 2D band to a higher wavenumber. The Raman scattering from the underlying PET film is strong so that I_{2D} is relatively weak (Figs. 5.6(c) and (d)) even for the spectrum obtained with the direction of propagation of the laser beam parallel to the Z axis (perpendicular to the surface of the film), nevertheless it can still be clearly resolved, as shown in Fig. 5.6(e), the fitting procedure used to determine I_{2D} . The difference in the 2D band position for the graphene monolayers between the graphene-Cu and graphene-PET is the result of different laser excitations employed for the two systems (633 nm and 514 nm respectively).

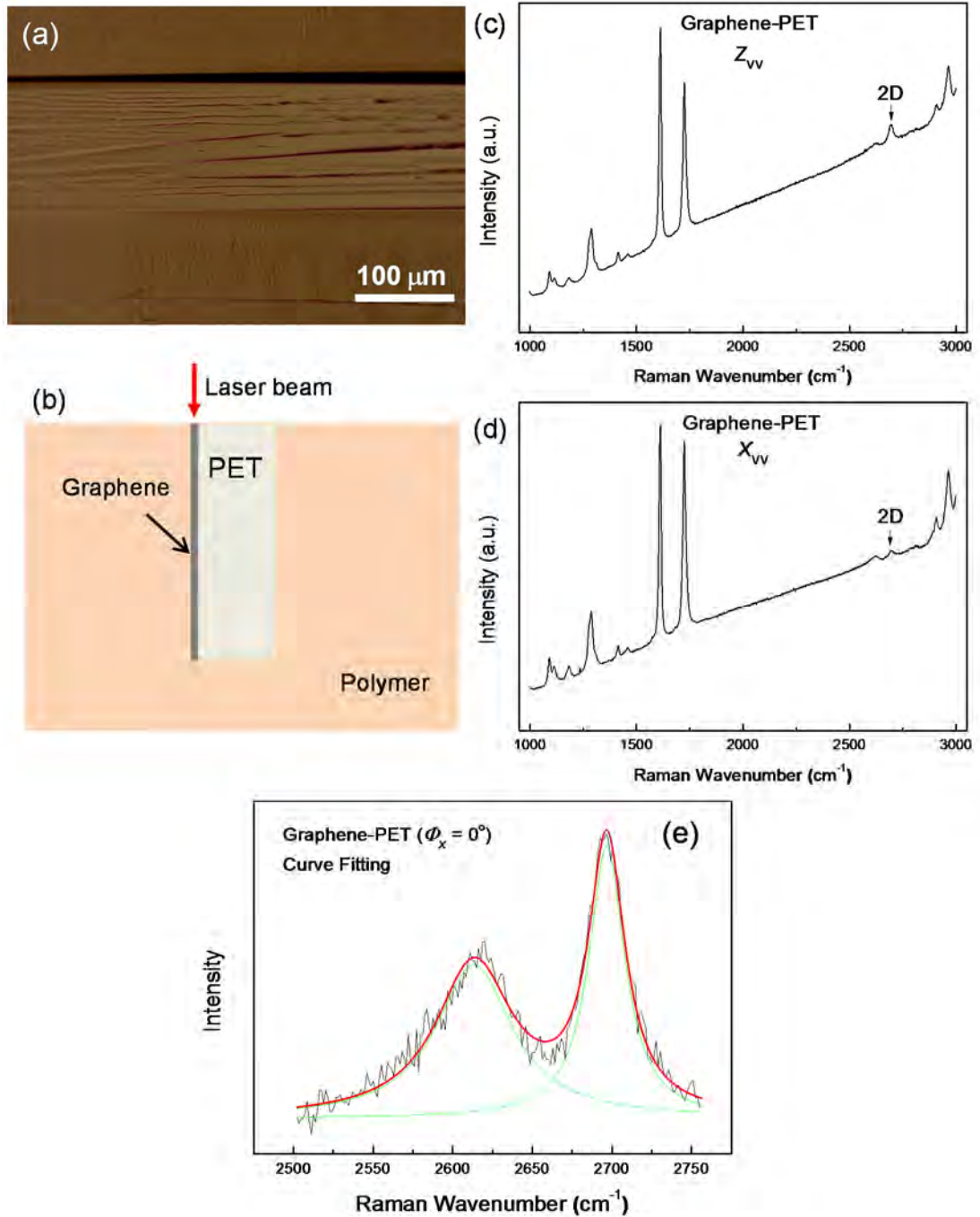


Figure 5.6 (a) Optical micrograph of a microtomed transverse section of the PET film. (b) Schematic diagram of the transverse section of the PET film mounted in a polymer resin. (c) Raman spectrum of the graphene-PET obtained with the laser beam parallel to the Z-axis ($\Phi_Z = 0^\circ$). (d) Raman spectrum of the graphene-PET obtained with the laser beam parallel to the X-axis ($\Phi_X = 0^\circ$). (e) Fitting procedure employed to determine the band intensity. The experimental spectrum, fitting for the spectrum and fitting for individual band are shown with black, red and green lines, respectively.

I_{2D} is found to be independent of the angle Φ_Z (Fig. 5.7(a)), similar to the behaviour of the graphene-Cu shown in Fig. 5.4(a). I_{2D} is relatively weak in the transverse section of the graphene-PET but can still be resolved, that a strong angular dependence of I_{2D} upon Φ_X is again obtained for the transverse section (Fig. 5.7(b)) although it is difficult to resolve the 2D band from the background scattering above $\Phi_X \sim 60^\circ$.

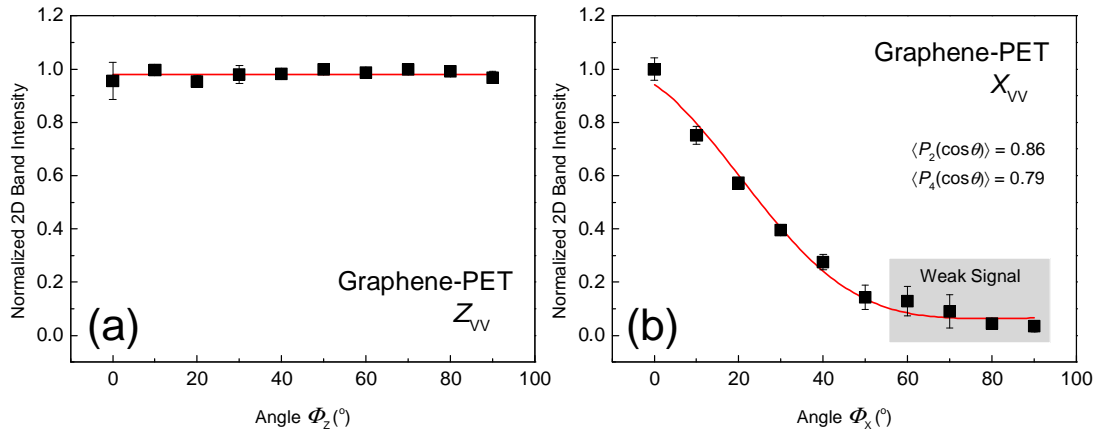


Figure 5.7 (a) I_{2D} variation with the laser beam parallel to the Z-axis as a function of the angle Φ_Z . (f) I_{2D} variation with the laser beam parallel to the X-axis as a function of the angle Φ_X . The red lines are the average value in (a) and curve fitting using Eq. 5.10 in (b), for the data points. The data were averaged for three measurements on one point, respectively.

Fig. 5.8 is the intensity of the PET band at $\sim 2615 \text{ cm}^{-1}$ as the function of Φ_X obtained and another individual polarized Raman spectroscopy test on PET only. Unlike the graphene-Cu, when the specimens were rotated in X direction, the intensity of the PET Raman band in both experiments changed due to its high degree of molecular orientation (Fig. 5.8) [22].

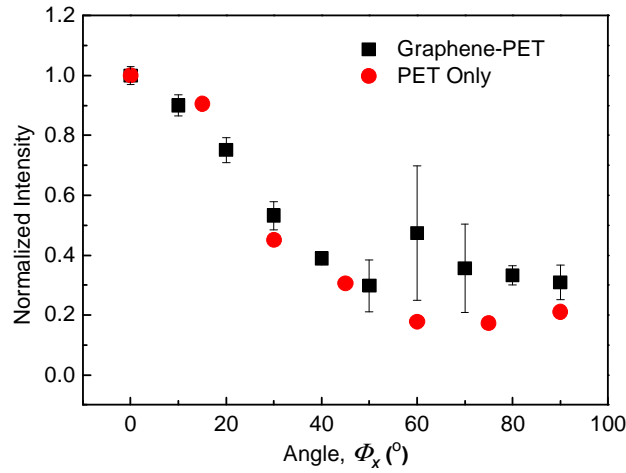


Figure 5.8 The intensity of the PET band at around 2615 cm^{-1} as the function of Φ_x obtained along with graphene-PET and from another individual polarized Raman spectroscopy test on the PET only.

Previous studies undertaken upon transverse sections of multilayer graphene or graphite crystals [6-8] have found that the variation of Raman band intensities with Φ for single crystal graphite with a laser beam in the X direction (parallel to the graphene planes) with VV polarization should be of the form:

$$I_{\text{sample}}^{\text{VV}}(\Phi) \propto \cos^4 \Phi \quad (5.1)$$

It can be seen from Figs. 5.4(b) and 5.7(b) that although the data show relationships of this form, the equation is not followed exactly since the intensity does not fall to zero at $\Phi = 90^\circ$. Eq. 5.1 can be modified to give a better fit to the experimental data by fitting to an equation of the form:

$$I_{\text{sample}}^{\text{VV}}(\Phi) \propto C_1 \cos^4 \Phi + C_2 \quad (5.2)$$

where C_1 and C_2 are constants such that $C_1 + C_2 = 1$. A similar relationship was used by Gupta et al. [2] for the intensity variation of the D band with laser polarization angle relative to the edge of a graphene flake to take into account the non-uniformity of the edge. Although it is clear that the parameter C_2 will be related to any non-uniform alignment of the graphene, it has no physical significance, meaning that it is impossible to characterize the orientation of the graphene quantitatively using this

empirical approach. A more rigorous approach is used to quantify the alignment of the graphene in terms of an ODF.

5.3.3 Spatial Orientation of Graphene

Fig. 5.9(a) describes the spatial orientation of one graphene flake inside a specimen. The local spatial orientation of a graphene sheet is most conveniently defined by the surface normal vector, shown in Fig. 5.9(a) as the z -direction with the graphene in the x,y plane. This is related to the coordinate system of the sample (X,Y,Z) by the Euler angles (θ, ϕ, ξ) as indicated. θ and ϕ are the polar coordinates of z -direction in (X,Y,Z) , and ξ is the rotation angle for graphene. Fig. 5.9(b) is the laboratory coordinates, showing how the specimens were rotated with angle Φ with regard to the laser polarization directions. The incident and scattered light propagate along the X, X' axis whilst the polarization direction of the incident light is in Y' direction and of the analyser is in Y' direction (VV) or Z' direction (VH).

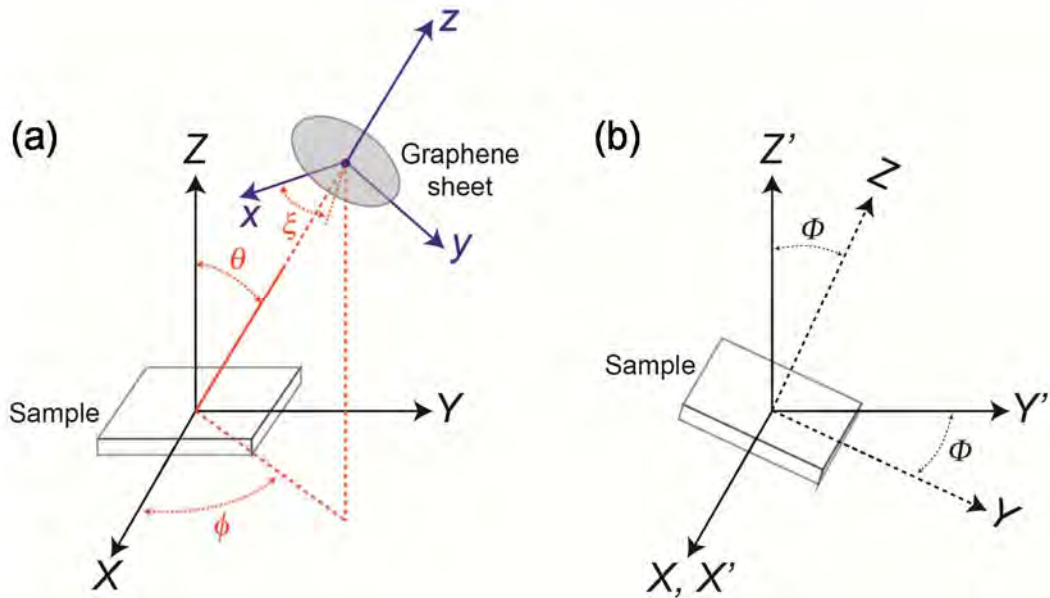


Figure 5.9 Schematic diagram of the local orientation of graphene within the sample and of the sample relative to the experimental polarised Raman spectroscopy measurement parameters. (a) The local coordinate system of the graphene sheet (x,y,z) is related to that of the sample (X,Y,Z) by the Euler angles (θ, ϕ, ξ) . (b) For the polarised Raman spectroscopy measurements described in Fig. 5.1, the incident and scattered light propagate along the X, X' axis whilst the polarization direction of the

incident light is in Y' direction and of the analyser is in Y' direction (VV) or Z' direction (VH). (Courtesy of Dr. N. Wilson, University of Warwick)

The ODF of the surface normal can be written in general as $f_N(\theta, \phi, \xi)$ such that $f_N(\theta, \phi, \xi) \sin \theta d\theta d\phi d\xi$ is the probability of finding an area element of the graphene with surface normal between (θ, ϕ, ξ) and $(\theta + d\theta, \phi + d\phi, \xi + d\xi)$. Due to the in-plane symmetry of graphene, the rotation angle ξ is not considered. The system is greatly simplified when the ODF shows uniaxial symmetry; i.e. when the orientation of the graphene sheets varies uniformly around a common plane (as is the case for the predominantly flat graphene samples studied here). In that case the ODF can be written as $f_N(\theta)$. Following Liu and Kumar [9] and van Gurp [23], we can describe any ODF of this kind in terms of Legendre polynomials:

$$f_N(\theta) = \sum_{i=0}^{\infty} \frac{2i+1}{2} \langle P_i(\cos \theta) \rangle P_i(\cos \theta) \quad (5.3)$$

where $P_i(\cos \theta)$ is the Legendre polynomial of the i th degree and $\langle P_i(\cos \theta) \rangle$ is the average value, given by

$$\langle P_i(\cos \theta) \rangle = \frac{\int_{\theta=0}^{\theta=\pi} P_i(\cos \theta) f_N(\theta) \sin \theta d\theta}{\int_{\theta=0}^{\theta=\pi} f_N(\theta) \sin \theta d\theta} \quad (5.4)$$

The $P_i(\cos \theta)$ are the order parameters. For most non-polar materials $P_i(\cos \theta)$ are only non-zero for even i and polarised Raman spectroscopy can only be used to determine $\langle P_2(\cos \theta) \rangle$ and $\langle P_4(\cos \theta) \rangle$ [9, 24]. The parameter $\langle P_2(\cos \theta) \rangle = (3\langle \cos^2 \theta \rangle - 1)/2$ is more commonly known in polymer and composites science as the Hermans' orientation factor, f [25]. Generally, the larger the values of $\langle P_2(\cos \theta) \rangle$ and $\langle P_4(\cos \theta) \rangle$, the better the orientation. $\langle P_2(\cos \theta) \rangle$ is the primary parameter that contains the fundamental information (mean orientation angle) of graphene [24, 26]. $\langle P_4(\cos \theta) \rangle$ is less meaningful than $\langle P_2(\cos \theta) \rangle$ with regard to the mean orientation but its value can be used to determine and thus reconstruct the full

ODF [26, 27]. For example, generally $\langle P_2(\cos\theta) \rangle = (3\langle \cos^2\theta \rangle - 1)/2 = 0$ means the graphene flakes are randomly aligned where $\langle \cos^2\theta \rangle = 1/3$. However, it fails to describe an extreme situation where all the graphene flakes are oriented along the Z axis at an angle θ where $\cos^2\theta = 1/3$ thus $\langle \cos^2\theta \rangle = 1/3$. In this circumstance, the introduction of $\langle P_4(\cos\theta) \rangle$ is of great importance to characterize the orientation fully.

The polarised Raman scattering intensity is given by [7, 18]:

$$I \propto \sum_i |\vec{e}_s \cdot \alpha_i \cdot \vec{e}_i|^2 \quad (5.5)$$

where \vec{e}_i and \vec{e}_s are the unit vectors in the direction of the polarization of the incident and scattered light, respectively, and α_i is the polarizability tensor [7, 28]. We make the assumption that for 2D band, which is an A_{1g} vibrational mode, $\alpha_{A_{1g}}$ is isotropic within the plane of the graphene and 0 out of the plane since the scattering is due to in-plane phonons [29]. Therefore, in the local (x,y,z) coordinate system, $\alpha_{A_{1g}}$ is given by [30]:

$$\alpha_{A_{1g}} = \begin{pmatrix} 1 & 0 & 0 \\ 0 & 1 & 0 \\ 0 & 0 & 0 \end{pmatrix} \quad (5.6)$$

For the Raman G band, which is an E_{2g} vibrational mode, the polarizability tensor is given as [18, 30]:

$$\alpha_{E_{2g}(1)} = \begin{pmatrix} 1 & 0 & 0 \\ 0 & -1 & 0 \\ 0 & 0 & 0 \end{pmatrix} \quad \text{and} \quad \alpha_{E_{2g}(2)} = \begin{pmatrix} 0 & 1 & 0 \\ 1 & 0 & 0 \\ 0 & 0 & 0 \end{pmatrix} \quad (5.7)$$

Transforming \vec{e}_i (the Y' direction) and \vec{e}_s (either the Y' direction for VV or Z' for VH) (Fig. 5.9(b)) into the (x,y,z) coordinate system we find that the intensity of the Raman scattering from the graphene sheet in VV polarization is

$$I_{\text{gr}}^{\text{VV}}(\Phi) \propto [\cos^2 \phi \cos^2 \Phi + (\cos \theta \cos \Phi \sin \phi - \sin \theta \sin \Phi)^2] \quad (5.8)$$

To calculate the total Raman scattering intensity of the specimen, the intensity from all orientations of graphene must be added, giving

$$I_{\text{sample}}^{\text{VV}}(\Phi) \propto \frac{\int_{\xi=0}^{2\pi} \int_{\phi=0}^{2\pi} \int_{\theta=0}^{\pi} I_{\text{gr}}^{\text{VV}} f_N(\theta) \sin \theta d\theta d\phi d\xi}{\int_{\xi=0}^{2\pi} \int_{\phi=0}^{2\pi} \int_{\theta=0}^{\pi} f_N(\theta) \sin \theta d\theta d\phi d\xi} \quad (5.9)$$

Substituting the definition of the ODF (Eq. 5.3) and Eq. 5.8 into Eq. 5.9 gives the following equation for the Raman scattering intensity of the sample as a function of the polarisation angle Φ relative to the sample:

$$I_{\text{sample}}^{\text{VV}}(\Phi) = I_o \cdot \left\{ \frac{8}{15} + \langle P_2(\cos \theta) \rangle \left(-\frac{16}{21} + \frac{8}{7} \cos^2 \Phi \right) + \langle P_4(\cos \theta) \rangle \left(\frac{8}{35} - \frac{8}{7} \cos^2 \Phi + \cos^4 \Phi \right) \right\} \quad (5.10)$$

where the constant I_o is the amplitude. By fitting Eq. 5.10 to the experimental data, the parameters $\langle P_2(\cos \theta) \rangle$ and $\langle P_4(\cos \theta) \rangle$ can be determined for both specimens (Figs. 5.4(b) and 5.7(b)). Because of the difficulty in determining the exact alignment of graphene in graphene-Cu and graphene-PET specimens, an offset angle was added in the curve fitting and constrained as $[-10^\circ, 10^\circ]$ (it was not added into Eq. 5.10 as it was not considered in the curve fitting of HOPG and graphene paper described later as their alignments can be determined). As explained by van Gurp [23], these parameters are constrained as: $-1/2 \leq \langle P_2(\cos \theta) \rangle \leq 1$,

$$-3/7 \leq \langle P_4(\cos \theta) \rangle \leq 1, \quad \langle P_4(\cos \theta) \rangle \leq \frac{1}{12} (5 \langle P_2(\cos \theta) \rangle + 7), \quad \text{and}$$

$$\langle P_4(\cos \theta) \rangle \geq \frac{1}{18} (35 \langle P_2(\cos \theta) \rangle^2 - 10 \langle P_2(\cos \theta) \rangle - 7). \text{ It is noteworthy that Eq. 5.10 is}$$

applicable to both the E_{2g} mode G band and A_{1g} mode 2D band as identical results are generated regardless the polarizability tensors used in the calculation, so the values of $\langle P_2(\cos \theta) \rangle$ and $\langle P_4(\cos \theta) \rangle$ can be determined using either of the two bands. The E_{2g} mode G band is doubly degenerate, and the $\alpha_{E_{2g}(1)}$ and $\alpha_{E_{2g}(2)}$ tensors

correspond to two different in-plane vibrations with perpendicular directions [31]. In terms of the orientational study of graphene in this work, the G band intensity results from both of the in-plane polarizability tensors, with equivalent importance. Therefore both tensors were used in the calculation and the individual G band intensities were summed after calculation from their tensors using Eq. 5.5. The deduction for the VH polarization configuration shows that, differing from that for the VV polarization, the result for the E_{2g} mode G band (Eq. 5.11) differs from that of the A_{1g} mode 2D band (Eq. 5.12).

$$\text{G: } I_{\text{sample}}^{\text{VH}}(\Phi) = I_o \cdot \left\{ \frac{2}{5} - \frac{2}{7} \langle P_2(\cos \theta) \rangle + \langle P_4(\cos \theta) \rangle \left(-\frac{4}{35} + \cos^2 \Phi - \cos^4 \Phi \right) \right\} \quad (5.11)$$

$$\text{2D: } I_{\text{sample}}^{\text{VH}}(\Phi) = I_o \cdot \left\{ \frac{1}{15} + \frac{1}{21} \langle P_2(\cos \theta) \rangle + \langle P_4(\cos \theta) \rangle \left(-\frac{4}{35} + \cos^2 \Phi - \cos^4 \Phi \right) \right\} \quad (5.12)$$

It should be noted that when the graphene is perfectly aligned in the sample, here equivalent to being perfectly flat, $\langle P_2(\cos \theta) \rangle = \langle P_4(\cos \theta) \rangle = 1$, then Eq. (10) reduces to $I_{\text{sample}}^{\text{VV}}(\Phi) \propto \cos^4 \Phi$. Eqs. 5.11 and 5.12 similarly reduce to $I_{\text{sample}}^{\text{VH}}(\Phi) \propto \cos^2 \Phi - \cos^4 \Phi (= \sin^2 \Phi \cos^2 \Phi)$. Previous orientational studies of graphene and related materials showed angular dependencies of these general forms, when the laser beam was either perpendicular ($\theta = \pi/2$ and $\phi = 0$ in Fig. 5.9(a)) [2-5] or parallel ($\theta = 0$ in Fig. 5.9(a)) to the graphene flakes [6-8].

5.3.4 HOPG and Graphene Paper

The analysis was extended to HOPG, which is known to have a crystalline graphite structure [32], and graphene paper made by solvent exfoliation and vacuum filtration.

The Raman spectra of HOPG obtained for the laser beam in the Z and X directions with Φ_Z and $\Phi_X = 0^\circ$ are shown in Fig. 5.10(a). The presence of the D and D' bands for the laser beam in the X direction was reported to be due to the discontinuities at the edges of the graphene flake that can be regarded as defects [33]. The D and D' bands are absent with the beam in the Z direction because the HOPG basal planes are relatively defect-free. The 2D band of HOPG can be fitted with two components, the

2D1 and 2D2 bands. The intensity variation of the G, 2D1 and 2D2 bands of HOPG with respect to the direction of laser polarization in both X and Z directions are shown in Fig. 5.10(b). This is very similar to the behaviour of the I_{2D} of graphene-Cu and graphene-PET. The consistency between the intensity variation of G, 2D1 and 2D2 band further confirms that Eq. 5.10 is identical for both the E_{2g} mode G band and the A_{1g} mode 2D band. The small deviation found between the G band and 2D1 band may be due to the 2D1 band being partially from randomly-aligned graphene layers while well-aligned graphene layers contribute to the higher wavenumber 2D2 band [34, 35].

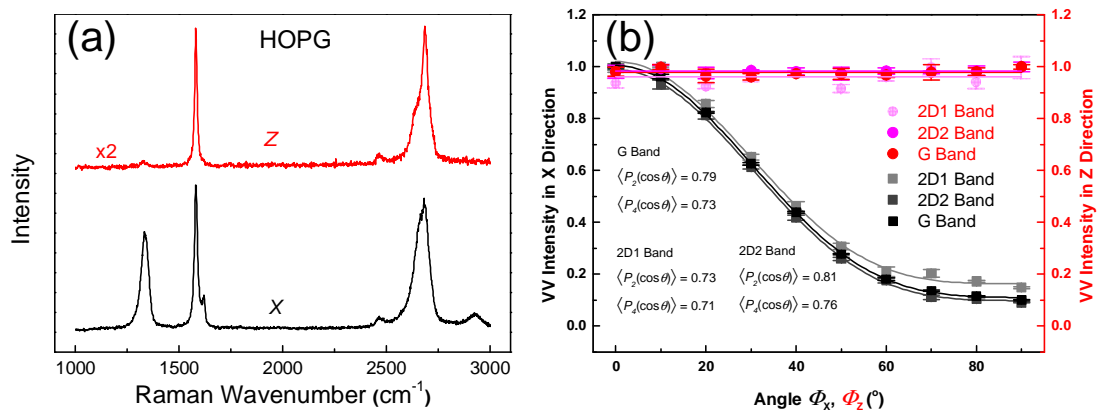


Figure 5.10 (a) Raman spectra of HOPG in X and Z directions and (b) the intensity variation of the G, 2D1 and 2D2 band of HOPG with the angle $\Phi_X(\Phi_Z)$ with the laser beam in X and Z directions, respectively. The lines in (b) are the average values for data points in Z direction and curve fitting using Eq. 5.10 for data in X direction.

The structure of graphene paper was also examined using polarized Raman spectroscopy, and the G band was used here because its 2D band is asymmetric. The variation of I_G with the polarization orientation angle $\Phi_X(\Phi_Z)$ is presented in Fig. 5.11. The significantly lower values of $\langle P_2(\cos \theta) \rangle$ and $\langle P_4(\cos \theta) \rangle$ in X direction imply a lower level of alignment of the graphene flakes in the paper than for the other materials.

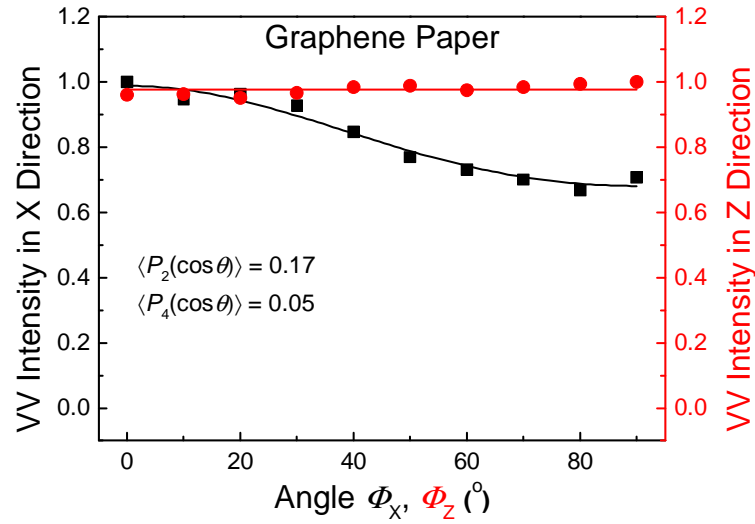


Figure 5.11 I_G variation for laser beam propagation in X and Z directions of graphene paper. The lines are the average value for data points in Z direction and curve fitting using Eq. 5.10 for data points in X direction.

5.3.5 Orientation Distribution Function

The values of $\langle P_2(\cos \theta) \rangle$ and $\langle P_4(\cos \theta) \rangle$ of the different materials studied are summarized in Table 5.1.

Table 5.1 Values of the order parameters determined for the four specimens.

Material	$\langle P_2(\cos \theta) \rangle$	$\langle P_4(\cos \theta) \rangle$
Graphene-Cu	0.85 ± 0.12	0.94 ± 0.05
Graphene-PET	0.76 ± 0.14	0.83 ± 0.05
HOPG	0.79 ± 0.01	0.73 ± 0.02
Graphene Paper	0.17 ± 0.01	0.05 ± 0.05

Based on this, a best guess of the actual ODF can be calculated following the maximum entropy approach as [9, 23]:

$$f_N(\theta) = A \exp[-(\lambda_2 P_2(\cos \theta) + \lambda_4 P_4(\cos \theta))] \quad (5.13)$$

where the coefficients A , λ_2 and λ_4 are found by numerically solving for them in three simultaneous equations:

$$\int_{\xi=0}^{2\pi} \int_{\phi=0}^{2\pi} \int_{\theta=0}^{\pi} f_N(\theta) \sin \theta d\theta d\phi d\xi = 1 \quad (5.14)$$

$$\int_{\xi=0}^{2\pi} \int_{\phi=0}^{2\pi} \int_{\theta=0}^{\pi} P_2(\cos \theta) f_N(\theta) \sin \theta d\theta d\phi d\xi = \langle P_2(\cos \theta) \rangle \quad (5.15)$$

$$\int_{\xi=0}^{2\pi} \int_{\phi=0}^{2\pi} \int_{\theta=0}^{\pi} P_4(\cos \theta) f_N(\theta) \sin \theta d\theta d\phi d\xi = \langle P_4(\cos \theta) \rangle \quad (5.16)$$

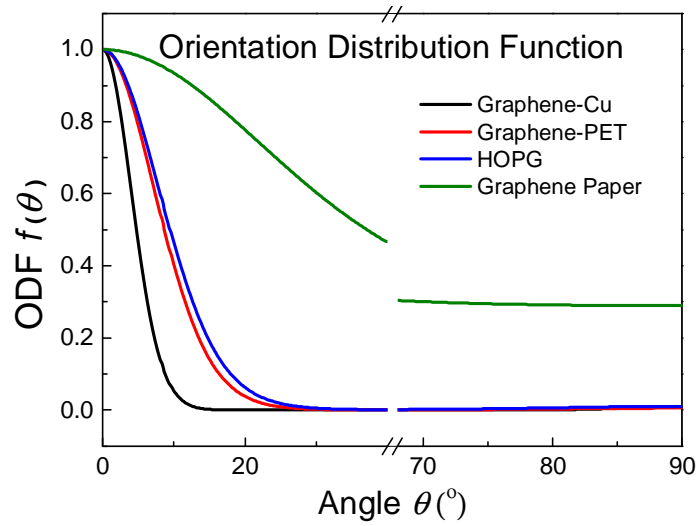


Figure 5.12 ODFs of the four specimens constructed with the measured orientation parameters $\langle P_2(\cos \theta) \rangle$ and $\langle P_4(\cos \theta) \rangle$.

Fig. 5.12 shows the calculated ODFs for the four specimens normalized to their corresponding 0° values. The good alignment of the graphene flakes in HOPG is further confirmed by the SEM image (Fig. 5.13(a)), which leads to the ODF of the HOPG being almost same that of the monolayer graphene (Fig. 5.12). In contrast, the alignment of graphene flakes in the graphene paper is significantly lower (Fig. 5.13(b)), which is also reflected by the lower values of $\langle P_2(\cos \theta) \rangle$ and $\langle P_4(\cos \theta) \rangle$, possibly due to the small size of the graphene [36].

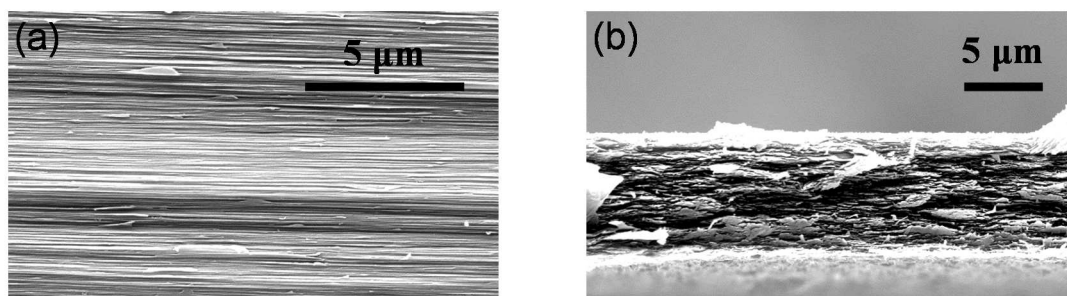


Figure 5.13 SEM images of the transverse sections of the (a) HOPG and (b) graphene paper.

It is interesting to observe that for both monolayer graphene specimens (graphene-Cu and graphene-PET) $\langle P_2(\cos\theta) \rangle$ and $\langle P_4(\cos\theta) \rangle < 1$ which means that in both cases the graphene is not exactly flat. In order to investigate this phenomenon, the topography of the graphene surfaces was studied using AFM by taking height scans (Fig. 5.14). In Fig. 5.14(a), it can be seen that the graphene monolayer follows the topography of the copper surface and so local Cu terraces or Cu grain boundaries will affect the flatness of the graphene [10]. In the case of the graphene-PET specimen it can be seen from Fig. 5.14(b) that the graphene on the PET is wrinkled. This may be due to factors such as differential thermal contraction or the process of transferring the graphene from the original substrate to the PET. Figs. 5.14(c) and (d) show histograms of the local slope determined from the AFM tapping-mode height scans across the graphene-Cu and graphene-PET surfaces, respectively, indicating the irregularity in the topography of the graphene. The local slope of the surface at each measurement point was computed using the Gwyddion software and the distribution of the angle θ corresponding to the tangent of the slope was determined. The open symbols in different colours correspond to the data obtained from the five $\sim 2\mu\text{m}$ square regions indicated in Figs. 5.14(a) and (b), which are approximately the same size as the Raman laser spot.

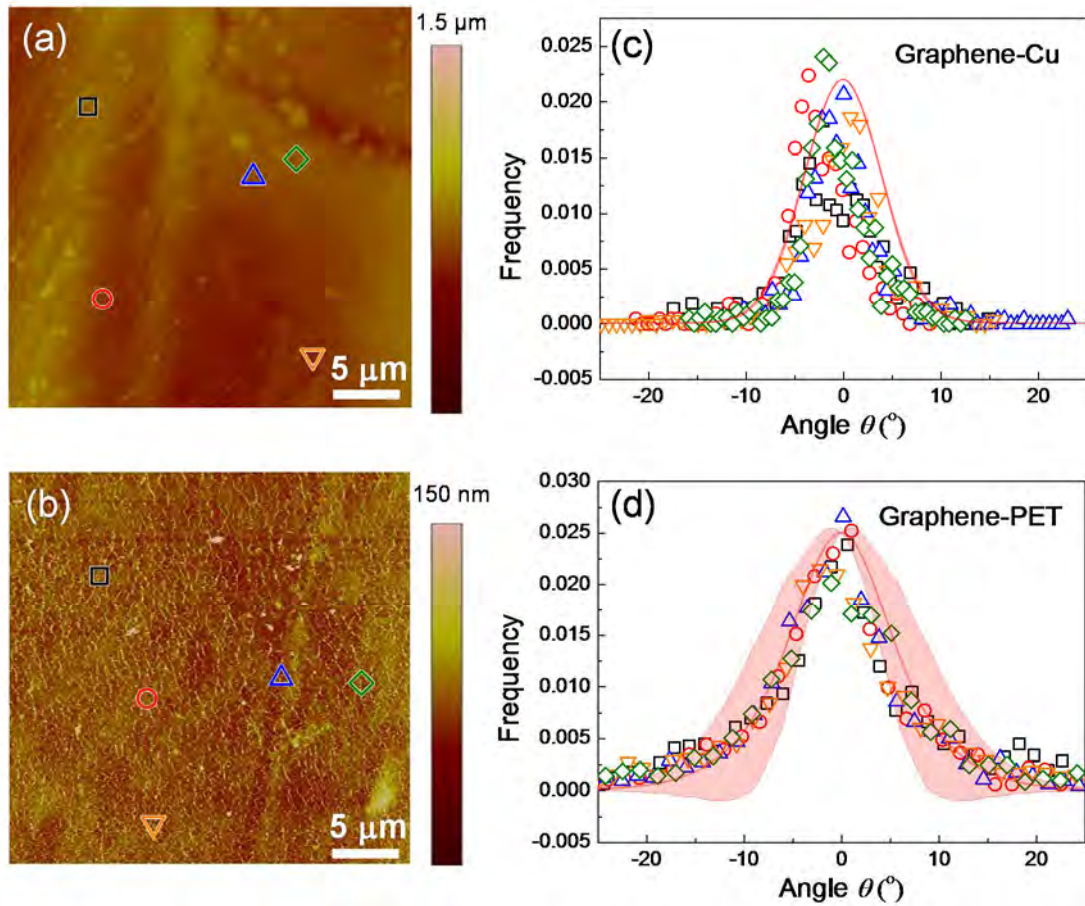


Figure 5.14 AFM analysis of the monolayer graphene on the substrates. Height scans of (a) graphene-Cu and (b) graphene-PET. (c) & (d) Frequency distributions of the angle θ of the local slopes of the graphene on the substrates determined from the AFM height scans. The open symbols in five different colours correspond to the data obtained from the five $\sim 2\mu\text{m}$ square regions the positions of which are indicated in Figs. 5.14(a) and (b). The red shade regions are the average ODF calculated from the polarized Raman measurements in Figs. 5.4(b) and 5.15(a) for graphene-Cu, and in Figs. 5.7(b) and 5.15(b) for graphene-PET.

The measurements of the angular dependence of I_{2D} were repeated from the transverse microtomes sections of the graphene-Cu and graphene-PET specimens (Fig. 5.15). The results are similar to those obtained from cut and polished specimens (Figs. 5.4(b) and 5.7(b)).

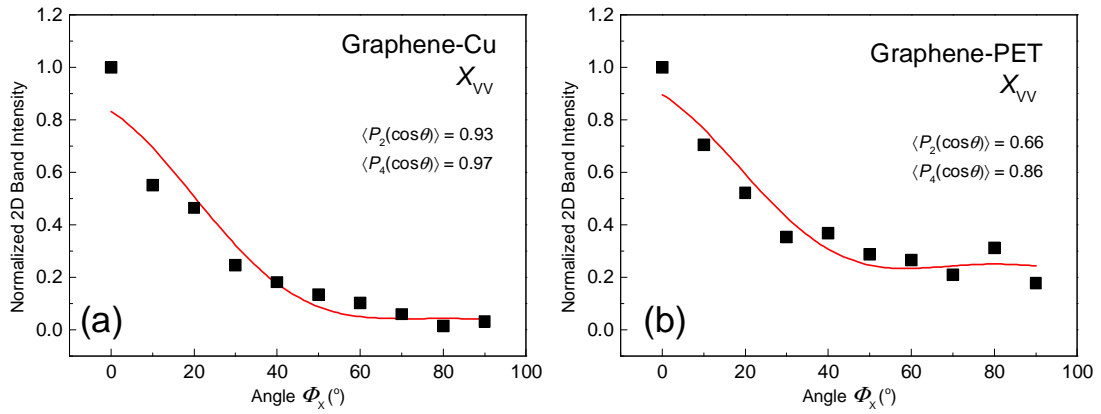


Figure 5.15 I_{2D} variation with the laser beam parallel to the X-axis as a function of the angle Φ_X for (a) graphene-Cu and (b) graphene-PET. The red lines are the curves fitted using Eq. 5.10.

Both sets of polarized Raman spectroscopic data for each material were used to reconstruct the average ODF using the maximum entropy approach as shown as the red shaded regions in Figs. 5.14(c) and (d). It can be seen that there is good correlation between the AFM data and the ODFs determined using polarized Raman spectroscopy. Although the surface of graphene-Cu appears to be rougher than that of graphene-PET, the standing wrinkles affect the orientation of the generally flat surface more severely, as indicated in the broader distribution curves determined from both Raman and AFM data (Figs. 5.14(c) and (d)). The similarity between the AFM distributions and ODFs gives confidence in the use of the polarized Raman technique to quantify the orientation of the graphene. Moreover, it confirms that the use of the Legendre polynomial expansion provides a general but rigorous approach that does not require prior knowledge of the ODF.

5.4 Conclusions

It has been demonstrated that well-defined Raman spectra can be obtained from transverse sections of graphene monolayers, only one atom thick, as a result of its strong resonance Raman scattering. It has also been shown that polarized Raman spectroscopy can be used to quantify the spatial orientation of graphene. The analysis has been found to be applicable not only to graphene with a high orientation degree such as on copper foil or polyester film, but also to bulk material such as HOPG and specimens with a lower orientation degree such as graphene paper. In

particular, it has been shown that it is possible to characterize the topography of buried graphene monolayers which would otherwise be difficult to access. Hence this analysis should find wide application as a characterization technique of graphene in a variety of different applications ranging from electronic devices to nanocomposites. In particular, it could enable the spatial orientation of graphene platelets in nanocomposites to be quantified and related to the mechanical properties of the materials, as will be shown in Chapter 6.

References

1. Lee, C.; Wei, X.; Kysar, J. W.; Hone, J., Measurement of the Elastic Properties and Intrinsic Strength of Monolayer Graphene. *Science* **2008**, 321, 385-388.
2. Gupta, A. K.; Russin, T. J.; Gutiérrez, H. R.; Eklund, P. C., Probing Graphene Edges via Raman Scattering. *ACS Nano* **2008**, 3, 45-52.
3. Casiraghi, C.; Hartschuh, A.; Qian, H.; Piscanec, S.; Georgi, C.; Fasoli, A.; Novoselov, K. S.; Basko, D. M.; Ferrari, A. C., Raman Spectroscopy of Graphene Edges. *Nano Letters* **2009**, 9, 1433-1441.
4. Cong, C.; Yu, T.; Wang, H., Raman Study on the G Mode of Graphene for Determination of Edge Orientation. *ACS Nano* **2010**, 4, 3175-3180.
5. Lee, J.-U.; Seck, N. M.; Yoon, D.; Choi, S.-M.; Son, Y.-W.; Cheong, H., Polarization Dependence of Double Resonant Raman Scattering Band in Bilayer Graphene. *Carbon* **2014**, 72, 257-263.
6. Liang, Q.; Yao, X.; Wang, W.; Liu, Y.; Wong, C. P., A Three-Dimensional Vertically Aligned Functionalized Multilayer Graphene Architecture: An Approach for Graphene-Based Thermal Interfacial Materials. *ACS Nano* **2011**, 5, 2392-2401.
7. Tan, P.; Hu, C.; Dong, J.; Shen, W.; Zhang, B., Polarization Properties, High-Order Raman Spectra, and Frequency Asymmetry between Stokes and Anti-Stokes Scattering of Raman Modes in a Graphite Whisker. *Physical Review B* **2001**, 64, 214301.
8. López-Honorato, E.; Meadows, P. J.; Shatwell, R. A.; Xiao, P., Characterization of the Anisotropy of Pyrolytic Carbon by Raman Spectroscopy. *Carbon* **2010**, 48, 881-890.
9. Liu, T.; Kumar, S., Quantitative Characterization of SWNT Orientation by Polarized Raman Spectroscopy. *Chemical Physics Letters* **2003**, 378, 257-262.
10. Wilson, N.; Marsden, A.; Saghir, M.; Bromley, C.; Schaub, R.; Costantini, G.; White, T.; Partridge, C.; Barinov, A.; Dudin, P.; Sanchez, A.; Mudd, J.; Walker, M.; Bell, G., Weak Mismatch Epitaxy and Structural Feedback in Graphene Growth on Copper Foil. *Nano Research* **2013**, 6, 99-112.
11. Li, X.; Cai, W.; An, J.; Kim, S.; Nah, J.; Yang, D.; Piner, R.; Velamakanni, A.; Jung, I.; Tutuc, E.; Banerjee, S. K.; Colombo, L.; Ruoff, R. S., Large-Area Synthesis of High-Quality and Uniform Graphene Films on Copper Foils. *Science* **2009**, 324, 1312-1314.

12. Kim, K. S.; Zhao, Y.; Jang, H.; Lee, S. Y.; Kim, J. M.; Kim, K. S.; Ahn, J.-H.; Kim, P.; Choi, J.-Y.; Hong, B. H., Large-Scale Pattern Growth of Graphene Films for Stretchable Transparent Electrodes. *Nature* **2009**, 457, 706-710.
13. Hernandez, Y.; Nicolosi, V.; Lotya, M.; Blighe, F. M.; Sun, Z.; De, S.; McGovern, I. T.; Holland, B.; Byrne, M.; Gun'Ko, Y. K.; Boland, J. J.; Niraj, P.; Duesberg, G.; Krishnamurthy, S.; Goodhue, R.; Hutchison, J.; Scardaci, V.; Ferrari, A. C.; Coleman, J. N., High-Yield Production of Graphene by Liquid-Phase Exfoliation of Graphite. *Nature Nanotechnology* **2008**, 3, 563-568.
14. Nicolosi, V.; Chhowalla, M.; Kanatzidis, M. G.; Strano, M. S.; Coleman, J. N., Liquid Exfoliation of Layered Materials. *Science* **2013**, 340.
15. Malard, L. M.; Pimenta, M. A.; Dresselhaus, G.; Dresselhaus, M. S., Raman Spectroscopy in Graphene. *Physics Reports* **2009**, 473, 51-87.
16. Ferrari, A. C.; Meyer, J. C.; Scardaci, V.; Casiraghi, C.; Lazzeri, M.; Mauri, F.; Piscanec, S.; Jiang, D.; Novoselov, K. S.; Roth, S.; Geim, A. K., Raman Spectrum of Graphene and Graphene Layers. *Physical Review Letters* **2006**, 97, 187401.
17. Begliarbekov, M.; Sul, O.; Kalliakos, S.; Yang, E.-H.; Strauf, S., Determination of Edge Purity in Bilayer Graphene Using μ -Raman Spectroscopy. *Applied Physics Letters* **2010**, 97, 031908-3.
18. Yoon, D.; Moon, H.; Son, Y.-W.; Samsonidze, G.; Park, B. H.; Kim, J. B.; Lee, Y.; Cheong, H., Strong Polarization Dependence of Double-Resonant Raman Intensities in Graphene. *Nano Letters* **2008**, 8, 4270-4274.
19. Chen, S.; Cai, W.; Piner, R. D.; Suk, J. W.; Wu, Y.; Ren, Y.; Kang, J.; Ruoff, R. S., Synthesis and Characterization of Large-Area Graphene and Graphite Films on Commercial Cu-Ni Alloy Foils. *Nano Letters* **2011**, 11, 3519-3525.
20. Hao, Y.; Wang, Y.; Wang, L.; Ni, Z.; Wang, Z.; Wang, R.; Koo, C. K.; Shen, Z.; Thong, J. T. L., Probing Layer Number and Stacking Order of Few-Layer Graphene by Raman Spectroscopy. *Small* **2010**, 6, 195-200.
21. Zaretski, A. V.; Marin, B. C.; Moetazed, H.; Dill, T. J.; Jibril, L.; Kong, C.; Tao, A. R.; Lipomi, D. J., Using the Thickness of Graphene to Template Lateral Subnanometer Gaps between Gold Nanostructures. *Nano Letters* **2015**, 15, 635-640.
22. Tanaka, M.; Young, R. J., Review Polarised Raman Spectroscopy for the Study of Molecular Orientation Distributions in Polymers. *Journal of Materials Science* **2006**, 41, 963-991.
23. van Gurp, M., The Use of Rotation Matrices in the Mathematical Description of Molecular Orientations in Polymers. *Colloid and Polymer Science* **1995**, 273, 607-625.
24. Perez, R.; Banda, S.; Ounaies, Z., Determination of the Orientation Distribution Function in Aligned Single Wall Nanotube Polymer Nanocomposites by Polarized Raman Spectroscopy. *Journal of Applied Physics* **2008**, 103, 074302-9.
25. Hermans, J. J.; Hermans, P. H.; Vermaas, D.; Weidinger, A., Quantitative Evaluation of Orientation in Cellulose Fibres from the X-Ray Fibre Diagram. *Recueil des Travaux Chimiques des Pays-Bas* **1946**, 65, 427-447.
26. Chatterjee, T.; Mitchell, C. A.; Hadjiev, V. G.; Krishnamoorti, R., Oriented Single-Walled Carbon Nanotubes-Poly(Ethylene Oxide) Nanocomposites. *Macromolecules* **2012**, 45, 9357-9363.

27. Bower, D. I., Orientation Distribution Functions for Uniaxially Oriented Polymers. *Journal of Polymer Science: Polymer Physics Edition* **1981**, 19, 93-107.
28. Gommans, H. H.; Alldredge, J. W.; Tashiro, H.; Park, J.; Magnuson, J.; Rinzler, A. G., Fibers of Aligned Single-Walled Carbon Nanotubes: Polarized Raman Spectroscopy. *Journal of Applied Physics* **2000**, 88, 2509-2514.
29. Proctor, J. E.; Gregoryanz, E.; Novoselov, K. S.; Lotya, M.; Coleman, J. N.; Halsall, M. P., High-Pressure Raman Spectroscopy of Graphene. *Physical Review B* **2009**, 80, 073408.
30. Loudon, R., The Raman Effect in Crystals. *Advances in Physics* **1964**, 13, 423-482.
31. Huang, M.; Yan, H.; Chen, C.; Song, D.; Heinz, T. F.; Hone, J., Phonon Softening and Crystallographic Orientation of Strained Graphene Studied by Raman Spectroscopy. *Proceedings of the National Academy of Sciences* **2009**, 106, 7304-7308.
32. Hiura, H.; Ebbesen, T. W.; Tanigaki, K.; Takahashi, H., Raman Studies of Carbon Nanotubes. *Chemical Physics Letters* **1993**, 202, 509-512.
33. Katagiri, G.; Ishida, H.; Ishitani, A., Raman Spectra of Graphite Edge Planes. *Carbon* **1988**, 26, 565-571.
34. Cançado, L. G.; Takai, K.; Enoki, T.; Endo, M.; Kim, Y. A.; Mizusaki, H.; Speziali, N. L.; Jorio, A.; Pimenta, M. A., Measuring the Degree of Stacking Order in Graphite by Raman Spectroscopy. *Carbon* **2008**, 46, 272-275.
35. Barros, E. B.; Demir, N. S.; Souza Filho, A. G.; Mendes Filho, J.; Jorio, A.; Dresselhaus, G.; Dresselhaus, M. S., Raman Spectroscopy of Graphitic Foams. *Physical Review B* **2005**, 71, 165422.
36. Lin, X.; Shen, X.; Zheng, Q.; Yousefi, N.; Ye, L.; Mai, Y.-W.; Kim, J.-K., Fabrication of Highly-Aligned, Conductive, and Strong Graphene Papers Using Ultralarge Graphene Oxide Sheets. *ACS Nano* **2012**, 6, 10708-10719.

Chapter 6 Determination of the Degree of Orientation of Graphene-based Nanoplatelets in Nanocomposites*

6.1 Introduction

The geometry and spatial orientation of the filler play vital roles in determining the mechanical property of composites [1], especially for composites reinforced by nano-filler, as it can be affected by quite a few factors [2-7]. In terms of identifying the spatial orientation of nano-filler, however, unlike the micron-size fibres, the traditional ways such as optical or electron microscopy only provide limited information [8]. There are just few techniques for this purpose, as reviewed in Chapter 1. Chapter 5 presented a study to quantify the three-dimensional spatial orientation of graphene in terms of an orientation distribution function (ODF). It is even more important, from the mechanics point of view, to know how the spatial orientation of graphene in the nanocomposites determines its mechanical properties. However, a quantitative analysis for this purpose is still lacking.

In this chapter, the general model established in Chapter 5 on basic graphene unit to quantify the spatial orientation of any graphitic material using an ODF has been extended to graphene-based nanocomposites. It is demonstrated further how the classical Krenchel orientation factor η_o [1] can be determined for plate-like fillers directly from the order parameters determined from the Raman data, and in particular, be used to correlate the degree of spatial orientation of the fillers with the mechanical properties of the nanocomposites.

* This chapter is based on a paper, 'Determination of the Degree of Orientation of Graphene-based Nanoplatelets in Nanocomposites', Submitted to *Composites Science and Technology* (2015).

6.2 Experimental

6.2.1 Materials

The graphite (Grade 2369) used to prepare the graphene oxide (GO) was supplied by Graphexel Ltd. The PVA ($M_w \sim 89000$ -98000, 99+% hydrolyzed) was purchased from Sigma Aldrich and used as received. All the other reagents were of analytical grade and used without further purification.

6.2.2 Preparation

The GO was prepared using the modified Hummers method (Chapter 4) [9, 10]. Briefly, 3 g graphite was added to 70 ml of concentrated sulfuric acid while stirring at room temperature. The mixture system was then cooled to 0 °C when 1.5 g sodium nitrate was added. While stirring, 9 g potassium permanganate was added slowly, to avoid a rapid temperature rise. The mixture was then placed into a 40 °C water bath for 0.5 h, followed by the addition of 140 ml of water and it was stirred for another 15 min. An additional 500 ml water and 20 ml of 6 % w/v H_2O_2 were added subsequently after which the colour of the mixture turned from brown to yellow. The mixture was then repeatedly washed with 250 ml of 1:10 HCl aqueous solution and centrifuged 3 times. Following this, the mixture was repeatedly washed with water and centrifuged until the pH was approximately 7. Finally, the GO was dispersed in water to make an aqueous suspension for later use.

The PVA powder was dissolved in water at 90 °C to give a 10 wt% PVA aqueous solution. The GO suspension and PVA solution were then mixed to form a series of dispersions with GO concentrations of 1 wt%, 2 wt%, 3 wt% and 5 wt%. These solutions were placed into a 120 W sonication bath for 30 min to obtain homogenous dispersions. They were then allowed to stand overnight to fully remove bubbles, and were cast and allowed to dry under ambient conditions to completely evaporate the solvent.

The 10 wt% GO reinforced poly(methyl methacrylate) nanocomposites (GO/PMMA) was kindly supplied by Dr. C. Vallés, The University of Manchester, and the

preparation was described elsewhere [3]. The 0.5 wt% GO reinforced epoxy resin nanocomposites (GO/epoxy) was kindly supplied by Dr. Z. Li, The University of Manchester, and the preparation was described elsewhere [11].

6.2.3 Characterization

Atomic force microscope (AFM) images were obtained using a Veeco CP-II system in conjunction with the 'RTESPA' probe (Bruker) in the tapping mode. Scanning electron microscope (SEM) image of the GO flakes was obtained using XL 30 FEG Philips. SEM image of the nanocomposite was obtained using EVO60 VPSEM (Zeiss), where the sample was fractured at room temperature, and coated with gold before analysis. X-ray diffraction (XRD) was carried out using an X'Pert DY609 X-Ray diffractometer (Philips) with a Cu K α radiation source ($\lambda = 1.542\text{\AA}$).

Polarized Raman spectra were obtained using Renishaw 1000/2000 spectrometers equipped with HeNe lasers ($\lambda = 633\text{ nm}$) with a laser spot around 1~2 μm in diameter, from either the cross-sections or the top surfaces of the nanocomposites. The so-called 'VV' polarization configuration was employed, where the polarization of incident and scattered radiation were both parallel to each other. Fig. 6.1(a) defines the Cartesian coordinate system with the X , Y and Z axes being used to describe the experimental arrangement in which specimens were analysed. In the Z direction (Fig. 6.1(b)), the direction of propagation of laser is along the Z axis, perpendicular to the top surface of the sample. In the X and Y directions (Fig. 6.1(c)), the laser beam was set along the X or Y axes, perpendicular to the transverse section (fracture surfaces of GO/PVA and polished surface of GO/epoxy and GO/PMMA) and parallel to the top surface of the specimen. With the polarization configurations fixed, the specimens were rotated to different angles, Φ_X , Φ_Y and Φ_Z for the laser beam parallel to the X , Y and Z axis respectively. For the materials that were thought to be transversely isotropic (GO/PVA), however, polarized Raman spectra were obtained only with the laser beam parallel to the Z and X directions.

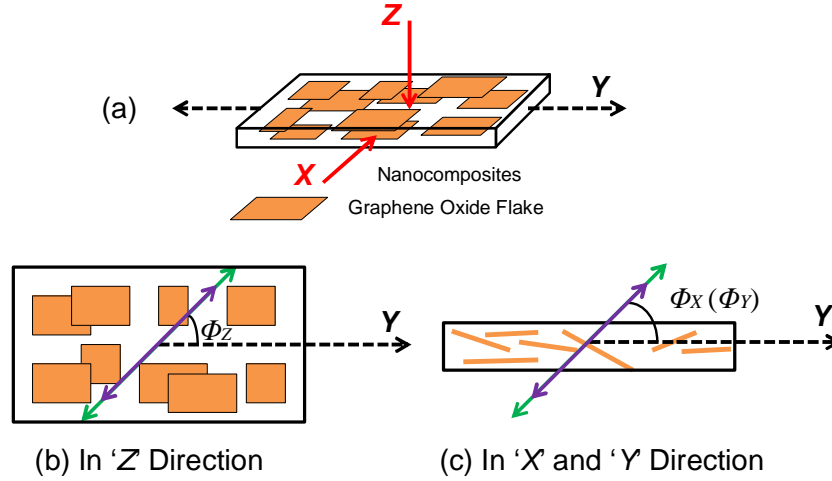


Figure 6.1 (a) Schematic illustration of the relationships between the sample geometries and polarization conditions used in the Raman spectroscopic analysis in three directions. View when laser beam parallel to (b) the Z direction and (c) the X and Y directions. The red arrows represent the direction of laser propagation and the purple and green arrows represent the directions of polarization of the incident radiation and scattered radiation, respectively.

6.3 Result and Discussion

6.3.1 Model of Spatial Orientation

As explained in Chapter 5, the local orientation of a graphene sheet is most conveniently defined by its surface normal vector, shown in Fig. 6.2 as the z direction with the graphene in the x,y plane. This is related to the coordinate system of the sample (X,Y,Z) by the Euler angles (θ,ϕ,ξ) indicated. The ODF of the surface normal can be written in general as $f_N(\theta,\phi,\xi)$ such that $f_N(\theta,\phi,\xi)\sin\theta d\theta d\phi d\xi$ is the probability of finding an area element of the graphene with surface normal between (θ,ϕ,ξ) and $(\theta+d\theta,\phi+d\phi,\xi+d\xi)$.

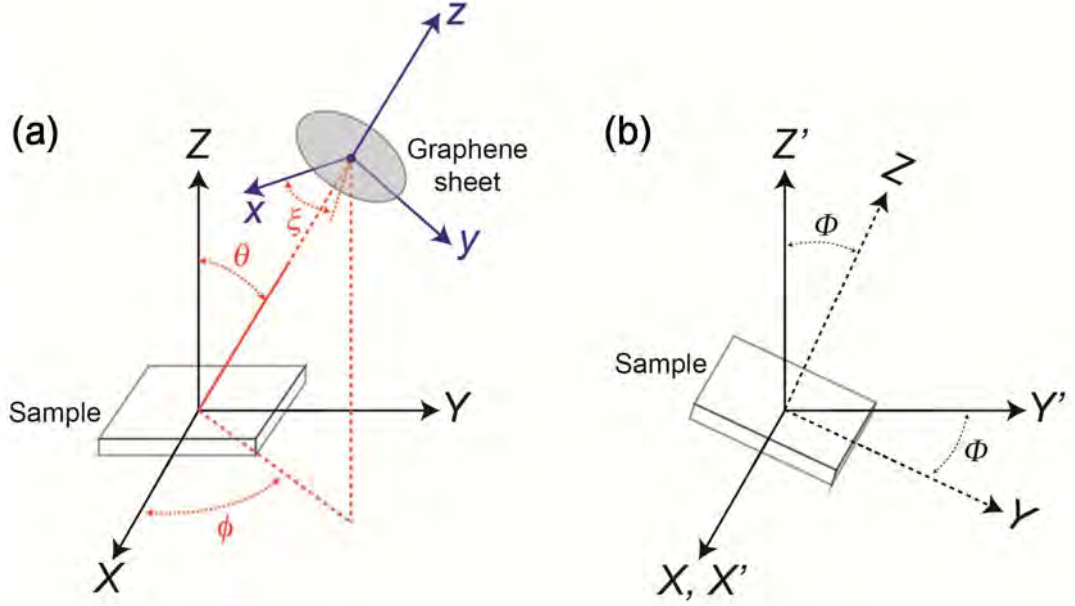


Figure 6.2 Schematic diagram of the local orientation of graphene within the sample and of the sample relative to the experimental polarised Raman spectroscopy measurement parameters. (a) The local coordinate system of the graphene sheet (x,y,z) is related to that of the sample (X,Y,Z) by the Euler angles (θ,ϕ,ξ). (b) For the polarised Raman spectroscopy measurements described in Fig. 6.1(c), the incident and scattered light propagates along the X, X' axis whilst the polarization of the incident and scattered light are in the Y' direction for VV polarization configuration. (Courtesy of Dr. N. Wilson, University of Warwick)

Based on the discussion in Chapter 5, the Raman scattering intensity of the sample as a function of the polarisation angle Φ ($\Phi_X/\Phi_Y/\Phi_Z$) relative to the sample for the VV polarization, $I_{\text{sample}}^{\text{VV}}(\Phi)$, can be described as:

$$I_{\text{sample}}^{\text{VV}}(\Phi) = I_o \cdot \left\{ \frac{8}{15} + \langle P_2(\cos\theta) \rangle \left(-\frac{16}{21} + \frac{8}{7} \cos^2 \Phi \right) + \langle P_4(\cos\theta) \rangle \left(\frac{8}{35} - \frac{8}{7} \cos^2 \Phi + \cos^4 \Phi \right) \right\} \quad (6.1)$$

where I_o is the amplitude. By fitting the experimental data to Eq. 6.1, a set of $\langle P_2(\cos\theta) \rangle$ and $\langle P_4(\cos\theta) \rangle$ values can be obtained to quantify the spatial orientation of graphene in graphitic materials. When the graphene in the specimen is perfectly aligned, here being equivalent to it lying perfectly flat in the XY plane, $\langle P_2(\cos\theta) \rangle = \langle P_4(\cos\theta) \rangle = 1$. Their values then decrease as the degree of alignment

decreases until $\langle P_2(\cos\theta) \rangle = \langle P_4(\cos\theta) \rangle = 0$, which is characteristic of isotropic materials. It should also be pointed out that the parameter $\langle P_2(\cos\theta) \rangle = (3\langle \cos^2\theta \rangle - 1)/2$ is more commonly known in polymer and composites science as the Hermans' orientation factor f [12]. If the Raman scattering intensity measured in the Z direction shows no angular dependence, which means the material is isotropic about that axis, then the result obtained in X direction is sufficient to describe the spatial orientation of graphene. Although GO undergoes structural distortions after oxidation, it essentially has a structure and vibrational modes similar to those of graphene. As the crystalline structure of GO is predominantly the same as that of graphene [13] but decorated by oxidative debris [14], it is assumed that the Raman polarizability tensors of GO are the same as those of graphene. Accordingly, it will then be shown how this technique can be extended to quantify the spatial orientation of GO in bulk nanocomposites.

6.3.2 GO/PVA Nanocomposites

For GO/PVA, the size of the GO flakes was examined using SEM (Fig. 6.3), and their average lateral dimension was measured in Chapter 4 as $\sim 14.85 \mu\text{m}$.

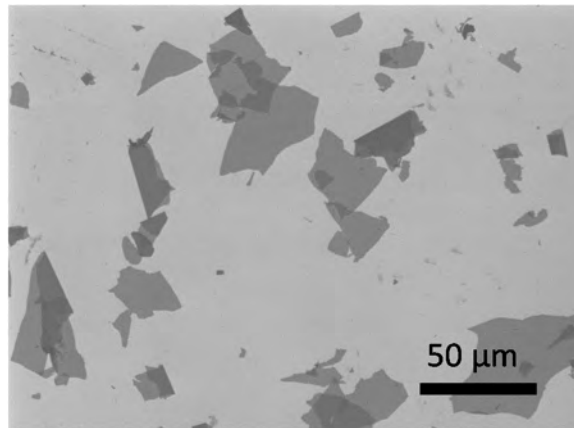


Figure 6.3 SEM micrograph of the GO flakes on SiO_2 substrate.

The thickness of the GO flake was measured by AFM height profile (Fig. 6.4(a)) to be the order of 1 nm (Fig. 6.4(b)), typical of exfoliated GO monolayer, demonstrating the complete exfoliation of the GO flakes after oxidation [7].

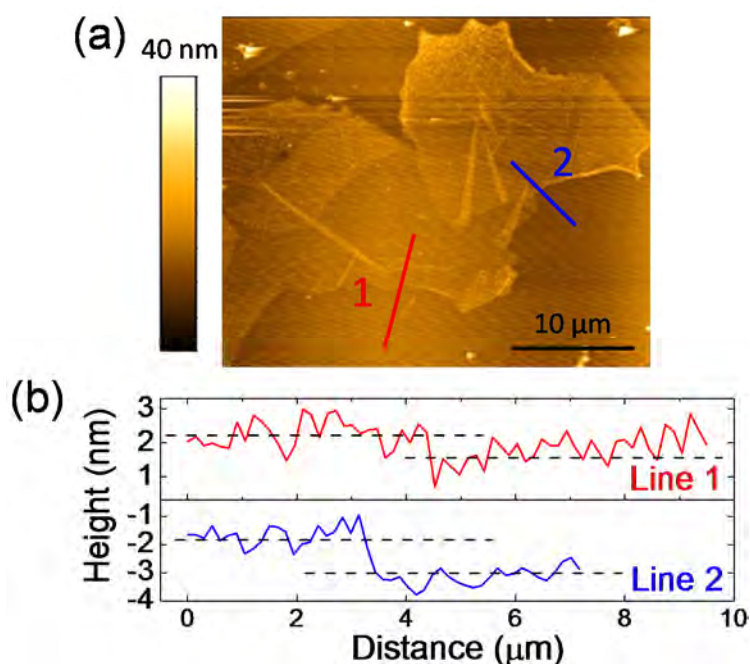


Figure 6.4 (a) AFM image of the GO flakes. (b) The height profiles with a typical thickness of the order of 1 nm.

The GO flakes were found using SEM to disperse well and align generally parallel the top surface of the nanocomposites film, as indicated in Fig. 6.5(a). Their dispersion was also confirmed by XRD (Fig. 6.5(b)). The diffraction peak of the pure GO at $2\theta = 10.5^\circ$ corresponds to a d -spacing of 0.84 nm. The similar patterns of the GO/PVA and neat PVA sample indicate the complete exfoliation of GO flakes in the nanocomposite [7].

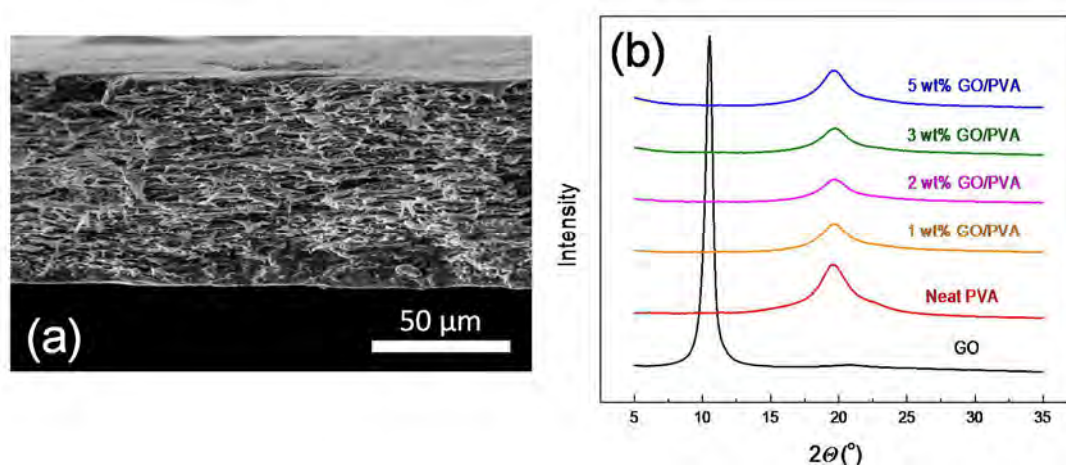


Figure 6.5 (a) SEM image of the cross section of the 2 wt% GO/PVA. (b) XRD patterns of GO, neat PVA and GO/PVA nanocomposites with different GO loadings.

The Raman spectra of the GO/PVA nanocomposites with different GO loadings when the laser beam was along the *X* and *Z* directions are shown in Fig. 6.6. In the similar spectra, the G band around 1600 cm^{-1} corresponds to the E_{2g} phonon at the Brillouin zone centre [15]. The D band, centred around 1335 cm^{-1} , is usually assigned to the A_{1g} symmetry, and is associated with the presence of defects [15].

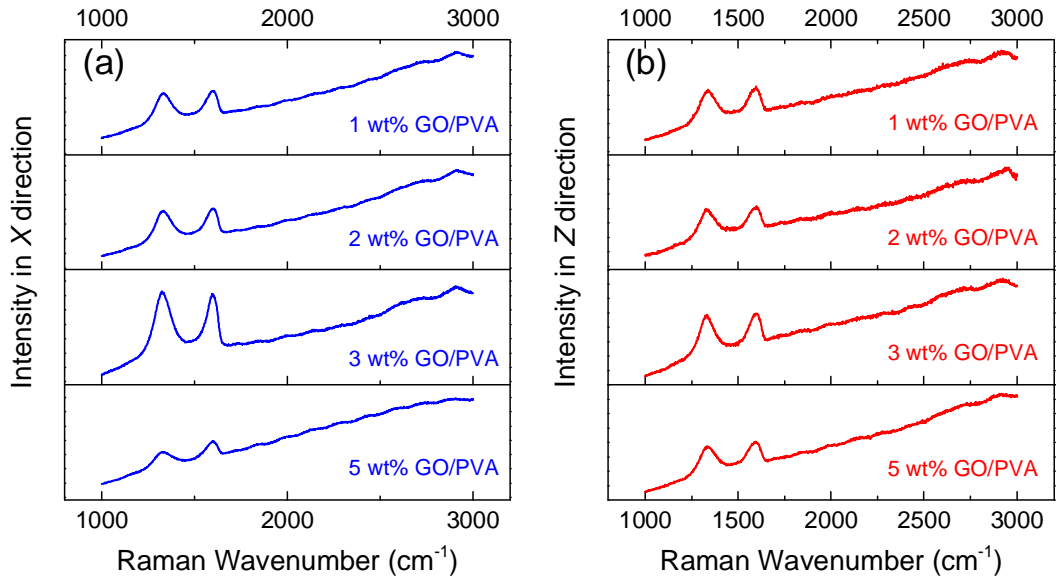


Figure 6.6 Raman spectra of the GO/PVA nanocomposites with the laser beam in (a) *X* (blue) and (b) *Z* (red) directions.

Given the good dispersion of GO in the nanocomposites, the spatial orientation of GO can be assessed using the strong G band. The variation of G band intensity (I_G) as the function of polarization angle (Φ_X/Φ_Z), along with the values of $\langle P_2(\cos\theta) \rangle$ and $\langle P_4(\cos\theta) \rangle$, obtained by fitting the experimental data with Eq. 6.1 are shown in Fig. 6.7. The I_G values measured in *X* direction imply a good spatial orientation of GO at 1 wt% loading, moderately aligned parallel to the films, but the alignment decreases as the GO loading increases, as indicated by the decreasing values of $\langle P_2(\cos\theta) \rangle$ and $\langle P_4(\cos\theta) \rangle$ (Fig. 6.7). The I_G values measured in the *Z* direction show no angular dependence, demonstrating that the materials are isotropic about that axis (Fig. 6.7). It is thought that the alignment of the GO occurs by settlement in the mould during the evaporation of the aqueous solvent. It appears that the settlement process does not take place so easily for higher loadings of GO leading to less well-aligned GO flakes.

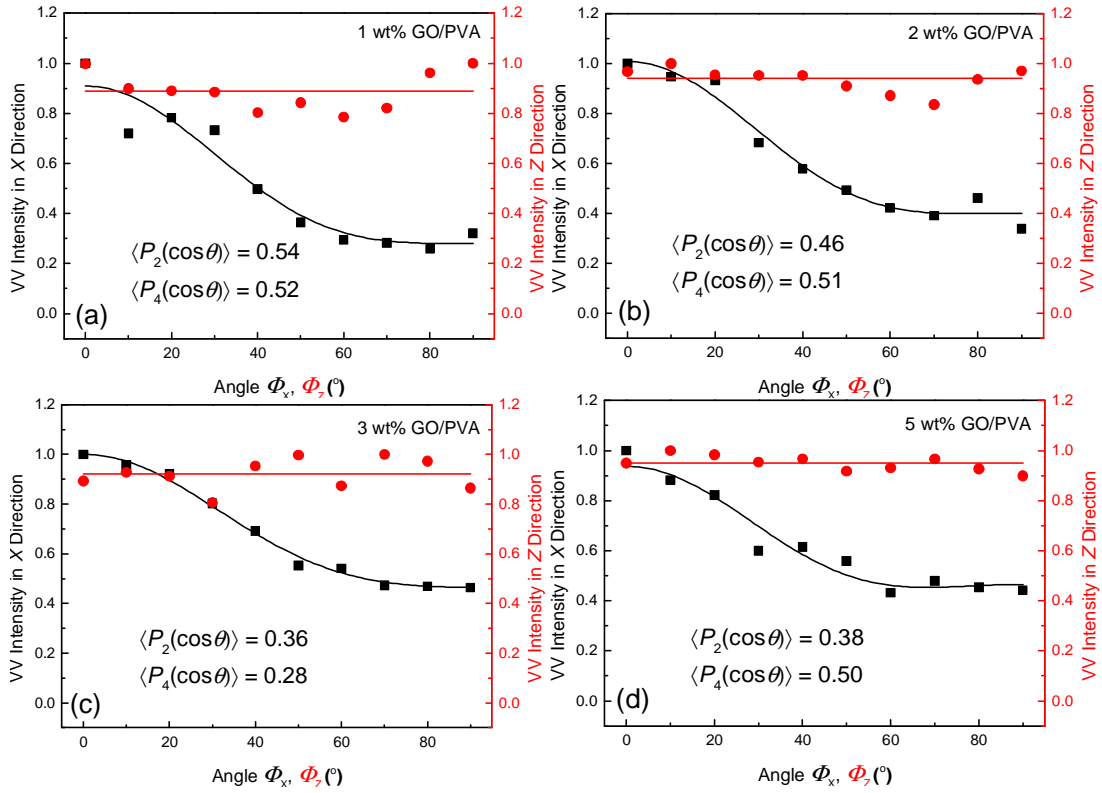


Figure 6.7 I_G variation with angle Φ_X / Φ_Z for GO/PVA nanocomposites with different loadings of GO with the laser beam in both X (black) and Z (red) directions. (a) 1 wt% GO, (b) 2 wt% GO, (c) 3 wt% GO and (d) 5 wt% GO/PVA. The black lines are curve fittings for data in X direction using Eq. 6.1, and red lines are the average values for data in Z direction.

6.3.3 GO/epoxy and GO/PMMA

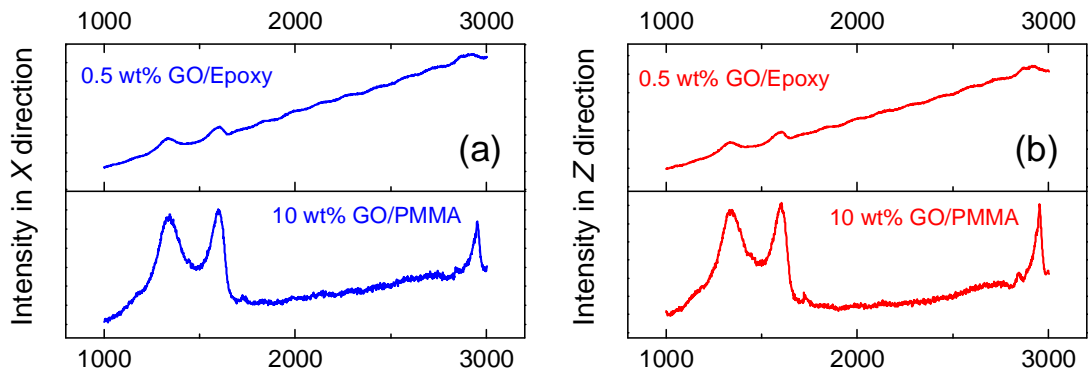


Figure 6.8 Raman spectra of GO/epoxy and GO/PMMA with the laser beam in (a) X (blue) and (b) Z (red) directions.

For comparison, two kinds of other GO-based nanocomposites, GO/PMMA and GO/epoxy, were assessed using the same technique. The Raman spectra for those two nanocomposites with the two laser configuration are shown in Fig. 6.8. Generally they are similar to that of the GO/PVA (Fig. 6.6), yet different in the level of fluorescent background.

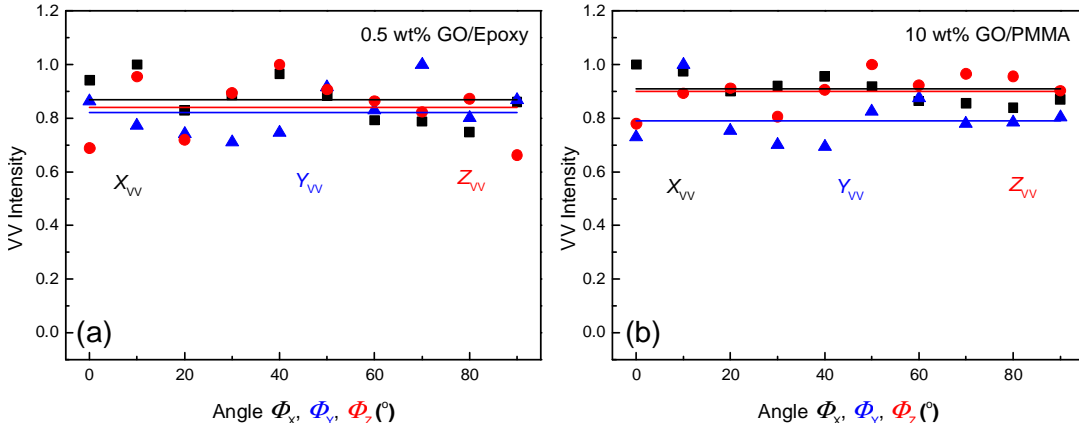


Figure 6.9 I_G variation with angle $\Phi_X/\Phi_Y/\Phi_Z$ for propagation of the laser beam in the X (black), Y (blue) and Z (red) directions for (a) GO/epoxy and (b) GO/PMMA. The straight lines are the average values for data in corresponding directions.

The spatial orientation of GO in these two nanocomposite systems [3, 11] were also assessed using polarized Raman spectroscopy. As there is no prior knowledge of their state of orientation for these materials, the variation of I_G with the angle Φ was determined for the direction of laser beam propagation in all the X, Y and Z directions (Fig. 6.9). The lack of variation of I_G with Φ showed that there is no preferred orientation of the GO in either of these two nanocomposites. The GO/epoxy nanocomposite was prepared by mixing the GO with the epoxy resin and casting into a mould [11]. In the case of the GO/PMMA, the GO had been blended in a twin-screw extruder with PMMA and injection moulded before consolidation by hot-pressing [3]. It appears that neither process led to any preferred alignment of the GO.

It is clear from the analyses of the range of different sp^2 -hybridized carbon materials investigated above that the angular dependence of the intensity reflects different degrees of spatial orientation of the GO planes in the materials. Since the form of the behaviour for all materials studied follows Eq. 6.1, it is possible to characterize the

graphene and GO spatial orientation in terms of the value of $\langle P_2(\cos\theta) \rangle$ and $\langle P_4(\cos\theta) \rangle$ for a given polarization configuration. Table 6.1 shows the values of $\langle P_2(\cos\theta) \rangle$ and $\langle P_4(\cos\theta) \rangle$ with the direction of laser propagation in X direction for all the materials tested, and the generally decreasing values imply a lower degree of spatial orientation of the flakes.

Table 6.1 Values of $\langle P_2(\cos\theta) \rangle$, $\langle P_4(\cos\theta) \rangle$ and Krenchel orientation factor determined with the direction of laser beam propagation parallel to the X direction for all the materials studied.

	$\langle P_2(\cos\theta) \rangle$	$\langle P_4(\cos\theta) \rangle$	η_o
1 wt% GO/PVA	0.54	0.52	0.78
2 wt% GO/PVA	0.46	0.51	0.75
3 wt% GO/PVA	0.36	0.28	0.69
5 wt% GO/PVA	0.38	0.50	0.72
0.5 wt% GO/epoxy	~0	~0	0.53
10 wt% GO/PMMA	~0	~0	0.53

6.3.4 Orientation distribution function (ODF)

Based on the $\langle P_2(\cos\theta) \rangle$ and $\langle P_4(\cos\theta) \rangle$ values determined, a best guess of the actual ODF can be obtained as indicated in Chapter 5 [16, 17]:

$$f_N(\theta) = A \exp[-(\lambda_2 P_2(\cos\theta) + \lambda_4 P_4(\cos\theta))] \quad (6.2)$$

where the coefficients A , λ_2 and λ_4 can be solved numerically. Using the values obtained, the spatial orientation of GO can be reconstructed (Fig. 6.10). For simplicity, all the ODFs have been normalized to their corresponding 0° values. It can be seen that the highest level of spatial orientation is found for the 1 wt% GO/PVA where $f_N(\theta)$ decreases rapidly with increasing θ , whereas it is independent of θ for the GO/PMMA and GO/epoxy, indicating the isotropic nature of the two nanocomposites.

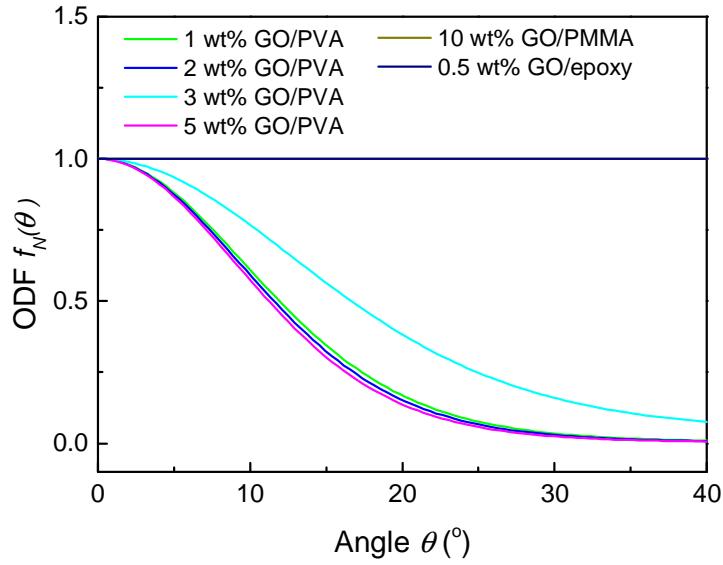


Figure 6.10 The ODF for the materials studied.

6.3.5 Krenchel orientation factor η_o

Although the knowledge of $\langle P_2(\cos\theta) \rangle$ and $\langle P_4(\cos\theta) \rangle$ enables the ODF to be obtained, one of the most useful applications of these order parameters is in the determination of the Krenchel orientation factor, η_o , which defines the effect of the orientation of fillers, such as fibre [1] and carbon nanotube [18], upon the mechanical properties of composites. It is unity for perfectly-aligned fibres or nanotubes, $3/8$ for fibres or nanotubes oriented randomly 2D in plane and $1/5$ for materials with random 3D fibres or nanotubes [18].

In general, the Krenchel factor is not unique for a particular material and it depends upon the direction along which the mechanical properties are to be determined. For a single reinforcement element, $\eta_o = \cos^4\zeta$ where ζ is the angle between the element and the axis along which the stress is applied. For the platelet geometry shown in Fig. 6.2, with a symmetrical distribution of the surface normals and for deformation parallel to Y axis $\cos\zeta = \sqrt{1 - (\sin\theta \sin\phi)^2}$. To find the Krenchel factor for a specimen, an integration must take place over the ODF [1]:

$$\eta_o = \frac{\int_{\xi=0}^{2\pi} \int_{\phi=0}^{2\pi} \int_{\theta=0}^{\pi} (1 - (\sin \theta \sin \phi)^2)^2 f_N(\theta) \sin \theta d\theta d\phi d\xi}{\int_{\xi=0}^{2\pi} \int_{\phi=0}^{2\pi} \int_{\theta=0}^{\pi} f_N(\theta) \sin \theta d\theta d\phi d\xi} \quad (6.3)$$

Substituting in the definition of the ODF in Chapter 5 gives:

$$\eta_o = \frac{8}{15} + \frac{8}{21} \langle P_2(\cos \theta) \rangle + \frac{3}{35} \langle P_4(\cos \theta) \rangle \quad (6.4)$$

It should be noted that η_o depends only on $\langle P_2(\cos \theta) \rangle$ and $\langle P_4(\cos \theta) \rangle$ hence can be determined directly from the experimental Raman spectroscopy data. It has been shown in this present study that the lack of the intensity variation with the angle Φ_Z when the laser beam is parallel to the Z axis shows that the orientation of the graphene sheets varied uniformly around this axis. Thus the $\langle P_2(\cos \theta) \rangle$ and $\langle P_4(\cos \theta) \rangle$ values derived with the laser beam in X direction are sufficient to describe the orientation of graphene and GO.

As mentioned above for a perfectly-oriented material $\langle P_2(\cos \theta) \rangle = \langle P_4(\cos \theta) \rangle = 1$ while $\langle P_2(\cos \theta) \rangle = \langle P_4(\cos \theta) \rangle = 0$ for 3D randomly-oriented materials. Eq. 6.4 shows therefore that the Krenchel factor is predicted to be 1 for a perfectly-oriented material and 8/15 for a material reinforced with 3D-random platelets. Liu and Brinson [19] used the Mori-Tanaka model to model the elastic deformation of nanocomposites. Analysis of their data shows that for reinforcement of a polymer with nanoplatelets of a given aspect ratio, nanocomposite with random nanoplatelets would be expected to have a Young's modulus of around 8/15 of that for a nanocomposite with aligned nanoplatelets deformed parallel to the axis of alignment - a result identical to that found in this present study. The values of Krenchel factor η_o of the all the materials studied are shown in Fig. 6.11. It can be seen the Krenchel factor decreases as the degree of orientation of the materials decreases until it reaches the value 8/15 in the case of random orientation when $\langle P_2(\cos \theta) \rangle = \langle P_4(\cos \theta) \rangle = 0$.

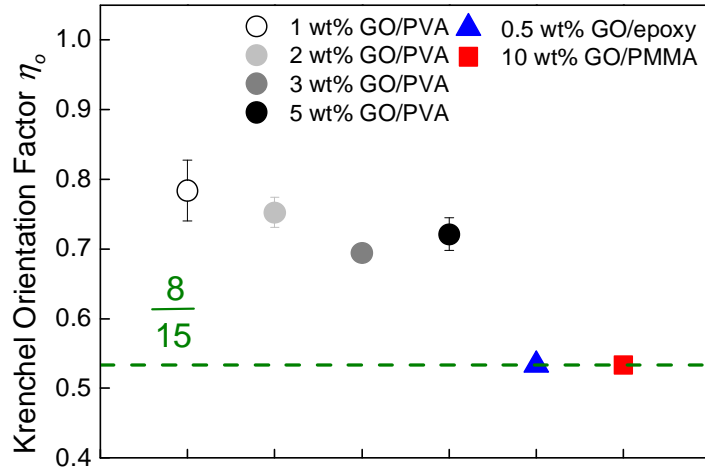


Figure 6.11 The Krenchel factors η_o of the materials studied. The dashed green line represents the Krenchel value of 8/15 for materials reinforced with 3D-random nanoplatelets.

Another point to bear in mind is the size effect (Chapter 1) as a result of the variation of stress across platelets of finite lateral dimensions due to shear-lag effects [20] will lead to the effective modulus of the filler being reduced by a further size factor η_i [21, 22]. Hence the best reinforcement will be achieved with well-aligned flat nanoplatelets that possess large lateral dimensions.

6.3.6 Comparison with the Hermans' model

Table 6.2 The value of $\langle P_2(\cos\theta) \rangle$, $\langle P_4(\cos\theta) \rangle$ and Krenchel factor η_o when graphene flakes are oriented randomly in bulk, and oriented parallel/perpendicular to the stress direction.

	$\langle P_2(\cos\theta) \rangle$ (Hermans' factor)	$\langle P_4(\cos\theta) \rangle$	Krenchel factor η_o
Parallel	1	1	1
Random	0	0	8/15
Perpendicular	-1/2	3/8	0 (3/8)*

* The model fails in this situation as discussed later

$\langle P_2(\cos\theta) \rangle$ is actually the Hermans' orientation factor, and Krenchel orientation factor is a combination of $\langle P_2(\cos\theta) \rangle$ and $\langle P_4(\cos\theta) \rangle$, as discussed above. As the Hermans' factor quantifies the general orientation but Krenchel factor relates the orientation to the mechanical properties, it would be instructive to give a brief comparison of the two orientation models.

Some of the values of the two orientation models at typical situations are shown in Table 6.2, where the graphene flakes are aligned parallel or perpendicular to the stress direction, or randomly aligned three-dimensionally. The values of Hermans' factor can be calculated according to its definition. Based on this, the corresponding $\langle P_4(\cos\theta) \rangle$ values at the parallel and perpendicular situations can be calculated using the constraints with regard to the value of $\langle P_2(\cos\theta) \rangle$ as shown in Chapter 5 and Ref. [23]. The random situation shows the importance of the additional $\langle P_4(\cos\theta) \rangle$ parameter compared to the $\langle P_2(\cos\theta) \rangle$ solely. For example, $\langle P_2(\cos\theta) \rangle = (3\langle \cos^2\theta \rangle - 1)/2 = 0$ generally means the random orientation, however, it is not able to describe the situation where all the graphene flakes are aligned uniaxially along the Z axis at the angle θ , where $\cos^2\theta = 1/3$ thus $\langle \cos^2\theta \rangle = 1/3$. As discussed earlier [23], $\langle P_4(\cos\theta) \rangle$ can be in a range if $\langle P_2(\cos\theta) \rangle = 0$, however, only when $\langle P_4(\cos\theta) \rangle = 0$ can the 'real' random orientation be determined.

Consequently, the values of the Krenchel orientation factors can be determined using Eq. 6.4. It has to be noticed that the perpendicular situation is an exception for this model, where all the graphene flakes are aligned perpendicular to the stress direction ($\theta=\phi=90^\circ$ in Fig. 6.2). It is understandable from the mechanics point of view that the Krenchel orientation factor should ideally be 0, though it is calculated to be 3/8 using Eq. 6.4. This is because this situation is in contrast to the assumption in this model that all the graphene flakes are aligned uniaxially along the Z axis (no ϕ in the calculation). Hence the calculated value of 3/8 is actually obtained when all the graphene flakes aligned as $\theta=90^\circ$ but $0 \leq \phi < 360^\circ$, which is equivalent to the situation of random fibres being oriented in a 2D plane when viewed in Z direction.

6.4 Conclusions

It has been demonstrated that it is possible to use the model established in Chapter 5 to quantify the spatial orientation of GO in a variety of different GO-based nanocomposite systems in terms of an ODF. It has been shown how it is possible to quantify the degree of spatial orientation of graphene and GO through the Krenchel orientation factor determined experimentally from Raman spectroscopy data. Another significant finding of this study is that the Krenchel factor η_o for randomly oriented nanoplatelets is 8/15. This means that random orientation of fillers such as graphene should reduce the Young's modulus of the nanocomposites by less than a factor of 2 compared with the fully aligned materials. Compared to the reduction in the modulus of a factor of 5 from aligned to 3D-random fibres and nanotubes [1], it means that better levels of reinforcement should be achievable with misaligned nanoplatelets compared with nanotubes and there is less need to ensure accurate alignment of the nanoplatelet. Beyond just graphene and GO, this approach should be more widely applicable to other nanoplatelet fillers for which well-defined Raman spectra can be obtained.

References

1. Krenchel, H., *Fibre Reinforcement*. Akademisk Forlag: Copenhagen, 1964.
2. Kim, H.; Macosko, C. W., Processing-Property Relationships of Polycarbonate/Graphene Composites. *Polymer* **2009**, 50, 3797-3809.
3. Vallés, C.; Kinloch, I. A.; Young, R. J.; Wilson, N. R.; Rourke, J. P., Graphene Oxide and Base-Washed Graphene Oxide as Reinforcements in PMMA Nanocomposites. *Composites Science and Technology* **2013**, 88, 158-164.
4. Yousefi, N.; Gudarzi, M. M.; Zheng, Q.; Aboutalebi, S. H.; Sharif, F.; Kim, J.-K., Self-Alignment and High Electrical Conductivity of Ultralarge Graphene Oxide-Polyurethane Nanocomposites. *Journal of Materials Chemistry* **2012**, 22, 12709-12717.
5. Bortz, D. R.; Heras, E. G.; Martin-Gullon, I., Impressive Fatigue Life and Fracture Toughness Improvements in Graphene Oxide/Epoxy Composites. *Macromolecules* **2011**, 45, 238-245.
6. Liang, J.; Huang, Y.; Zhang, L.; Wang, Y.; Ma, Y.; Guo, T.; Chen, Y., Molecular-Level Dispersion of Graphene into Poly(Vinyl Alcohol) and Effective Reinforcement of Their Nanocomposites. *Advanced Functional Materials* **2009**, 19, 2297-2302.
7. Zhao, X.; Zhang, Q.; Chen, D.; Lu, P., Enhanced Mechanical Properties of Graphene-Based Poly(Vinyl Alcohol) Composites. *Macromolecules* **2010**, 43, 2357-2363.

8. Huang, Y.; Young, R. J., Analysis of the Fragmentation Test for Carbon-Fibre/Epoxy Model Composites by Means of Raman Spectroscopy. *Composites Science and Technology* **1994**, 52, 505-517.
9. Hummers, W. S.; Offeman, R. E., Preparation of Graphitic Oxide. *Journal of the American Chemical Society* **1958**, 80, 1339-1339.
10. Xu, Y.; Sheng, K.; Li, C.; Shi, G., Self-Assembled Graphene Hydrogel via a One-Step Hydrothermal Process. *ACS Nano* **2010**, 4, 4324-4330.
11. Li, Z.; Wang, R.; Young, R. J.; Deng, L.; Yang, F.; Hao, L.; Jiao, W.; Liu, W., Control of the Functionality of Graphene Oxide for Its Application in Epoxy Nanocomposites. *Polymer* **2013**, 54, 6437-6446.
12. Hermans, J. J.; Hermans, P. H.; Vermaas, D.; Weidinger, A., Quantitative Evaluation of Orientation in Cellulose Fibres from the X-Ray Fibre Diagram. *Recueil des Travaux Chimiques des Pays-Bas* **1946**, 65, 427-447.
13. Wilson, N. R.; Pandey, P. A.; Beanland, R.; Young, R. J.; Kinloch, I. A.; Gong, L.; Liu, Z.; Suenaga, K.; Rourke, J. P.; York, S. J.; Sloan, J., Graphene Oxide: Structural Analysis and Application as a Highly Transparent Support for Electron Microscopy. *ACS Nano* **2009**, 3, 2547-2556.
14. Rourke, J. P.; Pandey, P. A.; Moore, J. J.; Bates, M.; Kinloch, I. A.; Young, R. J.; Wilson, N. R., The Real Graphene Oxide Revealed: Stripping the Oxidative Debris from the Graphene-Like Sheets. *Angewandte Chemie International Edition* **2011**, 50, 3173-3177.
15. Ferrari, A. C.; Basko, D. M., Raman Spectroscopy as a Versatile Tool for Studying the Properties of Graphene. *Nature Nanotechnology* **2013**, 8, 235-246.
16. Liu, T.; Kumar, S., Quantitative Characterization of SWNT Orientation by Polarized Raman Spectroscopy. *Chemical Physics Letters* **2003**, 378, 257-262.
17. van Gurp, M., The Use of Rotation Matrices in the Mathematical Description of Molecular Orientations in Polymers. *Colloid and Polymer Science* **1995**, 273, 607-625.
18. Cooper, C. A.; Young, R. J.; Halsall, M., Investigation into the Deformation of Carbon Nanotubes and Their Composites through the Use of Raman Spectroscopy. *Composites Part A: Applied Science and Manufacturing* **2001**, 32, 401-411.
19. Liu, H.; Brinson, L. C., Reinforcing Efficiency of Nanoparticles: A Simple Comparison for Polymer Nanocomposites. *Composites Science and Technology* **2008**, 68, 1502-1512.
20. Gong, L.; Kinloch, I. A.; Young, R. J.; Riaz, I.; Jalil, R.; Novoselov, K. S., Interfacial Stress Transfer in a Graphene Monolayer Nanocomposite. *Advanced Materials* **2010**, 22, 2694-2697.
21. Deng, L.; Eichhorn, S. J.; Kao, C.-C.; Young, R. J., The Effective Young's Modulus of Carbon Nanotubes in Composites. *ACS Applied Materials & Interfaces* **2011**, 3, 433-440.
22. Hull, D., *An Introduction to Composite Materials*. 1st ed.; Cambridge University Press: Cambridge, 1981.
23. Bower, D. I., Orientation Distribution Functions for Uniaxially Oriented Polymers. *Journal of Polymer Science: Polymer Physics Edition* **1981**, 19, 93-107.

Chapter 7 Interfacial Stress Transfer in Graphene Oxide Nanocomposites*

7.1 Introduction

Graphene [1] has attracted a rapid increase in attention for applications in a variety of fields, such as nanocomposites [2-4]. Its derivative - graphene oxide (GO) is also playing an increasingly important role, because of its excellent properties and the ability to produce it in large quantities at relatively low cost [5]. The oxygen functional groups [3] enable the hydrophilic GO to be dispersed homogeneously in water and water-soluble polymers, such as poly(vinyl alcohol) (PVA) [6-9]. Therefore, GO, unlike graphene, has the potential to have better significant interfacial adhesion in nanocomposites, even though, the mechanical properties of GO itself are thought to be inferior to those of graphene [10]. According to a recent comparison [11], the mechanical properties of GO-based PVA nanocomposites are unexpectedly not as good as those of an equivalent graphene-based nanocomposite. It appears therefore that a balance needs to be struck between the inherent mechanical properties of the graphene-based filler and the strength of the interface between the filler and matrix.

Chapter 4 presented a study to monitor the deformation mechanics of monolayer GO on a substrate. It was demonstrated that the stress/strain sensitive Raman D band underwent downshift under tensile strain [12, 13], similar to what was found previously on graphene [4]. It was demonstrated that the Raman D band shift rate with strain ($d\omega_D/d\varepsilon$) can be used to measure the strain distribution across the GO flake along the direction of tensile stress.

Given the good interfacial adhesion, in real nanocomposites, especially for those reinforced by nano-fillers, the misorientation of the filler is inevitable. Chapter 5

* This chapter is based on a paper, 'Interfacial Stress Transfer in Graphene Oxide Nanocomposites', *ACS Applied Materials & Interfaces* **2013**, 5, 456-463.

presented a model to quantify the spatial orientation of graphene in terms of an orientation distribution function. This model was further extended in Chapter 6 to quantify the spatial orientation of graphene-based materials in bulk nanocomposites, and in particular, to determine classical Krenchel orientation factor η_o thus to correlate the degree of spatial orientation of the fillers with the mechanical properties of the nanocomposites.

Although a number of types of graphene can be used to reinforce nanocomposites, and these nanocomposites can be prepared by various methods, the fundamental understanding of the mechanics of graphene-based nanocomposites is still lacking, regardless of the particular type of graphene, matrix or preparation method. In the present chapter, a thorough investigation is undertaken using the $d\omega_D/d\varepsilon$ to monitor the reinforcement of PVA using GO, also taking into account the size and orientation effect of the GO fillers. The effective modulus of GO in the nanocomposites can be estimated, and the reasons leading to this effective modulus, lower than the Young's modulus of GO, are discussed.

7.2 Experimental

7.2.1 Materials

The PVA ($M_w \sim 89000$ - 98000 , 99+% hydrolyzed) was purchased from Sigma Aldrich and used as received. The graphite (Grade 2369) was supplied by Graphexel Ltd. All other reagents were of analytical grade and used without further purification.

7.2.2 Preparation

The GO was prepared using the modified Hummers method (Chapter 4) [14, 15]. Briefly, 3 g graphite was added to 70 ml of concentrated sulfuric acid while stirring at room temperature. The mixture system was then cooled to 0 °C when 1.5 g sodium nitrate was added. While stirring, 9 g potassium permanganate was added slowly, to avoid a rapid temperature rise. The mixture was then placed into a 40 °C water bath for 0.5 h, followed by the addition of 140 ml of water and it was stirred for another 15 min. An additional 500 ml water and 20 ml of 6 % w/v H_2O_2 were

added subsequently after which the colour of the mixture turned from brown to yellow. The mixture was then repeatedly washed with 250 ml of 1:10 HCl aqueous solution and centrifuged 3 times. Following this, the mixture was repeatedly washed with water and centrifuged until the pH was approximately 7. Finally, the GO was dispersed in water to make an aqueous suspension for later use.

The PVA powder was dissolved in water at 90 °C to give a 10 wt% PVA aqueous solution (Chapter 6). The GO suspension and PVA solution were then mixed to form a series of dispersions with GO concentrations of 1 wt%, 2 wt%, 3 wt% and 5 wt%. Neat PVA solution was used as a comparison. These solutions were placed into a 120 W sonication bath for 30 min to obtain homogenous dispersions. They were then allowed to stand overnight to fully remove any bubbles. For mechanical testing, the dispersions were cast into Petri dishes at room temperature for film formation. For the Raman deformation studies, the dispersions were cast onto PMMA beams. In both cases the nanocomposites formed were allowed to dry under ambient conditions to completely evaporate the solvent.

7.2.3 Characterization

Atomic force microscope (AFM) images were obtained using a Veeco CP-II system in conjunction with the 'RTESPA' probe (Bruker) in the tapping mode. Scanning electron microscope (SEM) images were obtained using a Philips XL30 FEGSEM for GO flakes and EVO60 VPSEM (Zeiss) for nanocomposites. The nanocomposite sample was fractured by hand at room temperature and fixed vertically with the fracture surface towards the electron gun and it was coated with gold before analysis. X-ray diffraction (XRD) was carried out using an X'Pert DY609 X-Ray diffractometer (Philips) with a Cu K α radiation source ($\lambda = 1.542\text{\AA}$).

The tensile properties of the neat PVA and GO/PVA nanocomposites with different loadings were evaluated using an Instron-1122 universal testing machine. The film samples were cut into dumbbell shape with a gauge length of 15 mm, a width of ~3.96 mm and a thickness of around 0.075 mm. Before testing the samples were left in a climate-controlled laboratory for 24 h at a temperature of $23.0 \pm 0.1^\circ\text{C}$ and a relative humidity of $50 \pm 5\%$. The specimens were deformed at a loading rate of 1

mm/min. The dynamic mechanical properties were evaluated using a DMA Q800 (TA Instruments). Specimens were heated from -10 °C to 120 °C at a rate of 3 °C/min and deformed using a frequency of 1 Hz and a static force of 0.005 N. Data were averaged from 2-3 specimens for each nanocomposite composition.

The GO loading is converted from mass fraction w_{GO} (wt%) to volume fraction V_{GO} (vol%) as [9]:

$$V_{GO} = \frac{w_{GO}\rho_{PVA}}{w_{GO}\rho_{PVA} + (1 - w_{GO})\rho_{GO}} \quad (7.1)$$

Here, ρ_{PVA} and ρ_{GO} represent the density of PVA and GO, which are 1.3 g/cm³ and 2.2 g/cm³, respectively [2, 7, 16]. As a result, the mass fractions of 1, 2, 3 and 5 wt% GO/PVA are equivalent to volume fractions of 0.6, 1.2, 1.8 and 3.0 vol%, respectively.

Raman spectroscopy test was conducted using a Renishaw 1000/2000 Raman spectrometer system with a HeNe laser (633 nm excitation). The PMMA beams with GO/PVA films on their surface were deformed in a four-point bending rig placed on the Raman microscope stage. A resistance strain gauge was bonded to the specimen surface using cyanoacrylate adhesive to measure the surface strain. The beam was deformed stepwise and Raman spectra were collected from the central area of nanocomposite at each strain level. The polarization of the incident laser was parallel to the tensile direction, and the laser beam focused to a spot of around 1~2 μm in diameter [17].

7.3 Results and Discussion

7.3.1 Microstructure of GO and GO/PVA Films

The thickness of the GO flake was measured by AFM height profile (Fig. 7.1). It can be seen the thickness is of the order of 1 nm, typical of exfoliated GO monolayers, demonstrating the complete exfoliation of the GO flakes after oxidation [2].

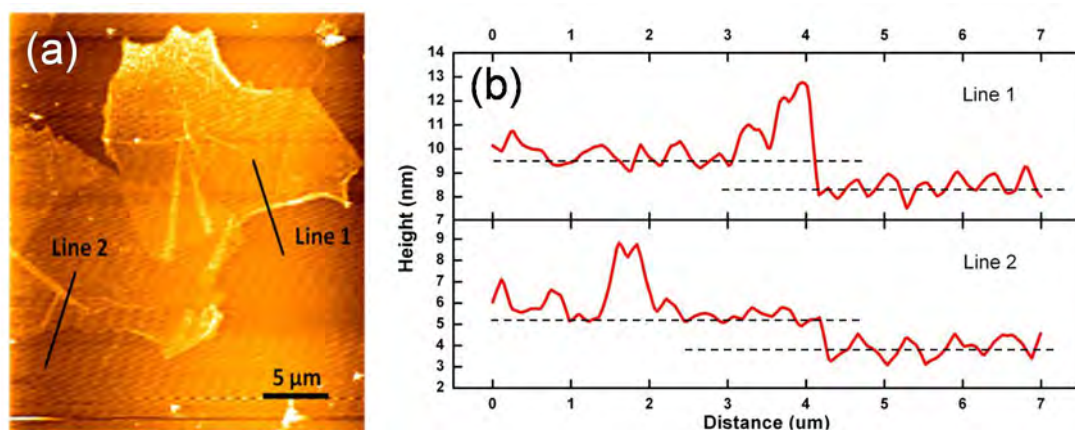


Figure 7.1 (a) AFM image of the GO flakes. (b) The height profiles with a typical thickness of the order of 1 nm.

Fig. 7.2 shows an SEM micrograph of the GO flakes, and their average lateral size was measured in Chapter 4 to be $\sim 14.85 \mu\text{m}$.

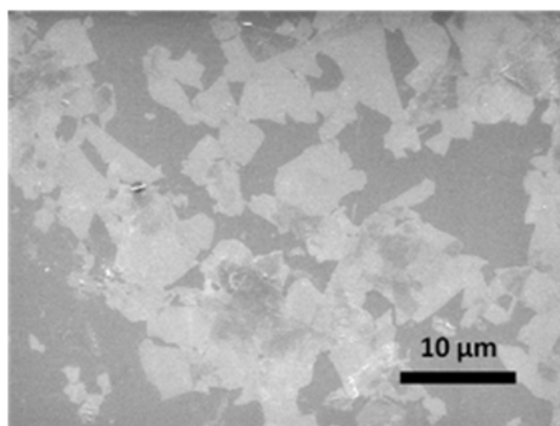


Figure 7.2 SEM micrograph of the GO flakes on SiO₂ substrate.

The dispersion of pure GO, neat PVA and GO/PVA with all the compositions was characterized by XRD (Fig. 7.3). The characteristic XRD diffraction peak of the pure GO is at $2\theta = 10.5^\circ$, corresponding to a d -spacing of 0.84 nm. The XRD pattern of the neat PVA is quite different with a peak at $2\theta = 19.6^\circ$. The XRD patterns of all of the GO/PVA nanocomposites films are similar to those of neat PVA sample, indicating the GO flakes have been exfoliated completely during the nanocomposite preparation [18]. No changes (including broadening or shifting) of the PVA peak in Fig. 7.3 were observed, indicating the degree of crystallinity and size of PVA crystals was not changed significantly by the incorporation of GO [19].

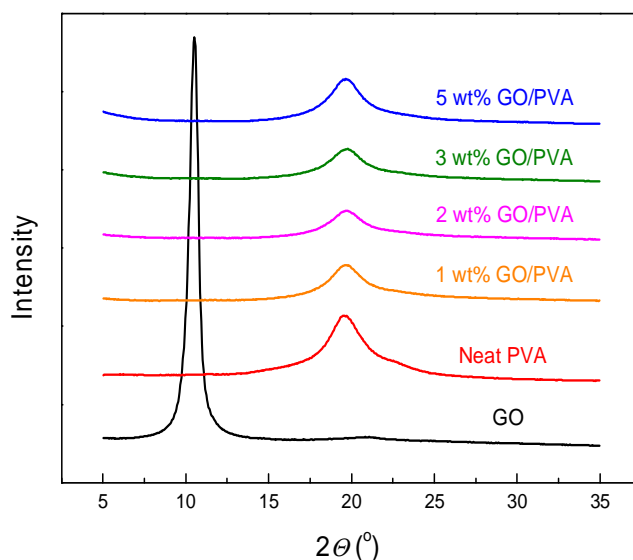


Figure 7.3 XRD patterns of GO, neat PVA and GO/PVA nanocomposites with different GO loadings.

Raman spectra were obtained from the middle of the nanocomposite films on the PMMA beams and a typical Raman spectrum of the 1 wt% GO/PVA nanocomposite is shown in Fig. 7.4, along with the spectra of neat PVA and neat GO powder. It can be seen that although the loading of the GO in the nanocomposite is only 1 wt% (0.6 vol%) the Raman bands of the GO dominate the spectrum for the nanocomposite. In the spectrum of GO, the G band around 1600 cm^{-1} corresponds to the E_{2g} phonon at the Brillouin zone centre (Γ point) [20]. The D band, which has a peak position at around 1335 cm^{-1} , is usually assigned to the \mathbf{K} point phonons of A_{1g} symmetry, and is associated with the presence of defects [21]. The spectra of the GO and the nanocomposite are similar to those reported in the literature [22]. They are quite different, however, from the spectrum of pristine graphene [23], which has one sharp G band and no D band. In addition pristine graphene has a 2D (or G') band which is absent in GO. The broad G and D bands, and a D band which is of higher intensity than the G band are thought to be due to the presence of sp^3 carbon as a result of the amorphization of the graphite during oxidation process [24].

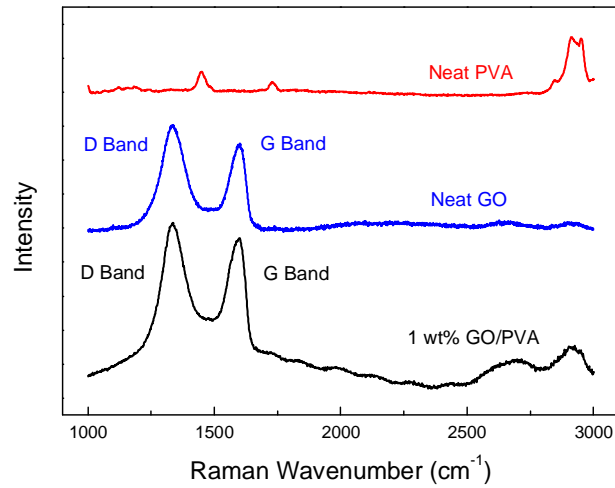


Figure 7.4 Raman spectra of neat PVA, neat GO and a 1 wt% GO/PVA nanocomposite.

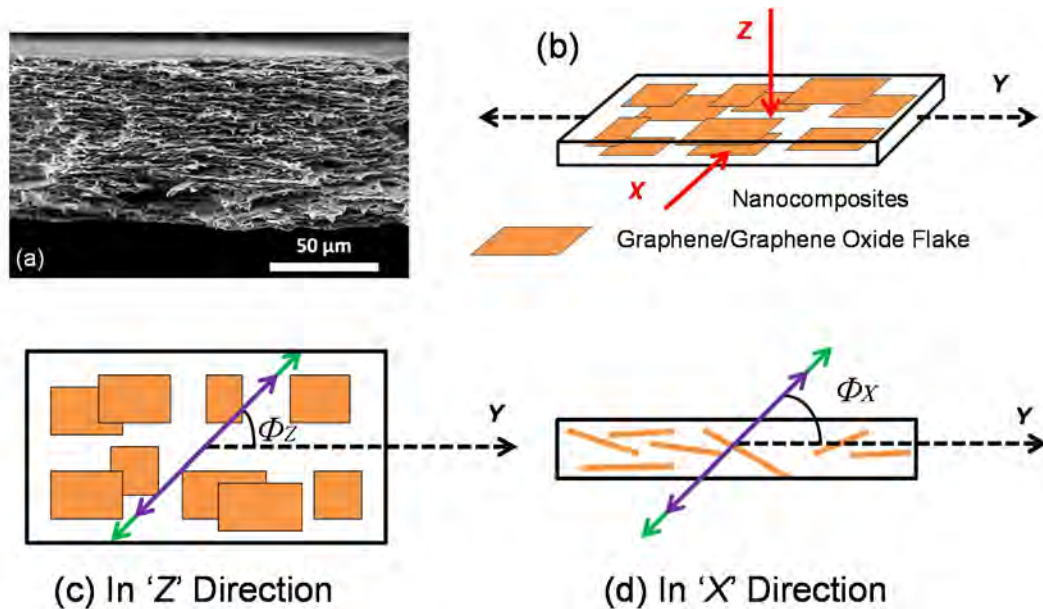


Figure 7.5 (a) SEM micrograph showing the layered microstructure of the 5 wt% GO/PVA nanocomposite. (b) Schematic illustration of the geometry of the Raman spectroscopic analysis of the GO/PVA nanocomposites films with (c) the laser beam parallel to Z direction, and (d) the laser beam parallel to X direction. The red arrows represent the direction of laser propagation and the purple and green arrows represent the directions of polarization of the incident radiation and scattered radiation, respectively.

Fig. 7.5 shows the SEM image of a room temperature fracture surface of a PVA nanocomposite film containing 5 wt% of GO in which a layered structure can be

clearly seen. Figs. 7.5(b), (c) and (d) show the definition of X, Y and Z direction, and the angles Φ_Z and Φ_X relative to the specimen through which the specimens were rotated and the polarized Raman spectroscopy was used to quantify the spatial orientation of the GO in the nanocomposites, as shown in Chapters 5 and 6. For the following deformation test, the tensile stress was applied along the Y axis.

7.3.2 Mechanical Properties of GO/PVA Films

The mechanical properties of the materials were studied by tensile testing. Typical stress-strain curves for the different nanocomposites and pure PVA are shown in Fig. 7.6(a). It can be seen that the Young's modulus and yield stress of the nanocomposites increases as the GO loading increases, whereas the elongation to failure decreases. This behaviour is typical of that found in previous investigations on similar systems [9].

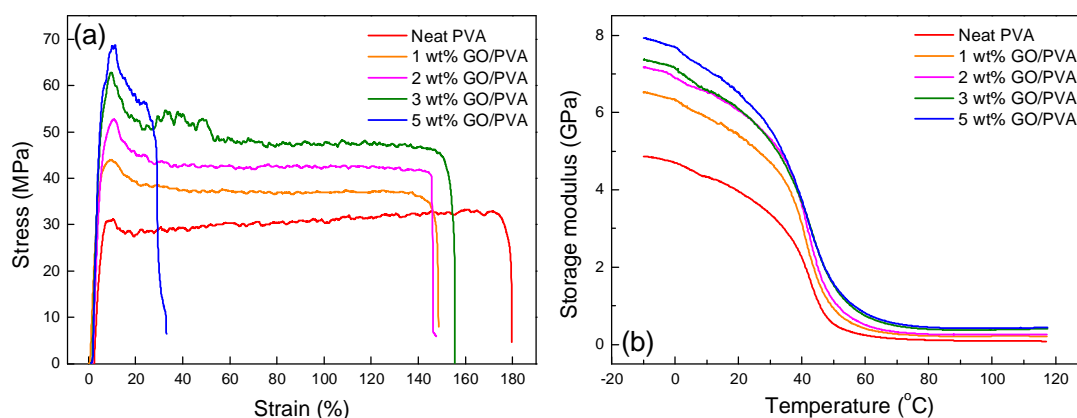


Figure 7.6 Mechanical properties of the neat PVA and GO/PVA nanocomposites with different GO loadings. (a) Stress-strain curves at 23 ± 1 °C and (b) Storage modulus as a function of temperature.

The variation of the storage modulus of the nanocomposites with temperature is also shown in Fig. 7.6(b). It can be seen that the addition of the GO increases the storage modulus at all temperatures. Table 7.1 gives the values of the storage modulus for each of the compositions at 20 °C. As the GO loading increase from 0 wt% to 5 wt%, the average storage modulus at 20 °C increases from 4.4 GPa to 6.5 GPa. This nearly 50 % increase indicates that the dynamic mechanical properties have also

been enhanced by the incorporation of GO. It is instructive to compare this behaviour with that expected from theoretical considerations.

Table 7.1 Storage modulus of the GO nanocomposites at 20 °C and the corresponding $E_{\text{eff}}(\text{GO})$ determined using the rule of mixtures.

Materials	Storage modulus (GPa)	$E_{\text{eff}}(\text{GO})$ (GPa)
Neat PVA	4.4 ± 0.7	-
1wt% GO/PVA	5.1 ± 0.9	121 ± 21
2wt% GO/PVA	5.7 ± 0.4	113 ± 8
3wt% GO/PVA	6.1 ± 0.1	99 ± 2
5wt% GO/PVA	6.5 ± 0.7	74 ± 8

The mechanics of the reinforcement of polymers by graphene has been reviewed recently [4]. The simplest approach to use is the rule of mixtures that provides an upper bound for the Young's modulus of a graphene-based composite E_{comp} as [25]:

$$E_{\text{comp}} = \eta_l \eta_o E_{\text{GO}} V_{\text{GO}} + (1 - V_{\text{GO}}) E_m = E_{\text{eff}}(\text{GO}) V_{\text{GO}} + (1 - V_{\text{GO}}) E_m \quad (7.2)$$

where E_m is the Young's modulus of matrix. η_o and η_l are the Krenchel orientation factor and the size factor of the GO in the nanocomposites. $E_{\text{eff}}(\text{GO}) = \eta_o \eta_l E_{\text{GO}}$, is the effective modulus of GO, as a measure of the GO modulus that takes into effect in the nanocomposites. This equation would be appropriate for the situation where both the matrix and the filler were subjected to uniform strain [25]. This is the situation, for example, in the case of long aligned fibres in a matrix, for which the in-plane aligned GO layers in our GO/PVA composites are a 2D analogy. The calculation of the $E_{\text{eff}}(\text{GO})$ of the nanocomposite films using Eq. 7.2 shows the $E_{\text{eff}}(\text{GO})$ falls from around 121 GPa for 1 wt% GO loading to 74 GPa at 5 wt% loading (Table 7.1).

As discussed in Chapter 1, the effect of size of the embedded fillers on the mechanical property of the nanocomposites can be determined by the size factor η_l :

$$\eta_l = 1 - \frac{\tanh\left(\frac{ns}{\sqrt{2}}\right)}{\frac{ns}{\sqrt{2}}} \quad (7.3)$$

where

$$n = \sqrt{\frac{2G_m}{E_{GO}} \left(\frac{V_{GO}}{1 - V_{GO}} \right)} \quad (7.4)$$

s is the aspect ratio of the GO flakes, and G_m is the shear modulus of the matrix polymer, which can be obtained by [26]:

$$E_m = 2G_m(1 + \nu) \quad (7.5)$$

where ν is the Poisson's ratio of the PVA matrix, taken as 0.4 [27]. Herein the value of η_l is the function of the GO aspect ratio and also the GO concentration in the nanocomposites. If the average lateral size and thickness of GO flakes are taken as 14.85 μm (Chapter 4) and 0.84 nm (Fig. 7.3), respectively, the corresponding η_l for the GO/PVA with different GO concentration are calculated as shown in Table 7.2.

Table 7.2 Size factor η_l and Krenchel orientation factor η_o for the GO/PVA nanocomposites.

Specimens	Size factor η_l	Krenchel orientation factor η_o
1wt% GO/PVA	0.99	0.78
2wt% GO/PVA	0.99	0.75
3wt% GO/PVA	0.99	0.69
5wt% GO/PVA	0.99	0.72

It is shown in Chapter 6 that the spatial orientation of GO can be well reflected by the values of Krenchel orientation factor η_o , which are also summarized in Table 7.2. Table 7.2 shows how η_l and η_o vary as the GO loading changes in the nanocomposites. It can be seen that the η_l is almost constant because the size of the GO flakes are relatively large [28], and the strain distribution along the flake is almost constant, as discussed in Chapter 4. Nevertheless the value of η_o drops as the GO loading increases, possibly due to the incorporation of extra GO making it more

difficult for the other GO flakes to be well aligned. Substituting $E_{\text{eff}}(\text{GO})$ in Table 7.1 and η_l and η_o in Table 7.2 into Eq. 7.2, E_{GO} can be calculated as around 100~160 GPa, slightly lower than the values obtained by direct measurement [10, 29]. There are two possible reasons for this: (1) the invisible cracks and wrinkles in the GO flakes may damage their structural continuity thus stop the stress transfer across the entire flake, being equal to the situation with a patchwork of small flakes [28], and this leads to an overestimation of the length factor η_l when it was measured directly from the SEM image; (2) the edge-by-edge aggregation of the GO flakes that decreases $E_{\text{eff}}(\text{GO})$ [30].

7.3.3 Deformation of Nanocomposites

It is well established that Raman spectroscopy can be used to follow the micromechanics of deformation in a wide range of different carbon-based systems [12, 13, 31-34], and the technique gives unprecedented insight into the deformation processes involved from the stress-induced Raman bands shifts. Most of the studies have been undertaken using shifts of either the G or 2D (G') bands but there are also reports of the D band undergoing stress-induced shifts in graphene [35] and there is one report of stress-induced shifts of the Raman G band during the deformation of impregnated GO paper [36]. Raman spectroscopy has been employed to follow deformation micromechanics in graphene reinforced model nanocomposite [32, 37, 38], but to our knowledge, the technique has not yet been used for the analysis of deformation micromechanics in GO-based nanocomposites.

In this present study Raman spectra were obtained from the GO nanocomposites, with the laser beam parallel to the Z axis (Fig. 7.5). Because the G band in GO is known to consist of at least two components [36] and the overall shape of the band is asymmetric and it was difficult to detect any well-defined band shifts, during deformation and so the D band position (ω_D) was monitored as a function of strain ε . Fig. 7.7 shows the D band for the 1 wt% GO/PVA nanocomposite before and after tensile deformation to 0.4% strain and it can be seen that there is a significant strain-induced downshift of the band. Strain modifies the crystal phonons in graphene, with tensile strain resulting in mode softening [13, 31]. Thus the downshift of the D band can be understood in terms of the elongation of the C-C bonds.

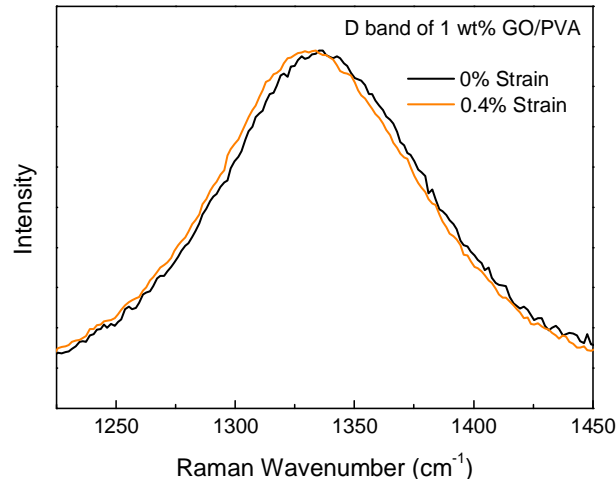


Figure 7.7 D band of 1 wt% GO/PVA nanocomposite before and after tensile deformation. (The intensity of D band has been rescaled to same level)

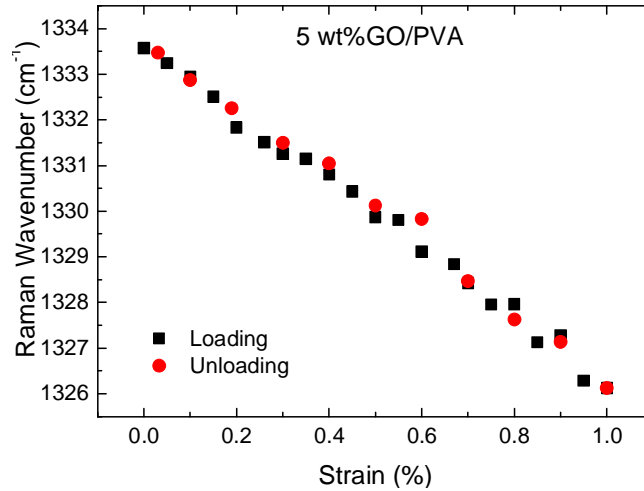


Figure 7.8 Shift of the ω_D with strain for the 5 wt% GO/PVA nanocomposite, for loading to 1% strain followed by unloading.

It should be noted that shifts of these bands could also be obtained without any deformation during exposure of the nanocomposites to the Raman laser beam, especially at high power levels, presumably due to degradation of the unstable GO material in the laser beam. The data shown in this present study were all obtained at low laser power, so avoiding any problem with beam damage. Fig. 7.8 shows the shift of ω_D for the 5 wt% GO/PVA nanocomposite and it can be seen that there is an approximately linear shift of ω_D with strain that is reversible upon unloading, excluding the possibility that the downshift is from the laser heating effect. It is noteworthy that the data points are less scattered than that in Figs. 4.6 and 4.7, and

this is because that the large amount of GO flakes in the GO/PVA nanocomposites give much stronger Raman scattering intensity than just a monolayer GO flake, leading to a higher signal-to-noise ratio.

Fig. 7.9(a) shows the downshift of the Raman D band with tensile strain, fitted using a single Lorentzian peak, for all the nanocomposite compositions. The goodness of fit in each case can be seen from Figs. 7.9(b) show that there is a linear relationship between ω_D and strain ε . For each composition the Raman D bands shift approximately linearly to a lower wavenumber as the strain increases indicating good interfacial stress transfer between the GO and PVA matrix, with no obvious slippage [32].

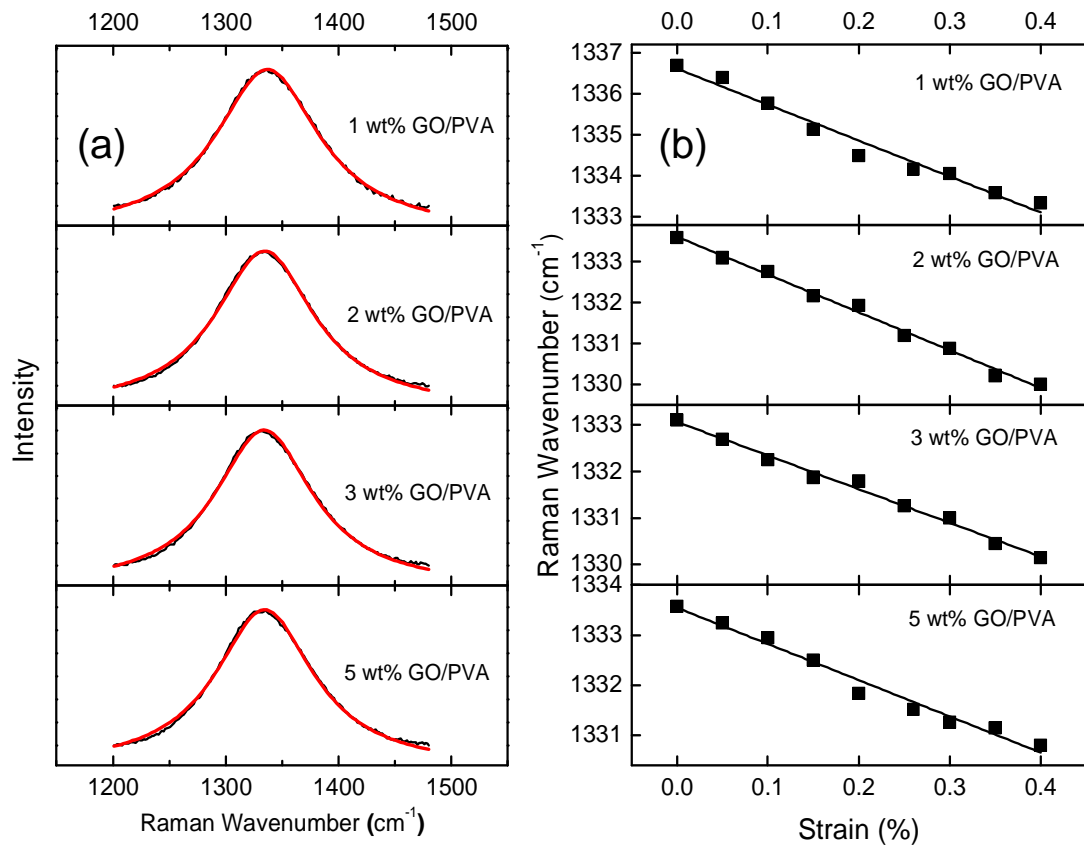


Figure 7.9 (a) Experimental (black) and Lorentz fitted (red) D band and (b) Shift of ω_D as a function of applied strain of the GO/PVA nanocomposites with different loadings.

At least two tests were repeated for each composition and the average D band shift rate with strain ($d\omega_D/d\varepsilon$) for 1 wt%, 2 wt%, 3 wt% and 5 wt% GO loadings are

shown in Fig. 7.10. It can be seen that the $d\omega_D/d\varepsilon$ falls slightly with GO loading with an average value of around $-8 \text{ cm}^{-1}/\%$ strain.

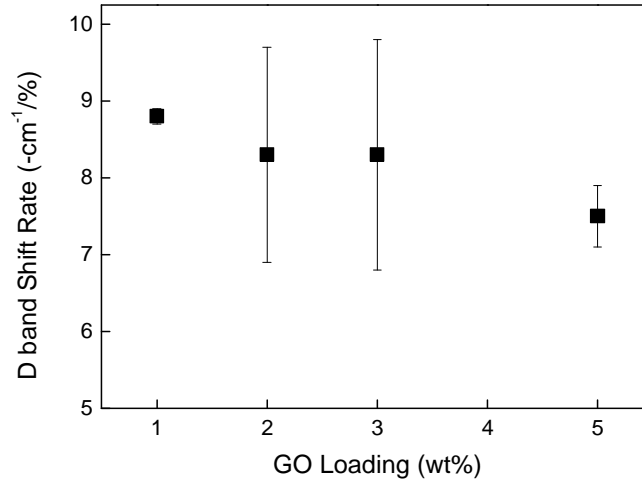


Figure 7.10 Average $d\omega_D/d\varepsilon$ of two measurements as the function of GO loading for the GO/PVA nanocomposites.

7.3.4 Mechanics of Deformation

It is well established that for carbon-based systems the Raman band shift rate for a composite can be used to estimate both the efficiency of stress transfer and the effective Young's modulus of the filler, for both the 2D and G bands [34, 39]. In order to do this with the $d\omega_D/d\varepsilon$ value in this study it is necessary to introduce the Grüneisen parameter. This is a measure of how the phonon frequency is altered under a small change in the volume of the crystallographic unit cell [40]. In our case, with exfoliated GO layers, only the changes in the longitude and traverse directions during deformation need to be considered. Thus, the simplified Grüneisen parameter of the Raman D band γ_D , defined as [13, 41]

$$\gamma_D = -\frac{1}{\omega_D^0} \frac{d\omega_D}{d\varepsilon} (1 - \nu) \quad (7.6)$$

can be employed. ω_D^0 is the ω_D at zero strain, and ν is either the Poisson's ratio of the matrix of nanocomposites or of the graphene itself for freestanding graphene. This relationship can be used to estimate the band shift as a function of applied strain for GO, from knowledge of the behaviour of graphene.

In the literature [13, 35, 41], it is found that the measured value of the Grüneisen parameter for graphene varies as a result of the interaction of graphene and the substrate [36]. We have therefore chosen the value for free-hanging graphene of $\gamma_D = 3.55$ [13, 41]. If $\nu = 0.40$ is taken here for the PVA matrix [27], the $d\omega_D/d\varepsilon$ of embedded graphene is calculated to be around $-30 \text{ cm}^{-1}/\%$, which is, of course, approximately half the value of $-60 \text{ cm}^{-1}/\%$ strain found experimentally for the 2D band in graphene [13]. Using a same value of $\gamma_D = 3.55$, and the Poisson's ratio of graphene $\nu = 0.15$ [42], the $d\omega_D/d\varepsilon$ for freestanding graphene is calculated around $-40 \text{ cm}^{-1}/\%$ [13]. However, this value is 2~3 times the calculated $d\omega_D/d\varepsilon$ for freestanding monolayer GO ($\sim -14 \text{ cm}^{-1}/\%$) as shown in Chapter 4. To exclude the effect of the different Poisson's ratio of the polymer matrix and for general purpose, all the $d\omega_D/d\varepsilon$ in the following discussions are converted to the values (Table 7.3) for freestanding materials using the similar manner [13].

Table 7.3 The values of measured and calculated (using Eq. 7.6) $d\omega_D/d\varepsilon$, and of $E_{\text{eff}}(\text{GO})$, determined using Eq. 7.7, for the different nanocomposite compositions.

Samples	Measured $d\omega_D/d\varepsilon$ ($\text{cm}^{-1}/\%$)	Calculated $d\omega_D/d\varepsilon$ ($\text{cm}^{-1}/\%$)	$E_{\text{eff}}(\text{GO})$ (GPa)
1wt% GO/PVA	-8.8 ± 0.1	-12.5 ± 0.1	133 ± 1
2wt% GO/PVA	-8.3 ± 1.4	-11.8 ± 2.0	125 ± 21
3wt% GO/PVA	-8.3 ± 1.5	-11.8 ± 2.1	125 ± 22
5wt% GO/PVA	-7.5 ± 0.4	-10.6 ± 0.6	113 ± 6

The calculated $d\omega_D/d\varepsilon$ for freestanding GO and the Krenchel orientation factor η_o obtained for the GO/PVA, GO/epoxy [43] and GO/PMMA nanocomposites [44] (Chapter 6) are plotted in Fig. 7.11, where in the calculation the Poisson's ratio of epoxy and PMMA is taken as 0.38 [45] and 0.35 [46], respectively. A clear drop in the $d\omega_D/d\varepsilon$ can be found when the GO concentration in the PVA matrix increases, but they are still higher than those of GO/epoxy and GO/PMMA. Those data points can be fitted a straight line, the extension of which indicates that the $d\omega_D/d\varepsilon$ for freestanding GO is around $-20 \text{ cm}^{-1}/\%$ when the Krenchel orientation factor η_o equals unity, that is, when the GO flake is perfectly oriented. It is noted that this $d\omega_D/d\varepsilon$ is

half of that for freestanding monolayer graphene, in broad agreement with the value ($\sim 14 \text{ cm}^{-1}/\%$) obtained experimentally in Chapter 4.

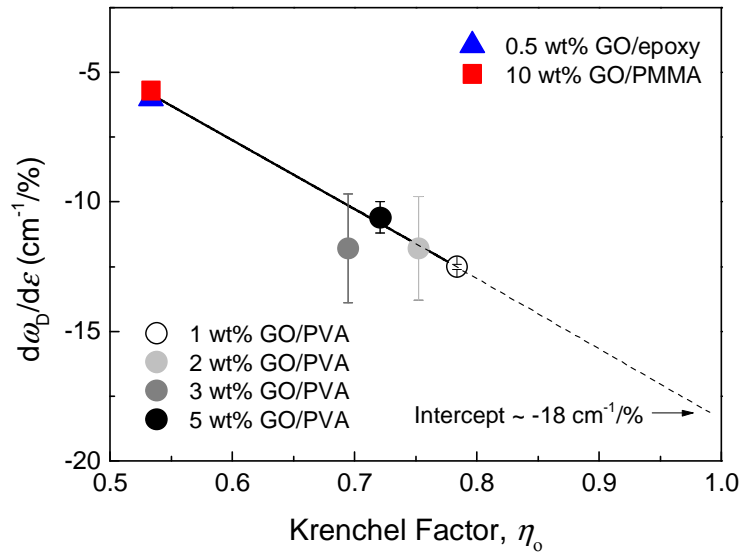


Figure 7.11 The correlation between $d\omega_D/d\epsilon$ and Krenchel orientation factor η_o for a variety of GO-based nanocomposites.

Gomez-Navarro, Burghard and Kern [29] investigated the elastic deformation of chemically-reduced GO monolayers using an AFM indentation technique on a suspended film of material similar to that employed in an earlier study of exfoliated graphene [47]. GO single layers of up to $1 \mu\text{m}^2$ in size were suspended over a trench in a SiO_2/Si wafer and force-displacement curves were obtained as the AFM tip was pushed into the film. A Young's modulus of $250 \pm 150 \text{ GPa}$ was determined, although considerable scatter was obtained in their data. Suk et al. [10] undertook a similar study of the AFM indentation of GO that had not been reduced and measured an E_{GO} of $208 \pm 23 \text{ GPa}$ when they assumed an effective thickness of 0.7 nm for the GO.

A theoretical study was undertaken by Paci et al. [48] to compare the stress-strain behaviour of graphene and GO containing both epoxide and hydroxyl groups and they predicted a modulus of $>1000 \text{ GPa}$ for the pristine graphene. They simulated the structural modification to form GO and found that it led to a prediction of it having a modulus of half of that for a graphene monolayer with the same thickness ($\sim 0.34 \text{ nm}$). They pointed out that the doubled thickness of GO compared to that of

graphene further halves the modulus to the measured values [29]. As a result, it is thought the structural distortion by functionalization and the increase in thickness are the two main reasons that reduce the stiffness of GO to 250 GPa when compared to that of graphene [10, 48, 49].

As structural distortion reduces the modulus of GO by a factor of 2 [48], also considering the value of $d\omega_D/d\varepsilon$ of GO ($-20 \text{ cm}^{-1}/\%$) halves that of graphene ($-40 \text{ cm}^{-1}/\%$), it is proposed that it is the structural distortion that causes the half reduction of $d\omega_D/d\varepsilon$ compared to that of graphene as discussed in Chapter 4. Based on the derived $d\omega_D/d\varepsilon$ for GO, it is instructive to determine how the Raman band shift can be correlated to the mechanical property of GO, so that the effective level of reinforcement can be evaluated, similar to what has been reported for other graphitic materials [34, 39].

Since monolayer freestanding graphene with a Young's modulus E_{gra} of 1050 GPa [47] has a $d\omega_D/d\varepsilon = -40 \text{ cm}^{-1}/\%$ strain, it is possible to determine the $E_{\text{eff}}(\text{GO})$ in the nanocomposites from the $d\omega_D/d\varepsilon$ listed in Table 7.3 using the following expression:

$$E_{\text{eff}}(\text{GO}) = \frac{d\omega_D/d\varepsilon}{(d\omega_D/d\varepsilon)_{\text{ref}}} \times \frac{t_{\text{gra}}}{t_{\text{GO}}} \times E_{\text{gra}} \quad (7.7)$$

where $(d\omega_D/d\varepsilon)_{\text{ref}}$ denote the reference value of $d\omega_D/d\varepsilon$ for freestanding graphene ($= -40 \text{ cm}^{-1}/\%$) [13, 41]. t_{gra} and t_{GO} represent the thickness of monolayer graphene (0.34 nm) [9] and GO (0.84 nm, obtained from the XRD (Fig. 7.3)), respectively, to account for the effect of the increased thickness on the decrease of the Young's modulus [48]. Again to exclude the effect of the different Poisson's ratio of the matrix, all the $d\omega_D/d\varepsilon$ values may be converted to the value for freestanding materials. The effect of the spatial orientation is not included as any mis-orientation leads to a proportionate reduction in the $E_{\text{eff}}(\text{GO})$ determined either from the storage modulus or through $d\omega_D/d\varepsilon$ [50].

The Raman band shift data gives an independent estimate of the $E_{\text{eff}}(\text{GO})$ in the nanocomposites as shown in Table 7.3. It can be seen that the values are all around 120 GPa and similar to the $E_{\text{eff}}(\text{GO})$ determined from the storage modulus data at low GO loading, further confirming the validity of this model. Even though, these

values are still lower than the Young's modulus of monolayer GO [10, 29]. Fig. 7.12 shows a schematic illustration of the factors that may lead to this discrepancy.

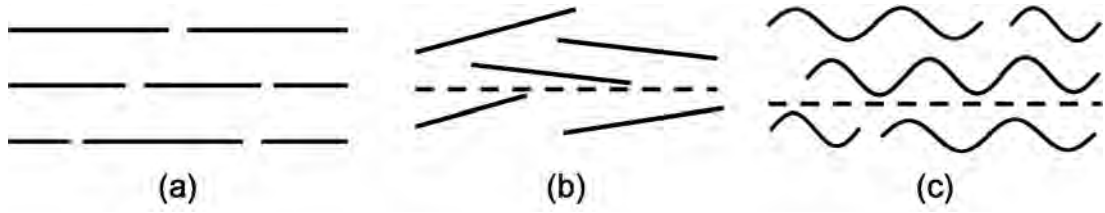


Figure 7.12 Illustrations of the possible arrangements of GO in nanocomposites (a) perfect aligned, (b) misoriented and (c) wrinkled. The solid lines represent side views of GO flakes.

Fig. 7.12(a) shows the situation for perfectly-aligned GO flakes of finite length. In this case, as shown in Chapter 4, large GO flakes still follow the 'shear lag effects' and the flake can be nearly uniformly stressed along the stress direction [37, 51], hence the rule of mixtures should be obeyed with the strain in the GO being equal to the strain in the matrix. Despite the size of the flakes is considerably large, as measured using SEM in Chapter 4, invisible cracks and wrinkles in the GO flakes may damage their structural continuity thus reduce the stress transfer across the entire flake, being equal to the situation with a patchwork of small flakes [28], leading to an overestimation of the size factor η_l .

Fig. 7.12(b) shows the misorientation of GO flakes. It is clear that GO aligned in the direction of stress, gives rise to the majority of the reinforcement in the system. As indicated in Chapter 6, the spatial orientation of GO decreases as the GO loading increase, which is reflected by the generally decrease of the values of $\langle P_2(\cos\theta) \rangle$, $\langle P_4(\cos\theta) \rangle$ and Krenchel orientation factor. The value of Krenchel orientation factor, between 8/15 and 1, can also be used to estimate the $E(\text{GO})$ using the rule of mixtures (Eq. 7.2).

Another factor that will lead to a lower $E_{\text{eff}}(\text{GO})$ is its waviness or the wrinkled geometry (Fig. 7.12(c)). There are two effects in this circumstance, one is that the wrinkled structure can also be understood as the misalignment of GO; the other one may not be so obvious that, the presence of the wrinkle can diminish the structural continuity of individual flake thus stopping the continuous stress transfer over the

entire flake as discussed in Chapter 3. The decrease of $E_{\text{eff}}(\text{GO})$ can also be from the aggregation of GO flakes, and it decreasing with the increase of GO loading seen in Tables 7.2 and 7.3 may be a reflection of more aggregation occurring at higher GO loading. However, the results of XRD (Fig. 7.3) suggest the aggregation might not be from the interlayer stacking, but through edge-by-edge aggregation [30].

The calculated $d\omega_D/d\varepsilon = -14 \text{ cm}^{-1}/\%$, indicated in Chapter 4 is to be the same order of the value of $d\omega_D/d\varepsilon$ ($\sim -20 \text{ cm}^{-1}/\%$) derived here, and an $E_{\text{eff}}(\text{GO})$ can be obtained as $\sim 150 \text{ GPa}$ for the monolayer GO in that case, slightly lower than the values obtained using direct measurement [10]. The difference can be explained as due to the absence of direct bonding formed between the GO flake and the PMMA substrate, as the GO flake was just deposited onto the PMMA substrate without further treatment or top coating.

7.4 Conclusions

A new insight has been obtained into the reinforcement of PVA by GO through the use of Raman spectroscopy. It has also been demonstrated that it is possible to follow stress transfer between the PVA matrix to the GO from stress-induced shifts of the Raman D band. Moreover, it has been shown that it is possible to use the Grüneisen parameter to estimate the $E_{\text{eff}}(\text{GO})$ in the nanocomposites from the $d\omega_D/d\varepsilon$ value to be around 120 GPa . The $E_{\text{eff}}(\text{GO})$ value determined by this method is similar to that obtained using the measured storage modulus and the simple rule of mixtures. In both cases $E_{\text{eff}}(\text{GO})$ was found to decrease as the wt% of GO increases and this has been shown to be consistent with a decrease in the degree of alignment of the GO with increasing loading determined using polarized Raman spectroscopy and also aggregation effects. It is clear that the technique of using Raman spectroscopy to follow the deformation of GO in nanocomposites that has been developed in this study will have important implications in the future for the analysis of graphene-based nanocomposites.

References

1. Novoselov, K. S.; Geim, A. K.; Morozov, S. V.; Jiang, D.; Zhang, Y.; Dubonos, S. V.; Grigorieva, I. V.; Firsov, A. A., Electric Field Effect in Atomically Thin Carbon Films. *Science* **2004**, 306, 666-669.
2. Stankovich, S.; Dikin, D. A.; Dommett, G. H. B.; Kohlhaas, K. M.; Zimney, E. J.; Stach, E. A.; Piner, R. D.; Nguyen, S. T.; Ruoff, R. S., Graphene-Based Composite Materials. *Nature* **2006**, 442, 282-286.
3. Kim, H.; Abdala, A. A.; Macosko, C. W., Graphene/Polymer Nanocomposites. *Macromolecules* **2010**, 43, 6515-6530.
4. Young, R. J.; Kinloch, I. A.; Gong, L.; Novoselov, K. S., The Mechanics of Graphene Nanocomposites: A Review. *Composites Science and Technology* **2012**, 72, 1459-1476.
5. Dikin, D. A.; Stankovich, S.; Zimney, E. J.; Piner, R. D.; Dommett, G. H. B.; Evmenenko, G.; Nguyen, S. T.; Ruoff, R. S., Preparation and Characterization of Graphene Oxide Paper. *Nature* **2007**, 448, 457-460.
6. Xu, Y.; Hong, W.; Bai, H.; Li, C.; Shi, G., Strong and Ductile Poly(Vinyl Alcohol)/Graphene Oxide Composite Films with a Layered Structure. *Carbon* **2009**, 47, 3538-3543.
7. Liang, J.; Huang, Y.; Zhang, L.; Wang, Y.; Ma, Y.; Guo, T.; Chen, Y., Molecular-Level Dispersion of Graphene into Poly(Vinyl Alcohol) and Effective Reinforcement of Their Nanocomposites. *Advanced Functional Materials* **2009**, 19, 2297-2302.
8. Putz, K. W.; Compton, O. C.; Palmeri, M. J.; Nguyen, S. T.; Brinson, L. C., High-Nanofiller-Content Graphene Oxide-Polymer Nanocomposites via Vacuum-Assisted Self-Assembly. *Advanced Functional Materials* **2010**, 20, 3322-3329.
9. Zhao, X.; Zhang, Q.; Chen, D.; Lu, P., Enhanced Mechanical Properties of Graphene-Based Poly(Vinyl Alcohol) Composites. *Macromolecules* **2010**, 43, 2357-2363.
10. Suk, J. W.; Piner, R. D.; An, J.; Ruoff, R. S., Mechanical Properties of Monolayer Graphene Oxide. *ACS Nano* **2010**, 4, 6557-6564.
11. Bao, C.; Guo, Y.; Song, L.; Hu, Y., Poly(Vinyl Alcohol) Nanocomposites Based on Graphene and Graphite Oxide: A Comparative Investigation of Property and Mechanism. *Journal of Materials Chemistry* **2011**, 21, 13942-13950.
12. Cronin, S. B.; Swan, A. K.; Ünlü, M. S.; Goldberg, B. B.; Dresselhaus, M. S.; Tinkham, M., Measuring the Uniaxial Strain of Individual Single-Wall Carbon Nanotubes: Resonance Raman Spectra of Atomic-Force-Microscope Modified Single-Wall Nanotubes. *Physical Review Letters* **2004**, 93, 167401.
13. Mohiuddin, T. M. G.; Lombardo, A.; Nair, R. R.; Bonetti, A.; Savini, G.; Jalil, R.; Bonini, N.; Basko, D. M.; Galiotis, C.; Marzari, N.; Novoselov, K. S.; Geim, A. K.; Ferrari, A. C., Uniaxial Strain in Graphene by Raman Spectroscopy: G Peak Splitting, Grüneisen Parameters, and Sample Orientation. *Physical Review B* **2009**, 79, 205433.
14. Hummers, W. S.; Offeman, R. E., Preparation of Graphitic Oxide. *Journal of the American Chemical Society* **1958**, 80, 1339-1339.
15. Xu, Y.; Sheng, K.; Li, C.; Shi, G., Self-Assembled Graphene Hydrogel via a One-Step Hydrothermal Process. *ACS Nano* **2010**, 4, 4324-4330.

16. Salavagione, H. J.; Martinez, G.; Gomez, M. A., Synthesis of Poly(Vinyl Alcohol)/Reduced Graphite Oxide Nanocomposites with Improved Thermal and Electrical Properties. *Journal of Materials Chemistry* **2009**, 19, 5027-5032.
17. Deng, L.; Eichhorn, S. J.; Kao, C.-C.; Young, R. J., The Effective Young's Modulus of Carbon Nanotubes in Composites. *ACS Applied Materials & Interfaces* **2011**, 3, 433-440.
18. Yang, X.; Li, L.; Shang, S.; Tao, X.-m., Synthesis and Characterization of Layer-Aligned Poly(Vinyl Alcohol)/Graphene Nanocomposites. *Polymer* **2010**, 51, 3431-3435.
19. Kim, H. M.; Lee, J. K.; Lee, H. S., Transparent and High Gas Barrier Films Based on Poly(Vinyl Alcohol)/Graphene Oxide Composites. *Thin Solid Films* **2011**, 519, 7766-7771.
20. Zabel, J.; Nair, R. R.; Ott, A.; Georgiou, T.; Geim, A. K.; Novoselov, K. S.; Casiraghi, C., Raman Spectroscopy of Graphene and Bilayer under Biaxial Strain: Bubbles and Balloons. *Nano Letters* **2011**, 12, 617-621.
21. Ferrari, A. C.; Robertson, J., Interpretation of Raman Spectra of Disordered and Amorphous Carbon. *Physical Review B* **2000**, 61, 14095-14107.
22. Kudin, K. N.; Ozbas, B.; Schniepp, H. C.; Prud'homme, R. K.; Aksay, I. A.; Car, R., Raman Spectra of Graphite Oxide and Functionalized Graphene Sheets. *Nano Letters* **2007**, 8, 36-41.
23. Ferrari, A. C.; Meyer, J. C.; Scardaci, V.; Casiraghi, C.; Lazzeri, M.; Mauri, F.; Piscanec, S.; Jiang, D.; Novoselov, K. S.; Roth, S.; Geim, A. K., Raman Spectrum of Graphene and Graphene Layers. *Physical Review Letters* **2006**, 97, 187401.
24. Moon, I. K.; Lee, J.; Ruoff, R. S.; Lee, H., Reduced Graphene Oxide by Chemical Graphitization. *Nature Communications* **2010**, 1, 73.
25. Young, R. J.; Lovell, P. A., *Introduction to Polymers*. 3rd ed.; CRC Press: Boca Raton, 2011.
26. May, P.; Khan, U.; O'Neill, A.; Coleman, J. N., Approaching the Theoretical Limit for Reinforcing Polymers with Graphene. *Journal of Materials Chemistry* **2012**, 22, 1278-1282.
27. Urayama, K.; Takigawa, T.; Masuda, T., Poisson's Ratio of Poly(Vinyl Alcohol) Gels. *Macromolecules* **1993**, 26, 3092-3096.
28. Zhao, J.; Pei, S.; Ren, W.; Gao, L.; Cheng, H.-M., Efficient Preparation of Large-Area Graphene Oxide Sheets for Transparent Conductive Films. *ACS Nano* **2010**, 4, 5245-5252.
29. Gómez-Navarro, C.; Burghard, M.; Kern, K., Elastic Properties of Chemically Derived Single Graphene Sheets. *Nano Letters* **2008**, 8, 2045-2049.
30. Shen, X.; Lin, X.; Yousefi, N.; Jia, J.; Kim, J.-K., Wrinkling in Graphene Sheets and Graphene Oxide Papers. *Carbon* **2014**, 66, 84-92.
31. Huang, M.; Yan, H.; Chen, C.; Song, D.; Heinz, T. F.; Hone, J., Phonon Softening and Crystallographic Orientation of Strained Graphene Studied by Raman Spectroscopy. *Proceedings of the National Academy of Sciences* **2009**, 106, 7304-7308.
32. Young, R. J.; Gong, L.; Kinloch, I. A.; Riaz, I.; Jalil, R.; Novoselov, K. S., Strain Mapping in a Graphene Monolayer Nanocomposite. *ACS Nano* **2011**, 5, 3079-3084.

33. Robinson, I. M.; Zakikhani, M.; Day, R. J.; Young, R. J.; Galiotis, C., Strain Dependence of the Raman Frequencies for Different Types of Carbon Fibres. *Journal of Materials Science Letters* **1987**, 6, 1212-1214.
34. Cooper, C. A.; Young, R. J.; Halsall, M., Investigation into the Deformation of Carbon Nanotubes and Their Composites through the Use of Raman Spectroscopy. *Composites Part A: Applied Science and Manufacturing* **2001**, 32, 401-411.
35. Ding, F.; Ji, H.; Chen, Y.; Herklotz, A.; Dörr, K.; Mei, Y.; Rastelli, A.; Schmidt, O. G., Stretchable Graphene: A Close Look at Fundamental Parameters through Biaxial Straining. *Nano Letters* **2010**, 10, 3453-3458.
36. Gao, Y.; Liu, L.-Q.; Zu, S.-Z.; Peng, K.; Zhou, D.; Han, B.-H.; Zhang, Z., The Effect of Interlayer Adhesion on the Mechanical Behaviors of Macroscopic Graphene Oxide Papers. *ACS Nano* **2011**, 5, 2134-2141.
37. Gong, L.; Kinloch, I. A.; Young, R. J.; Riaz, I.; Jalil, R.; Novoselov, K. S., Interfacial Stress Transfer in a Graphene Monolayer Nanocomposite. *Advanced Materials* **2010**, 22, 2694-2697.
38. Gong, L.; Young, R. J.; Kinloch, I. A.; Riaz, I.; Jalil, R.; Novoselov, K. S., Optimizing the Reinforcement of Polymer-Based Nanocomposites by Graphene. *ACS Nano* **2012**, 6, 2086-2095.
39. Frank, O.; Tsoukleri, G.; Riaz, I.; Papagelis, K.; Parthenios, J.; Ferrari, A. C.; Geim, A. K.; Novoselov, K. S.; Galiotis, C., Development of a Universal Stress Sensor for Graphene and Carbon Fibres. *Nature Communications* **2011**, 2, 255.
40. Grimvall, G., Phonons in Real Crystals: Anharmonic Effects. In *Thermophysical Properties of Materials*, Elsevier Science B.V.: Amsterdam, 1999; pp 136-152.
41. Ferralis, N., Probing Mechanical Properties of Graphene with Raman Spectroscopy. *Journal of Materials Science* **2010**, 45, 5135-5149.
42. Kudin, K. N.; Scuseria, G. E.; Yakobson, B. I., C₂F, BN, and C Nanoshell Elasticity from *Ab Initio* Computations. *Physical Review B* **2001**, 64, 235406.
43. Li, Z.; Young, R. J.; Wang, R.; Yang, F.; Hao, L.; Jiao, W.; Liu, W., The Role of Functional Groups on Graphene Oxide in Epoxy Nanocomposites. *Polymer* **2013**, 54, 5821-5829.
44. Vallés, C.; Kinloch, I. A.; Young, R. J.; Wilson, N. R.; Rourke, J. P., Graphene Oxide and Base-Washed Graphene Oxide as Reinforcements in PMMA Nanocomposites. *Composites Science and Technology* **2013**, 88, 158-164.
45. Smith, A.; Wilkinson, S. J.; Reynolds, W. N., The Elastic Constants of Some Epoxy Resins. *Journal of Materials Science* **1974**, 9, 547-550.
46. Lu, H.; Zhang, X.; Knauss, W. G., Uniaxial, Shear, and Poisson Relaxation and Their Conversion to Bulk Relaxation: Studies on Poly(Methyl Methacrylate). *Polymer Engineering & Science* **1997**, 37, 1053-1064.
47. Lee, C.; Wei, X.; Kysar, J. W.; Hone, J., Measurement of the Elastic Properties and Intrinsic Strength of Monolayer Graphene. *Science* **2008**, 321, 385-388.
48. Paci, J. T.; Belytschko, T.; Schatz, G. C., Computational Studies of the Structure, Behavior Upon Heating, and Mechanical Properties of Graphite Oxide. *The Journal of Physical Chemistry C* **2007**, 111, 18099-18111.
49. Liu, L.; Zhang, J.; Zhao, J.; Liu, F., Mechanical Properties of Graphene Oxides. *Nanoscale* **2012**, 4, 5910-5916.

50. Andrews, M. C.; Day, R. J.; Hu, X.; Young, R. J., Dependence of Fibre Strain on Orientation Angle for Off-Axis Fibres in Composites. *Journal of Materials Science Letters* **1992**, 11, 1344-1346.
51. Jang, H.-K.; Kim, H.-I.; Dodge, T.; Sun, P.; Zhu, H.; Nam, J.-D.; Suhr, J., Interfacial Shear Strength of Reduced Graphene Oxide Polymer Composites. *Carbon* **2014**, 77, 390-397.

Chapter 8 Conclusions and Suggestions for Future Work

8.1 Conclusions

8.1.1 Model Monolayer Graphene and Graphene Oxide Nanocomposites

The Raman 2D band was used to monitor the deformation of a monolayer graphene nanocomposite – CVD graphene placed onto the top of PET substrate. Unlike the exfoliated graphene flakes studied before, this CVD graphene has wrinkled networks that separate the graphene into isolated islands with average lateral size of around 1~1.5 μm . It has been found that Raman 2D band behaviour deviates from what has been found previously, showing a large band broadening. It was proposed the deviation is a result of the graphene networks as the size of the mechanically isolated graphene islands is too small to fully transfer the stress from the substrate to graphene. Also the size is comparable to the resolution of Raman spectrometer - laser spot size. Based on this, a new model has been established to deconvolute the Raman spectrum by separating the graphene island into elementary units. Thus it can be considered as the summation of the Raman scattering from all the units to take account both the non-uniformity of local strain in the graphene island and the variation of laser intensity in the laser spot. In this circumstance, the Raman scattering, from the units bearing higher strain, shifts more than those from units with lower strain, resulting in the abnormal observation. The good fit between the experimental data and the prediction confirms the appropriateness of this model, validating the use of this technique in estimating the effect of defects such as wrinkles on the performance of graphene-based devices. It also implies that when the characteristic dimensions of the microstructure are of similar size to the spatial resolution of the Raman spectrometer laser spot, the conventional analysis has to be corrected to take into account both the structural non-uniformity and the resolution of the laser beam.

The deformation mechanics of monolayer graphene oxide (GO) has been revealed for the first time by Raman spectroscopy. It was found that the Raman D band

underwent downshift under tensile strain. According to the knowledge of Grüneisen parameter [1], the Raman D band shift rate with strain ($d\omega_D/d\varepsilon$) is just 1/3~1/2 of the value of the monolayer graphene, probably due to the structurally distorted basal plane of GO caused by the introduction of functional groups during oxidation [2]. It has been further demonstrated that the measured $d\omega_D/d\varepsilon$ can be used to monitor the strain distribution from the GO flake edge thus its deformation mechanics can be revealed. It was found that the GO flake also obey continuum mechanics that the stress can be completely transferred from the substrate to the central region of the GO flake, resulting in a strain plateau but it dropped sharply at the edge. This almost constant strain distribution from the GO flake indicates that most part of the flake is able to reinforce a matrix, thus a higher stress transfer efficiency of GO compared to that of graphene can be expected.

8.1.2 Spatial Orientation of Graphene and GO

It has been demonstrated for the first time that well-defined Raman spectra can be obtained from transverse sections of graphene monolayers, as a result of its strong resonance Raman scattering. Based on this, polarized Raman spectroscopy was used to quantify the spatial orientation of graphene in terms of an orientation distribution function (ODF). This analysis was further verified by the height profile of the monolayer graphene showing a similar ODF. Beyond CVD graphene with a high orientation degree, the analysis was also found to be applicable to bulk materials such as HOPG and specimen with a lower orientation degree such as graphene paper. This analysis was extended to quantify the degree of spatial orientation of graphene and GO in the bulk nanocomposites, and related to the mechanical properties of composites through the Krenchel orientation factor η_o [3]. It was found that the spatial orientation of GO decreases as its loading increases in the nanocomposites, possibly because of the added GO flakes make it more difficult for the other flakes to be well aligned.

Another significant new finding of this study is that the Krenchel orientation factor η_o for randomly oriented nanoplatelets is 8/15. This means that random orientation of fillers such as graphene should reduce the Young's modulus of the nanocomposites by less than a factor of 2 compared with the fully-aligned materials.

Compared to the reduction in the modulus of a factor of 5 from aligned to 3D random fibres and nanotubes [3], it means that better levels of reinforcement should be achievable with misaligned nanoplatelets compared with nanotubes and there is less need to ensure accurate alignment of the nanoplatelets.

8.1.3 Deformations Mechanics of GO in Nanocomposites

The method to monitor the deformation of GO in model nanocomposites, and to quantify the spatial orientation of GO in bulk nanocomposite have been used for the first time to monitor the reinforcement of PVA by GO. The size factor η_l and Krenchel orientation factor η_o have been considered to reveal the impact of size and orientation of the filler on the effective modulus of GO ($E_{\text{eff}}(\text{GO})$) in nanocomposites, according to the simple rule of mixtures using the measured storage modulus data.

It was also found that the measured $d\omega_D/d\varepsilon$ for the nanocomposites with different GO loading can be correlated to the corresponding Krenchel orientation factor η_o and hence the value of $d\omega_D/d\varepsilon$ for perfectly aligned GO can be derived, in broad agreement to the experimental value obtained on monolayer GO, which is approximately half of that of graphene. Based on this, it was proposed that the structural distortion after oxidization halves the $d\omega_D/d\varepsilon$ value as well as the Young's modulus of GO [2]. The Young's modulus of GO is further halved by the increased thickness compared to that of graphene, leading to modulus being around 1/4 of that of graphene, in accordance with direct measurements [4, 5].

Moreover, it has been shown that it is possible to interpret the $d\omega_D/d\varepsilon$ using the knowledge of Grüneisen parameter to estimate the $E_{\text{eff}}(\text{GO})$ in the nanocomposites to be around 120 GPa, comparable to the values obtained using the measured storage modulus and the simple rule of mixtures. In both cases the $E_{\text{eff}}(\text{GO})$ was found to decrease as the GO loading increases and this has been shown to be consistent with a decrease in the degree of alignment of the GO with increasing loading determined using polarized Raman spectroscopy. It is clear that the technique of using the Raman spectroscopy to follow the deformation of GO in nanocomposites that has been developed in this study will have important implications in the future for the analysis of GO-based nanocomposites. Beyond just graphene and GO, this approach

should be more widely applicable to other nanoplatelet fillers for which well-defined Raman spectra can be obtained.

8.2 Suggestions for Future Work

8.2.1 Deformation Mechanics of Mono- and Few- Layer GO Flake

It was shown in Chapter 4 that monolayer GO still follows continuum mechanics in the microscale and the strain distribution across the GO flake is almost constant. It was also reported that the reinforcement efficiency of graphene generally decreases as the number of layers increases, due to its poor interlayer shear modulus [6], which has also been confirmed by the direct measurement where the Young's modulus of monolayer is higher than that of few-layer graphene [4, 7]. However for GO membrane, an almost constant Young's modulus has been observed for different number of GO layers using a similar method [5]. This can be understood as the interlayer anchoring or locking because of the bonding formed between the functional groups of adjacent GO flakes [8]. If this can be proved, it will demonstrate that there is less need to exfoliate GO into monolayer or even few-layers in the matrix. This would be particularly useful for certain polymers like epoxy, PMMA etc. [9], and for some solvent-free preparation methods, where the complete exfoliation of GO is not easy [10]. At the same time, the reason why the value of $d\omega_D/d\varepsilon$ of GO is only 1/3~1/2 of that for graphene is worth further investigation.

8.2.2 Nanocomposites Reinforced Using Liquid Exfoliated Graphene

Graphene exfoliated by solvent is an alternative material to be used in nanocomposites for its potential for mass production at a low cost [11]. Although its reinforcement upon the matrix has been observed by methods like mechanical testing [12], the deformation of these flakes has not been observed so far in the microscale, i.e. using Raman spectroscopy. According to the study in Chapter 3, it is proposed that the small flake size of the liquid exfoliated graphene leads to a very small, if not completely absent, Raman band shift. Furthermore, the small size may also cause a poor spatial orientation of the flakes compared to that with big lateral size. The two possible mechanisms lead to a poor reinforcement efficiency of such liquid

exfoliated graphene flakes. In the future study, if any method can be utilized to experimentally observe, or model the deformation of the liquid exfoliated graphene in nanocomposites, its reinforcement mechanisms can be better revealed, to pave the way of using graphene of this kind in nanocomposites in industrial applications.

8.2.3 Wrinkling of Graphene and GO

It has been discussed in details in Chapter 7 that the size and spatial orientation of graphene affect the reinforcement efficiency in the nanocomposites remarkably. However, another almost inevitable effect on its mechanical property is the wrinkling of the graphene and GO flakes. Graphene intrinsically shows a wavy structure [13], while for GO the basal plane is highly distorted due to the introduction of defects and functional groups [2].

In fact the wrinkled structure has two different impacts. The waviness can be understood as a deviation of the spatial orientation, as observed on the monolayer graphene on substrates (Chapter 5). Meanwhile the wrinkles can also reduce or even stop the structural continuity of graphene thus the stress transfer is interrupted, as discussed in Chapter 3. Hence the effect of wrinkles should also be considered in the future study on the mechanics of graphene and GO or other 2D materials.

8.2.4 Other Two-Dimensional (2D) Materials

Graphene is clearly an excellent material for future applications. Its counterparts, other 2D materials like boron nitride [14], molybdenum disulphide [15] and tungsten disulfide, etc. [16], also possess comparable properties so they would as well be good candidates for the application of electronic device and nanocomposites. Particularly, unlike graphene, their bandgap [16] enable them to be more widely applied in the application of electronic devices. Furthermore, those 2D crystals, including graphene, can be artificially re-stacked at an angle with each other to obtain a heterostructures, showing unusual phenomena [16]. Likewise, well-defined Raman spectrum can be obtained on these 2D materials, which has already been used to identify the number of layers [14], and the crystallographic orientation [17]. In addition the strain induced Raman band shifts has been observed when the specimen was deformed [15, 17]. As the models proposed in this thesis are all based on the crystal structure

(Grüneisen parameter) and the vibrational mode (polarizability tensor) of graphene, as a result, if any Raman band of these 2D crystals can be assigned to one vibrational mode, it can as well be used to investigate the mechanics and spatial orientation of this 2D crystal in either devices or nanocomposites.

References

1. Mohiuddin, T. M. G.; Lombardo, A.; Nair, R. R.; Bonetti, A.; Savini, G.; Jalil, R.; Bonini, N.; Basko, D. M.; Galiotis, C.; Marzari, N.; Novoselov, K. S.; Geim, A. K.; Ferrari, A. C., Uniaxial Strain in Graphene by Raman Spectroscopy: G Peak Splitting, Grüneisen Parameters, and Sample Orientation. *Physical Review B* **2009**, 79, 205433.
2. Paci, J. T.; Belytschko, T.; Schatz, G. C., Computational Studies of the Structure, Behavior Upon Heating, and Mechanical Properties of Graphite Oxide. *The Journal of Physical Chemistry C* **2007**, 111, 18099-18111.
3. Krenchel, H., *Fibre Reinforcement*. Akademisk Forlag: Copenhagen, 1964.
4. Lee, C.; Wei, X.; Kysar, J. W.; Hone, J., Measurement of the Elastic Properties and Intrinsic Strength of Monolayer Graphene. *Science* **2008**, 321, 385-388.
5. Suk, J. W.; Piner, R. D.; An, J.; Ruoff, R. S., Mechanical Properties of Monolayer Graphene Oxide. *ACS Nano* **2010**, 4, 6557-6564.
6. Gong, L.; Young, R. J.; Kinloch, I. A.; Riaz, I.; Jalil, R.; Novoselov, K. S., Optimizing the Reinforcement of Polymer-Based Nanocomposites by Graphene. *ACS Nano* **2012**, 6, 2086-2095.
7. Frank, I. W.; Tanenbaum, D. M.; van der Zande, A. M.; McEuen, P. L., Mechanical Properties of Suspended Graphene Sheets. *Journal of Vacuum Science & Technology B* **2007**, 25, 2558-2561.
8. Dreyer, D. R.; Park, S.; Bielawski, C. W.; Ruoff, R. S., The Chemistry of Graphene Oxide. *Chemical Society Reviews* **2010**, 39, 228-240.
9. Putz, K. W.; Compton, O. C.; Palmeri, M. J.; Nguyen, S. T.; Brinson, L. C., High-Nanofiller-Content Graphene Oxide-Polymer Nanocomposites via Vacuum-Assisted Self-Assembly. *Advanced Functional Materials* **2010**, 20, 3322-3329.
10. Liang, J.; Huang, Y.; Zhang, L.; Wang, Y.; Ma, Y.; Guo, T.; Chen, Y., Molecular-Level Dispersion of Graphene into Poly(Vinyl Alcohol) and Effective Reinforcement of Their Nanocomposites. *Advanced Functional Materials* **2009**, 19, 2297-2302.
11. Paton, K. R.; Varrla, E.; Backes, C.; Smith, R. J.; Khan, U.; O'Neill, A.; Boland, C.; Lotya, M.; Istrate, O. M.; King, P.; Higgins, T.; Barwich, S.; May, P.; Puczkarski, P.; Ahmed, I.; Moebius, M.; Pettersson, H.; Long, E.; Coelho, J.; O'Brien, S. E.; McGuire, E. K.; Sanchez, B. M.; Duesberg, G. S.; McEvoy, N.; Pennycook, T. J.; Downing, C.; Crossley, A.; Nicolosi, V.; Coleman, J. N., Scalable Production of Large Quantities of Defect-Free Few-Layer Graphene by Shear Exfoliation in Liquids. *Nature Materials* **2014**, 13, 624-630.

12. May, P.; Khan, U.; O'Neill, A.; Coleman, J. N., Approaching the Theoretical Limit for Reinforcing Polymers with Graphene. *Journal of Materials Chemistry* **2012**, 22, 1278-1282.
13. Meyer, J. C.; Geim, A. K.; Katsnelson, M. I.; Novoselov, K. S.; Booth, T. J.; Roth, S., The Structure of Suspended Graphene Sheets. *Nature* **2007**, 446, 60-63.
14. Gorbachev, R. V.; Riaz, I.; Nair, R. R.; Jalil, R.; Britnell, L.; Belle, B. D.; Hill, E. W.; Novoselov, K. S.; Watanabe, K.; Taniguchi, T.; Geim, A. K.; Blake, P., Hunting for Monolayer Boron Nitride: Optical and Raman Signatures. *Small* **2011**, 7, 465-468.
15. Rice, C.; Young, R. J.; Zan, R.; Bangert, U.; Wolverson, D.; Georgiou, T.; Jalil, R.; Novoselov, K. S., Raman-Scattering Measurements and First-Principles Calculations of Strain-Induced Phonon Shifts in Monolayer MoS₂. *Physical Review B* **2013**, 87, 081307.
16. Geim, A. K.; Grigorieva, I. V., Van der Waals Heterostructures. *Nature* **2013**, 499, 419-425.
17. Wang, Y.; Cong, C.; Qiu, C.; Yu, T., Raman Spectroscopy Study of Lattice Vibration and Crystallographic Orientation of Monolayer MoS₂ under Uniaxial Strain. *Small* **2013**, 9, 2857-2861.